Characterization of Exoplanet Atmospheres: Spectral Retrieval and Chemistry

Thesis by

Michael R. Line

In Partial Fulfillment of the Requirements

for the Degree of

Doctor of Philosophy

California Institute of Technology

Pasadena, California

2013

(Defended May 17th, 2013)

I dedicate this thesis to those grad students who have fallen and to those that will fall further down the academic rabbit hole.

Acknowledgements

As a youngster I always found science to be a fun hobby. I loved to play around with pond scum, blow things up, launch model rockets, and probably many other things I shouldn't say. I have to first and foremost thank my parents, Bob and Deb, for fostering my creativity over the years, even if I almost blew up the basement or lit the car on fire, and for giving me more opportunities to engage my curiosity. When they got me my first telescope, I was hooked on space. I knew I wanted to study astronomy. Little did I know it would spiral out of control and turn into a Ph.D!

I also have to thank my beautiful wife Adria for marrying me and putting up with my grad student-ness for the past 4+ years. You have been a real trooper. I hope you enjoyed the ride as much as I did. The journey continues.

My years at Caltech, despite misconceptions people may have, were the best years of my life–yes, even better than at Wisconsin. What makes this place so enjoyable are the people. I was pleasantly surprised by how fun and relaxed everyone seemed to be in South Mudd. For this I must thank the PAD, 156 S. Mudd. There have been several members of the PAD since its inception: Nick Heavens, Konstantin Batygin, Ajay Limay, and Alex Lockwood. You guys are great. Nick, thanks for filling my head with the most obscure and useless facts imaginable. Konstantin, thank you for not competing and teaching me

how to fly remote controlled airplanes. Ajay, my Badger Brother, thank you for keepin' it real. Alex, thanks for being the "girl" in the office for those first few years. You put up with a lot of our crude humor. But you also fostered it. I must also thank you for keeping my wife entertained when I was busy. To the relative newcomers, Adam Waszczak (and appendage, Kelley), Masha Klesheva, and Josh Kammer, thanks. You guys fit in nicely and are worthy PAD members. Remember the rules: 1. Conservation of Suck, 2. People Care too Much, 3. The Chocolate Easter Bunny Dictates All, 4. Computers make people dumberer, 5. Don't compete!–if you do, don't complete, 6. The computer is always right, and 7. $\frac{\partial sanity}{\partial t} < 0$. I also want to thank a couple of non-PAD members of South Mudd: Aaron Wolf and Alejandro Soto. Thanks for having useful discussions with me.

I also want to thank the ChE.ESE.PSr group for the, well, for lack of a better word, *interesting* Chandler lunchtime conversations. This includes, Lindsay Yee, Jill Craven, Mandy Grantz, Christine Loza, Da Yang, Joey Ensberg, Anne Laraia, and Devin Wiley.

Thanks to Jeff Thompson for being a good friend and roomie at the Cats, even though you went to USC. I also want to thank Jacob Notbohm for teaching me how to properly grill bratwursts. Good brain food. Zach Lebo, thanks for showing me how to brew beer. This is an extremely important life skill that I will continue to practice.

I also want to thank my Cali friends outside of Caltech: Dan Isla, Elan Borenstein and Dustin Jepperson. You guys kept me sane when I needed to get away from the Caltech culture.

Thank you to my JPL colleagues: Gautam Vasisht, Pin Chen, Mark Swain, Pieter Deroo, and Glenn Orton. Gautam, you got me hooked on Lucky Baldwins. I don't know

whether to thank you or yell at you! It's good beer, but expensive. In any case, it has been a pleasure working with you. Mark, thanks for involving me in the FINESSE project. It was a tremendously insightful experience. Glenn, you introduced me to Caltech when I was a SURF student with you at JPL. You let Yuk abduct me. That was a good thing; I can't thank you enough.

I also want to thank members of Yuk Yung Mafia including, Run-Lie Shia, Xi Zhang, Le Kuai, and Li Cheng, And of course, thank you Yuk. I learned a lot from working with you not only about academic things, but some life tricks as well. The Sunday meetings were excellent character building exercises.

And finally, I'd like to thank my Thesis Advisory Committee: Andy Ingersoll, Dave Stevenson, Heather Knutson, and Geoff Blake. Thank you for guiding me to the light at the end of the tunnel.

Abstract

The study of exoplanets is rapidly evolving into an important and exciting field of its own. My investigations over the past half-decade have focused on understanding just a small sliver of what they are trying to tell us. That small sliver is their atmospheres. Atmospheres are the buffer between the bulk planet and the vacuum of space. The atmosphere is an important component of a planet as it is the most readily observable and contains the most information about the physical processes that can occur in a planet. I have focused on two aspects of exoplanetary atmospheres. First, I aimed to understand the chemical mechanisms that control the atmospheric abundances. Second, I focused on interpreting exoplanet atmospheric spectra and what they tell us about the temperatures and compositions through inverse modeling. Finally, I interpreted the retrieved temperature and abundances from inverse modeling in the context of chemical disequilibrium in the planetary atmospheres.

Contents

List of Figures

List of Tables

Chapter 1

Preface

Two decades ago we only knew of 9 planets. Now we know of $\sim$ 3000! We know of more planets outside of our solar system then we do inside. This justifies the importance of these exoplanets. They exist in a wide variety of stellar environments ranging from highly magnetized pulsars to cool red dwarfs, and, of course, solar-type environments. They also span a wide range of properties from small rocky earth-like planets to massive highly irradiated hot Jupiters. Most exoplanet investigations have focused on planet occurrence statistics and bulk properties of the planet. This is because the most common exoplanet discovery surveys are from radial velocity, which determine the planet masses, and through transit photometry surveys, which determine their radii. These two quantities can place constraints on the planetary density which can in turn be used to place very limited constraints on the interior structure. A planet is more than just a rock. Most planets have some type of atmosphere. The first hints of an exoplanet atmosphere were discovered in 2002 with detection of the sodium D lines in a transit transmission spectrum. This changed our view of these planets from uninteresting point masses to physically interesting objects....ones in which a planetary scientist would want to investigate. Since then, there have been several dozen measurements of the atmospheres of exoplanets. Thus the dawn

of the field of exo-atmospheres.

This thesis focuses on understanding the compositions of exoplanet atmosphere from both the observations and first-principles modeling. More specifically, Chapters 2 and 3 focus on the one-dimensional chemical structure of the atmospheres. Chapter 2 describes the photochemical processes that can occur in the upper atmospheres of hot Jupiters, using HD189733b as a template. Chapter 3 describes the different chemical processes occurring throughout the entire atmosphere. Mainly, this chapter focuses on the transition between the thermochemical equilibrium regime in the deep hot atmosphere and the vertically mixed portion of the atmosphere, and the implications this transition has for the abundances of CO and CH_4. Chapters' -4 and 5 take a different direction and focus on inverse techniques used to determine the compositions and temperatures from exoplanet spectra. Chapter 4 describes the optimal estimation retrieval approach as a fast approach to determining the compositions and temperatures. Additionally, Chapter 4 focuses on the information content aspect of the retrieval problem and how the mathematical formalism of optimal estimation can be used to direct the design of future instruments. In Chapter 5 I introduce CHIMERA, the **C**altec**H** **I**nverse **M**od**E**ling and **R**etrieval **A**lgorithms. Chapter 5 compares three different common inverse approaches on synthetic observations and how different quality observations produce different levels of temperature and abundance uncertainties. I also discuss the implications that the priors have on the derived C/O ratio of a planet's atmosphere. Finally, Chapter 6 discusses a new way of assessing chemical disequilibrium in planetary atmospheres. Each chapter stands on its own as it is either an accepted, submitted, or in preparation-publication.

Chapter 2

High-Temperature Photochemistry in the Atmosphere of HD189733b

Originally published in:
Line, M. R., Liang, M. C., & Yung, Y. L., 2010, ApJ, 717, 496
Reproduced by permission of the AAS

2.1 Summary

Recent infrared spectroscopy of hot exoplanets is beginning to reveal their atmospheric composition. Deep within the planetary atmosphere, the composition is controlled by thermochemical equilibrium. Photochemistry becomes important higher in the atmosphere, at levels above $\sim$1 bar. These two chemistries compete between $\sim$1–10 bars in hot Jupiter-like atmospheres, depending on the strength of the eddy mixing and temperature. HD189733b provides an excellent laboratory in which to study the consequences of chemistry of hot atmospheres. The recent spectra of HD189733b contain signatures of CH_4, CO_2, CO and H_2O. Here we identify the primary chemical pathways that govern the abundances of CH_4, CO_2, CO and H_2O in the cases of thermochemical equilibrium chemistry, photochemistry, and their combination. Our results suggest that the disequilibrium mechanisms can signif-

icantly enhance the abundances of these species above their thermochemical equilibrium value, so some caution must be taken when assuming that an atmosphere is in strict thermochemical equilibrium.

2.2 Introduction

Of the more than four hundred exoplanets discovered thus far, dozens of them are transiting hot exoplanets, dubbed hot Jupiters, from which we can obtain limited spectral information. A variety of chemical species have been detected in hot Jupiter atmospheres. These include atomic species like sodium (Na) (Charbonneau et al. 2002), atomic hydrogen (Vidal-Madjar et al. 2003), atomic carbon and oxygen (Vidal-Madjar et al., 2004), and the molecular species: CO, CO_2, H_2O and CH_4 (Tinetti et al. 2007; Swain et al. 2009a, 2009b). The detection of these species allows us to begin to explore the chemical pathways that control the observed abundances of these species. The species so far identified suggest that hydrocarbon chemistry via CH_4 photolysis as well as oxygen and water reactions is important.

The primary chemical pathways that determine chemical abundances in our own solar system are thermoequilibrium chemistry and photochemistry. Ion chemistry may also be important in these hot, highly irradiated atmospheres as it is important in the upper atmospheres of our own solar system planets (Kim & Fox 1994; Friedson et al. 2005; Vuitton et al. 2009). Current atmospheric modeling of hot-Jupiter atmospheres typically assume an atmospheric chemical composition consistent with thermochemical equilibrium (Burrows et al. 1997; Fortney et al. 2005; Sharp & Burrows 2006; Marley et al. 2007; Showman et

al. 2009; Rogers et al. 2009; Fortney et al. 2010; ODonovan et al. 2010). Photochemical or other disequilibrium mechanisms, such as quenching, have not received the same attention (see, however, Liang et al. 2003, 2004; Cooper & Showman 2006; Zahnle et al. 2009a, 2009b). Thermoequilibrium chemistry occurs in high temperature and pressure regimes where chemical timescales are shorter than potential disequilibrium mechanisms, typically occurring deep within the planetary atmosphere (Yung & DeMore 1999, pg 135). Abundances are determined solely by the thermodynamic properties of compounds in the system via the minimization of the Gibbs free energy (Yung & DeMore 1999, pg 56, pg135). Photochemistry is a disequilibrium process due to UV alteration by the host star. Photochemistry therefore should be important in hot-Jupiter atmospheres, given their proximity to their host stars (Liang et al. 2003).

Liang et al. (2003) were the first to explore the photochemistry that may occur on highly irradiated giant planets through modeling the sources of atomic hydrogen in HD209458b. However, some of the rate coefficients used in that study are unsuitable for these high-temperature regimes, and several key reactions governing the production and loss of H_2O and CO_2 were not included. Additionally, better estimates of temperature and vertical transport profiles can be obtained from more sophisticated general circulation model (GCM) simulations.

Zahnle et al. (2009a, 2009b) explored products of sulfur photochemistry and how they may be responsible for the strong UV absorbers that cause thermal inversions as well as the formation of hydrocarbon soot. So far there have been no detections of sulfur species on these hot Jupiters.

The goal of this investigation is to understand the chemistry that produces the observed abundances of $\sim 1\times10^{-5}$ –1×10^{-3}, $\sim 1\times10^{-6}$ –1×10^{-3}, 1×10^{-5} –1×10^{-3}, and $\sim 1\times10^{-6}$ –1×10^{-7} for CO, CO_2, H_2O and CH_4, respectively, as derived from the dayside emission spectrum of HD189733b (Swain et al. 2009a, Madhusudhan & Seager 2009) by combining separate photochemical and thermochemical models and then comparing the results to simulations using photochemistry/thermochemistry alone. Furthermore, it has been recently suggested by Madhusudhan & Seager (2009) that there may be as much as 700 ppm of CO_2 present in the atmosphere of HD189733b. The discrepancy between this value and the value from Swain et al. (2009a) is due to the assumed vertical distribution of CO_2 in the atmosphere (constant, versus high concentration at one pressure level), which is not well constrained. This discrepancy suggests that there is much degeneracy in retrieving temperature and mixing ratio profiles, and that the exact values of the mixing ratios, or their vertical distributions, of the detected species are not well known. In this study, we identify the important mechanisms that govern the abundance of these detected species and their vertical distribution, using HD189733b as an example.

2.3 Modeling

We use both a thermochemical model and a photochemical model to explain the observed abundances of CO, CO_2, H_2O and CH_4 in the atmosphere of HD189733b. The inclusion of sulfur or nitrogen species (e.g., see Zahnle et al. 2009a, 2009b) is beyond the scope of this paper and will be explored in later studies. Currently, we want to understand the effects that temperature and eddy mixing have on the photochemically derived mixing ratios. We

adopt a hot profile representative of dayside temperatures and cool profile representative of night-side temperatures for 30 N from Showman et al. (2009) (Figure 2.1). We assume isothermal profiles above the upper boundary of the Showman et al. (2009) GCM for the sake of simplicity. These two profiles appear to have a thermal inversion near 1 mbar with a day-night contrast of $\sim$500 K. The use of two T-P profiles will illuminate the day/night contrast of the modeled species. Though HD189733b is not expected to have an inversion, we still choose these T-P profiles because they span the range of hot Jupiter temperature profiles in the literature (Fortney et al. 2006; Tinetti et al. 2007; Burrows et al. 2008), and the existence of an inversion does not affect the major chemical pathways.

In order to determine the thermoequilibrium abundances we use the Chemical Equilibrium with Applications model developed by Gordon & McBride (1994). These abundances at the appropriate lower boundary (explained later) will be used for our lower mixing ratio boundary condition in the photochemical model. Thermochemical calculations require only pressure and temperature along with the relative molar mixing ratios of the atomic species involved in the compounds of interest, in this case C, O and H (no N or S because they have not yet been detected). For the sake of simplicity, and in the absence of any other information, we assume solar abundance of these species ([C]/[H]$\sim 4.4\times10^{-4}$, [O]/[H]$\sim 7.4\times10^{-4}$, where [i] denotes the concentration of species i (Yung & DeMore 1999 pg. 112). The thermochemical model computes the abundances of all possible compounds formed by those atomic species via a Gibbs free energy minimization routine (Gordon & McBride 1994). We compute the equilibrium abundances at each pressure-temperature level for our chosen temperature profiles. We would expect to see thermochemical equi-

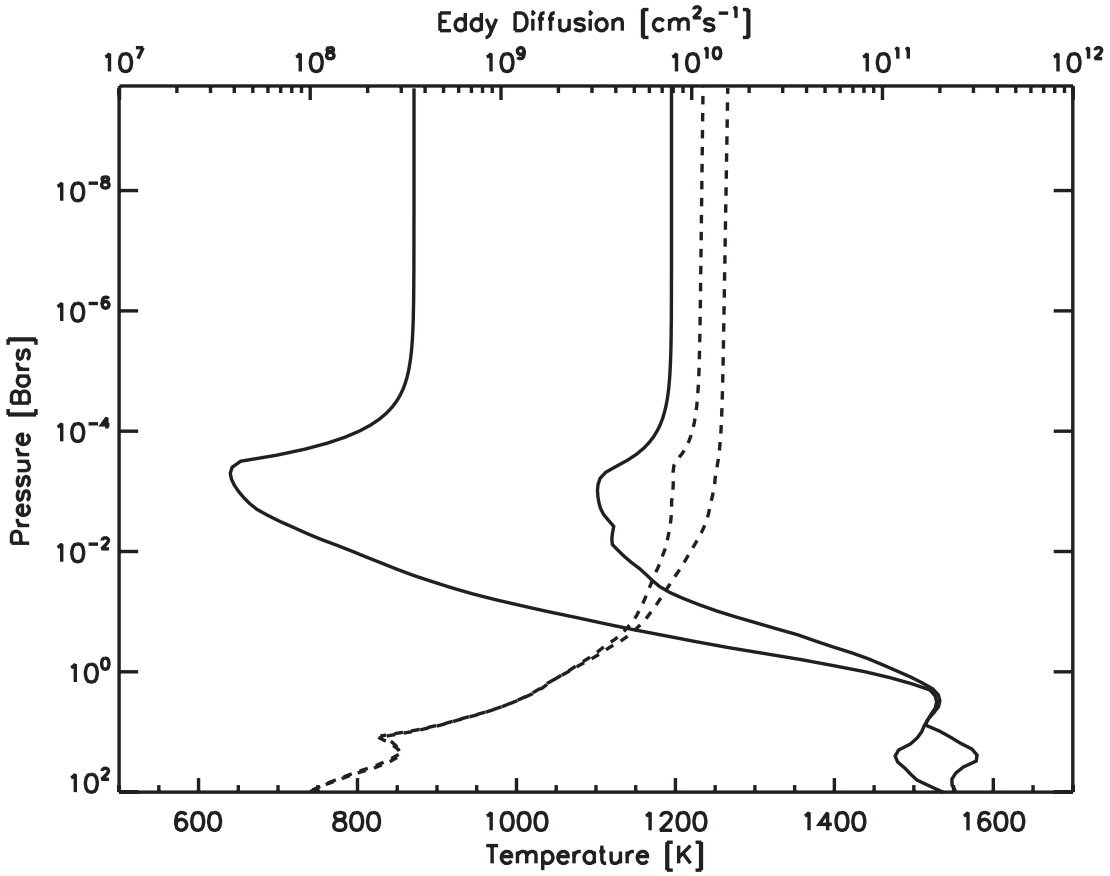

Figure 2.1: Temperature (solid) and eddy diffusion (dashed) profiles for the model atmosphere. The cooler temperature profile is taken from 30° N from the night side of the model by Showman et al., (2009). The hotter temperature profile is taken from the dayside at the same latitude. The larger eddy diffusion is estimated as discussed in the text (the larger values are for the dayside). Eddy diffusion is read along the top axis, temperature is read along the bottom axis.

librium abundances in an atmosphere that is not undergoing any dynamical or photochemical alterations, or where chemical timescales are much shorter than any disequilibrium timescales (Prinn & Barshay 1977; Smith 1998; Cooper & Showman 2006).

To compute the photochemical abundances of the species of interest, we use the Caltech/JPL-KINETICS 1D photochemical model (Allen et al. 1981; Yung et al. 1984; Gladstone et al. 1996; Moses et al. 2005) for HD189733b. HD189733b is in a 2.2 day period orbiting at 0.03 AU around a K2V star. We use the UV stellar spectrum from HD22049 which is also a K2V star (Segura et al. 2003). This K2V star has $\sim$2 orders of magnitude less flux below $\sim$3000 than the solar spectrum used in Zahnle et al. (2009a, 2009b) giving significantly different results. The model computes the abundances for 32 species involving H, C and O in 258 reactions including 41 photolysis reactions and includes both molecular and eddy diffusion. The model uses the same hydrocarbon and oxygen chemistry as in Liang et al. (2003) and Liang et al. (2004) but with high-temperature rate coefficients for the key reactions involved in the production and loss of H, CH_4, CO_2, CO, OH and H_2O. The reaction rates given in the remainder of this paper are taken from Baulch et al. (1992) unless otherwise noted. We have also added two key reactions involved in the destruction of H_2O and CO_2 . We have not, however, added a complete suite of reactions in order to achieve thermochemical equilibrium kinetically (e.g., Visscher et al. 2010). We do not expect this omission to invalidate our results, as we have included the key chemical pathways that govern the production and loss of the species of interest. The model atmosphere for the photochemical model uses the two temperature profiles described above. The lower boundary of the photochemical model is important in determining the mixing ratios throughout

the atmosphere. We will estimate this lower boundary using quench level arguments rather than arbitrarily choosing some level. For more details on quench level estimation we refer the reader to Prinn & Barshay (1977), Smith (1998), and Cooper & Showman (2009),.

Eddy and molecular diffusion are key parameters determining the quench level and the distribution of the abundances in the atmosphere. Eddy diffusion is the primary vertical transport mechanism in our 1D model. The strength of vertical mixing will determine where in the atmosphere the species become chemically quenched, and thus defines the lower boundary conditions for the photochemical model (Prinn & Barshay 1977; Smith 1998). Following Prinn & Barshay (1977), the transport timescale is given by

$$\tau_{trans} \simeq \frac{L^2}{K_z} \tag{2.1}$$

where L is a vertical length scale typically chosen to be the scale height and K_z is the eddy diffusion coefficient. The chemical loss timescale of species i is given by

$$\tau_{chem,i} = \frac{[i]}{L_i} \tag{2.2}$$

where $[i]$ is the concentration of species i and L_i is the loss rate of species i, typically determined by the bottleneck reaction. The quench level for species i is defined where $\tau_{trans} = \tau_{chem,i}$. For levels where $\tau_{trans} < \tau_{chem,i}$ the mixing ratio of species i is fixed at the quench level value. For levels below the quench level, the compounds reach thermochemical equilibrium.

In order to determine the quench level in the atmosphere HD189733b, we must first

estimate the strength of eddy mixing and the timescale for the conversion of CO to CH_4 (Prinn & Barshay 1977; Griffith & Yelle 1999). The eddy diffusion profile adopted in this model is derived from a globally root-mean-squared (RMS) averaged vertical wind profile from a GCM (Showman 2010 private communication) and is estimated by

$$K_z \sim wL \tag{2.3}$$

where w is the RMS averaged of the vertical wind velocity. Smith (1998) suggests that the appropriate length scale is some fraction of the scale height. Here we assume that it is the scale height, thus giving us an upper limit on eddy diffusion. The GCM derived RMS-averaged vertical winds range from 0 (at $\sim$200 bars) to 7 m/s ($\sim$0.8 mbar). The vertical wind is assumed to be constant above this height. Combining this with a typical scale height of $\sim$200 km gives an eddy diffusion of $\sim 10^{10}$ cm^2 s^{-1} (Figure 2.1). Typical transport timescales from Equation 2.1 are on the order of $\sim 10^5$ s.

The rate-limiting step in the conversion of CO to CH_4, and thus the reaction determining the chemical lifetime of CO, is

$$\mathrm{H} + \mathrm{H_2CO} + \mathrm{M} \rightarrow \mathrm{CH_3O} + \mathrm{M} \tag{2.4}$$

(Yung et al. 1988; Griffith & Yelle 1999; Cooper & Showman 2006). The rate coefficient in reaction 2.4 has not been measured in the lab, but its high-pressure ($\sim$1 bar) reverse

reaction rate has been measured to be

$$k_r = 1.4 \times 10^{-6} T^{-1.2} e^{-7800/T} cm^6 s^{-1} \tag{2.5}$$

where T is the temperature at which the reaction takes place (Page et al. 1989). If we assume the high-pressure limit, which is reasonable for where quenching is expected to occur, k_f can be estimated via

$$\frac{k_f}{k_r} = K_{eq} = e^{(G_f - G_r/RT)} \tag{2.6}$$

where K_{eq} is the equilibrium constant for the net thermochemical reaction (Yung et al. 1988)

$$\mathrm{H} + \mathrm{H_2CO} \rightleftharpoons \mathrm{CH_3O} \tag{2.7}$$

where G_f and G_r are the Gibbs free energies of the reaction, given, respectively, by $H[H] + H[H2CO] - T(S[H] + S[H2CO])$ and $H[CH3O] - TS[CH3O]$ with $H[X]$ being the enthalpy of formation of species X and $S[X]$ being the entropy of species X. The enthalpies and entropies of the given species are taken to be at 1000 K and can be found at http://www.grc.nasa.gov/WWW/CEAWeb/ceaThermoBuild.htm. With the relevant thermochemical data and equations 2.5 and 2.6 we can estimate the forward reaction rate of reaction 2.4 to be

$$k_r = 3.07 \times 10^{-12} T^{-1.2} e^{3927/T} \tag{2.8}$$

The CO chemical lifetime can then be determined using:

$$\tau_{chem} \sim \frac{[CO]}{k_f[H][H_2CO]} \tag{2.9}$$

where the concentrations of CO, H and H_2CO are determined via the thermochemical model. Upon equating 2.9 with Equation 2.1 using the dayside temperature profile we determine the quench level, and thus the lower boundary to be $\sim$3 bars ($\sim$1530 K) which is similar to the results of Cooper & Showman (2006) for HD209458b. This pressure level is much higher than that of Jupiter ($\sim$100 bars) (Prinn & Barshay 1977) and is similar to that of brown dwarfs ($\sim$6 bars) (Griffith & Yelle 1999). Choosing a length scale less than the scale height as suggested by Smith (1998) can move the quench level to a higher pressure. This is because the chemical timescale in Equation 2.9 increases with increasing altitude and lower temperature. Using a length scale of 0.1H instead of H moves the quench level to $\sim$8 bars, at where there is very little change in the thermochemical mixing ratios from $\sim$3 bars (Figure 2.2). Additionally, there is no significant difference in quench level between the nightside and dayside because the two T-P profiles converge near the quench level.

We assume a zero concentration gradient at the lower boundary in order to allow photochemical products to sink down into the deeper atmosphere except for the observed species of CO, H_2O, CH_4, CO_2. For these species we fix the mixing ratios to be the thermochemically derived values at the $\sim$3 bar quench level: 8.41×10^{-4}, 6.36×10^{-4}, 4.09×10^{-5}, and 1.96×10^{-7}, respectively, for the dayside and 8.39×10^{-4}, 6.38×10^{-4}, 4.25×10^{-5}, and 1.98×10^{-7}, respectively, for the nightside. We assume a zero flux boundary condition for the top of the atmosphere, i.e., little or no atmospheric escape, though this assumption may

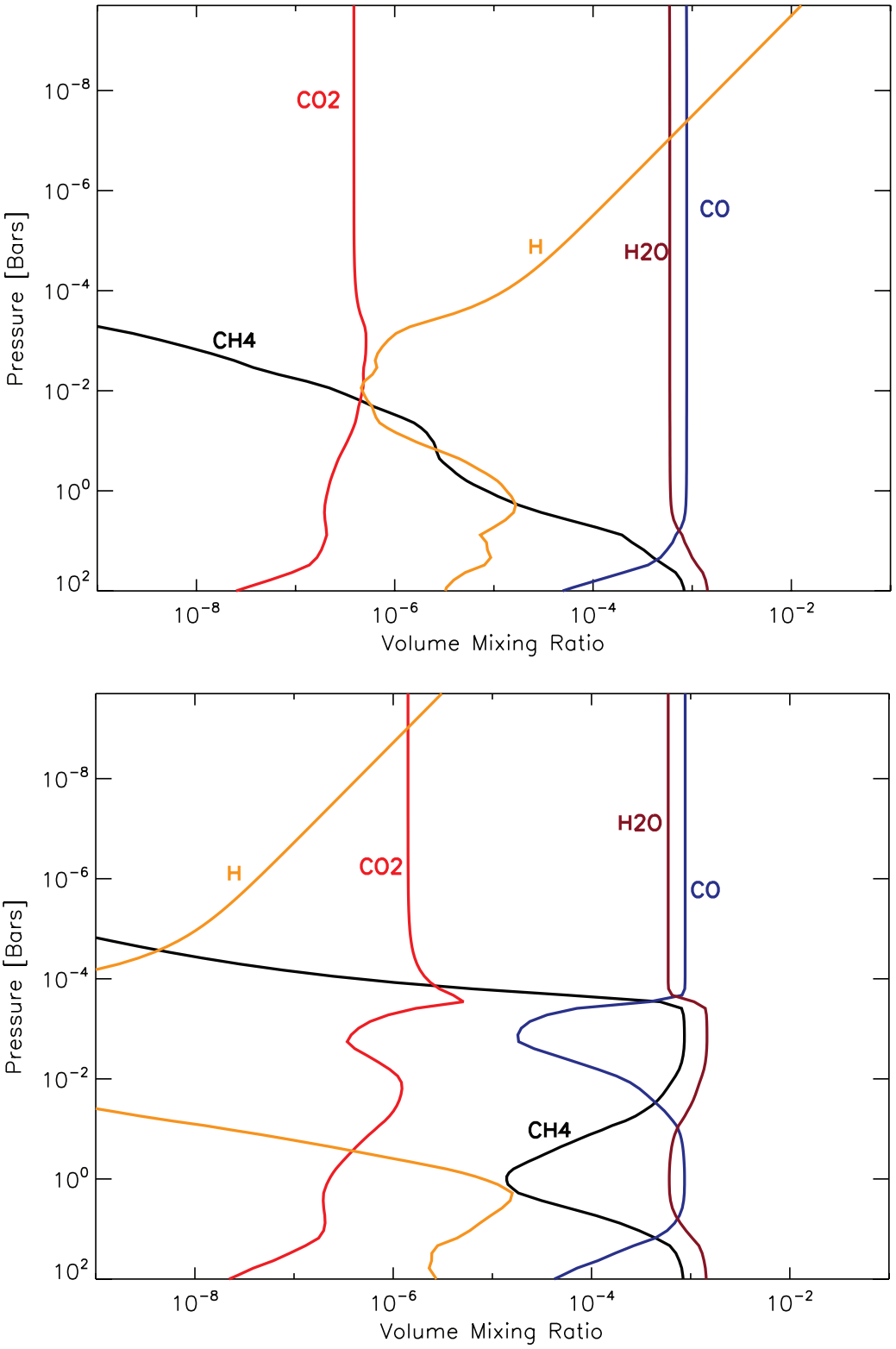

Figure 2.2: Thermochemical equilibrium mixing ratios derived from the temperature profiles in Figure 2.1. The top Figure shows the mixing ratios derived for the dayside (hotter) profile. The bottom Figure shows the mixing ratios derived for the (nightside) cooler profile.

not be entirely true for atomic hydrogen (Vidal-Madjar et al. 2003). This assumption has a negligible effect on the results.

2.4 Results

The thermochemically derived mixing ratios (relative to H_2) are shown in Figure 2.2. Again, these are the expected mixing ratios if there were no dynamical or photochemical process occurring in the atmosphere, which we know not to be true. If we focus first on the dayside profiles, we can see that CO is the dominant carbon bearing species and remains relatively constant with altitude as do H_2O and CO_2. We also notice that CH_4 falls off rapidly with increasing altitude (decreasing pressure). We can understand this result by noting that CO, CH_4 and H_2 abundances are related through the net thermochemical reactions

$$\mathrm{CH_4 + H_2O \rightleftharpoons CO + 3H_2} \tag{2.10}$$

$$\mathrm{CO + H_2O \rightleftharpoons CO_2 + H_2} \tag{2.11}$$

Then by Le Chateliers principle, as the total partial pressure of the atmosphere decreases, the system will want to resist that decrease in order to maintain equilibrium by producing more molecules (smaller molecules), which in this case results in the production of CO and H_2. Upon comparing the dayside profiles to the cooler nightside profile, we notice that CH_4 becomes more abundant. CH_4 is more energetically favorable at lower temperatures and is much more sensitive to the effects of temperature than CO and CO_2. We also note that atomic hydrogen is more abundant at warmer temperatures than at cooler temperatures due

to the entropy term in the Gibbs free energy. From a thermochemical perspective, we can expect $\sim$10 mbar mixing ratios of the observable species, CO, H_2O, CH_4 and CO_2 to range from: (2–9)$\times 10^{-4}$, (6–13)$\times 10^{-4}$, (2.6–6758)$\times 10^{-7}$, (4.7–16)$\times 10^{-7}$, respectively, due to the day/night contrast. For comparison, the measured values from Swain et al. (2009a) and Madhusudan & Seager (2009) for CO, H_2O, CH_4 and CO_2 are, respectively, $\sim 10^{-4}$–10^{-2}, 10^{-5}–10^{-3}, $\sim 10^{-7}$, and 10^{-6}–10^{-3}.

2.4.1 Photochemical Results

We run four cases of our photochemical model (Figure 2.3) in order to compare the effects of temperature and photolysis versus no photolysis on the mixing ratios (relative to H_2) for H, CO, H_2O, CO_2 and CH_4 . In the following subsections we will discuss the important reactions governing the production and loss of each of the relevant species.

2.4.1.1 H_2O, OH, and H

The primary reactions that govern the production and loss of H_2O are

$$\mathrm{H_2O + h\nu \rightarrow H + OH} \qquad \mathrm{J_{71} = 2.587 \times 10^{-8} s^{-1} (1\ mbar)} \qquad R71$$

$$\mathrm{OH + H_2 \rightarrow H_2O + H} \qquad \mathrm{k_{137} = 1.7 \times 10^{-16} T^{1.6} e^{-1660/T} cm^3 s^{-1}} \qquad R137$$

$$\mathrm{H + H_2O \rightarrow OH + H_2} \qquad \mathrm{k_{254} = 7.5 \times 10^{-16} T^{1.6} e^{-9718/T} cm^3 s^{-1}} \qquad R254$$

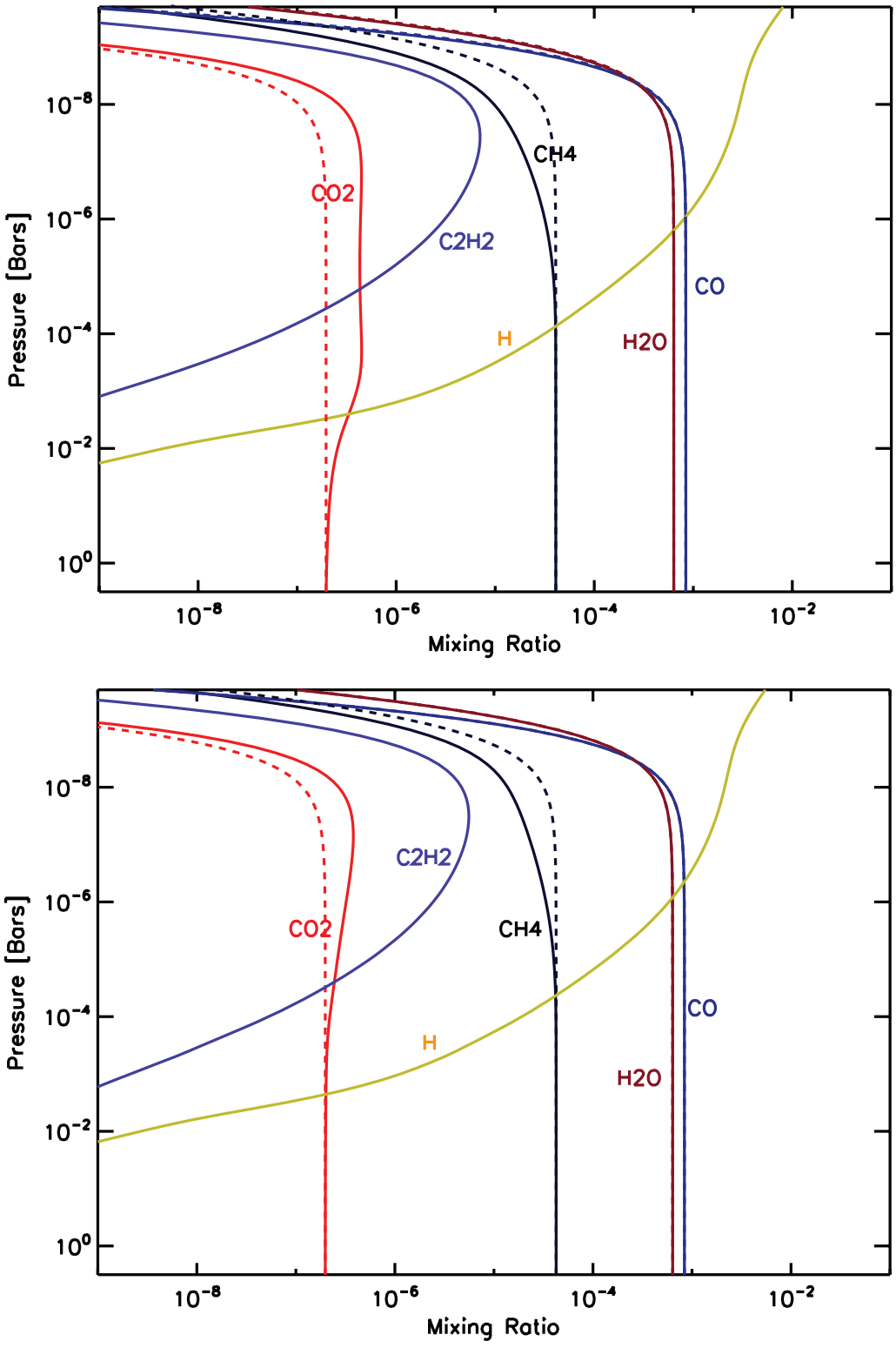

Figure 2.3: Photochemical mixing ratios (solid) compared to the case with no photochemistry and only quenching (dashed) for the day (top) and night (bottom) temperature profiles. The dashed curves on the bottom plot are representative of what may be seen on the night side of the planet. Note that there is virtually no H or C_2H_2 for the cases in which photochemistry is turned off (e.g., the dashed curves for these species are not in the plot range).

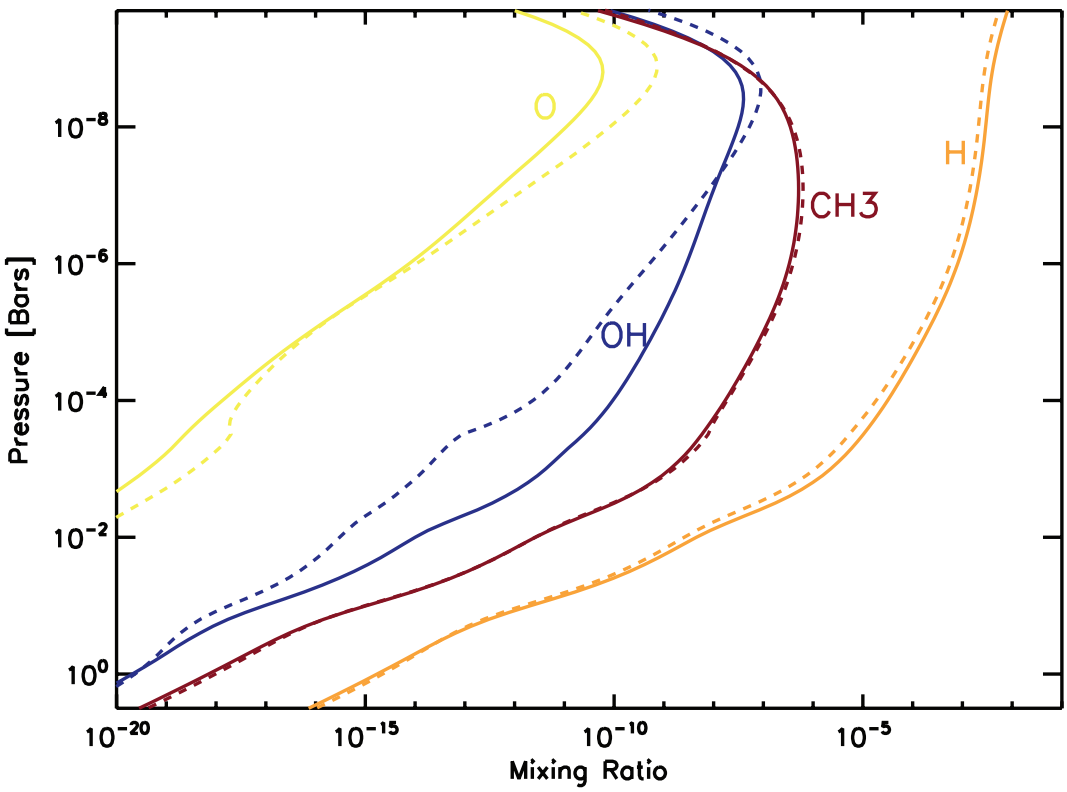

Figure 2.4: Important radical species involved in pathways governing the abundances of CH_4, H_2O, CO and CO_2. Solid is for the dayside temperature profile, dashed is for the nightside temperature profile. The abundances of radicals increase with decreasing pressure due to the availability of dissociating photons higher in the atmosphere.

R137 and R254 are fast enough to readily recycle each other so that the abundance of H_2O remains relatively constant with altitude at the quench level value of $\sim 6.36 \times 10^{-4}$ below the homopause at $\sim$10 nbar. The photolysis of H_2O does not significantly affect its abundance in the observable atmosphere as can be seen in Figure 2.3, because the loss timescale of H_2O when struck by photolysis is everywhere longer than the transport timescale, thus allowing recently photolyzed parcels to be readily replenished by upwelling. The photolysis of H_2O, however, does produce the important OH and H radicals that drive the remainder of the chemistry (Figure 2.4), with the net result being the conversion of H_2 to 2H.

H_2O photodissociates into OH and H at wavelengths lower than 2398 Å. For HD189733b below this wavelength there are $\sim 2 \times 10^{15}$ photons cm^{-2} s^{-1} available for H_2O photolysis. For comparison, the UV flux below this wavelength at Jupiter is $\sim 7 \times 10^{12}$ photons cm^{-2} s^{-1} and for HD209458b, $\sim 10^{17}$ photons cm^{-2} s^{-1}. OH and H increase with increasing altitude due to the availability of more UV photons. The production of H at high altitudes via H_2O photolysis may be the driver of hydrodynamic escape on hot Jupiters (Liang et al. 2003).

In short, the abundance of H_2O is primarily set by the thermochemical equilibrium value at the lower boundary condition, taken here to be the quench level, and rapidly decreases with altitude above the homopause. If the quench level changes, the observable value of H_2O will change but not significantly, as can be seen in Figure 2.2. The derived value here is slightly higher than the Swain et al. 2009a dayside emission observations of $(0.1–1) \times 10^{-4}$ but is more consistent with the value obtained by the Tinetti et al. (2007) terminator observations of $\sim 5 \times 10^{-4}$. The day to night contrast is nearly unnoticeable in Figure 2.3.

2.4.1.2 CO & CO_2

Thermochemically, CO is the dominant carbon reservoir in hot atmospheres above $\sim$10 bars (Figure 2.2). The abundance of CO is set by the quench level thermochemical equilibrium abundance of 8.4×10^{-4}. The abundance of CO_2 is determined via the interconversion of oxygen from the large reservoirs of CO and H_2O into CO_2 via the OH radical. Deeper down in the atmosphere, say, below the quench level, or in the presence of weak vertical transport (low eddy diffusion), oxygen is moved into CO_2 via the following reactions

$$\mathrm{OH + H_2 \rightarrow H_2O + H} \qquad \mathrm{k_{137} = 1.7 \times 10^{-16} T^{1.6} e^{-1660/T} cm^3 s^{-1}} \qquad R137$$

$$\mathrm{OH + CO \rightarrow CO_2 + H} \qquad \mathrm{k_{152} = 1.05 \times 10^{-17} T^{1.5} e^{250/T} cm^3 s^{-1}} \qquad R152$$

$$\mathrm{H + H_2O \rightarrow OH + H_2} \qquad \mathrm{k_{254} = 7.5 \times 10^{-16} T^{1.6} e^{-9718/T} cm^3 s^{-1}} \qquad R254$$

$$\mathrm{H + CO_2 \rightarrow OH + CO} \qquad \mathrm{k_{137} = 2.51 \times 10^{-10} e^{-13350/T} cm^3 s^{-1}} \qquad R255$$

R152 is the reaction that gives the oxygen from H_2O and CO to CO_2. There is no net production or loss of species from these reactions, meaning they will assume thermochemical equilibrium. Assuming steady state, these 4 reactions can be combined to give the kinetically achieved thermochemical mixing ratio of CO_2 in terms of the rate constants (k) and mixing ratios (f) of the large reservoirs of CO and H_2O

$$f_{CO_2} \sim \frac{k_{152} k_{254}}{k_{137} k_{255}} f_{H_2O} f_{CO} = 1.85 \times 10^{-7} T^{1.5} e^{5542/T} f_{H_2O} f_{CO} \tag{2.12}$$

This relation would determine the mixing ratio of CO_2 in the absence of any disequilibrium mechanisms such as photochemistry or quenching. Using the thermochemical mixing ratios of H_2O ($\sim 6 \times 10^{-4}$) and CO ($\sim 9 \times 10^{-4}$) and evaluating the rate constants at the daytime temperature (T$\sim$1200 K) we obtain a CO_2 mixing ratio of $\sim 4 \times 10^{-7}$ which is consistent with Figure 2.2.

In the photochemical limit (in the absence of eddy mixing), the photolysis reactions, R71 and R75 become more important and effectively replace R254 and R255, so the im-

portant chain of reactions becomes

$$\mathrm{OH + H_2 \rightarrow H_2O + H} \qquad \mathrm{k_{137} = 1.7 \times 10^{-16} T^{1.6} e^{-1660/T} cm^3 s^{-1}} \qquad R137$$

$$\mathrm{OH + CO \rightarrow CO_2 + H} \qquad \mathrm{k_{152} = 1.05 \times 10^{-17} T^{1.5} e^{250/T} cm^3 s^{-1}} \qquad R152$$

$$\mathrm{H_2O + h\nu \rightarrow H + OH} \qquad \mathrm{J_{71} = 2.587 \times 10^{-8} s^{-1} (1\ mbar)} \qquad R71$$

$$\mathrm{CO_2 + h\nu \rightarrow CO + O} \qquad \mathrm{J_{75/76} = 4.4 \times 10^{-10} e^{-13350/T} s^{-1}} \qquad R75/76$$

$$\mathrm{Net : OH + H_2 \rightarrow 3H + O}$$

Combining these reactions allows us to estimate the photochemical mixing ratio of CO_2 with

$$f_{CO_2} \sim \frac{k_{152} J_{71}}{k_{137} J_{75+76}} f_{H_2O} f_{CO} = 0.062 T^{-0.1} e^{1910/T} \frac{J_{71}}{J_{75+76}} f_{H_2O} f_{CO} \qquad (2.13)$$

where J is the photolysis rate of the indicated photolysis reaction. As an extreme case we assume the top of atmosphere photolysis rate of H_2O is $\sim 10^{-5} s^{-1}$, the photolysis rate of CO_2 is $\sim 5 \times 10^{-8}$ s^{-1} , and the dayside temperature is $\sim$1200 K, giving an upper limit of $\sim$few $\times$ 10^{-5} for f_{CO_2}. Equation 2.13 suggests that the abundance of CO_2 is photochemically enhanced rather than reduced. The abundance of CO_2 in the presence of only quenching (no photochemistry) will remain fairly constant below the homopause at $\sim$1 nbar (Figure 2.3). This is due to the lack of excess OH produced in R71 used to drive R152 to produce CO_2. Again, for comparison, the observed mixing ratio of CO_2 from Swain et

al. (2009a) and Madhusudhan & Seager (2009) range from $\sim 10^{-6}$–10^{-3}.

2.4.1.3 CH_4 and Heavier Hydrocarbons

The primary fate of CH_4 in the upper atmosphere is reaction with H to produce CH_3, which immediately reacts with H_2 to restore CH_4,

$$\mathrm{CH_4 + H \rightarrow CH_3 + H_2} \qquad \mathrm{k_{28} = 2.20 \times 10^{-20} T^3 e^{-4041/T} cm^3 s^{-1}} \qquad R28$$

$$\mathrm{CH_3 + H_2 \rightarrow CH_4 + H} \qquad \mathrm{k_{53} = 1.14 \times 10^{-20} T^{2.6} e^{-4739/T} cm^3 s^{-1}} \qquad R28$$

The result is a closed loop. However, the above recycling is not perfect, and the following sequence of reactions occur in the upper atmosphere

$$\mathrm{2[CH_4 + H \rightarrow CH_3 + H_2]} \qquad \mathrm{k_{28} = 2.20 \times 10^{-20} T^3 e^{-4041/T} cm^3 s^{-1}} \qquad R28$$

$$\mathrm{2[CH_3 + h\nu \rightarrow CH_2 + H]} \qquad \mathrm{J_4 = 1.95 \times 10^{-3} s^{-1} (1\ mbar)} \qquad R4$$

$$\mathrm{CH_2 + CH_2 \rightarrow C_2H_2 + 2H} \qquad \mathrm{k_{48} = 1.80 \times 10^{-10} e^{-400/T} cm^3 s^{-1} (1\ mbar)} \qquad R4$$

$$\mathrm{Net : 2CH_4 \rightarrow C_2H_2 + 2H_2 + 2H}$$

The net result is production of C_2H_2 in the upper atmosphere at the $\sim$1 ppm level. No other C_2 hydrocarbons are produced in significant quantities. The primary fate of C_2H_2 from the

upper atmosphere is downward transport, followed by hydrogenation back to CH_4. The abundance of CH_4 is $\sim 4 \times 10^{-5}$, which is several order of magnitudes larger than the $\sim 10^{-7}$ detected by Swain et al. (2009) and used by Liang et al. (2003) but is more consistent with the terminator observations of CH_4 giving mixing ratios of up to 5×10^{-5} (Swain et al. 2008). The abundance of CH_4 produced via quenching is also many orders of magnitude larger than the expected thermochemical equilibrium values (see Figures 2 and 3) with very little thermochemically derived CH_4 ($< 10^{-9}$) present above 0.1mbar.

2.5 Discussion

We have analyzed the important disequilibrium mechanisms, photochemistry and simple dynamical quenching that govern the vertical distribution of the observed species in hot-Jupiter atmospheres. The important chemical pathways that govern the abundances of the observable species are illustrated in Figure 2.5. With the exception of methane, our derived abundances are consistent with the observations of Swain et al. (2009a). We obtained a value of $\sim 4 \times 10^{-5}$, while the observations suggest two orders of magnitude less (Swain et al. 2009a). The observed value of $\sim 10^{-7}$ corresponds to the thermochemical equilibrium value at $\sim$10 mbar. This would mean the quench level would have to be at this pressure, suggesting an eddy diffusion on the order of $\sim 10^3$ cm^2 s^{-1} from Equation 2.9 and Equation 2.1. Alternatively, it may be possible that the observations are probing above the homopause where the mixing ratio can be substantially less than $\sim 10^{-5}$ (Figure 2.3). Our value of methane is also several orders of magnitude larger than reported by Liang et al. (2003) for HD209458b. This is because the temperature at the lower boundary used in

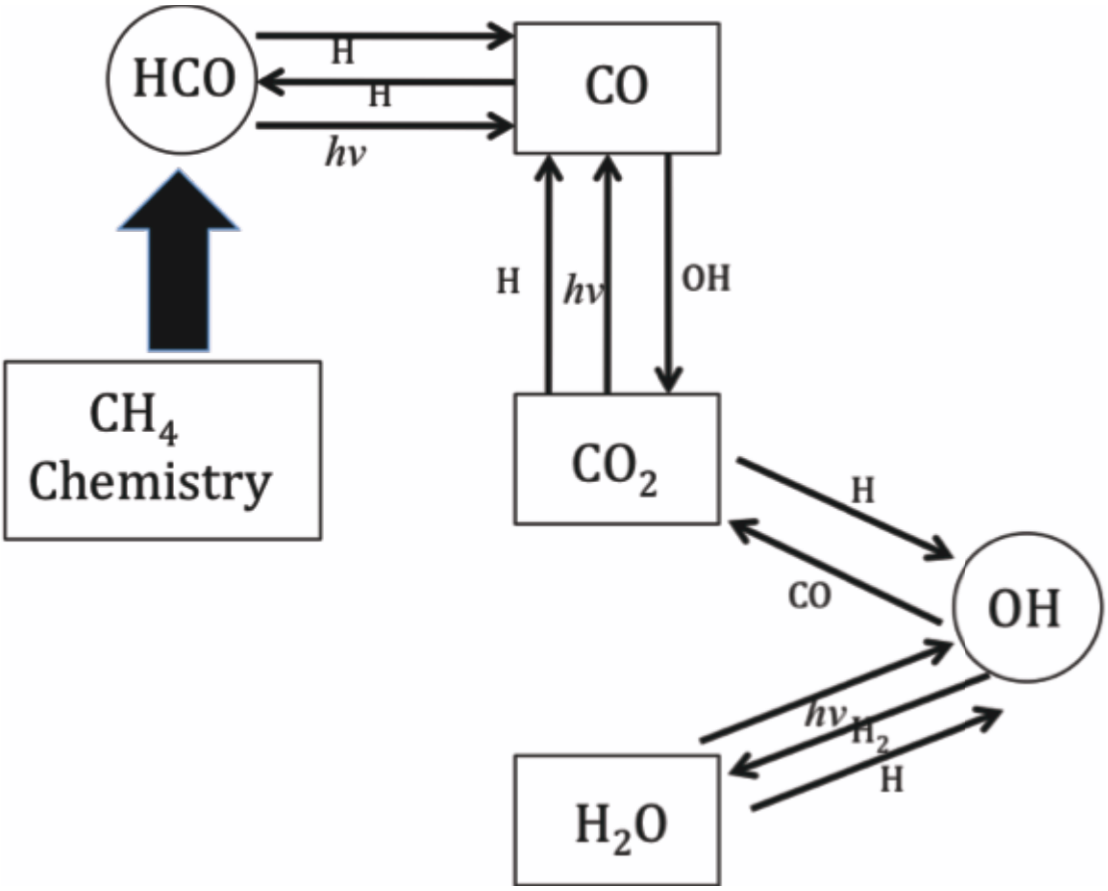

Figure 2.5: Photochemical web illustrating the important chemical pathways that govern the production and loss of the observable species. The boxes represent the observed species and the circles represent species yet to be observed but are key in the production and loss of the observed constituents.

Liang et al. (2003) for HD209458b is ∼700 K hotter than our lower boundary temperature of ∼1530 K and methane is less stable at higher temperatures. The vertical profile for CH_4 derived here falls off much slower than that in Zahnle et al. (2009a). This is because the K2V UV flux used in this investigation is ∼2 orders of magnitude less than the solar UV flux used in Zahnle et al. (2009a). The more UV photons available, as there would be around a solar type G star, the greater the destruction of CH_4, and hence the greater the production of C_2H_2.

The metallicity of these hot Jupiters is not well constrained. Swain et al. (2009a)

suggests that the metallicity for HD189733b may be subsolar and that the [C]/[O] ratio is between 0.5 and 1. We assumed solar metallicity, but we can explore what might happen if this is not the case. Changes in metallicity will affect the thermochemical equilibrium abundances. This will in turn change the lower boundary mixing ratios. We varied the metallicity (taken here to be ([C]+[O])/[H]) from one tenth solar up to ten times solar to see what effect it would have on our lower boundary mixing ratios (Figure 2.6). The thermochemical mixing ratios of CO, H_2O and CO_2 vary by several orders-of-magnitude over the range of metallicities, where as CH_4 changes very little. This orders of magnitude change at the lower boundary due to metallicity will affect our photochemical results by the same amount. With ten times the solar metallicity we could expect mixing ratios of CO and H_2O to be as high as $\sim$0.1 and CO_2 as high as 10^{-5}. CO_2 is more readily affected by metallicity than the other species because it has two oxygens as opposed to COs one oxygen (Fegley & Lodders 2002; Zahnle et al. 2009a). Even higher metallicites will produce more extreme abundances of CO, CO_2 and H_2O.

The [C]/[O] ratio, also affects the thermochemical abundances. Here we vary the [C]/[O] ratio from 0.1 to 10 times the solar ratio of $\sim$0.6 while keeping the overall metallicity ([C]+[O])/[H]) constant at the solar value (Figure 2.6). The mixing ratio of CO does not vary significantly, but can get as high as $\sim 10^{-3}$ given a slightly super-solar [C]/[O] ratio. CO_2 rapidly decreases for ratios above solar and can get as low as 0.1 ppb for 10 times the solar ratio. As the [C]/[O] ratio increases past 1, H_2O and CH_4 swap roles in taking up H and can change as much as 3 orders of magnitude.

There appears to be minor compositional variability between the nightside and dayside.

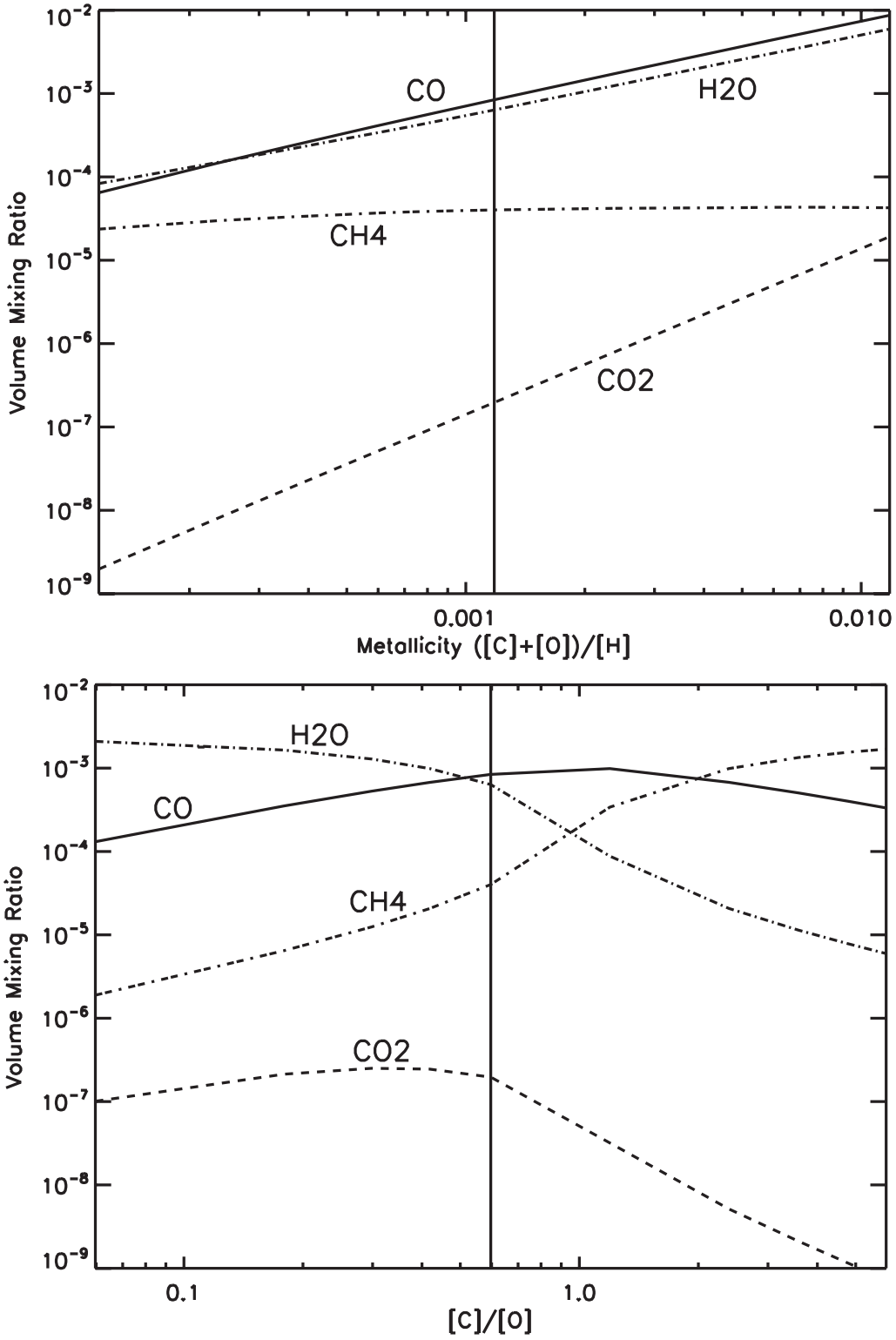

Figure 2.6: The effects of changing metallicity (top) and C/O ratio (bottom) on the 3 bar quench level mixing ratios for CO, H_2O, CO_2 and CH_4. The vertical lines in each plot represent the solar values.

Comparing the solid curves in the top of Figure 2.3 to the dashed curves in the bottom of Figure 2.3 gives some sense of the magnitude of the day-night variability. There are no dissociating photons on the nightside, so the quench level mixing and atmospheric circulation determine the abundance throughout the rest of the atmosphere below the homopause. There is a less than 1% maximum variability in CO and H_2O, a factor of $\sim$3 more CH_4 on the nightside over the dayside and up to a factor of 2 more CO_2 on the dayside. CO_2 and CH_4 concentrations experience more variability, because they are most affected by photochemical reactions that only occur on the dayside (CH_4 gets destroyed due to R141 and photolysis, CO_2 enhanced via Equation 2.13). C_2H_2 would exhibit much variability since it is produced strictly from photochemistry. We could expect to see up to 1 ppm on the dayside of these hot planets with very minute amounts on the nightside where it would be readily thermochemically recycled back to methane. Terminator observations should fall somewhere between the dayside and nightside values.

2.6 Conclusions

We have shown that both photochemistry and vertical quenching can significantly alter the abundances of CO_2, CH_4 and C2H2 in hot-Jupiter atmospheres. Vertical quenching determines the lower boundary values and thus the mixing ratios of CO and H_2O, which are not significantly affected photochemically. CO_2 can be photochemically produced above its quench level value by the reaction described in Equation 2.13), and CH_4 can be readily photochemically destroyed. However as a whole, the vertical quenching primarily dictates the abundances of these species in the observable portion of the atmosphere. These ideas

can be extended to other hot Jupiter atmospheres, though we used HD189733b as our test case. One can see from Equation 2.13) that the fate of CO_2 is determined by the temperature of the atmosphere, and the ratio of the H_2O photolysis rate to the CO_2 photolysis rate which all depend on the stellar type and the distance. Knowledge of these terms will allow us to predict the abundance of CO_2 in any hot-Jupiter atmosphere. Though we have not included sulfur and nitrogen species in this study as in Zahnle et al. (2009) we have still shown that simple C, O and H chemistry and their interplay with vertical quenching is consistent with the detected abundances of CO, CH_4, CO_2 and H_2O. Finally, the vertical distribution of species derived from thermochemical equilibrium can deviate substantially from those derived via quenching, photochemistry and diffusion, and the simple assumption of thermochemical equilibrium may not be valid in the observable regions of these atmospheres.

2.7 Acknowledgements

We especially thank Adam Showman for providing us his GCM outputs for temperature and vertical winds making it possible for us to determine the eddy diffusion coefficient both of which form the basis of our model atmosphere. We also thank Run-Li Shia, Giovanna Tinetti, Xi Zhang, Konstantin Batygin, Mimi Gerstell, Chris Parkinson, Vijay Natraj, Kuai Le, Mark Swain, Julie Moses, Wes Traub, Pin Chen, Gautam Vasisht, Nicholas Heavens, Heather Knutson, Sara Seager, the anonymous referee and the Yuk Yung group for very useful discussions and reading the manuscript. MRL was supported by the JPL Graduate Fellowship (JPLGF). MCL was supported in part by an NSC grant 98-2111-M-

001-014-MY3 to Academia Sinica. YLY was supported by NASA grant NX09AB72G to the California Institute of Technology.

Bibliography

Allen, M., Yung, Y. L., & Waters, J. W. 1981, J. Geophys. Res., 86, 3617

Burrows, A., Budaj, J., & Hubeny, I. 2008, ApJ, 678, 1436

Burrows, A., Marley, M., Hubbard, W. B., et al. 1997, ApJ, 491, 856

Bauerle, S., Klatt, M., Wagner, H.Gg. 1995, Ber. Bunsenges. Phys. Chem., 99, 870-879.

Baulch, D.L., Cobos, C.J., Cox, R.A., Esser, C., Frank, P., Just, Th., Kerr, J.A., Pilling, M.J., Troe, J., Walker, R.W., Warnatz, J. 1992, J. Phys. Chem. Ref. Data, 21, 411-429.

Charbonneau, D., Brown, T. M., Noyes, R. W., & Gilliland, R. L. 2002, ApJ, 568, 377

Cooper, C. S., & Showman, A. P. 2006, ApJ, 649, 1048 Fortney, J. J., & Marley, M. S. 2007, ApJL 666, L45

Fortney, J. J., Marley, M. S., Lodders, K., Saumon, D., & Freedman, R. 2005, ApJL, 627, L69

Fortney, J. J., Saumon, D., Marley, M. S., Lodders, K., & Freedman, R. S. 2006, ApJ, 642, 495

Fortney, J. J., Shabram, M., Showman, A. P., et al. 2010, ApJ, 709, 1396

Friedson, A. J., Wilson, E. H., & Moses, J. I. 2005, Bulletin of the American Astronomical Society, 37, 683

Gladstone, G. R., Allen, M., & Yung, Y. L. 1996, Icarus, 119, 1

Gordon, S., McBride, B.J., & NASA Tech. Info. Program, 1994, Computer program for calculation of complex chemical equilibrium compositions and applications, National Aeronautics and Space Administration, Office of Management, Scientific and Technical Information Program

Griffith, C. A., & Yelle, R. V. 1999, ApJl, 519, L85

Kim, Y. H., & Fox, J. L. 1994, Icarus, 112, 310

Liang, M.-C., Parkinson, C. D., Lee, A. Y.-T., Yung, Y. L., & Seager, S. 2003, ApJl, 596, L247

Liang, M.-C., Seager, S., Parkinson, C. D., Lee, A. Y.-T., & Yung, Y. L. 2004, ApJl, 605, L61

Madhusudhan, N., & Seager, S. 2009, ApJ, 707, 24

Marley, M. S., Fortney, J. J., Hubickyj, O., Bodenheimer, P., & Lissauer, J. J. 2007, ApJ, 655, 541

Moses, J. I., Fouchet, T., Bézard, B., Gladstone, G. R., Lellouch, E., & Feuchtgruber, H. 2005, Journal of Geophysical Research (Planets), 110, 8001

O'Donovan, F. T., Charbonneau, D., Harrington, J., et al. 2010, ApJ, 710, 1551

Page, M., Lin, M.C., He, Y., Choudhur, T.K. 1989, J. Phys. Chem., 93, 4404-4408.

Prinn, R. G., & Barshay, S. S. 1977, Science, 198, 1031

Rogers, J. C., Apai, D., López-Morales, M., Sing, D. K., & Burrows, A. 2009, ApJ, 707, 1707

Sharp, C. M., & Burrows, A. 2007, ApJS, 168, 140

Segura, A., Krelove, K., Kasting, J. F., Sommerlatt, D., Meadows, V., Crisp, D., Cohen,

M., Mlawer, E. 2003, Astrobiology, 3, 689-708.

Showman, A. P., Fortney, J. J., Lian, Y., Marley, M. S., Freedman, R. S., Knutson, H. A., & Charbonneau, D. 2009, ApJ, 699, 564

Smith, M. D. 1998, Icarus, 132, 176

Srinivasan, N.K., Su, M.C., Sutherland, J.W., Michael, J.V., 2005, J. Phys. Chem. A, 109, 1857-1863.

Swain, M. R., Bouwman, J., Akeson, R. L., Lawler, S., & Beichman, C. A. 2008, ApJ, 674, 482

Swain, M. R., Vasisht, G., Tinetti, G., Bouwman, J., Chen, P., Yung, Y., Deming, D., & Deroo, P. 2009, ApJl, 690, L114

Swain, M. R., Tinetti, G., Vasisht, G., et al. 2009b, ApJ, 704, 1616

Tinetti, G., Liang, M.-C., Vidal-Madjar, A., et al. 2007, ApJL, 654, L99

Vidal-Madjar, A., Lecavelier des Etangs, A., Dsert, J.-M., Ballester, G. E., Ferlet, R., Hbrard, G., Mayor, M. 2003, Nature, 422, 143-146.

Visscher, C., Moses, J. I., & Saslow, S. A. 2010, Icarus, 209, 602

Vuitton, V., Lavvas, P., Yelle, R. V., Galand, M., Wellbrock, A., Lewis, G. R., Coates, A. J., Wahlund, J.-E. 2009, P&SS, 57, 1558-1572.

Yung, Y. L., Allen, M., Pinto, J. P. 1984, ApJS, 55, 465-506.

Yung, Y. L., & Demore, W. B. 1999, Photochemistry of planetary atmospheres New York- : Oxford University Press.- QB603.A85 Y86 1999

Yung, Y. L., Drew, W. A., Pinto, J. P., & Friedl, R.R. 1988, Icarus, 73, 516

Zahnle, K., Marley, M. S., & Fortney, J. J. 2009, arXiv:0911.0728

Zahnle, K., Marley, M. S., Freedman, R. S., Lodders, K., & Fortney, J. J. 2009, ApJl, 701, L20

Chapter 3

Thermochemical and Photochemical Kinetics in Cooler Hydrogen-Dominated Extrasolar Planets: A Methane-Poor GJ436b?

Originally published in:
Line, M. R., Vasisht, G., Chen, P., Angerhausen, D., & Yung, Y. L. 2011a, ApJ, 738, 32
Reproduced by permission of the AAS

3.1 Summary

We introduce a thermochemical kinetics and photochemical model. We use high-temperature bidirectional reaction rates for important H, C, O and N reactions (most importantly for CH_4 to CO interconversion), allowing us to attain thermochemical equilibrium, deep in an atmosphere, purely kinetically. This allows the chemical modeling of an entire atmosphere, from deep-atmosphere thermochemical equilibrium to the photochemically dominated regime. We use our model to explore the atmospheric chemistry of cooler ($T_{eff} < 10^3$ K) extrasolar giant planets. In particular, we choose to model the nearby hot Neptune GJ436b, the only planet in this temperature regime for which spectroscopic measurements

and estimates of chemical abundances now exist. Recent *Spitzer* measurements with retrieval have shown that methane is driven strongly out of equilibrium and is deeply depleted on the dayside of GJ 436b, whereas quenched carbon monoxide is abundant. This is surprising because GJ 436b is cooler than many of the heavily irradiated hot Jovians and thermally favorable for CH_4, and thus requires an efficient mechanism for destroying it. We include realistic estimates of ultraviolet flux from the parent dM star GJ 436, to bound the direct photolysis and photosensitized depletion of CH_4. While our models indicate fairly rich disequilibrium conditions are likely in cooler exoplanets over a range of planetary metallicities, we are unable to generate the conditions for substantial CH_4 destruction. One possibility is an anomalous source of abundant H atoms between 0.01-1 bars (which attack CH_4), but we cannot as yet identify an efficient means to produce these hot atoms.

3.2 Introduction

Currently, transiting extrasolar planets offer virtually exclusive [2] opportunities for observing physical and chemical states of exoplanetary atmospheres. Over the past four years, retrievals of atmospheric molecules from multicolor transit photometry (i.e. transit spectra) have compelled the development of progressively more sophisticated atmopheric models to interpret the observations and understand underlying chemical and dynamical processes. In particular, atmospheric-chemistry modeling is evolving from strictly thermo-equilibrium models with stationary chemical species, to coupled models (Zahnle et al. 2009a,b; Line et al. 2010; Moses et al. 2011) incorporating thermo-kinetics, vertical transport, and pho-

[2]The exceptions to the exclusivity are the few young, self-luminous planets as in the HR8799 system

tochemistry. Thus far, such efforts have been devoted to hot-Jupiter planets, especially HD 209458b and HD 189733b, due to their favorable transit depths and eclipse brightnesses and, therefore, far greater availability of observational data. However, with the recent retrieval of molecular abundances in the atmosphere of GJ 436b (Stevenson et al. 2010; Madhusudhan & Seager 2011), exoplanetary science is venturing into a new territory: hot-Neptune atmospheric chemistry. GJ 436b is bound to serve as a prototypical planet anchoring the theoretical framework for understanding the hot-Neptune class of exoplanets, much as how HD 209458b and HD 189733b have for hot Jupiters. It is also the first planet with observable thermal emission that transits an M star. M stars are of particular interest since they constitute the majority of stars in the solar neighborhood, and they have close-in habitable zones, which enhances radial velocity detectability and transit observability; therefore, M stars present the best opportunities to discover and characterize rocky, potentially habitable exoplanets in the near future. GJ 436b and GJ 1214b provide the only present test cases for atmospheric chemistry of planets orbiting M dwarfs. Therefore, an era of intensive investigations of this planet is commencing. This paper presents our application of a state-of-the-art model seamlessly integrating thermo-kinetics, vertical transport, and photochemistry to simulate the atmospheric chemistry of GJ 436b in a similar manner to Visscher et al. (2010) and Moses et al. (2011) , along with realisitic estimates of UV fluxes for this planet.

The first transiting hot Neptune discovered (Butler et al. 2004, Gillon et al. 2007), GJ 436b, revolves around an M dwarf merely 10 pc away from Earth and has received much attention due to its interesting orbital dynamics (Ribas et al. 2008, Mardling 2008,

Batygin et al. 2009), interior properties (Nettelmann et al. 2010, Kramm et al. 2011), and atmospheric properties (Stevenson et al. 2010, Lewis et al. 2010, Madhusudhan & Seager 2011, Shabram et al. 2011). The slightly eccentric orbit (eccentricity = 0.16) has a mean orbital radius of 0.0287 AU (Torres et al. 2008), and the planet probably has a pseudo-synchronous rotation (Deming et al. 2007). The planet's mass is 23 $M_{\oplus}$, and its density of 1.7 g/cm^3 resembles that of the ice giant Neptune (1.63 g/cm^3). Analyses of its mass-radius relationship and transit depth indicates a layer of H/He dominated atmosphere is clearly required (Figueira et al. 2009; Nettelmann et al. 2010; Rogers & Seager 2010). The host star has an effective temperature of $\sim$ 3400 K and an estimated age of 3 – 9 Gyr (Torres et al. 2008). Assuming zero albedo and global thermal re-distribution, the planet's effective temperature is 650 K. Of the confirmed transiting exoplanets (Wright et al. 2011), GJ 436b is one of the least irradiated and has one of the coolest atmospheres. Therefore, this planet represents a significant departure from hot Jupiters in terms of size, thermal environment, and UV flux.

Although GJ 436b was discovered in 2004 (Butler, by radial velocity), it was not until 2010 that a retrieval of explicit molecular abundances in its atmosphere was reported (Stevenson et al. 2010), where six channels of secondary eclipse photometry data ranging from 3.6 to 24 μm were analyzed by generating $\sim 10^6$ simulated spectra using varying combinations of molecular compositions and temperature profiles to find the best fit to observations. A more recent paper (Madhusudhan & Seager 2011) provides further details and updated results of a re-analysis of the same dataset using the same general retrieval method. In short, 10^6 combinations of ten physio-chemical free parameters, each spanning a large

range of values, were used to generate synthetic dayside emission spectra. In each of the 10^6 scenarios, six of the ten parameters were used to define the temperature-pressure (T-P) profile, whereas the other four parameters specified vertically uniform abundances of four molecules: H_2O, CO, CH_4, and CO_2. Additionally, the 1-D atmospheric model restricted the ratio of emergent flux output to incident stellar flux input on the day side to within the range between zero and unity. Given six data points and ten free parameters, the retrieval problem was mathematically underdetermined. Nonetheless, sampling a million points in parameter-phase space allowed the authors to examine the joint probability contours, as defined by the goodness-of-fit (chi-square) function, projected on multiple-parameter spaces. Furthermore, by placing physical-plausibility constraints (in consideration of believable departures from thermo-equilibrium chemistry) on the molecular abundances, the authors were able to confine the physical space to a fairly narrow, "best-fit," range for chi-square ≤ 3. Depending on the wavelength, the photospheric altitude varies from 9 bar to 0.2 bar levels. The main conclusions are as follows: 1) temperature inversion is ruled out (i.e., no stratosphere); 2) 6 ppm (parts per million) is the absolute upper limit for CH_4 abundance; 3) 300 ppm is the absolute upper limit for H_2O abundance; 4) CO_2 and CO abundances are anti-correlated; 5) taking physical-plausibility into consideration, the best-fit spectrum represents $X_{\mathrm{H_2O}}$ = 100 ppm, $X_{\mathrm{CH_4}}$ = 1 ppm, X_{CO} = 7000 ppm, and $X_{\mathrm{CO_2}}$ = 6 ppm, where X_{i} is the number density of molecule i divided by that of H_2. Also, note that even in the best-fit scenario, X_{CO_2} can range anywhere from 1 – 100 ppm. The Stevenson et al. (2010) and the Madhusudhan & Seager (2011) efforts are the most comprehensive studies of atmospheric composition on GJ 436b thus far.

From a theoretical point of view, the preceding abundance limits and values pose a very interesting challenge due to their drastic departures from thermo-equilibrium predictions, which indicate the following rough-order-of-magnitude values: $X_{\mathrm{H_2O}}$ = 1000 (3×10^4) ppm, $X_{\mathrm{CH_4}}$ = 1000 (10^4) ppm, X_{CO} = 60 (10^4) ppm, and $X_{\mathrm{CO_2}}$ = 0.1 (1000) ppm for 1x (50x) solar metallicities at $\sim$ 1bar. In either metallicity scenario, water and methane remain abundant ($\geq$ 1000 ppm), whereas the retrieval shows water being relatively depleted and methane being drastically depleted. Moreover, the thermo-equilibrium abundances of carbon monoxide and carbon dioxide are positively correlated (either both low in the $1\times$ case or both high in the $50\times$ case), in contrast with the retrieval's anti-correlation. In particular, the retrieved partitioning of carbon overwhelmingly in oxidized species amidst a hydrogen-dominated (reducing), temperate atmosphere is very surprising. For instance, at 1-bar pressure and solar metallicity, CH_4 is the thermodynamically dominant carbon-bearing molecule for temperatures less than 1100 K (Lodders & Fegley 2002). The common practices of simply adjusting metallicity and/or the C/O ratio cannot simultaneously reconcile these discrepancies. Therefore, one must investigate disequilibrium mechanisms.

Madhusudhan & Seager (2011) posited that high metallicity combined with vertical mixing can explain the disequilibrium abundance of carbon oxides. Basically, enhanced metallicity ($\sim 10\times$ solar) can provide the requisite abundance of CO_2. Since equilibrium CO abundance drops sharply with respect to temperature (Lodders & Fegley 2002) the retrieved uniformly high abundance of CO requires eddy mixing to populate upper, cooler, atmospheric layers. However, vertical eddy mixing alone cannot explain the large deple-

tion of CH_4 due to its innately high thermochemical abundance in the deep atmosphere. Therefore, Madhusudhan & Seager (2011) invoked photochemistry as the potential culprit, based on Zahnle et al.'s (2009a,b) studies of photochemistry on hot Jupiters. In such a scheme, photosensitized sulfur chemistry produces atomic H, which then destroys CH_4 to form higher hydrocarbons. However, the Zahnle et al. (2009a,b) model uses solar-type stellar irradiance and an isothermal atmosphere (i.e., constant temperature versus altitude). As such, neither the photochemical driver nor the thermal environment is tailored for our planet in question. More severely, Moses et al. (2011) pointed out that a typo in a key rate coefficient in the Zahnle et al. (2009a,b) model caused the apparent conversion of methane into higher hydrocarbons at pressures larger than 1 mbar. Generally speaking, at pressures larger than 1 mbar in a hydrogen-abundant atmosphere, hydrogenation of unsaturated hydrocarbons and reaction intermediates efficiently recycle species back to methane, preventing its large- scale destruction. Moses et al. (2011) also discussed the inadequacies of isothermal atmospheric models due to their suppression of transport-induced quenching. Hence, the observed CH_4 depletion still awaits adequate explanation. The low abundance of H_2O also has not been addressed.

In addition to secondary eclipse observations, primary transit observations of GJ 436b exist as well (Pont et al. 2009, Ballard et al. 2010, Beaulieu et al. 2011, Knutson et al. 2011), and various groups have analyzed them to retrieve molecular abundances in the planet's terminator regions (Beaulieu et al. 2011, Knutson et al. 2011). In contrast to the secondary eclipse retrieval, Beaulieu et al. (2011) were able to fit a compendium of their and Ballard et al.'s transit observations between 0.5 and 9 μm with 500 ppm CH_4 in

a H_2 atmosphere, and finding no clear evidence for CO or CO_2. Moreover, Beaulieu et al. presented that a methane-rich atmosphere, with temperature inversion, can be consistent with the said secondary eclipse data as well (but see Shabram et al. 2011). More recently, Knutson et al. acquired Spitzer transit photometry at 3.6, 4.5, and 8.0 μm during 11 visits. The multiple-visit data showed high transit-depth variability, which the authors attribute to potential stellar activity in the dM host. They did not find any compelling evidence for methane, and data excluding ones believed to be most affected by stellar activity appear to place an upper limit of 10 ppm for methane mixing ratio. The best-fit spectrum to this select data set assumes 1000 ppm H_2O, 1000 ppm CO, 1 ppm CH_4, with CO_2 abundance poorly constrained, roughly in agreement with Madhusudhan et al. Therefore, primary-transit data is currently inconclusive due to different interpretations by different groups.

Our primary goal is to advance the fundamental understanding of processes impacting the chemical state of GJ 436b by developing a 1-D atmospheric model that integrates all of the aforementioned equilibrium and disequilibrium processes. An important aspect of our model is the seamless integration of thermochemistry, kinetics, vertical mixing, and photochemistry in a manner that directly follows from Visscher et al. (2010), and contemporaneously with Moses et al. (2011), obviating the conventional quench level estimation (Prinn & Barshay 1977).

The quench level approach assumes that the deep atmosphere is in thermochemical equilibrium because high temperatures provide sufficient kinetic energy to overcome reaction barriers in either direction. However, as vertical transport lifts a gas parcel to cooler, higher altitudes, chemistry becomes rate limited rather than thermodynamically de-

termined. There comes a point in altitude where the kinetic conversion time scale becomes slower than the transport time scale, and the rate-limiting reaction for a molecule of interest is not allowed time to reach completion. At altitudes above this point, the molecule's concentration is frozen/quenched (therefore, the term "quench level"). In effect, the quench level approach partitions the atmosphere into two parts: below the quench level, thermochemical equilibrium determines chemical abundances; above the quench level, molecular abundances are uniform versus altitude, with values equal to the equilibrium value at the appropriate quench level for each species. Although this approach has a long record of success (e.g., Prinn & Barshay 1977; Smith 1998; Griffith & Yelle 1999; Saumon et al. 2003; 2006; 2007; Hubeny & Burrows 2007; Cooper & Showman 2006), it does have some limiting assumptions and caveats that require great judiciousness. Specifically, one needs to determine the appropriate rate-limiting, interconversion reaction for each set of coupled species of interest (e.g., interconversion between CH_4 & CO). The correct reaction choice is not always readily apparent (see, e.g., Visscher et al. 2010) and the appropriate length scale for deriving the mixing time scale from the vertical eddy diffusion coefficient (K_{zz}) is still under some debate. Furthermore, since a basic assumption is that temperature decreases with altitude, atmospheric temperature inversions can complicate matters.

Therefore, we implemented a fully reversible kinetic model in the following manner. Every measured forward reaction rate in our list is reversed using the equilibrium constant and the principle of microscopic reversibility. Given enough pathways, both forward and backwards, a given set of chemical species will reach thermochemical equilibrium, kinetically. This provides a seamless transition from the thermochemical equilibrium regime

to the disequilibrium-dominated regimes. We can investigate the disequilibrium effects on atmospheric composition in a much more holistic, systematic manner, compared to heuristically identifying plausible disequilibrium processes.

In the remainder of this manuscript we describe the disequilibrium processes that may be occurring in GJ436b's atmosphere. In §2 we describe thermochemical and chemical kinetics models as well as our estimate for the stellar UV flux. In §3 we show the modeling results as well as a description of the important reaction schemes governing the abundances of various species. Finally in §4 we discuss the relevant implications and conclude.

3.3 Description of Models

We use joint thermochemistry and "1-D chemical kinetics with photochemistry" models to study the atmosphere's departure from thermal equilibrium. External inputs to our models are the metals fraction (denoted further on by ζ), the pressure and temperature (T-P) profile, the eddy diffusion coefficient profile, and the incident stellar flux; note that we fix the T-P profile and the chemistry is decoupled from it, i.e., there is no self-consistent, radiative-convective adjustment of temperature structure when the chemistry is evolved towards steady state. We initialize the 1-D atmospheres using the NASA Chemical Equilibrium with Applications (CEA) model (Gordon & McBride 1996). Given the initial elemental abundances of H, He, C, O, N, and S in an atmospheric layer, along with the layer's pressure and temperature, CEA uses a Gibbs free-energy minimization and mass balance routine to calculate the equilibrium species abundances.

Whereas chemical equilibrium concentrations are useful for initializing the atmosphere,

they do not provide the correct chemical state above pressure levels of $\simeq 10$ bars (Prinn & Barshay 1977; Griffith & Yelle 1999; Cooper & Showman 2006; Line et al. 2010; Moses et al. 2011). We simply supply the equilibrium mixing ratios as boundary conditions in the deep atmosphere for the kinetics calculations, and thereafter evolve the chemical state over multiple timesteps until a steady state is reached.

The computations are carried out with the Caltech/JPL photochemical and kinetics model, KINETICS (a fully implicit, finite difference code), which solves the coupled continuity equations for each involved species, and includes transport via molecular and eddy diffusion (Allen et al. 1981; Yung et al. 1984; Gladstone et al. 1996; Moses et al. 2005). We use the H, C, and O chemical reaction list originally described in Liang et al.(2003; 2004) and references therein updated to high temperatures, recently augmented with a set of N reactions. We have not included the chemistry of sulfur in any great detail, because much of its kinetics is poorly constrained (see, e.g., Moses et al. 1996). However we do consider a small, but well measured, set of H_2S reactions. This helps us appraise if and how the introduction of S affects the abundances of the main molecular reservoirs of H, C, N, O such as CH_4.

We use high-temperature rate coefficients for reactions from Line et al. (2010). All reactions are bidirectional, and we reverse them by calculating the back-reaction rates using thermodynamic data (see Appendix A and Appendix B). With appropriate reaction pathways and proper rates for the back-reactions, the models can converge to chemical equilibrium purely kinetically in the deep planetary atmosphere where reaction timescales are short compared to transport timescales, and photochemical reactions are unimportant. As

mentioned earlier, this removes the cumbersome requirement of having to choose a lower boundary for individual species through *ad hoc* quench level arguments (Prinn & Barshay 1977; Smith et al. 1998).

We solve for 51 hydrogen, carbon, oxygen and nitrogen bearing species including H, He, H_2, C, CH, $^1CH_2$, $^3CH_2$, CH_3, CH_4, C_2, C_2H, C_2H_2, C_2H_3, C_2H_4, C_2H_5, C_2H_6, O, O(1D), O_2, OH, H_2O, CO, CO2, HCO, H_2CO, CH_2OH, CH_3O, CH_3OH, HCCO, H_2CCO, CH_3CO, CH_3CHO, C_2H_4OH, N, N_2, NH, NH_2, NH_3, N_2H, N_2H_2, N_2H_3, N_2H_4, NO, HNO, NCO, HCN, CN, CH_3NH_2, CH_2NH_2, CH_2NH, H_2CN, with a total of ~ 700 reactions, 55 of which are photolysis reactions. The chemical pathway for reducing CO to CH_4, described recently for Jupiter's deep atmosphere (Visscher et al. 2010), is included in our reaction list, along with the reverse pathways for CH_4 to CO oxidation. Photolysis absorption cross sections are from Moses et al. (2005) and the thermodynamic data (i.e., the compilation of entropies and enthalpies) used to reverse the kinetic rate coefficients are from JANAF and CEA thermobuild databases; e.g., CEA uses data from Chase et al. (1998) and Gurvich et al. (1989) (see Zehe et al. 2002).

3.3.1 Model Parameters

We model a large pressure and altitude range, 10^3 to 10^{-11} bars ($\sim$5000 km or $\sim$0.2 R_p from the 1 bar level), so as to capture the three major atmospheric regimes and the transitions between them. These three dominant portions of the atmosphere are – the thermal equilibrium regime in the deep hot atmosphere, the eddy transport dominated regime at intermediate pressures, and the photochemical regime at low pressures. A total of 190 pressure levels,

uniform in logarithmic space, are used between the abovementioned levels, giving a resolution of about 14 levels per decade of pressure. Altitudes above the homopause remain relatively cool in our models, and we disregard the possibility of a hot thermosphere despite the models extend up to exosphere levels at 10^{-11} bars; this simplification has little or no bearing on the state of the atmosphere below the homopause ($P \sim 1\mu$bar). We adopt the $\zeta = 1$ T-P profile from Lewis et al. (2010) (see Figure 3.1), noting its similarity to the T-P profile retrieved in Madhusudhan & Seager (2011) and Stevenson et al. (2010). Whereas GJ 436 itself is slightly subsolar in abundances (Bean et al. 2006), we allow for a span of planetary metallicities, covering the cases $\zeta = 0.1, 1, 50$, and allowing for the possibility that the planet is either enriched or depleted; we used solar abundances from the standard text of Yung & DeMore (1999)[2]. For non-solar atmospheres we tune the fractions of C, N, O, and S relative to H but not relative to each other (e.g., C/O, N/O, S/O, are always fixed).

The eddy diffusion strength (parameterized by a coefficient, K_{zz}) determines the pressure level at which a species is chemically quenched. At the quench level for chemical X, the timescale for vertical transport (τ_{trans}) equals the chemical loss timescale ($\tau_{chem,X}$). Above that level, which includes the visible portion of the atmosphere, the mixing virtually "freezes" the concentration of that species. Below the quench level, $\tau_{chem,X} \ll \tau_{trans}$, and thermochemical balance is achieved. Line et al. (2010) and Moses et al. (2011) have used piecewise estimates of the eddy diffusion profiles, $K_{zz}(P)$. The recipe has been to estimate K_{zz} in the deep adiabatic troposphere ($\sim 10^3$ bars) using mixing length theories (e.g.,

[2]Yung & DeMore (1999) tabulate the abundances of Anders & Ebihara (1982). These values predate the more recent downward revision of elements C, O etc. in the solar photosphere (reviewed in Asplund et al. 2009). Our C/H, O/H, N/H and S/H ratios are a factor 1.66, 1.52, 1.35 and 1.43 higher than those recommended in Asplund et al. (2009). On this revised scale we are modeling a planet with $\zeta \simeq 0.16, 1.6, 80$. This was brought to our attention by the anonymous referee.

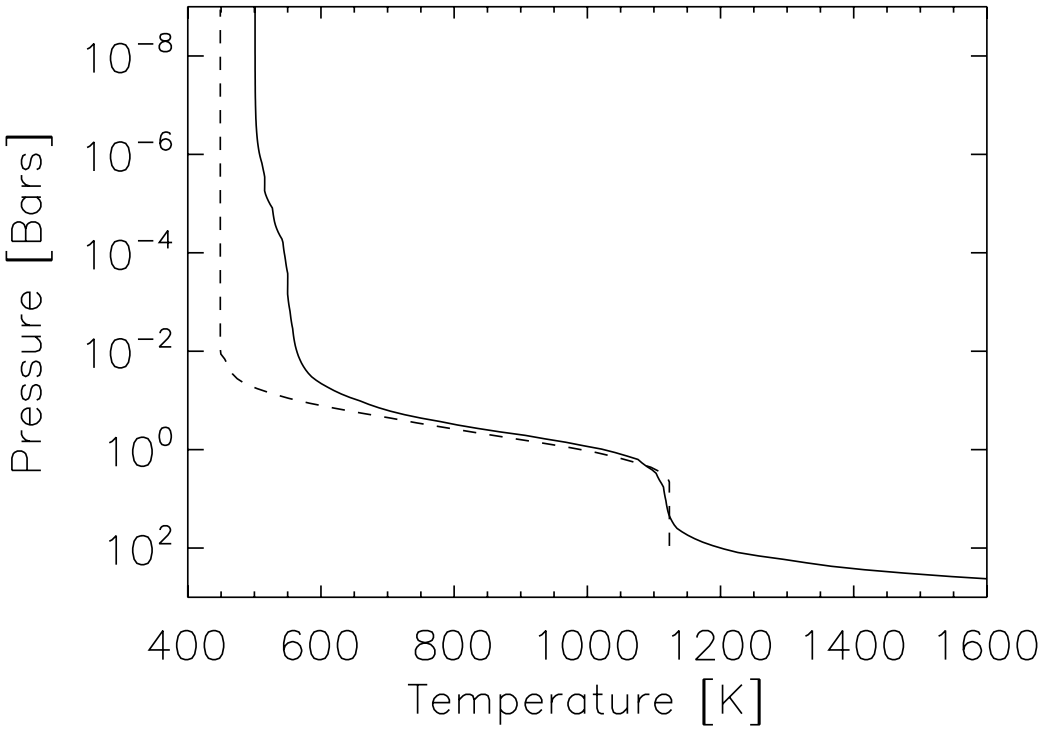

Figure 3.1: Estimated temperature profiles for GJ 436b. The dashed profile is the disk averaged dayside profile retrieved by Stevenson et al. (2010). The solid curve is the $\zeta = 1$ profile from the global circulation model of Lewis et al. (2010). We use the latter T-P profile for our chemical models.

Flasar & Gierasch 1977) and stitch this to global circulation model (GCM) derived profiles obtained by multiplying the (horizontally averaged) GCM vertical winds of Showman et al. (2009) by the local scale height. Lewis et al. (2010) apply this procedure to their GJ 436b circulation model, and estimate that K_{zz} increases from $\sim 10^8$ at depth (100 bars) to 10^{11} cm^2 s^{-1} at lower pressures (1 mbar).

Such procedures have gnawing uncertainties – for example, the appropriate eddy mixing length may only be a fraction of the scale height, or the vertical wind strengths could well be overestimated. Smith (1998) has demonstrated theoretically that using an eddy length scale equal to the scale height is inappropriate, and may lead to gross over-estimates of the length scale (L) and the timescale ($\tau_{trans} = L^2/K_{zz}$). Herein, we simplify matters by choosing a constant $K_{zz}(P) = 10^8$ cm^2 s^{-1} profile; this value is similar to that for the deep atmosphere in the Lewis et al. GCM. This simplification has a couple of redeeming features. First, this gives quench levels similar to those that would be derived had we used a GCM-inspired K_{zz} profile. Second, whereas a low K_{zz} may underestimate the mixing strength at higher altitudes, it has the effect more lethargic replenishment of methane and other photodissociated species from the lower atmosphere (it bolsters the photochemical timescale, relative to τ_{trans}).

3.3.2 The Ultraviolet Emission from GJ 436

dM stars such as GJ 436 show very little photospheric emission in the near to far ultraviolet (UV). Nevertheless, non-radiative energetic processes can transport energy to power a hot outer atmosphere, and this energy is partially dissipated in the form of cooling, chromo-

spheric UV emission. Because the UV emission levels depend on many factors, *ab initio* estimates of it are difficult. We use GALEX and ROSAT derived estimates for GJ 436 and combine these with a $T_{eff} \simeq 3400$ K continuum from the stellar photosphere. This combined emission is used to drive photochemical reactions in GJ 436b.

In the planetary atmosphere both H_2 and He are weak absorbers relative to other molecular species, but are enormously more abundant. Helium ceases to absorb longwards of 500 Å, and H_2 longwards of 1000 Å. Methane, a carbon reservoir and the molecule of particular interest herein, has a large absorption cross section shortwards of 1600 Å. Whereas methane (and water) is largely shielded by H_2 and He from very shortwave radiation, it is photodissociated by radiation between 1000-1600 Å, and is therefore susceptible to possible intense H I Ly α ($\lambda = 1216$ Å) from the M star host. Longwards of $\lambda = 1600$ Å, direct photolysis of methane dwindles due to a combination of the falling cross section and weak stellar flux. Hydrogen sulfide photodissociates at much longer wavelengths, $\lambda < 2600$ Å, and if present in substantial quantities, is poorly shielded by other reservoir molecules H_2, CH_4, H_2O, etc. H_2S photolysis and the resultant hot atomic hydrogen may be influential if $\lambda \simeq 2600$ Å photons can penetrate deep into the planetary atmosphere (more in §3.3.5).

GJ 436 is detected in a GALEX survey exposure in the near-UV channel with flux $f_{nuv} = 21.0 \pm 3.7$ μJy (near-UV channel, $\bar{\lambda} = 2267$ Å, $\Delta\lambda_{FWHM} = 616$ Å). It is undetected in the GALEX far-UV band, with a 3σ upper limit of $f_{fuv} \leq 24$ μJy (far-UV channel, $\bar{\lambda} = 1516$ Å, $\Delta\lambda_{FWHM} = 270$ Å). These can be converted to incident UV photon fluxes at the mean orbital separation of GJ 436b. The near UV detection implies a flux of 9×10^{10} photons cm^{-2} s^{-1} Å^{-1} $\lambda = 1960 - 2580$ Å at the planetary substellar point. This dosage

at GJ 436b is about 0.2 PELs (present-Earth-levels); mean Solar photon flux at Earth is 4.7×10^{11} photons cm^{-2} s^{-1} Å^{-1} between 2000-2500 Å (Yung & DeMore 1999). The 3σ flux upper bound (GALEX far-UV channel) is $\leq 1.3 \times 10^{11}$ photons cm^{-2} s^{-1} Å^{-1} $\lambda = 1450 - 1650\mathring{A}$; this is just a factor of two higher than present-Earth-levels in an equivalent passband.

H Ly α emission can be powerful in the upper chromospheres of cool stars. Because it is strongly absorbed in the interstellar medium, direct line strength estimates are difficult. We make an indirect determination based on empirical correlations with soft x-ray fluxes. Soft x-ray emission from GJ 436 has been observed in the ROSAT All Sky Survey (Hünsch et al. 1999), with $f_x \simeq 5.4 \times 10^{-14}$ erg cm^{-2} s^{-1} (0.1-2.4 keV; ROSAT PSPC), implying a fractional x-ray luminosity of $L_x/L_{bol} \sim 8 \times 10^{-6}$; this fraction is a factor ~ 100 lower than that observed from the most active dM stars and is consistent with GJ436b's estimated advanced age, 6 ± 3 Gyr. More recent XMM-Newton EPIC measurements (Sanz-Forcada et al. 2010) give a factor of 8 lower L_x, which may well be due to x-ray activity. Herein, we adopt the ROSAT flux because larger x-ray fluxes imply proportionally larger Ly α fluxes.

To estimate the Ly α output, we use an an empirical correlation of the x-ray and Ly α emission of stars, derived from stellar samples that include several late type stars (e.g., Landsman & Simon 1993 and Woods et al. 2004; in these papers, measurements of Ly α lines were made from *International Ultraviolet Explorer* and *Hubble Space Telescope* spectra, after applying a model-based correction of ISM absorption). Inverting the Woods et al. (2004) empirical power law, $\log F_x \simeq 2.2 \log F_{Ly\alpha} - 7.76$, we determine a photon flux of $f_{Ly\alpha} \sim 1.5 \times 10^{14}$ photons cm^{-2} s^{-1} at GJ 436b[3]. The solar H Ly α flux at Earth

[3]Very recently, Ehrenreich et al. (2011) estimate a Ly α flux using HST-STIS observations of GJ436.

is $\simeq 10^{12}$ photons cm^{-2} s^{-1}, a factor 100 lower. The reliability of x-ray derived Lyman α line flux may be assessed by comparing $F_{Ly\alpha}$ with the GJ 436b's H α line flux. H α observed in GJ436 in absorption, with an equivalent width of 0.32 Å (Palomar-Michigan State Nearby Star Spectroscopic Survey; Gizis, Reid & Hawley 2002), implies a line flux of $F_{H\alpha} \simeq 2 \times 10^5$ erg cm^{-2} s^{-1}, and a line strength ratio of H Ly α to H α of 2.2. For dM stars, where H Ly α is seen in emission and for which the intrinsic Ly α line strengths have been measured, this line strength ratio varies between 3-5, with some stars having ratios as low as 2 and others as high as 8 (Doyle et al. 1997).

3.4 Chemical Model Results

3.4.1 Thermochemical Equilibrium

Equilibrium vertical mixing ratios for the three metallicity cases are shown in Figure 3.2: these are sub-solar $\zeta = 0.1$, solar $\zeta = 1$ and super-solar $\zeta = 50$ heavy elemental abundances. Because GJ 436b is significantly cooler than HD 189733b and HD 209458b, CH_4 is the thermochemically favored carbon carrier; higher effective temperatures drive equilibrium towards CO in the two hot Jupiters. The thermochemical abundances of CH_4, CO and H_2O along the T-P profile are readily understood through the net reaction

$$\mathrm{CO} + 3\mathrm{H_2} \rightleftharpoons \mathrm{CH_4} + \mathrm{H_2O} \tag{3.1}$$

Their estimated line flux is a factor $1.5\times$ smaller than the estimate based on L_x used herein

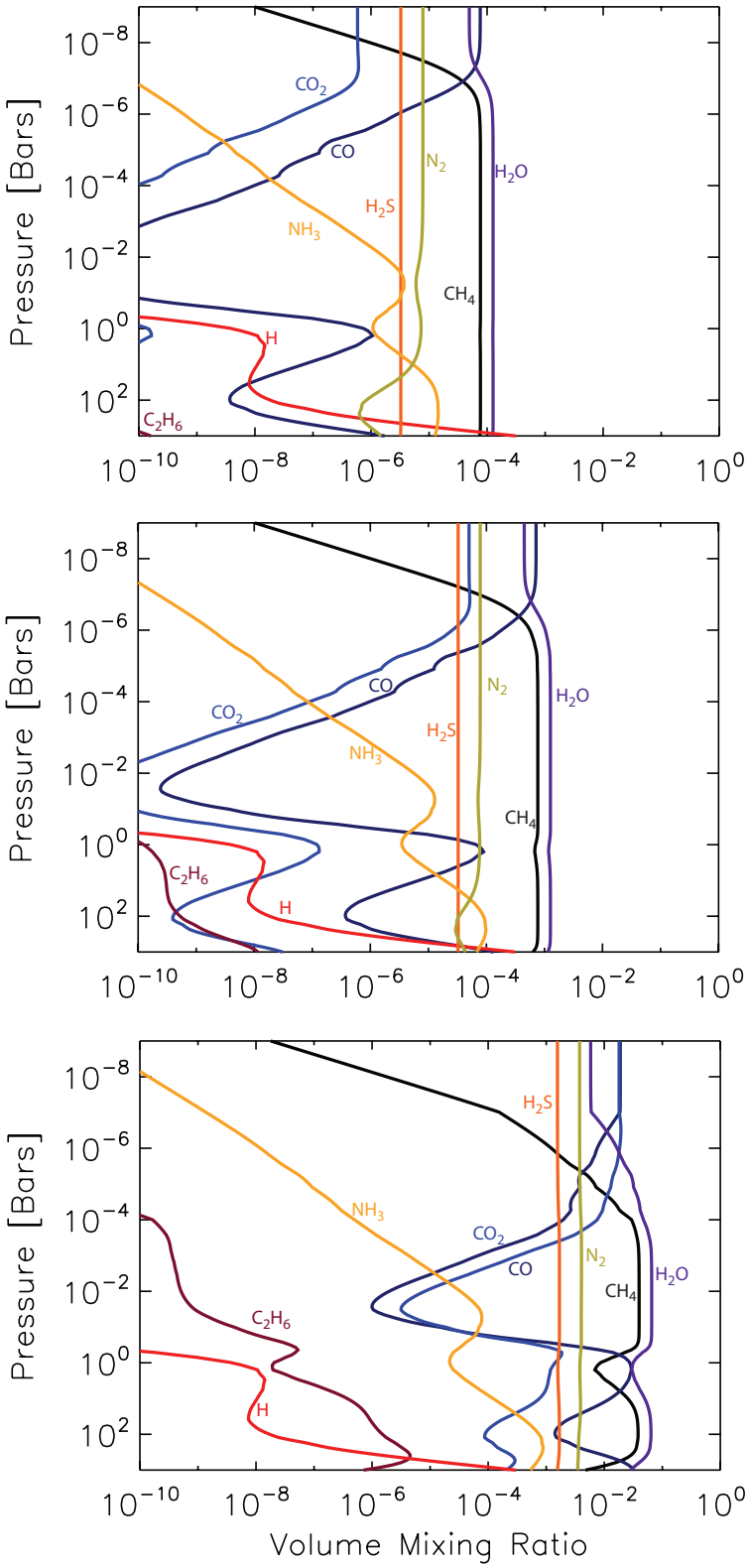

Figure 3.2: Thermochemical equilibrium vertical distributions for abundant H, C, O, N, and S species assuming the temperature profile in Figure 3.1. Three metallicity cases are shown ($\zeta = 0.1$, 1, and 50, from top to bottom). The thermochemical equilibrium mixing ratios are derived using the CEA Gibbs free energy minimization code for each atmospheric T-P level.

along with the law of mass action:

$$\frac{X_{CH_4} X_{H_2O}}{X_{CO} X_{H_2}^3} \frac{1}{P^2} = K_{eq}(T) \tag{3.2}$$

derived by minimizing the Gibbs free energy of net reaction in (1), with the mixing ratio X_i of species i, with ambient pressure P, and a temperature dependent equilibrium constant $K_{eq}(T)$; the T dependence is governed by the van 't Hoff equation ($\Delta G = -RT \log K_{eq}$, with ΔG as the standard Gibbs free energy change). At a given pressure P, $K_{eq}(T)$ behaves in a manner that rising T drives the equilibrium towards CO. At a fixed T, increasing/decreasing pressures favor higher CH_4/CO concentrations. These relationships are exemplified in the $\zeta = 1$ equilibrium profiles shown in Figure 3.2 (middle panel). As P and T decrease along the adiabat between $1000 - 100$ bars, the equilibrium constant dominates over the adverse P^2 dependence, resulting in a drop in the CO fraction. In the isothermal region between $10 - 1$ bars, decreasing pressure now favors the production of CO. Between 1 bar and $\approx 10^{-2}$ bars, the CO fraction falls because of the rapid decrease in temperature with altitude. At levels above the $\sim 10^{-2}$ level the temperature structure is nearly isothermal, and the decreasing pressure favors higher CO fractions. Similarly, NH_3 is the favored N carrier deep in the atmosphere, but is less favored at lower atmospheric pressures. Sulfur can be predominant as H_2S, HS, or S depending on pressure and temperature, but for conditions prevalent in GJ 436b, gas phase H_2S is the dominant sulfur reservoir and its concentration is unaffected by the temperature structure. Heavier hydrocarbons, such as ethane (C_2H_6), are relatively scarce any pressure or temperature (but more common at the highest metallicities).

Enriching the atmosphere to $\zeta = 50$ increases the mixing ratios of the reservoir species in proportion, however the shapes of the vertical profiles are much the same as for solar metallicities. Similarly, decreasing the metallicity of the atmosphere to $\zeta = 0.1$ lowers the mixing ratios of the heavy gases, by a factor $\sim \zeta$ for CH_4 and ζ^2 for CO, etc. The shapes of vertical distributions are nonetheless preserved, and relatively insensitive to ζ.

For all three metallicity cases considered, the chemical equilibrium abundances of CH_4 and H_2O stay relatively high – there is always enough hydrogen present to build these molecules. One can imagine an extreme situation where H is highly depleted, but such an atmosphere would be incompatible with the observed planetary radius. Conversely, the planet could be impoverished in metals to greatly subsolar levels $\zeta \ll 0.1$, although unreasonably low metallicities ($\leq 1 \times 10^{-5}\times$ solar) would be required to deplete CH_4 and other common molecules to levels below 1 ppm. These simple cases serve to show that, based solely on chemical thermodynamics, CH_4 has to be relatively abundant in GJ 436b and other $T_{eff} = 500 - 1000$ K H-rich planets.

3.4.2 Vertical Mixing & Chemical Quenching

Vertical turbulent mixing has been invoked to explain the anomalously large observed abundance of CO in Jupiter (Prinn & Barshay 1977) and brown dwarfs such as GL 229b (Griffith & Yelle 1999). Diffusive tropospheric mixing, in combination with detailed CO chemistry, has recently been used to infer the water inventory in the deep Jovian atmosphere (Visscher et al. 2010). Cooper & Showman (2006) parameterized the quench chemistry of CH_4 in order to study its horizontal and vertical transport in their GCM of HD 189733b. The

recent paper by Moses et al. (2011) discusses in detail the quench chemistry of H,C,N,O molecular species in the relatively hot atmospheres of HD 189733b and HD 209458b.

In our kinetics models we set thermochemical abundances as boundary conditions; these equilibrium abundance boundary conditions also define the metallicity of the system. We affix the 10^3 bar mixing ratios of the large carbon, oxygen and nitrogen reservoirs, CH_4, H_2O, CO, N_2, and NH_3, at their thermochemically derived values (here we are excluding sulfur), and set all other species to obey a zero flux condition at the lower boundary. The exact location of this lower boundary is unimportant, provided it is at depths much greater than the quench level (≥ 100 bars), and conditions (the high densities and temperatures) favor thermochemical equilibrium concentrations for practically all species. The nominal case has a solar abundance atmosphere ($\zeta = 1$), vertical mixing with strength $K_{zz} = 1 \times 10^8$ cm^2 s^{-1}, and no photochemistry. In Figure 3.3 we compare an atmosphere with vertical mixing to one purely in equilibrium. Below 10s of bars, the mixing ratios converge, satisfying the condition that equilibrium concentrations have been reached kinetically. Now consider the abundances of quenched CO. At pressure levels deeper than 10s of bars, the eddy mixing time, τ_{trans}, must be longer than the chemical loss timescale. As a check for internal consistency, we estimate

$$\tau_{trans} = \frac{L^2}{K_{zz}} \simeq 8 \times 10^5 \text{ s} \tag{3.3}$$

where L is a fraction f of the scale height H, $L = fH$ (Smith et al. 1998). We estimate $f = 0.3$ for both quenched CO and N_2. To estimate τ_{chem} for CO, we need to identify the rate-limiting reaction in CO and CH_4 interconversion.

$$\mathrm{H + CO + M \rightarrow HCO + M} \qquad R605$$

$$\mathrm{H_2 + HCO \rightarrow H_2CO + H} \qquad R234$$

$$\mathrm{H + H_2CO + M \rightarrow CH_3O + M} \qquad R611$$

$$\mathrm{H_2 + CH_3O \rightarrow CH_3OH + H} \qquad R351$$

$$\mathrm{H + CH_3OH \rightarrow CH_3 + H_2O} \qquad R295$$

$$\mathrm{H_2 + CH_3 \rightarrow CH_4 + H} \qquad R61$$

$$\mathrm{Net : 3H_2 + CO \rightarrow CH_4 + H_2O} \qquad I$$

This set of reactions is identical to the ones identified for CO quenching in Jupiter (Yung et al. 1988; Visscher et al. 2010). The rate-limiting reaction is R351, the inverse of a hydrogen abstraction from methanol. The chemical loss timescale for CO is,

$$\tau_{chem,\mathrm{CO}} = \frac{[\mathrm{CO}]}{k_{351}[\mathrm{H_2}][\mathrm{CH_3O}]} \tag{3.4}$$

where $[X]$ denotes the concentration X, and $k_{351} = 2.10 \times 10^{-25} T^{4.0} e^{-2470/T}$ cm^3 mol^{-1} s^{-1} (Jodkowski et al. 1999) the rate coefficient for R351. Figure 3.4 shows that equality

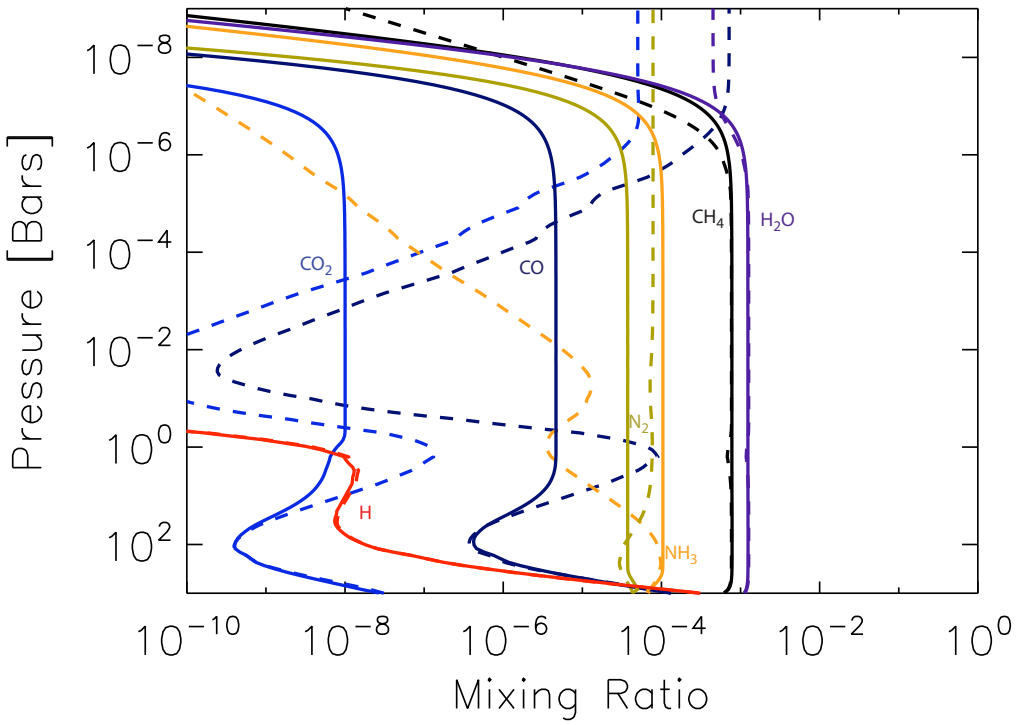

Figure 3.3: Effects of vertical mixing on the distributions of H_2O, CH_4, NH_3, N_2, CO, CO_2, and H. The dashed curves are the thermochemical equilibrium profiles for the $\zeta = 1$ case from Figure 3.2 (middle panel). The solid curves are the vertical profiles derived kinetically with only eddy ($K_{zz} = 1 \times 10^8$ cm^2 s^{-1}) and molecular diffusion (no photochemistry) using the 1000 bar $\zeta = 1$ mixing ratios as the lower boundary condition. Note that kinetically derived profiles begin to match the thermochemical equilibrium profiles at levels below a few 10's of bars. The rapid fall-off of the solid curves near 1 μbar is due to the sedimentation of the heavier molecules because of molecular diffusion.

of these two timescales, $\tau_{chem,CO} \approx \tau_{trans}$, gives a CO quench level of ~30 bars, which furthermore agrees well with quench level depicted by the CO mixing ratio profiles in Figure 3.3.

In an analogous manner the N_2 quench level may be calculated by identifying the rate-limiting step in the series of reactions that convert nitrogen to ammonia, and vice versa. These reactions are

$$\mathrm{H} + \mathrm{N_2} + \mathrm{M} \rightarrow \mathrm{N_2H} + \mathrm{M} \qquad R629$$

$$\mathrm{H_2} + \mathrm{N_2H} \rightarrow \mathrm{N_2H_2} + \mathrm{H} \qquad R478$$

$$\mathrm{H_2} + \mathrm{N_2H_2} \rightarrow \mathrm{NH_2} + \mathrm{NH_2} \qquad R450$$

$$2(\mathrm{H_2} + \mathrm{NH_2} \rightarrow \mathrm{NH_3} + \mathrm{H}) \qquad R453$$

$$\mathrm{Net} : 4\mathrm{H_2} + \mathrm{N_2} \rightarrow 2\mathrm{NH_3} + 2\mathrm{H} \qquad II$$

In this $\mathrm{N_2} \rightleftharpoons \mathrm{NH_3}$ sequence R450 is the rate-limiting step, involving the N abstraction from diazene, giving a timescale

$$\tau_{chem,\mathrm{N_2}} = \frac{[\mathrm{N_2}]}{k_{450}[\mathrm{H_2}][\mathrm{N_2H_2}]} \tag{3.5}$$

with reaction rate $k_{450} = 2.06 \times 10^{-07} T^{-0.93} e^{-20614/T}$, obtained from that of its reverse reaction (Stothard et al. 1995). Calculating $\tau_{chem,\mathrm{N_2}}$ above gives a $\mathrm{N_2}$ quench level of $\sim$300 bars (see Figure 3.4), in agreement with the vertical profiles in Figure 3.3. The abovementioned quench levels for CO and $\mathrm{N_2}$ are for the adopted eddy diffusion coefficient, $K_{zz} = 10^8$ cm^2 s^{-1}. Increasing K_{zz} to a very large value, 10^{11} cm^2 s^{-1}, shortens the transport times considerably and increases the quench pressures of CO and $\mathrm{N_2}$ to ~ 150

bars and $\sim$ 620 bars, respectively. The effects of varying the quench level may be seen in Figure 3.2 – the atmospheric concentrations of the reservoir gases, CH_4, H_2O and NH_3, and quenched N_2, are relatively insensitive to the location of quench pressure. However, varying the quench level affects the concentration of CO and CO_2 by orders of magnitude.

Vertical dredging of gases leaves a reasonably altered composition in the 1 - 0.001 bar region, the range of pressure levels wherein the infrared photosphere is located (e.g., Knutson et al. 2009; Swain et al. 2009). For example, CO is up to a factor 10^4 more abundant than it would otherwise be. The deep quenching of N bearing gases causes NH_3 to be surprisingly abundant, dominating over the thermochemically favored N_2. In contrast, the largest C and O reservoirs and optically the most active gases, CH_4 and H_2O, are largely unaffected.

3.4.3 Photochemical Effects

Photochemistry can significantly alter atmospheric composition in the upper portions. The combination of the ultraviolet flux and molecular absorption cross sections gives the photolysis rates for all the species considered here. The altitude of peak production/loss (in units of cm^{-3} s^{-1}), set by the balance between the exponential fall-off of atmospheric density and the inward stellar UV attenuation, occurs near 1 μbar (this is the well-known Chapman function, see Yung & DeMore 1999 pg. 45). Primarily, photolysis breaks apart stable molecules into radicals, which can then react to alter the composition of the upper atmosphere. See Figures 5, 6 and 7 for the photochemically derived mixing ratios. Table 1 compares the column mixing ratios from our models to the observations over the 7 bar to

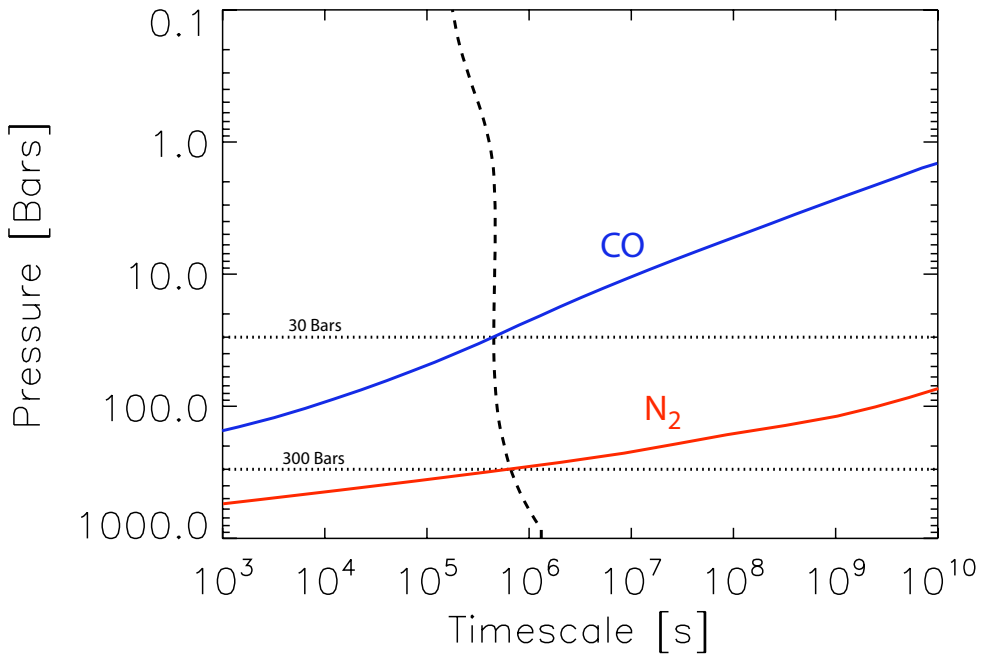

Figure 3.4: The blue curve is the CO chemical loss timescale calculated from Equation 3.4. The red curve is the N_2 chemical loss timescale calculated from Equation 3.5.. The dashed curve is the vertical mixing timescale from Equation 3.3. using a length scale of ~ 0.3H estimated from the Smith et al. (1998) procedure.. The intersection of the vertical mixing timescale and the chemical loss timescale is the quench level for the given species as indicated by the horizontal dotted lines.

0.1 bar range probed by the observations. Figure 3.8 illustrates how photochemistry alters the upper atmosphere. The resultant mixing ratio profiles are compared with those obtained via thermochemical equilibrium (Figure 3.2), and by vertical mixing (Figure 3.3).

3.4.3.1 Atomic H & H_2O

Arguably, the most important radical in these atmospheres is atomic hydrogen. Its relatively large abundance ($\sim$75% above 1 μbar, Figure 3.6) drives the bulk of disequilibrium chemistry in the upper atmosphere. As is seen in Figures 5-7, when the atomic H abundance increases with altitude, the concentration of disequilibrium species increases with it. Hydrogen attacks the large stable reservoirs, NH_3 and CH_4, to build these disequilibrium species. In the cold solar system giants, atomic hydrogen is primarily produced by the photosensitized dissociation of H_2 via heavier hydrocarbons, and the photodissociation of CH_4 and ethylene C_2H_4. In hotter giant planets, as in GJ 436b, the atomic hydrogen is made primarily by the photodissociation of water (Liang et al., 2003, Line et al. 2010, Moses et al., 2010). This is because, unlike in the solar system's giants, water is not sequestered in clouds and is readily available for photolysis. Its large UV cross section combined with a large thermochemical abundance, makes water the most important source of atomic hydrogen in GJ436b. The detailed mechanism for producing H is the photosensitization of H_2 using water via,

$$\mathrm{H_2O} + \mathrm{h}\nu \rightarrow \mathrm{OH} + \mathrm{H} \qquad R25$$

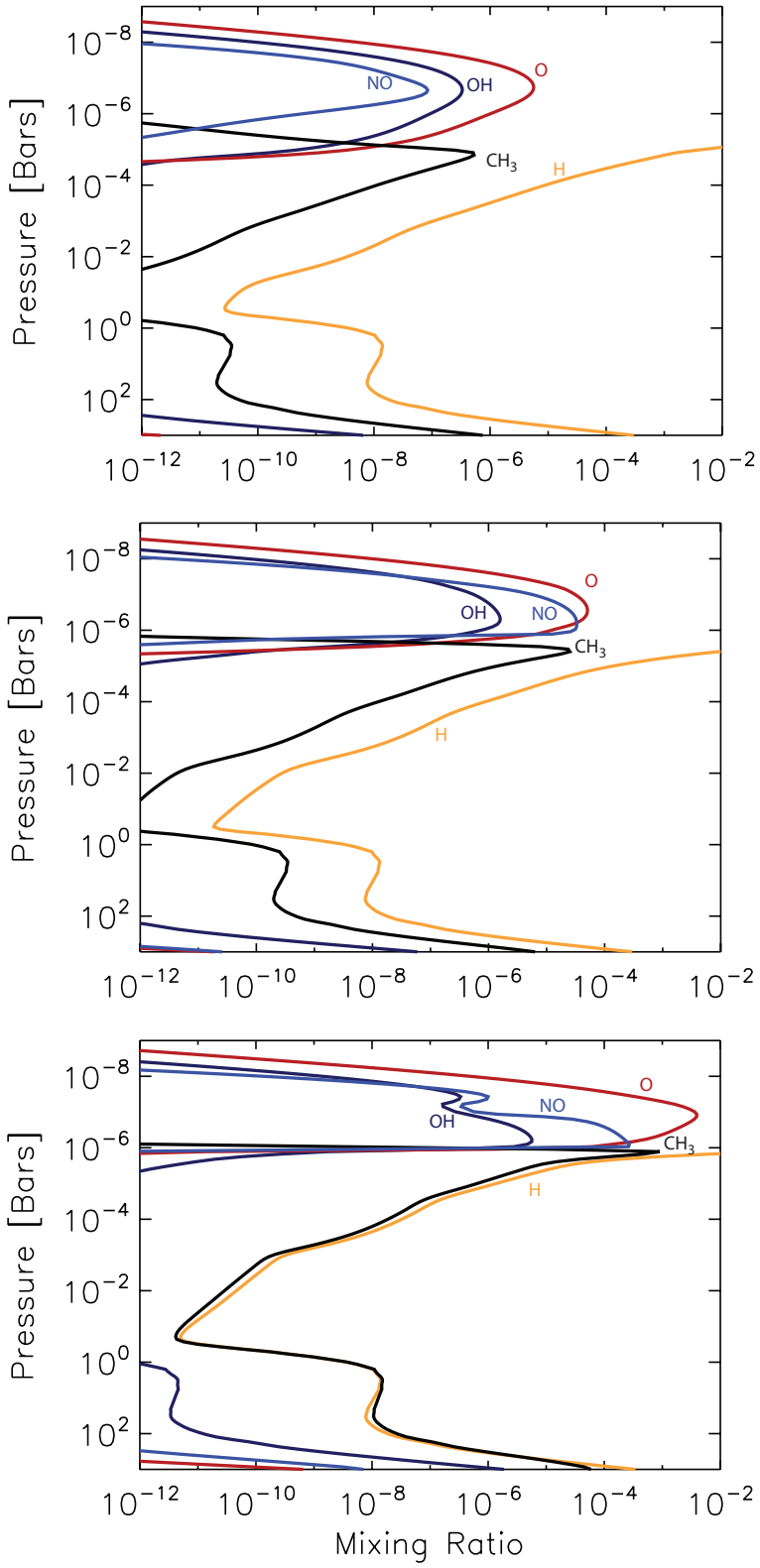

Figure 3.5: Mixing ratios for important radicals (OH, NO, O, H, and CH_3) that drive the photochemistry for three metallicities ($\zeta = 0.1$(top), $\zeta = 1$ (middle), and $\zeta = 50$ (bottom)). Note how the CH_3 profile very nearly tracks the H profile because CH_3 is a direct consequence of the oxidation of methane in R60

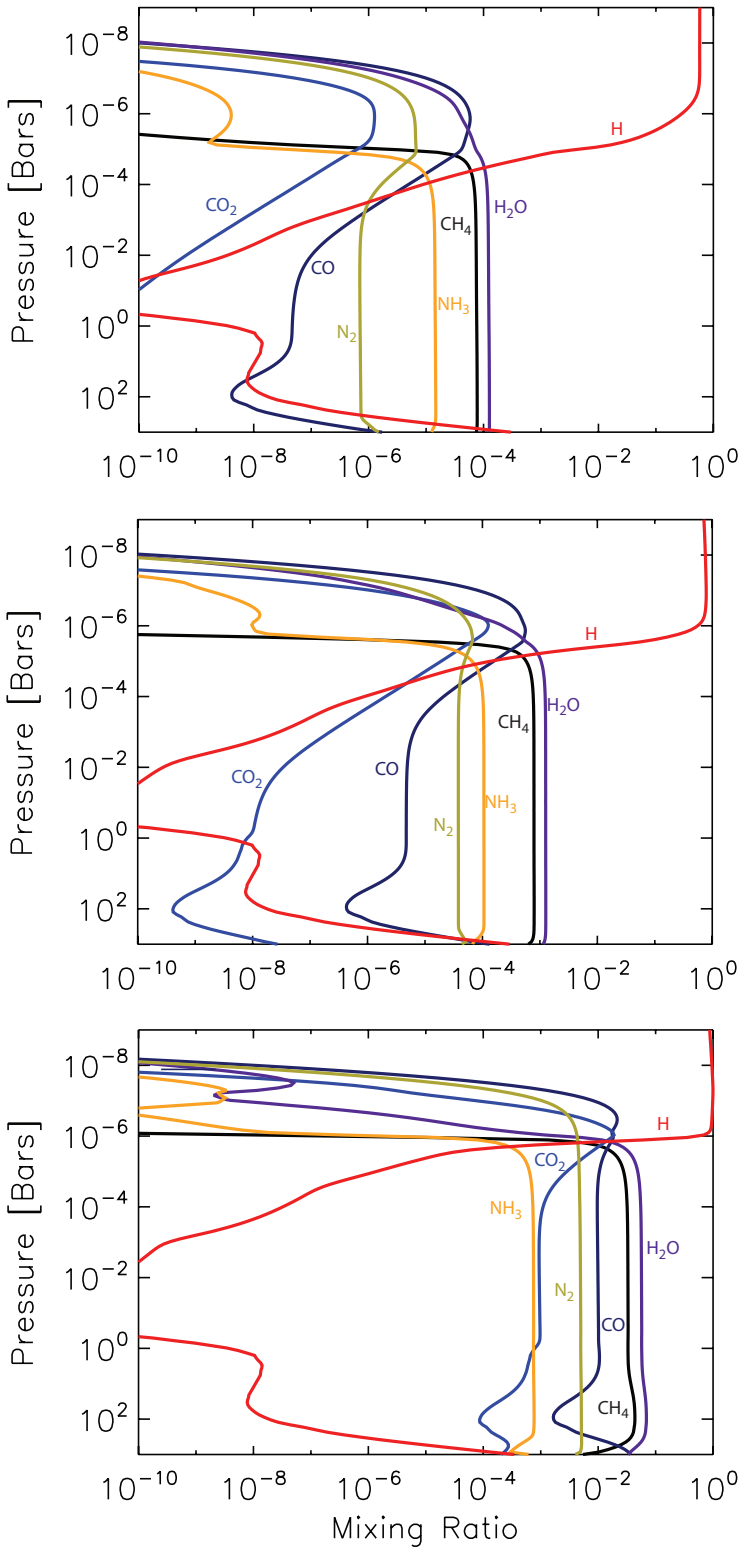

Figure 3.6: Photochemically derived mixing ratios for the abundant species (H_2O, CH_4, NH_3, N_2, CO, CO_2, and H) for $\zeta = 0.1$ (top), $\zeta = 1$ (middle), and $\zeta = 50$ (bottom).

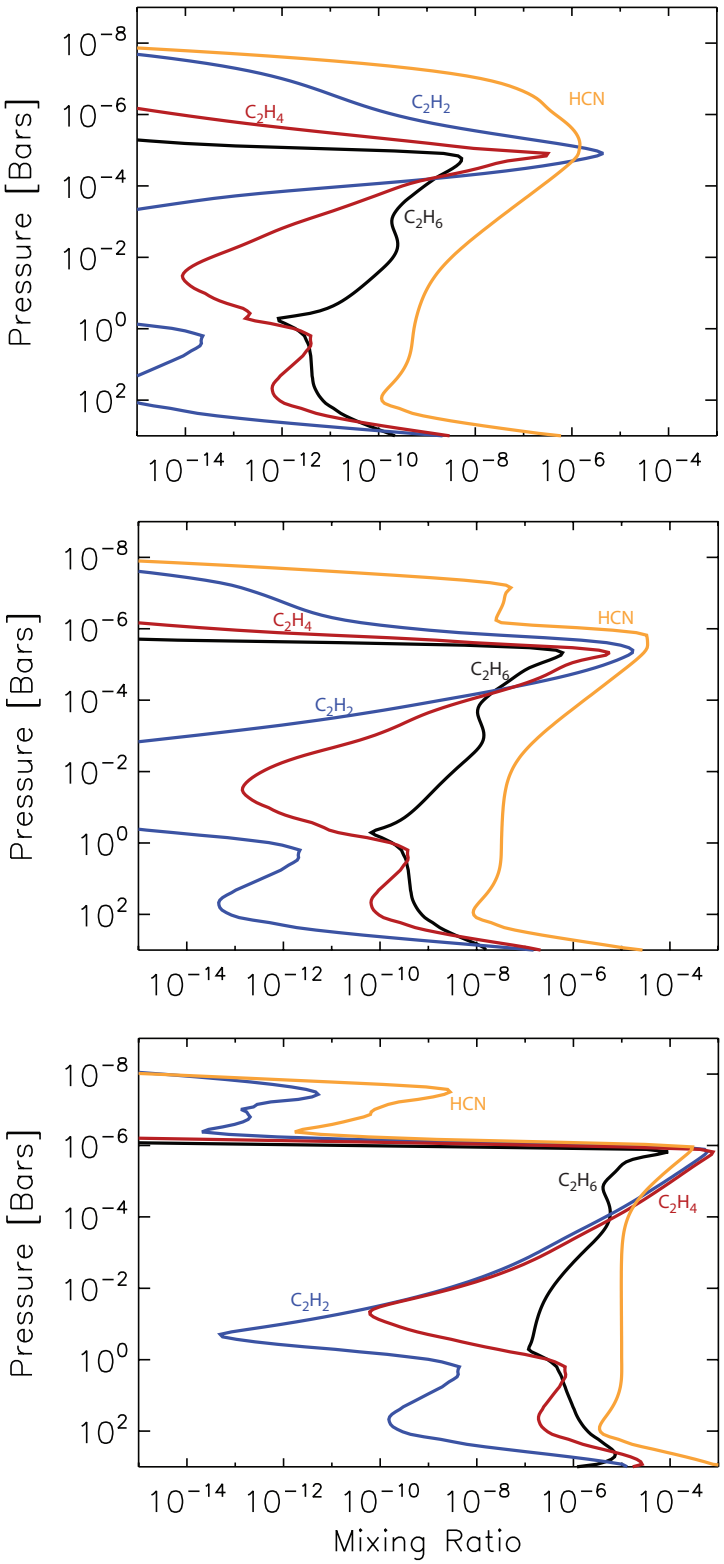

Figure 3.7: Photochemically derived mixing ratios for the disequilibrium species, the hydrocarbons and hydrogen cyanide, for $\zeta = 0.1$ (top), $\zeta = 1$ (middle), and $\zeta = 50$ (bottom)

$$H_2 + OH \rightarrow H_2O + H \qquad R169$$

$$\text{Net} : H_2 \rightarrow 2H \qquad III.$$

This photosensitization is efficient because H_2O dissociates out to $\sim$2000 Å, whereas H_2 dissociates only out to $\sim$800 Å. H_2O acts as a photon sink, with factor $\sim 10^4$ more photons available for its photolysis, than for direct H_2 photolysis. Because of these factors the net photosensitized destruction of H_2 by H_2O proceeds 5 orders of magnitude faster than the direct photolysis of H_2, and 3 orders of magnitude faster than the photosensitized destruction of H_2 via the hydrocarbons. The mixing ratio of water itself is largely unaltered below 1μbar levels.

3.4.3.2 CH_4 & Hydrocarbons

Thermochemically, methane is the most abundant hydrocarbon. Overall it is the fourth most abundant species after H_2O, H_2 and He, and it is the parent molecule for the synthesis of all other hydrocarbons. Methane mixing ratios are $\geq 10^{-4}$ at altitudes below the 0.1 mbar level, even for the lowest metallicities. The models generally have methane mixing ratios at least 3 orders of magnitude higher than concentrations retrieved from the observations (Madhusudhan & Seager 2011). Although photolysis seems not to significantly modify methane abundances, it does produce large concentrations of the methyl radical, CH_3; this radical is important in the synthesis of heavier hydrocarbons. CH_3 is formed

by photosensitized dissociation of methane. The free atomic hydrogen from scheme III readily attacks methane to produce H_2 and CH_3. The trigger and pathway for this is:

$$H_2O + h\nu \rightarrow OH + H \qquad R25$$

$$H_2 + OH \rightarrow H_2O + H \qquad R169$$

$$H + CH_4 \rightarrow CH_3 + H_2 \qquad R60$$

$$\text{Net} : CH_4 \rightarrow CH_3 + H. \qquad IV$$

The methyl radical's mixing ratios can be as high as $\sim 10^{-4}$, as in the $\zeta = 1$ case (Figure 3.5). Due to the warmer upper atmosphere, relative to that in the solar system giants, the oxidation of methane (via R60) is more than two orders of magnitude more efficient than direct photolysis. Because the forward reaction (R60) proceeds more sharply with rising temperature than the reverse (R61), hotter upper atmospheres (as in HD 189733b and HD 209448b) will have a tendency to destroy methane more readily, especially when there are large quantities of photochemically produced atomic hydrogen present. This photosensitized destruction of methane causes it to decline sharply above $\sim$10 μbars; this is well below the planetary homopause, but well above the infrared photosphere (Figure 3.8). It also drives the production of heavier hydrocarbons. Little to no heavier hydrocarbon

(C_nH_m, where $n, m \geq 2$) is expected via vertical mixing alone, with mixing ratios remaining below $\sim 10^{-10}$ at altitudes above 1 bar. Methane photosensitization (scheme IV) converts the carbon into ethylene (C_2H_4), acetylene (C_2H_2), and ethane (C_2H_6) via

$$H_2O + h\nu \rightarrow OH + H \qquad R25$$

$$H_2 + OH \rightarrow H_2O + H \qquad R169$$

$$2(H + CH_4 \rightarrow CH_3 + H_2) \qquad R60$$

$$CH_3 + CH_3 + M \rightarrow C_2H_6 + M \qquad R613$$

$$H + C_2H_6 \rightarrow C_2H_5 + H_2 \qquad R70$$

$$H + C_2H_5 \rightarrow C_2H_4 + H_2 \qquad R68$$

$$H + C_2H_4 \rightarrow C_2H_3 + H_2 \qquad R85$$

$$H + C_2H_3 \rightarrow C_2H_2 + H_2 \qquad R64$$

$$\text{Net} : 2CH_4 + 4H \rightarrow C_2H_2 + 5H_2 \qquad V$$

The net reaction ultimately produces C_2H_2, making it the most abundant heavy hydrocarbon. This scheme is different than the solar system gas giants where the most dominant

pathway for producing acetylene involves the binary collision between two $^3CH_2$ radicals. This difference can again, be owed to the overwhelming abundance of atomic H from water photolysis which can readily reduce the ethane produced R613 to acetylene. Over the range of metallicities considered ($\zeta = 0.1$ to 50), the peak values of C_2 hydrocarbons occur between 10 and 1 μbars. These mixing ratios of C_2H_4, C_2H_2, C_2H_6 lie between 3×10^{-7}-6×10^{-6}, 5×10^{-6}-4×10^{-4}, and 5×10^{-9}-6×10^{-5} (Figure 3.7; for integrated columns see Table 1). For comparison, the peak values in Jupiter are, respectively, $\sim 2\times10^{-6}$, 5×10^{-6}, and 20×10^{-6} (Moses et al. 2005). In the Solar System's giant planets, ethylene, acetylene, and ethane have strong mid-infrared stratospheric emission features at 10.5, 13.7 and 12.1 μm, respectively. These C_2 species can lead to further synthesis of higher-order hydrocarbons that can form hydrocarbon aerosols (Zahnle et al. 2009). However, the vapor pressures for these species are high (many bars) at these temperatures, so it may be difficult to form such aerosols. Additionally, Moses et al. 1992 showed that supersaturation ratios of 10 to 1000s may be required in order to trigger condensation due to the lack of nucleation particulates in Jovian-type atmospheres.

3.4.3.3 CO & CO_2

As described in §3.2, the CO abundance above 10 bars is determined by the reaction rate of scheme I, and the strength of vertical mixing. In the absence of incident stellar UV, a profile with a constant vertical mixing ratio up to the homopause is obtained. With incident UV radiation, there is a photochemical enhancement of CO near the 1 μbar level, of up to a factor of 10^2 for the $\zeta = 1$ case (Figure 3.6, 8). This high altitude enhancement is a property of the cooler atmosphere of GJ 436b; in hot-Jupiter atmospheres, as in HD 189733b and

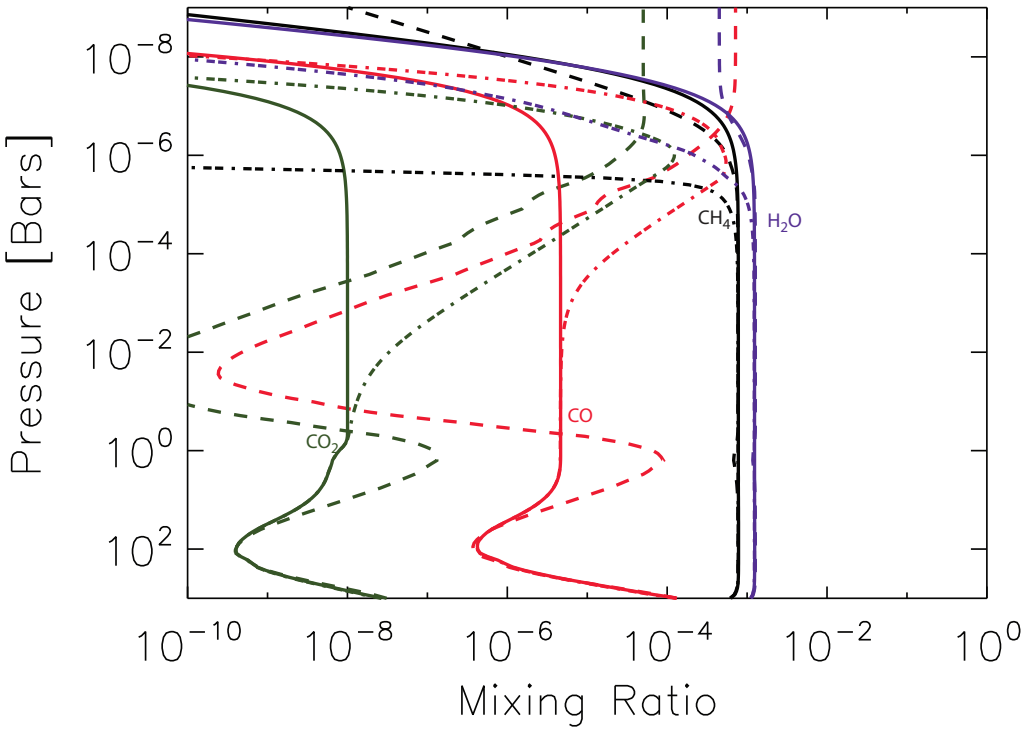

Figure 3.8: The effects of vertical mixing and photochemistry compared with the thermochemical equilibrium profiles for methane, water, carbon monoxide, and carbon dioxide under solar abundances (ζ=1). The dashed curves are the thermochemically derived mixing ratios (Figure 3.2 middle panel). The solid curves are the mixing ratios with eddy mixing (as in Figure 3.3 middle panel). The dot-dashed curves are the photochemical mixing ratios (Figure 3.5 middle panel). Note that methane becomes photochemically depleted near 1 μbar when compared to just vertical mixing (solid black curve). CO and CO_2 are photochemically enhanced above the 10 mbar level.

HD 209458b, such enhancements or deficits will tend to be driven back towards equilibrium values. The carbon in this extra CO is ultimately derived from the CH_4 reservoir, via the following reaction scheme:

$$H_2O + h\nu \rightarrow OH + H \qquad R25$$

$$H_2 + OH \rightarrow H_2O + H \qquad R169$$

$$H + CH_4 \rightarrow CH_3 + H_2 \qquad R60$$

$$H_2O + h\nu \rightarrow O + 2H \qquad R26$$

$$O + CH_3 \rightarrow H_2CO + H_2 \qquad R98$$

$$H + H_2CO \rightarrow HCO + H_2 \qquad R233$$

$$H + HCO \rightarrow CO + H_2 \qquad R213$$

$$\text{Net} : H_2O + CH_4 \rightarrow CO + 2H_2 + 2H \qquad VI$$

Scheme VI is driven by the water photolysis-driven dissociation of CH_4 to CH_3 via scheme IV. Atomic O is produced by photolytic fragmentation of water (R26); the net absorption cross section for this branch is $\simeq 0.1$ that of the main branch in R25. The two radicals, O

and CH_3, form formaldehyde in R98, and followed thereafter by a two-step conversion to CO (R233 and R213). An enhancement of CO_2 largely traces the enhancement of CO via:

$$\mathrm{H_2O} + \mathrm{h}\nu \rightarrow \mathrm{OH} + \mathrm{H} \qquad R25$$

$$\mathrm{OH} + \mathrm{CO} \rightarrow \mathrm{CO_2} + \mathrm{H} \qquad R187$$

$$\mathrm{Net} : \mathrm{H_2O} + \mathrm{CO} \rightarrow \mathrm{CO_2} + 2\mathrm{H} \qquad VII$$

Photochemically enhanced CO_2 mixing ratios reach $\sim 10^{-4}$ at 1 μbar for $\zeta = 1$. Column averaged mixing ratios are 5×10^{-6} and 6×10^{-9} (see Table 1). This is low compared to the observed mixing ratios of $\sim$1$\times10^{-4}$ and $\sim$1$\times10^{-7}$, respectively. Increasing the metallicity to $\zeta = 50$, increases the mixing ratios to $\sim$1$\times10^{-2}$ and $\sim$5$\times10^{-4}$, suggesting that the observed CO and CO_2 columns are consistent with a metallicity enhanced to levels observed in solar system's ice giant planets (Table 1).

3.4.3.4 Nitrogen & HCN

Ammonia and molecular nitrogen, N_2, are thermochemically the two most stable species in a reducing atmosphere and their relative abundance within the $1 - 0.001$ bar pressure levels is dictated by quench chemistry. Because it is relatively abundant, the addition of hot (quenched or otherwise) NH_3 (Tennyson et al. 2010) to the list of absorbers used for model

fitting and retrieval may well be quite important. Other important N species are mainly photochemical byproducts, with HCN being the most abundant photochemically produced molecule between 1 and 0.1 mbar levels, having mixing ratios of typically 10^{-6} ($\zeta = 1$) to 10^{-5} ($\zeta = 50$) at 0.1 mbar. Peak HCN occurs well above the photospheric levels, approaching 10^{-4} at 1 μbar. The synthesis of HCN is initiated via water and ammonia photolysis, and completed by subsequent reactions between the ammonia and methane derived radicals:

$$\mathrm{H_2O} + \mathrm{h}\nu \rightarrow \mathrm{OH} + \mathrm{H} \qquad R25$$

$$\mathrm{H_2} + \mathrm{OH} \rightarrow \mathrm{H_2O} + \mathrm{H} \qquad R169$$

$$\mathrm{H} + \mathrm{CH_4} \rightarrow \mathrm{CH_3} + \mathrm{H_2} \qquad R60$$

$$\mathrm{NH_3} + \mathrm{h}\nu \rightarrow \mathrm{NH_2} + \mathrm{H} \qquad R43$$

$$\mathrm{H} + \mathrm{NH_2} \rightarrow \mathrm{NH} + \mathrm{H_2} \qquad R455$$

$$\mathrm{NH} + \mathrm{CH_3} \rightarrow \mathrm{CH_2NH} + \mathrm{H} \qquad R685$$

$$\mathrm{H} + \mathrm{CH_2NH} \rightarrow \mathrm{H_2CN} + \mathrm{H_2} \qquad R655$$

$$\mathrm{H} + \mathrm{H_2CN} \rightarrow \mathrm{HCN} + \mathrm{H_2} \qquad R663$$

$$\mathrm{Net} : \mathrm{CH_4} + \mathrm{NH_3} \rightarrow \mathrm{HCN} + 3\mathrm{H_2} \qquad VIII$$

We note that R43, the photolysis of ammonia to amino radical, is the most important pathway for NH_2 formation at pressures greater than 10 μbar. At lower pressures this reaction is driven by ammonia photosensitization,

$$\mathrm{NH_3} + \mathrm{H} \rightarrow \mathrm{NH_2} + \mathrm{H_2}, \qquad R454$$

where the is H derived from H_2O photolysis. In conclusion when water, ammonia and methane are present, disequilibrium HCN is relatively abundant. The best chance for the detection of HCN is via the transmission spectroscopy of its vibrational fundamental bands at 3 and 14 μm (Shabram et al. 2011).

Because atomic H attacks both CH_4 and NH_3, we examine the role of H_2S as a source of free H (Zahnle et al. 2009); S is isoelectronic with and similar in chemical properties to O, but has a considerably reduced primordial abundance, with S/O $\simeq 0.02$. In a subset of models, we introduce the following (very restricted) set of sulfur reactions with accurate laboratory determined reaction rates:

$$\mathrm{H_2S} + \mathrm{h}\nu \rightarrow \mathrm{SH} + \mathrm{H} \qquad R705$$

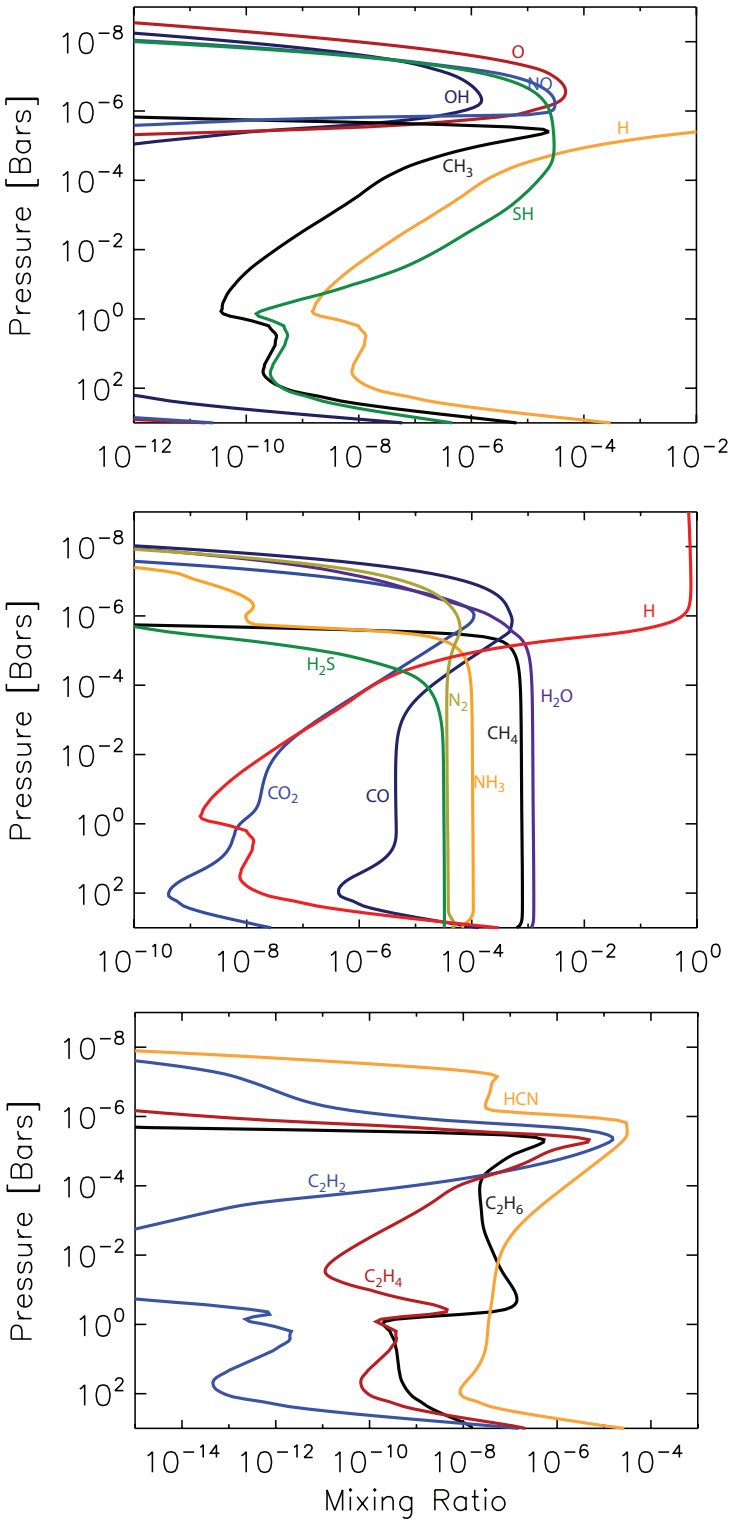

Figure 3.9: Photochemically derived mixing ratios for $\zeta = 1$ in the presence of sulfur species (H_2S and HS) for the radicals (top), abundant species (middle), and disequilibrium species (bottom). Compare this Figure to the $\zeta = 1$ cases in Figures 3.5, 3.6, and 3.7 to see the effects of H_2S on the mixing ratios. Note that the abundance of atomic H is enhanced by orders of magnitude between 1 and 10^{-4} bars as a result of scheme IX. This H increase enhances the hydrocarbon abundances significantly in this portion of the atmosphere.

$$H_2S + H \rightleftharpoons SH + H_2 \qquad R701,\ R702$$

$$H_2S + OH \rightleftharpoons SH + H_2O \qquad R703,\ R704$$

H_2S is an attractive source of free hydrogen due to its ability to photodissociate out to relative long wavelengths, $\sim$2600 Å. It has a photolysis rate constant comparable to that of H_2O, and we find a 10^2 enhancement in H between the pressure levels of 1 bar and 0.1 mbar upon including these two sulfur species (Figure 3.9); the relevant reactions are:

$$H_2S + h\nu \rightarrow SH + H \qquad R715$$

$$SH + H_2 \rightarrow H_2S + H \qquad R712$$

$$\text{Net} : H_2 \rightarrow 2H \qquad IX$$

This enhanced H abundance is catalyzed by the photolysis of H_2S (traced by the SH radical in Figure 3.9, top panel). The atomic H reacts efficiently with CH_4 in R60, producing an increased concentration of the radical CH_3, which in turn drives hydrocarbon production (scheme V) near the 0.1 bar level.

However, the free H in the middle atmosphere, does little to affect the CH_4 mixing ratios; this is because the S/C abundance ratio is low. Sulfur would need to be enriched by a substantial factor of $\sim$20, over the solar S/C value, in order for H_2S to have an appreciable

impact on atmospheric CH_4. Although the few considered sulfur species (H_2S, SH) do not much impact the overall chemistry, it is possible that another sulfur compound, such as SO, may act as a catalyst assisting in the conversion of reduced carbon into oxidized carbon. Previously, Moses (1996) has modeled the SL9 Jupiter impact and shown the importance of S in many reaction schemes involving both C and N species, and so the role of S chemistry in the hot extrasolar giants should continue to be investigated in the future (see Zahnle et al. 2009).

Table 3.1: Photochemical model abundances compared with the observations of Stevenson et al. 2010 (S10), Madhusudhan & Seager (2011) (MS10) and Beaulieu et al. (2010) (B10). The model abundances are the integrated column mixing ratios between 7 bars and 0.1 bars, the pressure levels sampled by the observations, for 0.1×, 1×, and 50× solar elemental abundances.

Molecule	0.1×	1×	50×	MS10	S10	B10
CH_4	7.66×10^{-05}	7.90×10^{-04}	2.96×10^{-02}	$(3–6) \times 10^{-06}$	1×10^{-07}	5×10^{-04}
CO	4.22×10^{-08}	4.29×10^{-06}	8.56×10^{-03}	$(3–100) \times 10^{-05}$	$(1–7) \times 10^{-04}$	–
CO_2	7.74×10^{-12}	6.09×10^{-09}	5.44×10^{-04}	$(1–10) \times 10^{-07}$	$(1–10) \times 10^{-07}$	–
H_2O	1.25×10^{-04}	1.26×10^{-03}	5.09×10^{-02}	$\leq 1 \times 10^{-03}$	$(3–100) \times 10^{-06}$	–
HCN	4.84×10^{-10}	3.09×10^{-08}	8.41×10^{-06}	–	–	–
C_2H_2	1.21×10^{-14}	1.18×10^{-12}	2.10×10^{-09}	–	–	–
NH_3	1.45×10^{-05}	1.06×10^{-04}	6.54×10^{-04}	–	–	–
H_2S	–	3.22×10^{-05}	–	–	–	–

3.5 Discussion & Conclusions

We have developed a 1D "thermochemical and photochemical kinetics with transport" model following Visscher et al. (2010) and recently, Moses et al. (2011) for extrasolar planet atmospheres. We use a compilation of bidirectional reactions of the five most abundant elements to model both the equilibrium and disequilibrium portions of the atmosphere. Using detailed balance with both forward and reverse reactions, allows our model to reach thermochemical equilibrium kinetically, thereby obviating the need to choose *ad hoc* lower

boundaries for multiple quenched species, and allowing a seamless transition between the transport dominated and the chemical equilibrium zones. A limitation is that we adopt a static temperature structure; a future improvement would allow the iterative adjustment and co-evolution of the temperature structure with the chemistry. Also, the eddy diffusivity profile $K_{zz}(z)$ is poorly constrained, and is essentially a free parameter in any of these models.

We have applied our models to study the atmosphere of the transiting Neptune-like planet GJ 436b. The elemental abundance of atmosphere, a key input parameter, is relatively uncertain, but mass-radius constraints suggest that GJ 436b must be enriched to at least $10\times$ solar levels. We model a range of atmospheric enrichment to cover this instrinsic uncertainty; we observe the trends when varying ζ, and rule out the possibility that intermediate values of ζ would spring any surprises. The UV fluxes of stars other than the Sun are often difficult to obtain. M dwarf hosts can be chromospherically hyperactive, and because UV photolysis may drive the depletion of weakly bonded molecules such as CH_4, NH_3 and H_2S, it is important to have an accurate UV estimate for GJ 436. We use a combination of GALEX and HST UV fluxes along with ROSAT and XMM-Newton soft x-ray fluxes to bound the UV continuum and line emission of GJ 436.

The GJ 436b model atmospheres show that a combination of photochemistry, chemical kinetics and transport-induced quenching drives the composition well out of equilibrium. While equilibrium conditions are maintained in the deep, hot, troposphere (below a 10s of bars for $\mathrm{CO} \rightleftharpoons \mathrm{CH_4}$, and 100s of bars for $\mathrm{N_2} \rightleftharpoons \mathrm{NH_3}$), the composition of the middle atmosphere is altered by the dredging up of quenched gases such as CO and NH_3. The

effects of transport disequilibrium are prominent in cooler planets such as GJ 436b because the quench points for major species depend on the temperature. As it gets colder, the pressure points for quenching are pushed deeper into the atmosphere due to the longer interconversion timescales from one species reservoir to another. In contrast to the quenched species (CO, CO_2, NH_3), the effect of vertical mixing on the reservoir gases such as CH_4 and H_2O is relatively feeble.

The reservoir gases H_2O and CH_4, and NH_3 are largely unaffected by photochemistry because of their (a) large abundances, and (b) rapid recycling. Nevertheless, it is their photolysis that drives the bulk of the disequilibrium chemistry in the upper atmosphere producing CH_4 and NH_3 sinks such as heavier hydrocarbons (such as C_2H_2, etc.) and simple nitriles (such as HCN). Much as in the hot Jupiters (Liang et al. 2003), H is the most important and active atom in the bulk of the atmosphere; it is created by the photosensitized destruction of H_2, catalyzed by the presence of H_2O and H_2S. The latter gas, though less abundant than water, is important because of its ability to capture incident starlight photons out wavelengths as long as 2600 Å. In most models, H replaces H_2 as the most abundant species in the atmosphere above the planetary homopause at $\simeq 1$ μbar. Because CH_4 is the largest C carrier in the planet's UV photosphere, we create abundant C_2 compounds (Figure 3.7) despite the relatively efficient hydrogenation back to CH_4. Species such as acetylene, C_2H_2, formed in abundance in our enriched models, are precursors for potential hydrocarbon soot formation in the upper atmosphere (as opposed to the hotter Jupiters such as HD 209458b and HD 189733b, wherein CO carries the bulk of carbon in the stratosphere). Our reaction lists for hydrocarbon chemistry are truncated at C_2, and so we do not

synthesize C_3 and heavier hydrocarbons and nitriles explicitly.

Within the range physical and chemical processes captured in our models, and the considered reaction sets and their kinetics, we find it difficult explain the observations suggesting a methane-poor GJ 436b. Except above 1 μbar pressure levels where CH_4 is photochemically converted to CO, HCN and C_2 hydrocarbons, it remains the predominant C reservoir in the lower atmosphere and in the region of the IR photosphere. The observed abundances of quenched CO and CO_2 are in agreement with an atmosphere enriched to levels intermediate between 1 to 50 times solar (as in Madhusudhan & Seager 2011). The depleted water may either contrarily suggest a sub solar metallicity (Table 1), or skewed heavy metals ratios; the latter is a possibility which we have not considered herein as there are far too many combinations to explore. In the $1\times$ solar models, the methane abundance is consistent with the values retrieved by Beaulieu et al. (2010) (Table 1) using transit observations. We suppose it is possible that a more complete inclusion of other relatively abundant elements such as S and P, or distorted elemental ratios (C/O or O/S, etc.), or ill-understood chemistry and exotic processes (not considered herein, such as the 3 dimensionality of the problem) could do more to explain the chemistry of this enigmatic atmosphere.

We agree with Moses et al. (2011) that quench level arguments can be used to predict abundances, so long as this is done with the appropriate level of caution. By this, we mean that the relevant rate-limiting reaction must necessarily be identified in order to properly calculate the timescale for chemical loss. Also, quenched gases do not share a common quench level and assuming so can result in gross under- or overestimation of their abun-

dances. For example, as shown herein, N_2 and CO have vastly different quench levels. For the moderate to high levels of incident UV flux, photolysis generates high concentrations of secondary byproducts, but does not significantly alter the abundances of the reservoir gases; in our estimation photochemistry cannot alter the dayside methane budget. Hotter atmospheres with sluggish vertical mixing and hot stratospheres are required for severe methane depletion. For example, in Figure 3.10, we approximate such as atmosphere as isothermal with $T = 1200$ K, $\zeta = 5$, and K_{zz}=1×10^6 cm^{2}s^{-1}, and with zero UV irradiation (similar to models by Zahnle et al. 2009). In this hypothetical atmosphere there is relatively little quenched methane. At $T = 1200$ K and low pressures, the rate determining step for $CH_4 \rightarrow$ CO (reverse of R351) is faster than the vertical transport time throughout the atmosphere, allowing the CH_4 to be in thermochemical equilibrium with CO everywhere (Figure 3.10). Since equilibrium conditions apply, the P^2 term in Equation 3.2. results in the rapid vertical fall-off of CH_4.

The models presented herein are by no means restricted in applicability to GJ 436b like Neptunes, and much of the modeled chemical state may be generalized to H/He dominated planets in the 500-1000 K temperature range. In this regime CH_4 is the primary carbon carrier and CO is quenched. The reverse is true in hotter atmospheres, $T > 10^3$ K, where CO is the primary carbon carrier and CH_4 is quenched. NH_3 is quenched deep in the atmosphere and can be quite abundant in the photosphere. Higher hydrocarbons and HCN are produced photochemically in relatively high abundances at mbar to μbar pressures. Similarly, an enhancement of CO and CO_2 over the quench concentrations, driven by the photolysis of H_2O, is observed in the high atmosphere. Water is in gaseous phase and

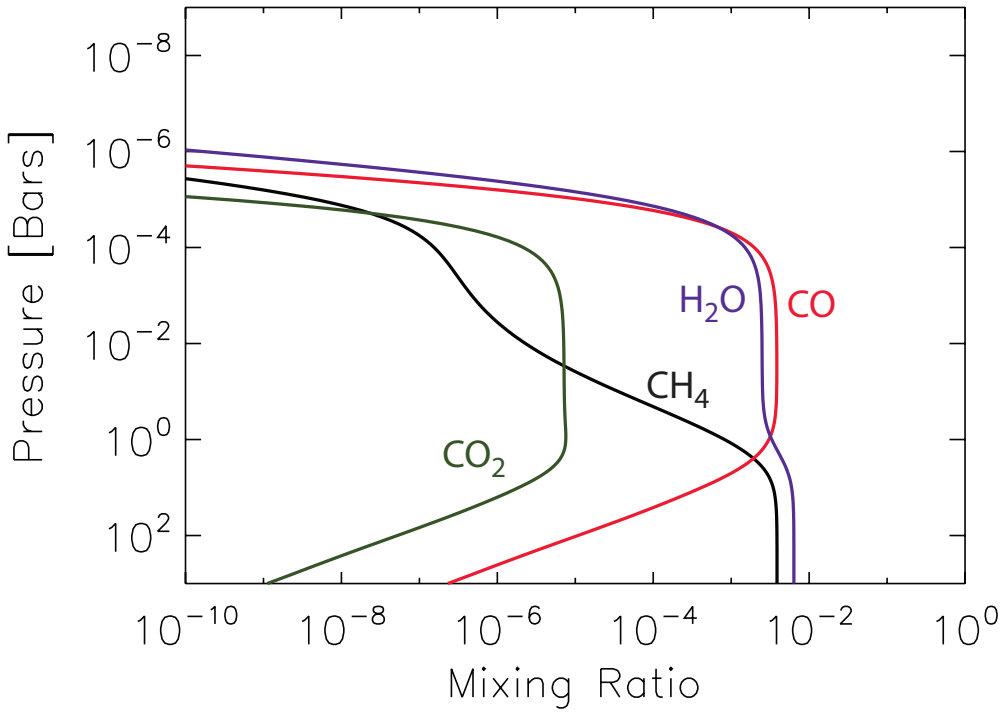

Figure 3.10: Mixing ratios for, CO, CH_4, CO_2, and H_2O assuming a T=1200 K isothermal atmosphere, $\zeta = 5$, and K_{zz}=1 $\times$ 10^6 cm^{2}s^{-1}, with no photochemistry. The observed methane fall-off is due to high temperatures alone; high temperatures imply a short chemical loss time for of CH_4. Because of the large transport time, CH_4 and CO are nearly in equilibrium at all altitudes.

abundant, and not condensed out as it would be in cooler atmospheres. GJ 1214b, a $T \simeq 500$ K low super Earth or mini Neptune, also orbiting an M dwarf primary (Charbonneau et al. 2009; Sada et al. 2010; Bean et al. 2010; Carter et al. 2011; Désert et al. 2011), falls in this regime of warm atmospheres. If GJ 1214b is in possession of a reducing H-He atmosphere (Croll et al. 2011; Crossfield et al. 2011), much of the atmospheric chemistry would be analogous to that in GJ 426b; this, however, is speculative as there is much current debate over the bulk composition of GJ 1214b.

3.6 Acknowledgements

We would like to thank Julie Moses, Channon Visscher, Karen Willacy, and M.C. Liang for useful chemistry discussions and tips. We would also like to thank Xi Zhang, Heather Knutson, Mimi Gerstell, Mark Allen, the Yuk Yung group, and the anonymous referee for reading the manuscript and providing valuable feedback. M. Line is supported by the JPL Graduate Fellowship funded by the JPL Research and Technology Development Program. P. Chen & G. Vasisht are supported by the JPL Research & Technology Development Program, and contributions herein were supported by the Jet Propulsion Laboratory, California Institute of Technology, under a contract with the National Aeronautics and Space Administration.

Bibliography

Allen, M., Yung, Y. L., & Waters, J. W. 1981, J. Geophys. Res., 86, 3617

Anders, E. & Ebihara, M., 1981, Geochem. Cosmo. Chem. Acta., 46, p. 2363

Asplund, M., Grevesse, N., Sauval, A. J., & Scott, P. 2009, ARA&A, 47, 481

Batygin, K., Laughlin, G., Meschiari, S., Rivera, E., Vogt, S., & Butler, P. 2009, ApJ, 699, 23

Bean, J. L., Benedict, G. F., & Endl, M. 2006, ApJl, 653, L65

Bean, J. L., Kempton, E. M.-R., & Homeier, D. 2010, Nature, 468, 669

Beaulieu, J.-P., et al. 2011, ApJ, 731, 16

Butler, R. P., Vogt, S. S., Marcy, G. W., Fischer, D. A., Wright, J. T., Henry, G. W., Laughlin, G., & Lissauer, J. J. 2004, ApJ,617, 580

Carter, J. A., Winn, J. N., Holman, M. J., Fabrycky, D., Berta, Z. K., Burke, C. J., & Nutzman, P. 2011, ApJ, 730, 82

Charbonneau, D., et al. 2009, Nature, 462, 891

Chase, Jr., M.W. & Davies, C. 1985, J. Phys. Chem. Ref. Data, 14, 1856

Croll, B., Albert, L., Jayawardhana, R., Miller-Ricci Kempton, E., Fortney, J. J., Murray, N., & Neilson, H. 2011, arXiv:1104.0011

Crossfield, I. J. M., Hansen, B. M. S., & Barman, T. 2011, arXiv:1104.1173

Cooper, C. S., & Showman, A. P. 2006, ApJ, 649, 1048

Doyle, J. G., Mathioudakis, M., Andretta, V., Short, C. I., & Jelinsky, P. 1997, A&A, 318, 835

Deming, D., Harrington, J., Laughlin, G., Seager, S., Navarro, S. B., Bowman, W. C., & Horning, K. 2007, ApJl, 667, L199

Désert, J.-M., et al. 2011, ApJl, 731, L40

Ehrenreich, D., Lecavelier Des Etangs, A., & Delfosse, X. 2011, A&A, 529, A80

Figueira, P., Pont, F., Mordasini, C., Alibert, Y., Georgy, C., & Benz, W. 2009, A&A, 493, 671

Gillon, M., Pont, F., Demory, B. O., Mallmann, F., Mayor, M., Mazeh, T., Queloz, D., Shporer, A., Udry, S., & Vuissoz, C. 2007, 472, L13

Gizis, J. E., Reid, I. N., & Hawley, S. L. 2002, AJ, 123, 3356

Gladstone, G. R., Allen, M., & Yung, Y. L. 1996, Icarus, 119, 1

Gordon, S., McBride, B.J., & NASA Tech. Info. Program, 1996, Computer program for calculation of complex chemical equilibrium compositions and applications, National Aeronautics and Space Administration, Office of Management, Scientific and Technical Information Program

Griffith, C. A., & Yelle, R. V. 1999, ApJl, 519, L85

Gurvich, L.V. and Veyts, IV and Alcock, CB, institut prikladno khimii (Soviet Union) 1989, Thermodynamic properties of individual substances, Hemisphere Publisher

Hubeny, I., & Burrows, A. 2007, ApJ, 669, 1248

Hünsch, M., Schmitt, J. H. M. M., Sterzik, M. F., & Voges, W. 1999, A&As, 135, 319

Jodkowski, J.T. and Rayez, M.T. and Rayez, J.C. and Bérces, T. and Dóbé, S. 1999, J. Phys. Chem. A., 103, 3750

Knutson, H. A., et al. 2009, ApJ, 690, 822

Kramm, U., Nettelmann, N., Redmer, R., & Stevenson, D. J. 2011, A&A, 528, A18

Landsman, W., & Simon, T. 1993, ApJ, 408, 305

Lewis, N. K., Showman, A. P., Fortney, J. J., Marley, M. S., Freedman, R. S., & Lodders, K. 2010, ApJ, 720, 344

Liang, M.-C., Parkinson, C. D., Lee, A. Y.-T., Yung, Y. L., & Seager, S. 2003, ApJl, 596, L247

Liang, M.-C., Seager, S., Parkinson, C. D., Lee, A. Y.-T., & Yung, Y. L. 2004, ApJl, 605, L61

Line, M. R., Liang, M. C., & Yung, Y. L. 2010, ApJ, 717, 496

Lodders, K. 2002, ApJ, 577, 974

Mardling, R. A. 2008, arXiv:0805.1928

Moses, J. I. 1996, IAU Colloq. 156: The Collision of Comet Shoemaker-Levy 9 and Jupiter, 243

Moses, J. I., Allen, M., & Yung, Y. L. 1992, Icarus, 99, 318

Moses, J. I., Fouchet, T., Bézard, B., Gladstone, G. R., Lellouch, E., & Feuchtgruber, H. 2005, Journal of Geophysical Research (Planets), 110, 8001

Moses, J. I., et al. 2011, arXiv:1102.0063

Nettelmann, N., Kramm, U., Redmer, R., & Neuhäuser, R. 2010, A&A, 523, A26

Prinn, R. G., & Barshay, S. S. 1977, Science, 198, 1031

Ribas, I., Font-Ribera, A., & Beaulieu, J.-P. 2008, ApJl, 677, L59

Rogers, L. A., & Seager, S. 2010, ApJ, 716, 1208

Sada, P. V., et al. 2010, ApJl, 720, L215

Sanz-Forcada, J., García-Álvarez, D., Velasco, A., Solano, E., Ribas, I., Micela, G., & Pollock, A. 2010, Pathways Towards Habitable Planets, 430, 530

Shabram, M., Fortney, J. J., Greene, T. P., & Freedman, R. S. 2011, ApJ, 727, 65

Showman, A. P., Fortney, J. J., Lian, Y., Marley, M. S., Freedman, R. S., Knutson, H. A., & Charbonneau, D. 2009, ApJ, 699, 564

Smith, M. D. 1998, Icarus, 132, 176

Stevenson, K. B., et al. 2010, Nature, 464, 1161

Stothard, N. and Humpfer, R. and Grotheer, H.H., 1995, Chem. Phys. Lett., 240, 474

Saumon, D., et al. 2007, ApJ, 656, 1136

Saumon, D., Marley, M. S., Cushing, M. C., Leggett, S. K., Roellig, T. L., Lodders, K., & Freedman, R. S. 2006, ApJ, 647, 552

Saumon, D., Marley, M. S., & Lodders, K. 2003, arXiv:astro-ph/0310805

Swain, M. R., Vasisht, G., Tinetti, G., Bouwman, J., Chen, P., Yung, Y., Deming, D., & Deroo, P. 2009, ApJl, 690, L114

Tennyson, J. 2010, European Planetary Science Congress 2010, held 20-24 September in Rome, Italy. ¡A href=”http://meetings.copernicus.org/epsc2010”¿http://meetings.copernicus.org/epsc2010¡/A¿, p.172, 172

Torres, G., Winn, J. N., & Holman, M. J. 2008, ApJ, 677, 1324

Visscher, C., Moses, J. I., & Saslow, S. A. 2010, Icarus, 209, 602

Walkowicz, L. M., Johns-Krull, C. M., & Hawley, S. L. 2008, ApJ, 677, 593

Woods, P. M., et al. 2004, ApJ, 605, 378

Wright, J. T., et al. 2011, ApJ, 730, 93

Yung, Y. L., & Demore, W. B. 1999, Photochemistry of planetary atmospheres, New York-: Oxford University Press, QB603.A85 Y86 1999

Yung, Y. L., Drew, W. A., Pinto, J. P., & Friedl, R.R. 1988, Icarus, 73, 516

Zahnle, K., Marley, M. S., & Fortney, J. J. 2009, arXiv:0911.0728

Zahnle, K., Marley, M. S., Freedman, R. S., Lodders, K., & Fortney, J. J. 2009, ApJl, 701, L20

Zehe, M.J. and Gordon, S. and McBride, B.J. 2001, CAP: a computer code for generating tabular thermodynamic functions from NASA Lewis coefficients, National Aeronautics and Space Administration, Glenn Research Center

Chapter 4

Information Content of Exoplanetary Transit Spectra: An Initial Look

Originally published in:
Line, M. R., Zhang, X., Vasisht, G., et al., 2012, ApJ, 749, 93
Reproduced by permission of the AAS

4.1 Summary

It has been shown that spectroscopy of transiting extrasolar planets can potentially provide a wealth of information about their atmospheres. Herein, we set up the *inverse* problem in spectroscopic retrieval. We use non-linear optimal estimation to retrieve the atmospheric state (pioneered for Earth sounding by Rodgers 1976, 2000). The formulation quantifies the degrees of freedom and information content of the spectrum with respect to geophysical parameters; herein, we focus specifically on temperature and composition. First, we apply the technique to synthetic near-infrared spectra, and explore the influence of spectral signal-to-noise ratio and resolution (the two important parameters when designing a future instrument) on the information content of the data. As expected, we find that the number of retrievable parameters increase with increasing signal-to-noise and resolution, although

the gains quickly level off for large values. Second, we apply the methods to the previously studied dayside near-infrared emission spectrum of HD 189733b, and compare the results of our retrieval with those obtained by others.

4.2 Introduction

Currently there are about 130 confirmed transiting exoplanets (www.exoplanet.org). Of these planets, several dozen have spectra that have been observed, either through broad-band photometry from instruments like the Spitzer Infrared Array Camera (IRAC) (Deming et al. 2005; Charbonneau et al. 2005;2008; Knutson et al. 2007; 2008; Harrington et al. 2006; 2007; Stevenson et al. 2011) or higher resolution spectroscopy from the Hubble Space Telescope (HST) Near Infrared Camera and Multi-Object Spectrometer (NICMOS) (Swain et al. 2009a; 2009b), Spitzer Infrared Spectrometer (IRS) (Grillmair et al. 2008), and recently, from ground-based instruments (Redfield et al. 2007; Snellen et al. 2008;2010;Swain et al. 2010; Mandel et al. 2011; Waldmann et al. 2011). Although the spectra are of low resolution ($R = \lambda/\Delta\lambda \sim 5 - 50$) and low signal to noise (S/N ≤ 10), they nevertheless provide useful information about the temperature and composition of the exoplanetary atmospheres (Tinetti et al. 2007; 2010a; Madahusudhan & Seager 2009; etc.). A typical approach to retrieving this information is to match the data set with forward models by manually tuning the model abundances and temperatures, until a possible best fit is obtained (Tinetti et al. 2007; 2010a; Swain et al. 2009a; 2009b). This approach does not provide an optimal solution to the atmospheric state; furthermore, it can be cumbersome and is susceptible to multiple degeneracies (Tinetti et al. 2007; Madhusudhan & Seager

2009)

Others have used multi-dimensional grid models to constrain atmospheric parameters (Madhusudhan & Seager 2009), a method that is well tuned to systematically searching the parameter space given sparse data (as with Spitzer IRAC color photometry). In this approach, an ensemble of forward models are generated using up to 10 gridded free parameters (6 to govern the shape of the temperature profile and 4 scaling factors for uniform mixing ratios of H_2O, CH_4, CO, and CO_2); model families that best describe the data are selected based on a chi-squared statistic criterion. Because of the degeneracies between the different gases, and between gases and temperature, thousands of solutions can exist within a given chi-squared region, thus only giving loose constraints on the atmospheric composition and temperature. Furthermore, the formalism provides no easy way to explore the change in information content associated with a change in the data phase space (e.g., R or S/N).

Here, we present the *inverse* approach (see also Lee et al. 2011) that determines the atmospheric "state" (i.e., its temperature structure and abundances) by minimizing a cost function that simultaneously takes into account new measurements and prior knowledge of atmospheric properties (such as a state retrieved from previous observations). Additionally we determine, within the context of our model, the quality of the spectra and the number of useful retrievable atmospheric properties. This work represents the first attempt at determining the amount of useful information that can be retrieved from typical exoplanet spectra. Furthermore, this paper represents the first attempt at using information theoretic limits for retrievals assuming certain instrument capabilities (such as R and S/N). Ulti-

mately, the theory is general and enables prediction of the advances that can be made with improvements in instrumentation and via more prudent choice of spectral ranges.

In §2 we outline the basics of the classic retrieval theory of Rodgers (2000). We first test the technique on an artificial dataset and explore how the number of retrievable parameters depends on R and S/N and discuss how these can be optimized to maximize the usefulness of a measurement in §3. We then apply these techniques to the well-studied HD189733b dayside emission spectra in §4. This is followed by a discussion and conclusions in §5.

4.3 Method

4.3.1 Retrieval Theory

The retrieval problem is well known in the field of Earth atmospheric studies (Rodgers 1976, Chahine 1968, Twomey 1977) and in studies of planetary atmospheres (see, e.g., Nixon et al. 2007). The fundamental problem is to determine the state vector, **x** of dimension n, often a vector of temperatures and mixing ratios at different altitudes (but could be other desirable variables), given some set of observations, **y** of dimension m, usually a vector of flux values at each wavelength. In the absence of any noise, they can be related through **y=F(x)**, where **F(x)** is a model that simulates the measurement at each wavelength given a representative atmosphere. In an idealized scenario, if the relationship between **x** and **y** is linear, we can linearize **F(x)** and write

$$\mathbf{y} = \mathbf{F}(\mathbf{x_a}) + \mathbf{K}(\mathbf{x} - \mathbf{x_a}) \tag{4.1}$$

where **K** is the $m \times n$ Jacobian matrix whose elements are given by the Frechet derivative

$$K_{ij} = \frac{\partial F_i(\mathbf{x})}{\partial x_j} \tag{4.2}$$

with F_i being the measurement in the i^{th} channel, and x_j the value of the j^{th} parameter. The vector $\mathbf{x}_a$ is the prior (*a priori*) state, which represents our best initial guess of the true state before the observations are made. The Jacobian describes the sensitivity of the measurement at each wavelength in a spectrum to a perturbation of a given parameter in the forward model. If the lengths of **x** and **y** are the same then Equation 4.1 may be readily inverted to

$$\mathbf{x} = \mathbf{x_a} + \mathbf{K^{-1}}(\mathbf{y} - \mathbf{F}(\mathbf{x_a})) \tag{4.3}$$

Real data are often noisy and usually have a large number of measurements that over constrain the atmospheric state. For this we must use a more sophisticated scheme to invert the data to determine the atmospheric properties. This can be readily achieved by using a Bayesian framework. In the remainder of this section, we present the basic formalism and useful equations and algorithms that we can use to retrieve atmospheric properties from spectra as well as their information content, following the derivations in Rodgers (2000). For further details, see either Rodgers (2000) or Jacob (2007).

Bayes theorem can be written as

$$P(\mathbf{x}|\mathbf{y}) \propto P(\mathbf{y}|\mathbf{x})P(\mathbf{x}) \tag{4.4}$$

where P(**x**) is the prior probability distribution, which is knowledge of the atmospheric state

before making a measurement, P($\mathbf{y}|\mathbf{x}$) is the likelihood function, that is the probability that the data exists within the context of a particular model, and P($\mathbf{x}|\mathbf{y}$) is the posterior probability distribution density function which can be interpreted as the probability that some state $\mathbf{x}$, in our case atmospheric state, exists given the observations, $\mathbf{y}$. If we assume Gaussian probability distributions for the observational error and for the *a priori* information, we can write

$$P(\mathbf{y}|\mathbf{x}) \propto e^{-\frac{1}{2}(\mathbf{y}-\mathbf{K}\mathbf{x})^T \mathbf{S_e^{-1}} (\mathbf{y}-\mathbf{K}\mathbf{x})} \tag{4.5}$$

$$P(\mathbf{x}) \propto e^{-\frac{1}{2}(\mathbf{x}-\mathbf{x_a})^T \mathbf{S_a^{-1}} (\mathbf{x}-\mathbf{x_a})} \tag{4.6}$$

where $\mathbf{S}_e$ is the $m \times m$ diagonal error covariance matrix (assuming no correlation between measurements) and $\mathbf{S}_a$ is the $n \times n$ *a priori* covariance matrix. The *a priori* covariance matrix represents our prior knowledge of the natural variability of the system and like $\mathbf{S}_e$, it is assumed to be diagonal. It essentially defines our "trust" region, or how far from the prior state we think the actual state can exist. In general, the prior constraint should be loose enough to allow flexibility in the retrieval but not so loose that the retrieval fails when a measurement contributes no information.

Using Bayes theorem from Equation 4.4 we can write the posterior probability distribution as a product of Equation 4.5 and Equation 4.6

$$P(\mathbf{x}|\mathbf{y}) \propto e^{-\frac{1}{2}J(\mathbf{x})} \tag{4.7}$$

where J(**x**) is the cost function and is given by

$$J(\mathbf{x}) = (\mathbf{y} - \mathbf{K}\mathbf{x})^T \mathbf{S_e^{-1}} (\mathbf{y} - \mathbf{K}\mathbf{x}) + (\mathbf{x} - \mathbf{x_a})^T \mathbf{S_a^{-1}} (\mathbf{x} - \mathbf{x_a}) \tag{4.8}$$

The first term in the cost function represents the contribution from the data. The second term represents the contribution from the prior knowledge. If the data is of good quality (high S/N, and high R) then the data term will dominate. Since the product of two Gaussians is a Gaussian, Equation 4.8 can be equivalently written as

$$J(\mathbf{x}) = (\mathbf{x} - \hat{\mathbf{x}})^T \hat{\mathbf{S}}^{-1} (\mathbf{x} - \hat{\mathbf{x}}) \tag{4.9}$$

where $\hat{\mathbf{x}}$ and $\hat{\mathbf{S}}$ are the mean and covariance, respectively, of the posterior probability distribution. A diagonal element of $\hat{\mathbf{S}}$ is the variance in the j^{th} component of the state vector, $\hat{S}_{jj} = \hat{\sigma}_j^2$, where $\hat{\sigma_j}$ is the retrieval uncertainty in the j^{th} parameter.

The goal of any retrieval is to obtain the most likely set of atmospheric parameters given the data. This is achieved when Equation 4.7 is maximized which occurs at the mean of the posterior probability function. Equating Equation 4.8 and Equation 4.9 we can solve for $\hat{\mathbf{x}}$ and $\hat{\mathbf{S}}$ to get

$$\hat{\mathbf{x}} = \mathbf{x_a} + \mathbf{G}(\mathbf{y} - \mathbf{K}\mathbf{x}) \tag{4.10}$$

where **G** is the gain matrix that describes the sensitivity of the retrieval to the observations (if **G=0**, no sensitivity, then the measurements do not contribute towards the retrieved state)

, given by

$$\mathbf{G} = \frac{\partial \hat{\mathbf{x}}}{\partial \mathbf{y}} = \hat{\mathbf{S}}\mathbf{K}^{\mathbf{T}}\mathbf{S}_{\mathbf{e}}^{-\mathbf{1}} \tag{4.11}$$

with

$$\hat{\mathbf{S}} = (\mathbf{K}^{\mathbf{T}}\mathbf{S}_{\mathbf{e}}^{-\mathbf{1}}\mathbf{K} + \mathbf{S}_{\mathbf{a}}^{-\mathbf{1}})^{-\mathbf{1}} \tag{4.12}$$

As the elements of $\mathbf{S_a}$ approach ∞ or the elements of $\mathbf{S_e}$ approach 0, then $\mathbf{G}$ approaches $\mathbf{K^{-1}}$ which is identically the sensitivity of the state vector to the observations, and thus the retrieval is fully characterized by the data.

If the forward model is linear, then Equation 4.10 can be solved to obtain the desired state vector. Often, the forward model is non-linear, generally the case in radiative transfer; it is then best to use a numerical iteration scheme to determine the state vector. In the non-linear case the **Kx** terms in the cost function in Equation 4.8 are replaced with **F(x)**. The Levenberg-Marquardt iteration scheme is used to find the minimum of the non-linear cost function. The prescribed scheme is given by

$$\begin{aligned}\mathbf{x_{k+1}} = \mathbf{x_k} + [(1+\gamma)\mathbf{S_a^{-1}} + \mathbf{K_k^T}\mathbf{S_e^{-1}}\mathbf{K_k}]^{-1} \\ \{\mathbf{K_k^T}\mathbf{S_e^{-1}}[\mathbf{y} - \mathbf{F}(\mathbf{x_k})] - \mathbf{S_a^{-1}}[\mathbf{x_k} - \mathbf{x_a}]\}\end{aligned} \tag{4.13}$$

where $\mathbf{x_k}$ and $\mathbf{x_{k+1}}$ are the state vectors for the k^{th} and $k+1^{st}$ iterations, and $\mathbf{K_k}$ is the Jacobian matrix calculated at the k^{th} iteration. γ is a factor that controls the rate of convergence and is adjusted at each iteration (Press et al. 1995). Equation 4.13 is iterated

until convergence, when

$$(\mathbf{x_k} - \mathbf{x_{k+1}})^{\mathbf{T}} \hat{\mathbf{S}}^{-\mathbf{1}} (\mathbf{x_k} - \mathbf{x_{k+1}}) << n \tag{4.14}$$

Upon convergence, we obtain the retrieved state, $\hat{\mathbf{x}}$ and its precision $\hat{\mathbf{S}}$.

4.3.2 Information Content & Degrees of Freedom

The information content (Shannon & Weaver 1962) and total number of degrees of freedom are useful quantities that can help diagnose the quality and ability of a spectral data set to contribute to our knowledge of the atmospheric state. The number of degrees of freedom represents how many independent parameters can be retrieved from the spectrum, and the information content is a metric of how much the precision in the retrieved parameters has improved as a result of the observation. In the simplest sense, if there are m independent measurements with no error (e.g., fluxes at m different wavelengths), then there will be at most be m independent pieces of information (degrees of freedom) that can be obtained from the observations. If m is fewer than the number of model parameters, n, the exact values of $n - m$ parameters cannot be obtained from the observations. We do not discuss those cases in this article, we choose only cases for which $m > n$. For a given forward model, with n parameters, the maximum number of obtainable degrees of freedom will be the smaller of n and m. In an ideal case the total number of degrees of freedom will be close to n, meaning that the observations can be fully characterized by those n parameters.

In reality, measurements are susceptible error, and the total number of degrees of freedom in the observed signal (denoted by d_s), and thus the number of parameters accessible

to our retrieval, may be fewer than the number of independent measurements, n. Some degrees of freedom, d_n, can be lost in the noise . The sum of d_s and d_n must add up to the total number of parameters we are seeking, n.

Before calculating the degrees of freedom it is useful to first introduce the averaging kernel, **A**. The averaging kernel tells us which of the parameters in the state vector have the greatest impact on the retrieval, that is, the sensitivity of the retrieval to a given parameter, given by

$$\mathbf{A} = \frac{\partial \hat{\mathbf{x}}}{\partial \mathbf{x}} = \frac{\partial \hat{\mathbf{x}}}{\partial \mathbf{y}} \frac{\partial \mathbf{y}}{\partial \mathbf{x}} = \mathbf{GK} \tag{4.15}$$

A is an $n \times n$ matrix whose elements are given by

$$A_{ij} = \frac{\partial \hat{x}_i}{\partial x_j} \tag{4.16}$$

If a diagonal element of **A** is unity, or close to it, then that means for a given change in the true atmospheric state, there is identically the same change in the retrieved state. This suggests that the parameter, x_j, is fully characterized by the data. If that diagonal element is less than unity, meaning that the data itself is not of a high enough quality to constrain that parameter, then some fraction of the *a priori* information must have been used in determining the value of that parameter. If each parameter is fully characterized by the data, that is if, all of the diagonal elements of **A** are unity, then we would expect to be able to retrieve all n parameters. If the diagonal elements are less than unity, then the sum of the diagonals would be less than n. In essence, the diagonal elements of the averaging kernel can be thought of as the degrees of freedom per parameter. If the value of

a particular diagonal element is 1, then that parameter is well characterized by the data. If it is much less than 1, then the data contributes little to our knowledge of that parameter. The total degrees of freedom from the signal can be determined by calculating the trace of **A**. The difference between n and the trace of **A** is the number of degrees of freedom lost to the noise.

The total degrees of freedom, again, tell us how many independent parameters can be determined from the observations. The information content, H, tells us quantitatively how well the observations increased our confidence in our estimate of the atmospheric state relative to the *a priori* knowledge. In a more precise language, the information content of a measurement is the reduction in the entropy of the probability that that an atmospheric state exists given some set of observations, or

$$H = entropy(P(\mathbf{x})) - entropy(P(\mathbf{x}|\mathbf{y})) \tag{4.17}$$

The entropy of a Gaussian distribution of width σ, which the prior and a posterior distributions are assumed to be, can be shown to be proportional to $ln(\sigma)$. Using this fact, and equations Equation 4.17, Equation 4.6, and Equation 4.9,

$$H = \frac{1}{2} ln(|\hat{\mathbf{S}}^{-\mathbf{1}}\mathbf{S_a}|) \tag{4.18}$$

From this we can see that if the data is good (small error bars), then the elements of $\hat{\mathbf{S}}$ will be small, resulting in a large H. Thus H is a quantitative measure of the reduction in our uncertainty in the retrieved atmospheric state as a result of the observations. The larger the

value of H, the more useful the observations are in constraining the atmospheric state.

In summary, both d_s and H are quantitative measures of the quality and usefulness of the observations in determining the atmospheric state, within the context of a given forward model. From their definitions we would expect that a spectrum with a higher S/N, or a higher R, would result in higher values. We will show this in section §3.

4.3.3 Forward Model

A relatively simple forward model, $\mathbf{F}(\mathbf{x})$, which nonetheless captures the basic physics and the measurement process, is at the core of our retrieval. We assume a simplified understanding of the physical and chemical state of the exoplanet atmosphere, i.e., a parameterized temperature structure, the major volatile constituents, the important radiative processes, and the instrument line profiles, etc. Our forward model, as most such models, is an approximation because the data are of limited quality, the underlying physics is relatively ill-understood, and simplifying approximations are necessary. Examples of physics missing in our $\mathbf{F}(\mathbf{x})$ include absent species, inaccurate line lists, clouds, aerosols, 3D effects, etc., or possibly insufficient parameterization of the atmosphere. Therefore, our retrievals must be taken in context of our chosen forward model. Herein, we only consider the dayside spectra of hot Jupiters with near solar metallicity, though the methods are easily be extended to other kinds of observations (transmission spectra) and exoplanets (hot Neptunes, mini Neptunes, super Earths, etc.) with relatively minor modifications to the forward model. For future instruments, with broader spectral coverage and higher spectral resolution, the forward models can increase in sophistication.

Lacking sufficient data (these are low signal-to-noise, low resolution spectra), we simplify our atmosphere to 8 parameters that characterize the temperature structure and gas concentrations. For sake of simplicity, we use an analytic temperature profile formulated by Guillot (2010), and since then modified by V. Parmentier & T. Guillot, (in preparation) to include three channels. The profile, derived using a 3 channel approximation, is given by

$$T^4(\tau) = \frac{3T_{int}^4}{4}(\frac{2}{3} + \tau) + \frac{3T_{irr}^4}{4}(1-\alpha)\xi_{\gamma_1}(\tau) + \frac{3T_{irr}^4}{4}\alpha\xi_{\gamma_2}(\tau) \tag{4.19}$$

where

$$\xi_{\gamma_i} = \frac{2}{3} + \frac{2}{3\gamma_i}[1 + (\frac{\gamma_i\tau}{2} - 1)e^{-\gamma_i\tau}] + \frac{2\gamma_i}{3}(1 - \frac{\tau^2}{2})\mathrm{E}_2(\gamma_i\tau) \tag{4.20}$$

with $\gamma_1 = \kappa_{v_1}/\kappa_{IR}$ and $\gamma_2 = \kappa_{v_2}/\kappa_{IR}$, where κ_{v_1}, κ_{v_2}, and κ_{IR} are the visible and infrared (thermal) opacities, respectively. The parameter α (range 1 to 0) partitions the flux between the two visible streams, and $E_2(\gamma\tau)$ is the second-order exponential integral function. The internal heat flux (from the net cooling history) is represented by the temperature T_{int}, while the solar flux at the top of the atmosphere is represented by T_{irr}; these two temperatures are fixed. Assuming zero albedo and unit emissivity, T_{irr} is

$$T_{irr} = (\frac{R_*}{2a})^{1/2}T_* \tag{4.21}$$

where R_* and T_* are the stellar radius and temperature, a, the star planet separation and τ is the infrared (thermal) optical depth

$$\tau = \frac{\kappa_{IR}P}{g} \tag{4.22}$$

with P the pressure and g the surface gravity (at 1 bar). In total there are 4 free parameters governing the temperature structure, κ_{IR}, κ_{v_1}, κ_{v_2} and α. We choose this parameterization with two visible streams as opposed to the traditional one visible stream (Hansen 2008; Guillot 2010) because the extra stream allows more freedom for a temperature inversion, though in some cases (as we shall see below) the second visible stream does not matter.

The remaining 4 parameters are the uniform mixing ratios for H_2O, CH_4, CO, CO_2, expected to be the major molecular opacity sources (Tinetti et al., 2007; Swain et al., 2009a). We choose vertically uniform mixing ratios for two reasons. First, the data lack sufficient information content to actually help resolve vertical structure in abundances, and second, chemical kinetics models (Moses et al. 2011; Line et al. 2010, 2011a), show that vertical mixing leads to constant vertical mixing ratios for these species within the IR photosphere, so even if we could resolve detailed vertical information, we would most likely find that the abundances remain fairly constant.

Since many of these parameters may vary over many orders of magnitude we find it convenient with the above formalism to solve for the logarithm of the atmospheric state.

With that, the state vector of parameters that we would like to retrieve can be given by

$$\mathbf{x} = \begin{bmatrix} \log(\kappa_{v_1}) \\ \log(\kappa_{v_1}) \\ \log(\kappa_{IR}) \\ \alpha \\ \log(f_{H2O}) \\ \log(f_{CH4}) \\ \log(f_{CO}) \\ \log(f_{CO2}) \end{bmatrix}$$

where f_i is the mixing ratio of species i in parts per million (ppm) and the opacities are in $\mathrm{cm}^2\mathrm{g}^{-1}$.

We also include H_2-H_2 and H_2-He collision-induced opacity. The mixing ratios of H_2 and He vary little with the atmospheric levels that produce the bulk of the dayside thermal emission (500-2000 K, 10-10^{-4} bar). We fix f_{H_2} and f_{He} to thermochemical abundances (assuming solar elemental abundances) of 0.86 and 0.14, respectively. These values may change on the tens of percent level in enriched atmospheres, however, this variation has negligible effect on the resultant infrared spectra. Also, we do not include NH_3 as an opacity source as it has little influence in the spectral region we consider.

We use the Reference Forward Model (RFM)[2], a line-by-line radiative transfer code, to calculate the disk integrated dayside emission spectra, modified to handle H_2-H_2 and H_2-He collisionally induced opacities. The collisionally induced opacity tables are taken

[2]see http://www.atm.ox.ac.uk/RFM/

from Barysow et al. (2001;2002) and Jørgensen et al. (2000). The molecular line strengths for H_2O, CO_2, and CO, are from the HITEMP (Rothman et al. 2010) database and CH_4[3] is from the HITRAN 2008 database (Rothman et al. 2009). In order to keep the molecular line-lists from becoming too unwieldy we make an intensity cutoff at 298 K of 10^{-40} cm molecule^{-1}, as recommended by Sharp & Burrows (2007).

4.4 Test on Synthetic Data

First, we test the retrieval method on a synthetic data set for which we know the answer. Using this synthetic spectrum, we explore the effect that signal-to-noise and spectral resolution have on the degrees of freedom and information content.

A hypothetical hot Jupiter atmosphere is generated using $\kappa_{v_1} = \kappa_{v_2} = 4 \times 10^{-3}$ cm^{2}g^{-1}, $\kappa_{IR} = 1 \times 10^{-2}$ cm^{2}g^{-1}, $\alpha = 0.5$, and fixed vertical mixing ratios of $f_{H2O} = 5 \times 10^{-4}$, $f_{CH4} = 1 \times 10^{-6}$, $f_{CO} = 3 \times 10^{-4}$, and $f_{CO_2} = 1 \times 10^{-7}$. The planet orbits around a G0V host star (e.g., HD 209458a) with $T_* = 6000$ K, $R_* = 1.14$ R$_\odot$ at a separation of $a = 0.064$ AU. The planetary properties are a radius of $1.35 R_J$, an internal temperature of $T_{int} = 200$ K, and $g = 21.1$ m s^{-2} (at 1 bar pressure). Using Equation 4.21 we find $T_{irr} = 1223$ K. The emission spectrum of the exoplanet (see Figure 4.1) is initially generated with a one wave-number resolution (resolving power, R $\simeq$5000 at 2 μm).

For the initial test, the synthetic spectrum (Figure 4.1) is degraded by convolving it

[3]Upon completion of our initial investigation it was also brought to light that there exists more appropriate high-temperature-based line lists for methane such as the STDS (http://icb.u-bourgogne.fr/OMR/SMA/SHTDS/HTDS.html). Using this line list over HITRAN makes absolutely no difference for our synthetic work since the synthetic data was produced using the HITRAN methane. We have also compared our HD189733b retrieval results for both methane line lists and found no difference.

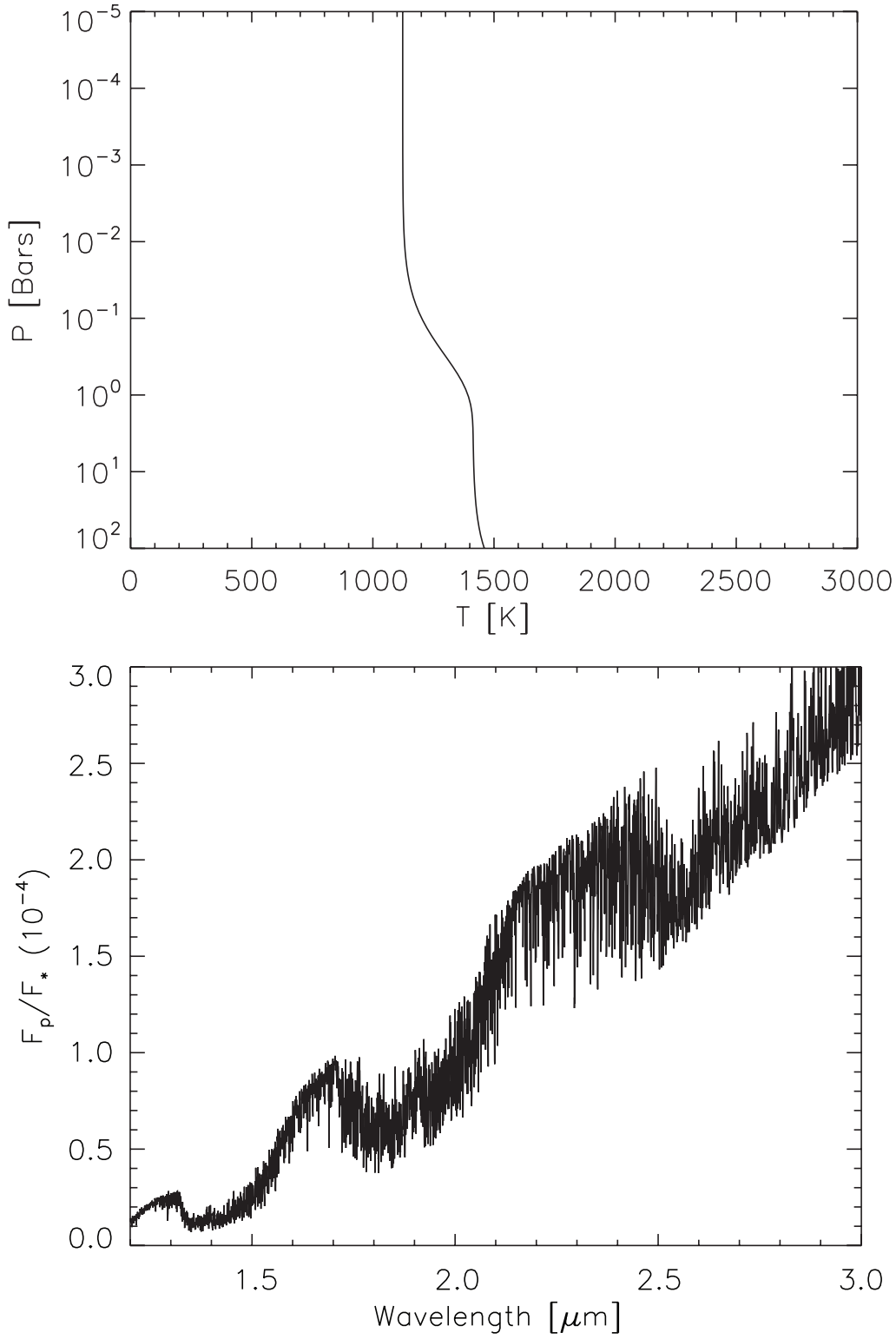

Figure 4.1: Synthetic spectrum (bottom) generated with the model atmosphere (top) with a spectral resolution of 1 cm^{-1}, or R$\sim$5000 at 2 μm. The model temperature profile is generated from equations Equation 4.19 and Equation 4.20 with $\kappa_{v_1} = \kappa_{v_2} = 4 \times 10^{-3}$ cm^{2}g^{-1}, $\kappa_{IR} = 1 \times 10^{-2}$ cm^{2}g^{-1}, $\alpha = 0.5$, $T_{irr} = 1223K$, and $T_{int} = 200K$. The constant-with-altitude mixing ratios are $f_{H2O} = 5 \times 10^{-4}$, $f_{CH4} = 1 \times 10^{-6}$, $f_{CO} = 3 \times 10^{-4}$, and $f_{CO2} = 1 \times 10^{-7}$.

with an instrumental profile matching the defocussed HST NIC3 camera with a spectral full width at half maximum of 0.055 μm (R $\simeq$ 40 at 2 μm; Swain et al. 2009a), and reducing the measurement signal-to-noise of each spectral channel to $\sim$ 10. Rather than be guided by physical and chemical models, or some previous observation of the object, we arbitrarily chose an *a priori* state, $\mathbf{x_a}$, far from the true physical state. The remaining unspecified quantity is the *a priori* covariance matrix, $\mathbf{S_a}$. Once more, the diagonal elements of $\mathbf{S_a}$ are allowed a large range as we are dealing with a relatively novel type of observations and lack detailed prior information. We also assume that there are no cross correlations between different state parameters (e.g., f_{CO} and f_{CO_2}, even though from chemical models we know that such quantities have high correlations). Because the state parameters are logarithmic, the elements of $\mathbf{S_a}$ are also logarithmic (with the exception of α) so we set, somewhat arbitrarily, $\sigma_{\kappa_{v1}} = 2$, $\sigma_{\kappa_{v2}} = 2$, $\sigma_{\kappa_{IR}} = 2$, $\sigma_{\alpha} = 0.5$, $\sigma_{f_{H2O}} = 6$, $\sigma_{f_{CH4}} = 6$, $\sigma_{f_{CO}} = 6$, and $\sigma_{f_{CO2}} = 6$ meaning that the opacities are permitted to span 4 orders of magnitude centered around their *a priori* value and the mixing ratios are allowed to span 12 orders of magnitude. Such large *a priori* uncertainties lead to a flat *a priori* distribution, relative to the data, reducing the current problem to a maximum likelihood estimation (as opposed to Bayesian), with the option of using the priori information if the data is sparse.

The entirety of the forward model can summarized with the Jacobian. Figure 4.2 shows the columns of the Jacobian evaluated at the true state (response of the flux in each channel to a perturbation in each of the parameters in **x**) for the synthetic data (Figure 4.3). The spectrum is most sensitive to perturbations in the opacities that govern the temperature profile. The 1.7 μm and 2.2 μm channels are most sensitive to changes in the temperature

profile. This is because there are not large absorption features at these wavelengths, meaning, these channels are most sensitive to the flux from deeper layers (1–10 bars). This also partially explains why κ_{IR} and κ_{v1} have opposite responses. An increase in κ_{IR} results in an increase in flux due to an increase in temperature in the deep layers probed by these channels, as can be seen in Equation 4.19. An increase in κ_{v1} results in a decrease of flux in these channels due to a decrease in temperature in the deeper layers. From Equation 4.19 an increase in κ_{v1} increases the temperature above the ~ 0.1bar level, and in order to maintain radiative equilibrium at the top of the atmosphere, a decrease in temperature in the deeper layers must occur, and also a higher κ_v prevents the stellar flux from penetrating into the deeper atmosphere. The opposite is true near 2.9 μm which is more sensitive to higher altitudes because of the large absorption, thus an increase in in κ_{v1} will result in an increase in temperature which in turn results in a flux increase. Also, in this particular case $\alpha = 0.5$ meaning both κ_{v1} and κ_{v2} have identically the same results. Additionally, κ_{v1}=κ_{v2} which causes the spectrum to have no sensitivity to changes in α.

The spectral response is most sensitive to the water abundance more than any other gas across all wavelengths in this example (Figure 4.2). This makes the retrieval of water more precise than the other species. The greatest sensitivity to changes in the CO_2 abundance occur at 2.1 and 2.8 μm, which both happen to be located near the sensitivity minima of CO and CH_4, though it still has to contend with water. Both CO and CH_4 have greatest sensitivity in the 2.3 μm band making it difficult to simultaneously retrieve both.

Figure 4.3 shows the retrieval process for this initial synthetic test case. We determine

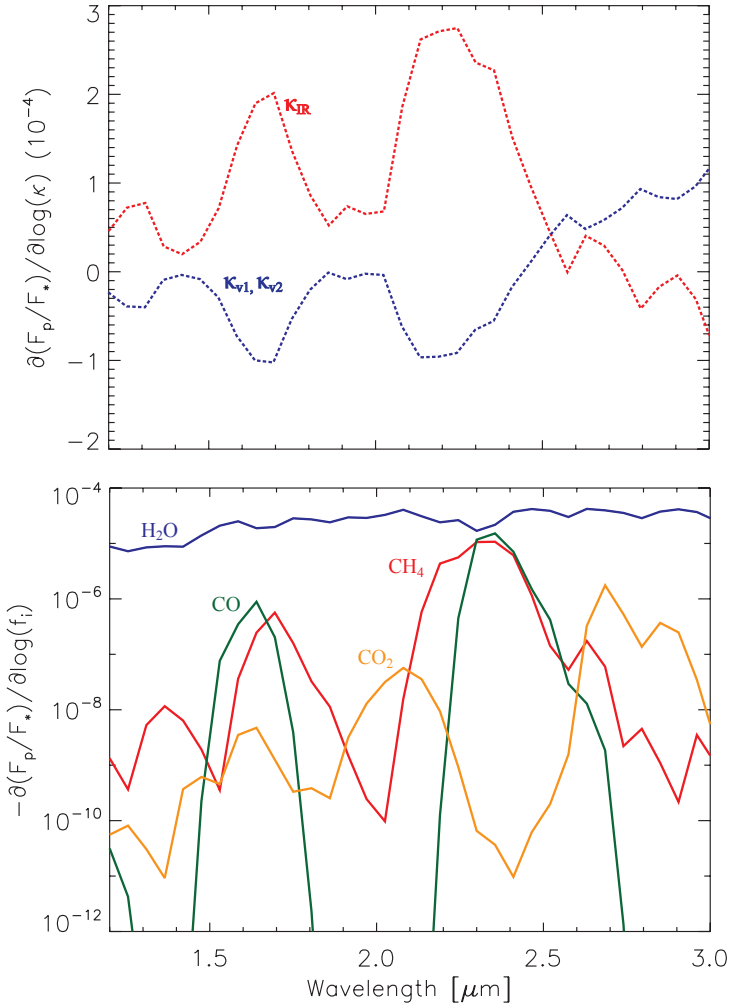

Figure 4.2: Columns of the Jacobian for the synthetic spectrum evaluated at the true state. This is the response of the flux as a function of wavelength due to a small positive perturbation in one of the parameters in **x**. The top panel is the flux response for the parameters that govern the temperature profile, κ_{v_1}, κ_{v_2}, κ_{IR}. The bottom panel is the flux response to a small perturbation in the gas mixing ratios, f_{H2O}, f_{CH4}, f_{CO}, and f_{CO2}. The Jacobian is calculated as a change in the planet-to-star flux ratio, $\Delta(F_p/F_*)$ to a positive logarithmic perturbation in a given parameter, $\Delta\log(x_j)$. Note that in the bottom panel an increase in the gas mixing ratios always results in a decrease in F_p/F_*. In this particular case, the spectrum is equally sensitive to κ_{v_2} and κ_{v_1} because α is 0.5. If $\alpha = 0$ than the spectrum will have no sensitivity to κ_{v_2} and if $\alpha = 1$ the spectrum will have no sensitivity to κ_{v_1}. Also, for this synthetic dataset κ_{v_2}=κ_{v_1} which results in no sensitivity to α

the quality of the retrieval using the standard reduced chi-squared given by

$$\chi^2 = \frac{1}{N}\sum_{i=1}^{N}\frac{(y_i - F_i)^2}{\sigma_i^2} \tag{4.23}$$

where N is the total number of data points, y_i, F_i, and σ_i, are defined in §2.1. If χ^2 is less than one, then the difference between the model fit and data is typically better than 1 σ. We should stress however, that a perfect fit ($\chi^2 = 0$) does not necessarily mean that the true state has been retrieved, because of the degeneracies between some of the parameters. Table 5.1 compares the true state to the retrieval results along with the retrieval precission. The synthetic retrieval demonstrates the robustness of the retrieval to a poor *a priori*. The reason for this can be seen by inspecting the elements of the averaging kernel. From Table 5.1, all but κ_{v1} and methane are fairly well characterized by the data (A_{jj} is close to 1). Summing these values gives the total degrees of freedom, and thus the total number of useful retrievable parameters of ~ 6.

Table 4.1: Synthetic retrieval results. κ_{v1}, κ_{v2}, and κ_{IR} are in units of (cm^{2}g^{-1}). f_i is the volume mixing ratio for species i. We also show the diagonal averaging kernel elements ($A_{jj} = \frac{\partial \hat{x}_j}{\partial x_j}$) for each parameter. The retrieval uncertainties are given as $\hat{x} - \hat{\sigma}$ to $\hat{x} + \hat{\sigma}$ for each parameter.

Parameter	True State ($\mathbf{x}$)	*A priori* ($\mathbf{x_a}$)	Retrieved State ($\hat{\mathbf{x}}$)	Retrieval Precision	$\frac{\partial \hat{x}_i}{\partial x_j}$
κ_{v1}	4.00×10^{-3}	1.00×10^{-3}	3.59×10^{-3}	2.76×10^{-3} - 4.68×10^{-3}	0.997
κ_{v2}	4.00×10^{-3}	1.00×10^{-2}	1.70×10^{-9}	1.70×10^{-11} - 1.70×10^{-7}	0.0
κ_{IR}	1.00×10^{-2}	3.16×10^{-2}	8.93×10^{-3}	7.13×10^{-3} - 1.12×10^{-2}	0.998
α	0.5	0.1	0.003	0.00 - 0.022	0.999
f_{H2O}	5.00×10^{-4}	1.00×10^{-6}	4.18×10^{-4}	2.58×10^{-4} - 6.76×10^{-4}	0.999
f_{CH4}	1.00×10^{-6}	1.00×10^{-4}	3.43×10^{-7}	4.34×10^{-12} - 2.70×10^{-2}	0.334
f_{CO}	3.00×10^{-4}	1.00×10^{-6}	1.96×10^{-4}	2.27×10^{-6} - 1.69×10^{-2}	0.896
f_{CO2}	1.00×10^{-7}	1.00×10^{-4}	7.70×10^{-7}	9.95×10^{-10} - 5.96×10^{-4}	0.768

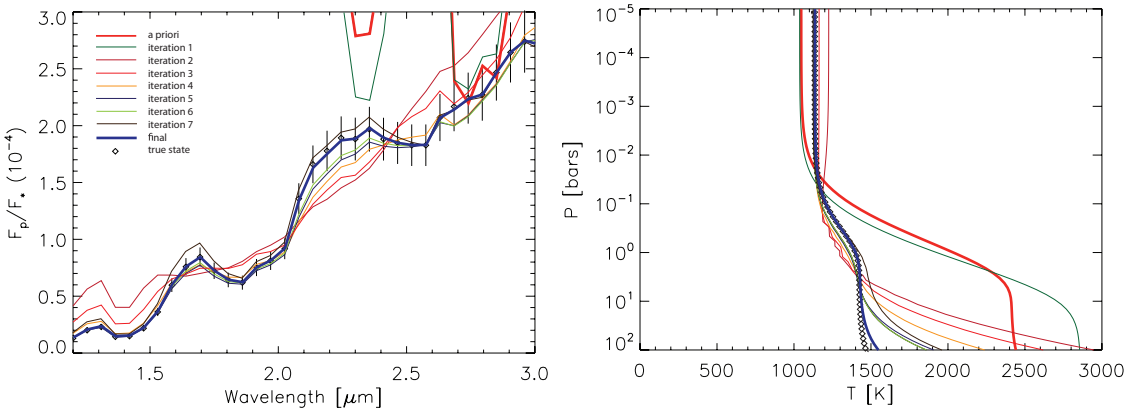

Figure 4.3: Synthetic spectrum retrieval. Left: Iteration sequence of the model spectrum, $\mathbf{F}(\mathbf{x_k})$. The diamonds with error bars are the synthetic data convolved down to a resolution of 0.055 μm (R$\sim$37 at 2 μm) and a signal-to-noise of 10. The thick red curve is the forward model spectrum generated from the *a priori*, $\mathbf{F}(\mathbf{x_a})$. Note that it is a poor fit to the data. Each subsequent curve is the new model spectrum after each iteration of Equation 4.13. The thick solid blue curve is the final retrieved model spectrum. Right: Evolution of the temperature profile with each iteration. The thick red curve is the *a priori* temperature profile. The thick blue curve is the retrieved temperature profile. The diamond symbol curve is the true temperature profile as in Figure 4.1. χ^2 converges to 0.007 after 8 iterations of Equation 4.13.

4.4.1 Resolution and Signal-to-Noise Effects on the Degrees of Freedom & Information Content

The S/N and R are two important factors that influence the quality and usefulness of a spectrum. It is thus imperative to consider them when designing a spectrometer. In this section we use our synthetic dataset to explore how the degrees of freedom, both total and per atmospheric parameter, and the information content evolve with increasing S/N and R.

We would intuitively expect d_s and H both to increase with increasing R and S/N. Figure 4.4 shows a contour plot of d_s and H calculated for the synthetic spectrum generated in Figure 4.1 for a variety of S/N's and R's. The maximum increase in both occurs with a simultaneous[4] increase in S/N and R.

[4]This is true if R and S/N are independent of each other. In most cases S/N decreases with increasing R

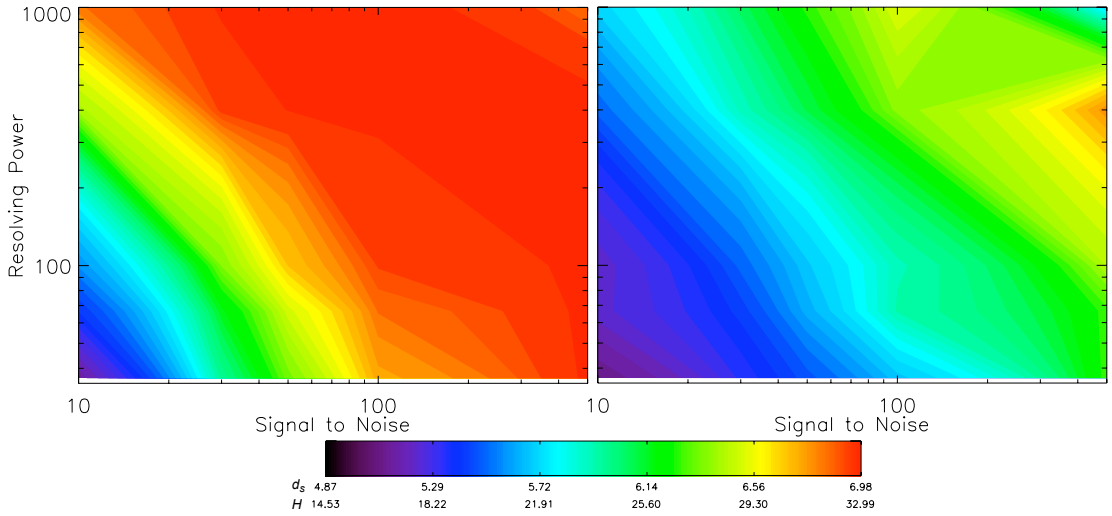

Figure 4.4: S/N and R effects on the total degrees of freedom (left) and the information content (right). In general, as S/N and R increase, the total number of degrees of freedom obtainable from the data, and the information content increase. See equations Equation 4.24 and Equation 4.25.

We point out that the contour plots in Figure 4.4 can only be taken in the context of the spectral window within which we are applying the retrieval, and the number of parameters we are trying to retrieve. In other words, for the 8 parameters we are retrieving here, there is no benefit to increasing R or S/N beyond a few hundred and $\sim$100, respectively. If we do happen to have a higher R and S/N, it is likely that we would be able to retrieve more forward model parameters such as the concentrations of other gases, or information on the vertical distributions of the gases. Current observations, like the HST NICMOS observations of HD189733b, generally fall towards the bottom left corners in Figure 6. This suggests that S/N and R's of such data are not high enough to fully constrain even our simple forward model, and thus even less constraining for more complicated models.

The increasing behavior in d_s with increasing S/N can be seen through the use of Equa-

because of the smaller spectral bins.

tion 4.11, Equation 4.12, and Equation 4.15. As S/N goes to infinity, the elements of $\mathbf{S_e}$ go to zero causing **G** to approach $\mathbf{K^{-1}}$, in turn causing **A** to approach the identity matrix, meaning the diagonal elements are all ones with a trace equal to the total number of parameters and thus the maximum number of degrees of freedom. The relationship between d_s and S/N can be seen in a 1-parameter 1-channel model, where $d_s = A$. Upon reducing the matrix equations, the one element averaging kernel becomes,

$$d_s = A = \frac{K^2\sigma_a^2}{K^2\sigma_a^2 + (F/(S/N))^2} = \frac{(S/N)^2}{(S/N)^2 + \frac{F^2}{K^2\sigma_a^2}} \tag{4.24}$$

and the relation of these parameters to the information content is

$$H = ln[1 + \frac{\sigma_a^2}{F^2}K^2(S/N)^2]. \tag{4.25}$$

where K, σ_a, and F are the 1-D analogs for **K**, $\mathbf{S_a}$, and **F(x)**, respectively. We also have assumed that σ_e, the 1-D analog for $\mathbf{S_e}$, is the flux, F, divided by S/N. In this case, d_s approaches unity as S/N goes to infinity, and zero, if S/N is zero. H approaches infinity as S/N goes to infinity, and approaches zero when S/N goes to zero. One important thing to note from these relations is that increasing S/N will matter only if the Jacobian, K, is non-zero, meaning that there must be some sensitivity of the flux to a perturbation in the desired parameter. Otherwise, no amount of S/N increase will improve our knowledge of the atmospheric state. Increasing R or adding more spectral channels can also contribute to an increase in d_s and H. If channels are chosen such that the K is large, meaning large sensitivity to a given parameter, then d_s and H will both increase. As K approaches infinity

(infinite sensitivity), d_s will approach unity and H will approach infinity.

From this simple analysis, though it may intuitively obvious, we can readily see that if we want to improve the characterization of a particular atmospheric property, it is best to design an instrument whose spectral regions offer the greatest sensitivity to that parameter, and to have a high S/N within those spectral regions.

4.5 Test on Real Data: HD189733b Dayside Emission

Now that we have demonstrated that this retrieval procedure works and provides useful information about the quality of a data set through the degrees of freedom and information content, we wish to apply it to the dayside emission spectra of one of the best-studied exoplanet atmospheres, HD189733b. We assume the same forward model and *a priori* covariances as in the synthetic work.

The dayside emission spectrum of HD189733b has been subject to much investigation (Swain et al., 2009a, Grillmair et al. 2007, Madhusudhan & Seager 2009, and many others), and often times different analyses come up with different solutions for its composition and temperature structure. For simplicity we investigate only the near-IR spectrum from Swain et al. (2009a). As an *a priori* atmospheric state we use the "Fortney 2π" (Fortney et al., 2010) temperature profile from Figure 4.2 of Moses et al. (2011) approximated with Equation 4.19 and the 0.1 bar mixing ratios for H_2O, CH_4, CO, and CO_2 from their Table 5.2 but assumed to be constant with altitude within the IR photosphere sampled by the observations (because of quenching arguments). Figure 4.5 and Table 5.2 show the results of the retrieval. The Jacobian in Figure 4.5 demonstrates the high sensitivity of the

spectrum to water and carbon dioxide, some sensitivity to CO near 2.3 μm, and very little sensitivity to methane at all wavelengths. The 1.7 and 2.2 μm channels are sensitive to the deep temperatures (effected by κ_{IR}) due to the higher transmittance at those wavelengths. The strong CO_2 absorption feature at 2.1 μm has less sensitivity to the deep temperatures and more sensitivity to temperatures higher up (controlled by κ_{v1} and κ_{v2}).

The diagonal elements of the averaging kernel in Table 5.2 quantitatively tell us which parameters we can and cannot retrieve from the dayside emission spectra. Again, H_2O, CO and CO_2 have averaging kernel elements that are near unity and are therefore well constrained by the data, as is also reflected in the retrieval uncertainty, which is smaller than the assumed *a priori* uncertainty. CH_4 is completely unconstrained. The retrieval uncertainty is the same as the *a priori* uncertainty, suggesting that the observations contribute no information about its abundance. The trace of the averaging kernel gives the total number of degrees of freedom, and thus the total number of retrievable parameters, to be $\sim$5.

Our results compare quite well with those of Madhusudhan & Seager (2009) and with Swain et al. (2009a) with the exception of CO_2 (Table 5.2) which appears to be underestimated by three orders of magnitude in Swain et al. (2009a). Our derived temperature profile (Figure 4.5, bottom right) also appears to fall within the spread given in Figure 4.5 of Madhusudhan & Seager (2009).

4.6 Discussion & Conclusions

We demonstrate retrieval by inverse modeling of extrasolar planetary spectra. We first apply the technique to a synthetic model spectrum of a solar metallicity $T \simeq 1200$ K hot Jupiter,

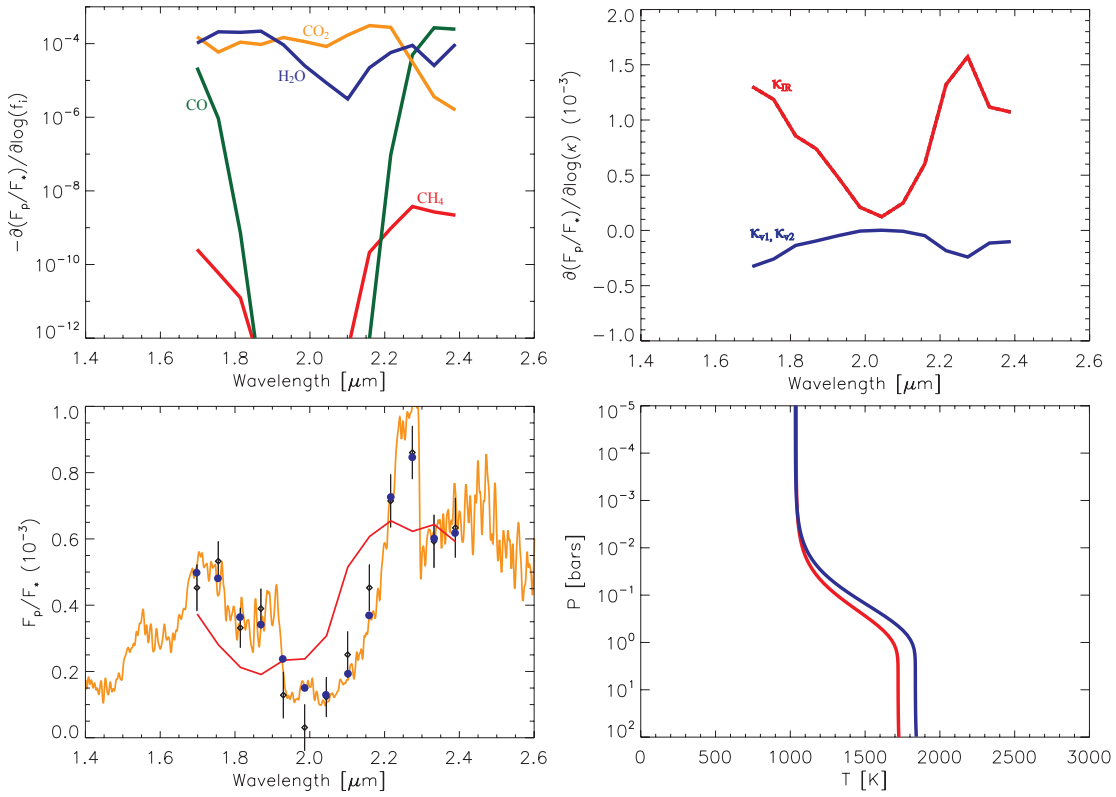

Figure 4.5: Retrieval results for the NICMOS dayside emission spectra of HD189733b from Swain et al. (2009a). Top Left: The sensitivity of the planet-to-star flux ratio to a perturbation in the mixing ratios of H_2O, CO_2, CO, and CH_4 at each channel in the NICMOS dataset. Top Right: The sensitivity of the planet-to-star flux ratio to a perturbation in the parameters governing the temperature profile. Bottom Left: The retrieved spectrum. The black diamonds with error bars are the Swain et al. (2009a) dayside emission data. The red curve is the *a priori* spectrum convolved with the instrumental broadening profile and sampled at the data wavelengths. The orange curve is retrieved spectrum at high resolution. The blue dots are the retrieved spectrum convolved with the instrumental broadening function and sampled at the data wavelengths. This optimal solution gives χ^2=0.76. Bottom Right: The *a priori* (red) and retrieved (blue) temperature profiles.

Table 4.2: Retrieval results for HD189733b. κ_{v1}, κ_{v2}, and κ_{IR} are in units of (cm^{2}g^{-1}). f_i is the volume mixing ratio for species i. We also show the diagonal averaging kernel elements ($A_{jj} = \frac{\partial \hat{x}_j}{\partial x_j}$) for each parameter. The total number of degrees of freedom for this spectrum is $\sim$5. The retrieval precisions are given as $\hat{x} - \hat{\sigma}$ to $\hat{x} + \hat{\sigma}$ for each parameter. We also show for comparison the abundances derived by Madhusudhan & Seager (2009) (MS10) and Swain et al. (2009a) (S09a).

Parameter	*A priori* ($\mathbf{x_a}$)	Retrieved State ($\hat{\mathbf{x}}$)	Retrieval Precision	$\frac{\partial \hat{x}_i}{\partial x_j}$	MS10	S09a
κ_{v1}	4.00×10^{-3}	4.71×10^{-3}	1.67×10^{-4} - 1.32×10^{-1}	0.475	-	-
κ_{v2}	4.00×10^{-3}	4.71×10^{-3}	1.67×10^{-4} - 1.32×10^{-1}	0.475	-	-
κ_{IR}	3.00×10^{-2}	4.70×10^{-2}	3.00×10^{-2} - 7.36×10^{-2}	0.990	-	-
α	0.5	0.5	0.00 -1.00	0.00	-	-
f_{H2O}	4.00×10^{-4}	1.19×10^{-4}	5.29×10^{-5} - 2.67×10^{-4}	0.997	$\sim 10^{-4}$	1×10^{-5} - 1×10^{-4}
f_{CH4}	1.00×10^{-6}	9.78×10^{-9}	9.79×10^{-15} - 9.77×10^{-3}	0.00	$\leq 6\times10^{-6}$	$\leq 1\times10^{-7}$
f_{CO}	5.00×10^{-4}	1.15×10^{-2}	3.60×10^{-3} - 3.64×10^{-2}	0.993	2×10^{-4} - 2×10^{-2}	1×10^{-4} - 3×10^{-4}
f_{CO2}	1.00×10^{-7}	3.37×10^{-3}	1.69×10^{-3} - 6.72×10^{-3}	0.998	7×10^{-4}	1×10^{-7} - 1×10^{-6}

and then to a previously published HST NICMOS spectrum of HD 189733b showing results that are consistent with previous studies. The approach herein is much more efficient that other methods such as a gridded parameter search, or Monte Carlo techniques, as it only requires $\sim 10^2$ forward model computations as opposed to millions. The formalism also allows robust estimation of the retrieval uncertainties.

We have also investigated the information theory aspects of the problem, in order to assess the quality and usefulness of a spectral data set in constraining atmospheric properties. First, we discuss how the Jacobian matrix can be used to determine which spectral channels are most sensitive to chosen atmospheric parameters. Second, we show the use of the averaging kernel as a diagnostic tool to guide us to which parameters can be usefully retrieved from the spectrum in question. Third, we calculated the number of available degrees of freedom and often found that, given the current limited observational capabilities, the number of retrievable parameters was less than the number of parameters in our forward model. Fourth, using simple expressions for the degrees of freedom and information content, we showed semi-quantitatively how S/N and R effect our knowledge of

the atmospheric state. These tools can be particularly useful in aiding the design of future instruments such that they can be optimized for observations of transiting exoplanets.

A recent paper (Lee et al. 2011) using the optimal estimation approach as applied to HD 189733b, was published while this article was in preparation. The details of the methodology in that paper are somewhat different from ours, i.e., in the parameterization of the atmospheric models and in the use of the correlated-K opacities (we use line-by-line radiative transfer). In addition, Lee et al. use multi-band (i.e., from various instruments inclusive of HST NICMOS, Spitzer IRAC, IRS and MIPS), multi-epoch measurements of HD 189733b as a representative snapshot of the planetary dayside. We restrict our retrieval to a single epoch, 13 spectral-channel NICMOS observation spanning less than one octave of total spectral coverage between 1.45-2.5 microns. Our retrievals agree for the most part with those of Lee et al., in that H_2O and CO_2 are retrieved with confidence but neither retrieval can say much about the abundance of methane (a trace species in HD 189733b). One clear discrepancy is that we are able to retrieve CO where as they cannot. Also, Lee et al. do not discuss the information content aspects of the atmospheric retrieval formulation presented in both of these papers.

In follow on investigations, we plan to use the information content analyses to study aspects of combining Spitzer broadband photometry with prior notions about the atmospheric state to constrain atmospheric properties such as CH_4/CO and C/O ratios. A powerful use of these methods is in optimizing the design of instruments that could be flown in NASA's *FINESSE* and ESA's *Exoplanet Characterization Observatory*, or in studying the potential of already designed instruments such as *JWST's NIRCAM* that offer various observing

modes, bandpasses and spectral resolving power.

4.7 Acknowledgements

We would like to thank Zhan Su, Aaron Wolf, Konstantin Batygin, Alejandro Soto, Run-Lie Shia, Leigh Fletcher, Kuai Le, Heather Knutson, Mimi Gerstell, Linda Brown, and the Yuk Yung group for reading the article and many useful discussions. M. Line is supported by the JPL Graduate Fellowship funded by the JPL Research and Technology Development Program. XZ and YLY are supported by a grant from the PATM program of NASA to the California Institute of Technology. P. Chen & G. Vasisht are supported by the JPL Research & Technology Development Program, and contributions herein were supported by the Jet Propulsion Laboratory, California Institute of Technology, under a contract with the National Aeronautics and Space Administration.

Bibliography

Borysow, A., Jørgensen, U.G., Fu, Y. 2001, JQSRT, 68, 235

Chahine, M. T. 1968, JOSA (1917-1983), 58, 1634

Charbonneau, D., Allen, L. E., Megeath, S. T., et al. 2005, ApJ, 626, 523

Charbonneau, D., Knutson, H. A., Barman, T., et al. 2008, ApJ, 686, 1341

Deming, D., Seager, S., Richardson, L. J., & Harrington, J. 2005, Nature, 434, 740

Fortney, J. J., Shabram, M., Showman, A. P., et al. 2010, ApJ, 709, 1396

Grillmair, C. J., Charbonneau, D., Burrows, A., et al. 2007, ApJl, 658, L115

Grillmair, C. J., Burrows, A., Charbonneau, D., et al. 2008, Nature, 456, 767

Guillot, T. 2010, A&A, 520, A27

Harrington, J., Hansen, B. M., Luszcz, S. H., et al. 2006, Science, 314, 623

Harrington, J., Luszcz, S., Seager, S., Deming, D., & Richardson, L. J. 2007, Nature, 447, 691

Hansen, B. M. S. 2008, ApJs, 179, 484

Jacob, D. 2007, Inverse modeling of atmospheric composition data, ARCNESS Winter School

Jørgensen, U. G., Hammer, D., Borysow, A., & Falkesgaard, J. 2000, A&A, 361, 283

Knutson, H. A., Charbonneau, D., Allen, L. E., et al. 2007, Nature, 447, 183

Knutson, H. A., Charbonneau, D., Allen, L. E., Burrows, A., & Megeath, S. T. 2008, ApJ, 673, 526

Knutson, H. A., et al. 2009, ApJ, 690, 822

Kuai, L., Natraj, V., Shia, R.-L., Miller, C., & Yung, Y. L. 2010, JQSRT, 111, 1296

Lee, J.-M., Fletcher, L. N., & Irwin, P. G. J. 2011, arXiv:1110.2934

Line, M. R., Liang, M. C., & Yung, Y. L. 2010, ApJ, 717, 496

Line, M. R., Vasisht, G., Chen, P., Angerhausen, D., & Yung, Y. L. 2011a, ApJ, 738, 32

Line, M. R.,Zhang, X., & Yung, Y. L. 2011b, EPSC-DPS Joint Meeting, 249

Madhusudhan, N., & Seager, S. 2009, ApJ, 707, 24

Mandell, A. M., Drake Deming, L., Blake, G. A., et al. 2011, ApJ, 728, 18

Moses, J. I., Visscher, C., Fortney, J. J., et al. 2011, ApJ, 737, 15

Nixon, C. A., Achterberg, R. K., Conrath, B. J., et al. 2007, Icarus, 188, 47

Press, W.H., Teukolksy, S., Vetterling, W.T., Fannery, B. 1995, Numerical Recipies: The art of scientific computing, sec. ed., Camb. Univ. Press

Redfield, S., Endl, M., Cochran, W. D., & Koesterke, L. 2007, Bulletin of the American Astronomical Society, 38, 134.10

Rodgers, C. D. 1976, Reviews of Geophysics and Space Physics, 14, 609

Rodgers, C.D., Inverse methods for atmospheric sounding, Theory and Practice, 2000

Rothman, L. S., Gordon, I. E., Barbe, A., et al. 2009, JQSRT, 110, 533

Rothman, L. S., Gordon, I. E., Barber, R. J., et al. 2010, JQSRT, 111, 2139

Shannon, C.E., & Weaver, W., A Mathematical Theory of Communication, University of Illinois Press, 1962

Sharp, C. M., & Burrows, A. 2007, ApJs, 168, 140

Snellen, I. A. G., Albrecht, S., de Mooij, E. J. W., & Le Poole, R. S. 2008, A&A, 487, 357

Snellen, I. A. G., de Kok, R. J., de Mooij, E. J. W., & Albrecht, S. 2010, Nature, 465, 1049

Stevenson, K. B., et al. 2010, Nature, 464, 1161

Swain, M. R., Vasisht, G., Tinetti, G., et al. 2009a, ApJl, 690, L114

Swain, M. R., Tinetti, G., Vasisht, G., et al. 2009b, ApJ, 704, 1616

Swain, M. R., Deroo, P., Griffith, C. A., et al. 2010, Nature, 463, 637

Tinetti, G., Vidal-Madjar, A., Liang, M.-C., et al. 2007, Nature, 448, 169

Tinetti, G., Griffith, C. A., Swain, M. R., et al. 2010, Faraday Discussions, 147, 369

Tinetti, G., Deroo, P., Swain, M. R., et al. 2010, ApJl, 712, L139

Twomey, S., Herman, B., & Rabinoff, R. 1977, JAS, 34, 1085

Waldmann, I. P., Tinetti, G., Drossart, P., et al. 2012, ApJ, 744, 35

Chapter 5

A Systematic Retrieval Analysis of Secondary Eclipse Spectra I: A Comparison of Different Atmospheric Retrieval Techniques

Submitted to the Astrophysical Journal as:
Line, M. R., Wolf, A. S., Zhang, X., Ellison, E., Deroo, P., Knutson, H., Crisp, D., Yung., Y. L., 2013, ApJ, submitted
Reproduced by permission of the AAS

5.1 Summary

Spectra of exoplanet atmospheres provide us the opportunity to improve our understanding of these objects just as remote sensing in our own solar system has increased our understanding of the solar system bodies. The challenge is to quantitatively determine the range of temperatures and abundances allowed by the data. This challenge is often difficult given the low information content of most exoplanet spectra which commonly leads to degeneracies in the interpretation. A variety of temperature and abundance retrieval approaches have been applied to exoplanet spectra, but no previous investigations have sought to compare these approaches. In this investigation we compare three different retrieval meth-

ods: optimal estimation, differential evolution Markov chain Monte Carlo, and bootstrap Monte Carlo. We call our suite of retrieval algorithms the **C**altec**H** **I**nverse **M**od**E**ling and **R**etrieval **A**lgorithms (CHIMERA). We discuss what we can expect in terms of uncertainties in abundances and temperatures given current observations as well as potential future observations and what conclusions can be drawn given those uncertainties. In general we find that the three approaches agree for high-quality spectra expected to come from potential future space-based missions, but disagree for low-quality spectra representative of current observations. We also show that the Gaussian posterior probability distribution assumption made in the optimal estimation approach is valid for high-quality spectral data. Furthermore we compare the results from a parameterized temperature profile versus a full classical level-by-level approach and discriminate in which situations each of these approaches is applicable. We also discuss the implications of our models for the inferred C-to-O ratios of exoplanetary atmospheres. More specifically we show that in the observational limit of a few photometric points, the retrieved C/O is biased towards values near solar and near one simply due to the assumption of uninformative priors.

5.2 Introduction

Thermal emission spectra ($\sim$ 1-30 microns) of extrasolar planets can tell us about their atmospheric temperatures and compositions (see, e.g., Tinetti et al. 2007; 2010; Grillmair et al. 2007; 2008; Swain et al. 2009a; 2009b; Madahusudhan & Seager 2009; Madhusudhan et al. 2011; Lee et al. 2012; Line et al. 2012). These observations, at the moment come in two types, broadband photometry mainly from the Spitzer Space Telescope (see e.g., Knut-

son et al. 2010) and ground-based instruments (Croll et al. 2010; Anderson et al. 2010; Gibson et al. 2010; Deming et al. 2012; Gillon et al. 2012), as well as higher resolution spectra such as Hubble Space Telescopes Wide Field Camera 3 (WFC3) (Berta et al. 2012; Swain et al. 2012; Deming et al. 2013) and Near Infrared Camera and Multi-Object Spectrometer (NICMOS) (Swain et al. 2009a; 2009b; Tinetti et al. 2010; Gibson et al. 2011; Crouzet et al. 2012). From these observations, signatures of a variety of molecules have been detected including H_2O, CH_4, CO and CO_2 (Tinetti et al. 2007; Swain et al. 2009a; 2009b; Tinetti et al. 2010), although the robustness of some of these detections has recently been called into question (Gibson et al. 2011). These same data have been used to infer the presence of atmospheric temperature inversions for a subset of hot Jupiters (e.g., Burrows et al. 2007, Knutson et al. 2008;2010; Forntey et al. 2008; Madhusudhan & Seager 2009; 2010).

While the above studies have given us insight into the nature of these planetary atmospheres, very few have focused on the uncertainties in temperatures and compositions. Until relatively recently (Madhusudhan & Seager 2009, Madhusudhan et al. 2011, Lee et al. 2012, and Line et al. 2012), most compositions and temperatures and thus the subsequent conclusions, were determined through self-consistent forward modeling approaches that only explore a few potential solutions without a well-defined characterization of the uncertainty distributions of the physical parameters (e.g., Burrows et al. 2005; Fortney et al. 2005; Burrows et al. 2007). Furthermore, some self-consistent solutions make physical assumptions that may not necessarily be valid in the exoplanetary atmospheres such as the assumption of thermochemical equilibrium gas concentrations or radiative-convective

temperature structures (that is they may ignore other potentially important processes such as vertical mixing, photochemistry, zonal winds, etc.). Additionally, this forward modeling approach is often unguided by the data and primarily driven by preconceived notions of how the atmosphere "should" look (as pointed out by Lee et al. 2012 and Benneke & Seager 2012) with the best solutions being the few that provide the lowest values of chi squared.

In order to more rigorously characterize the ranges of allowable temperatures and compositions, Madhusudhan & Seager (2009) developed a multidimensional grid search approach which can fully characterize the uncertainty distributions for each parameter. Subsequent studies (Madhusudhan et al. 2011; Benneke & Seager 2012) used the more sophisticated Markov chain Monte Carlo approach (MCMC) to accomplish this goal. However, such approaches require the computation of many millions of models in order to fully characterize the parameter uncertainties which may be unfeasible for more sophisticated forward models with many free parameters. In order to remedy this problem Lee et al. (2012) and Line et al. (2012) used the much faster optimal estimation (e.g., Rodgers 2000) approach to estimate the error distributions of each parameter. This approach is much faster due to the assumption that the parameter error distributions are Gaussian. However, this Gaussian assumption may result in an incorrect estimate of the error distributions (Benneke & Seager 2012).

The goals of this paper are to first understand the composition and temperature uncertainty distributions for different observational qualities, and second to understand how those derived uncertainty distributions differ between the two fundamental parameter esti-

mation approaches, optimal estimation and MCMC. This investigation represents the first direct comparison and synthesis of these retrieval approaches as applied to exoplanet atmospheres. A secondary goal is to understand how the derived composition uncertainties propagate into the C/O uncertainty. We accomplish these goals by comparing three different retrieval algorithms: optimal estimation (OE), a new MCMC algorithm known as differential evolution Markov chain Monte Carlo (DEMC), and the model-dependent bootstrap Monte Carlo approach (BMC). This investigation is analogous to the investigation carried out by Ford (2005) on radial velocity data. First we will describe the three different retrieval techniques as well as our forward model in §5.3. We call our three-pronged retrieval approach CHIMERA-**C**altec**H** **I**nverse **M**od**E**ling and **R**etrieval **A**lgorithms. Second, we compare the three spectral retrieval methods on different synthetic spectral data sets of varying observational quality in order to assess the robustness of the error estimations from each approach in §5.4. We will also compare the parameterized temperature profile approach (e.g., Madhusudhan & Seager 2009; Line et al. 2012) with the level-by-level profile approach (Lee et al. 2012). Finally, we will discuss the implications of these uncertainties for the estimated C-to-O ratios.

5.3 Methods

In this section we describe the retrieval techniques, the forward model, and the parameterizations we use to retrieve the temperatures and compositions from thermal emission spectra.

5.3.1 The Retrieval Techniques

We use three different retrieval techniques to infer the compositions and temperatures from a spectrum. The techniques are inherently Bayesian as they attempt to solve the inverse problem by summarizing the full shape of the posterior in terms of the location in parameter space of the maximum likelihood and the uncertainties about that location. The first, and the fastest (least number of forward model calls) of these approaches, is optimal estimation (OE), the second is the model-dependent bootstrap Monte Carlo (BMC), and the third is differential evolution Markov chain Monte Carlo (DEMC).

5.3.1.1 Optimal Estimation (OE)

The optimal estimation retrieval approach is well established in the fields of Earth atmosphere remote sensing (Rodgers 1976; Towmey 1996; Rodgers 2000; Livesay et al. 2006; Kuai et al. 2013), solar system atmosphere remote sensing (Conrath et al. 1998; Irwin et al. 2008; Nixon et al. 2007; Fletcher et al. 2007; Greathouse et al. 2011), and recently exoplanet atmosphere remote sensing (Lee et al. 2012; Line et al. 2012). The basic approach is to minimize a cost function to obtain the *maximum a posteriori* (MAP) solution. Using Bayes theorem and the assumption that the data likelihood, the prior, and the posterior are Gaussian , one can derive the following cost function (or log likelihood):

$$J(\mathbf{x}) = (\mathbf{y} - \mathbf{F}(\mathbf{x}))^T \mathbf{S_e^{-1}} (\mathbf{y} - \mathbf{F}(\mathbf{x})) + (\mathbf{x} - \mathbf{x_a})^T \mathbf{S_a^{-1}} (\mathbf{x} - \mathbf{x_a}) \tag{5.1}$$

where $\mathbf{y}$ is the set of n observations, $\mathbf{x}$ is the set of m parameters which we wish to retrieve or the state vector, $\mathbf{F}(\mathbf{x})$ is the forward model that maps the state vector onto the observations, $\mathbf{S_e}$ is the $n \times n$ data error covariance matrix (typically off diagonal terms are zero and the diagonal elements are the square of the 1σ error bars on the observations), $\mathbf{x_a}$ is the *a priori* state vector, and $\mathbf{S_a}$ is the $m \times m$ *a priori* covariance matrix. The first term in Equation 5.1 is simply "chi squared" and the second term represents the prior knowledge of the parameter distribution before we make the observations. For high-quality observations the second term is generally not important as most of the information in constraining the state vector comes from the observations. For low-quality observations it is just the opposite. Following Irwin et al. 2008 we minimize Equation 5.1 with Newton's iteration method given by

$$\mathbf{x_{i+1}} = \mathbf{x_a} + \mathbf{S_a^{-1}K_i^T}(\mathbf{K_i S_a^{-1} K_i^T} + \mathbf{S_e^{-1}}) \\ (\mathbf{F}(\mathbf{x}) - \mathbf{y} - \mathbf{K_i}(\mathbf{x_a} - \mathbf{x_i})) \tag{5.2}$$

where i is the iteration index and $\mathbf{K_i}$ is the Jacobian Matrix at i ($K_{nm} = \frac{\partial F_n}{\partial x_m}$). Rather than taking the full Newton step we damp the solution with

$$\mathbf{x_{i+1}^{'}} = \mathbf{x_i} + \frac{\mathbf{x_{i+1}} - \mathbf{x_i}}{\mathbf{1} + \lambda} \tag{5.3}$$

At each iteration we evaluate $\mathbf{J}(\mathbf{x_{i+1}})$ and $\mathbf{J}(\mathbf{x_{i+1}^{'}})$. If the latter is smaller, we set the state vector for the next iteration to $\mathbf{x_{i+1}^{'}}$ and decrease λ by 0.3. Otherwise we keep increasing λ by a factor of 10 and re-evaluate Equation 5.3 and Equation 5.1 until $\mathbf{J}(\mathbf{x_{i+1}^{'}})$ becomes

less than $\mathbf{J}(\mathbf{x_{i+1}})$. Convergence is achieved when $\mathbf{J}$ changes by less than 1×10^{-6} from the previous iteration, which typically occurs after $\sim$10s of iterations. The resulting state vector is the MAP solution. The uncertainties on the state vector parameters are given by the posterior covariance matrix

$$\hat{\mathbf{S}} = (\mathbf{K^T S_e^{-1} K} + \mathbf{S_a^{-1}})^{-1} \tag{5.4}$$

This matrix represents a multi-dimensional *normal* distribution (see Rodgers 2000 for the derivation). The diagonal elements are the square of the marginalized errors whereas the off diagonal terms describe the correlations/degeneracies amongst the parameters. The first term ,$\mathbf{K^T S_e^{-1} K}$, represents the uncertainties due to the measurement errors. This term uses the local gradient information to estimate the parameter uncertainties. The second term represents the prior uncertainties before making the measurements, which has less influence for higher quality data. Again, the major assumption in equations 5.1 and 5.4 is that the posterior for each parameter is Gaussian. This assumption is only valid when the region in phase space over which the forward model can be linearized is broader than the parameter uncertainties. However, it is this assumption that allows this approach to be extremely fast requiring only tens of forward model calls. As we shall see in §5.4, this assumption is valid for data that is of "good" quality, but breaks down for "poor" quality data.

5.3.1.2 Model Dependent Bootstrap Monte Carlo (BMC)

A common way to more robustly characterize errors is through a Monte Carlo resampling of the data (see e.g., Press et al. 2002 Chapter 15.6, Ford 2005 §4.2) in which many thousands of realizations of the original data (in our case, the spectra) are created using the uncertainties from the original dataset. These synthetic data are then refit using, say, OE, and the resulting best-fit parameter distributions represent the uncertainties. There are multiple ways of generating the synthetic data realizations. The most common way is the residual resampling approach in which data realizations are created by adding the randomly shuffled residual between the best-fit model and the data back to the original best-fit model. This new realization is then fit and the process is repeated many times. The approach we take is similar, but rather than generate a new spectrum using the residual, we simply take the best-fit, from OE, and then resample each point by drawing it from a normal distribution with a mean given by the best-fit value and the width given by the data error bar for that point. We chose this approach over the residual resampling approach because sparse coverage spectra, like those from broadband observations, have virtually no residual as they can be fit perfectly due to the greater number of parameters than data points. We typically generate $\sim$1000 spectra realizations that are then refit by optimal estimation to obtain the state vector parameter distributions.

5.3.1.3 differential evolution Markov chain Monte Carlo (DEMC)

The MCMC approach has revolutionized parameter estimation and error analysis in many fields. It is routinely used in radial velocity (Ford 2005) and transit light curve (e.g., East-

man, Gaudi, & Agol 2013) error analysis. Results from a well converged MCMC analysis can generally be considered as the best possible representation of the parameter uncertainties. Recently, this approach has been applied to the exoplanet atmosphere retrieval problem (Madhusudhan et al. 2011; Benneke & Seager 2012). Unlike optimal estimation, MCMC approaches make no assumptions about the shape of the posterior, but rather evaluate the posterior with millions of samples.

The basic approach of MCMC is to sample the posterior through a random walk process. The random walk is carried out by drawing states from some proposal distribution and evaluating whether or not the proposed state has an increased likelihood over the previous. Typically the proposal distribution is a normal distribution with a mean given by the current state in the chain ($\mathbf{x_i}$) and a user defined width to achieve a particular acceptance rate (Gibbs sampling or Metropolis-Hastings). If the proposed state ($\mathbf{x_p}$) has an improved likelihood over the current state, then that state is kept ($\mathbf{x_{i+1} = x_p}$) and a new proposal is made from that location. If the proposal state has not improved the likelihood that state is either rejected or accepted with some probability. This previous state dependent random walk constitutes a Markov Chain. Given enough samples this Markov Chain will converge to the target posterior (see Ford 2005 for a more detailed explanation).

Rather than standard MCMC approaches, we use an adaptive algorithm known as differential evolution Markov chain Monte Carlo (DEMC) (Ter Braak 2006; Ter Braak & Vrugt 2008). The purpose of this approach is to obtain more appropriate proposal states by identifying the proper scale and orientation of the current estimate of the posterior. This scale and orientation information comes from the chain history. This approach gives a more

efficient probing method for highly correlated parameter spaces and yields improved convergence rates. Our DEMC procedure is as follows:

1. Apply the OE technique to the measurements to obtain the best-fit state vector and posterior covariance matrix, $\hat{\mathbf{S}}$. This step provides an initial estimate of the posterior.

2. Initialize N_{init} links ($\mathbf{x_{i=0-N_{init}}}$) in each of N_{chains} (typically 3 chains, more chains will slow convergence) independent chains (arrays) by randomly drawing state vectors from the multivariate normal described by the posterior covariance matrix from step 1. Set the last link in one of the chains to the best-fit state vector obtained in step 1. This step provides a good starting history from which our initial proposal states can be drawn. Combine each of the independent chains into one long chain that composes the history, $\mathbf{X_{history}}$.

3. Evaluate the cost function, $\mathbf{J}$, in Equation 5.1 for the last link in each of the chains. If using a flat prior ignore the second term. This, again, is simply the equivalent of evaluating chi squared.

4. Draw two random numbers, R_1 and R_2, between zero and $N_{chains} \times i$, where i is the current state in the chain. Initially, $i = N_{init}$. Evaluate the proposed jump state given by

$$\mathbf{x_p} = \mathbf{x_i} + \gamma(\mathbf{x_{R1}} - \mathbf{x_{R2}}) + \mathbf{e} \tag{5.5}$$

where $\mathbf{x_{R_1}}$ and $\mathbf{x_{R_2}}$ are the states from different points in the chain history, $\mathbf{X_{history}}$. γ

is a scale factor typically set to $2.38/\sqrt{(2 * m)}$ (ter Braak 2006), where m is the number of parameters. This factor is meant to give acceptance rates of $\sim$0.23 for large m. $\mathbf{e}$ is a vector drawn from a multivariate normal distribution with a small variance relative to the chain variance in order to introduce a small amount of additional randomness. Repeat this process for the other $N_{chains} - 1$ chains.

5. Evaluate the Metropolis (Metropolis et al. 1953) ratio, $r = P(\mathbf{x_p})/P(\mathbf{x_i}) = e^{-\frac{1}{2}(\mathbf{J}(\mathbf{x_p})-\mathbf{J}(\mathbf{x_i}))}$. If r is larger than 1, set $\mathbf{x_{i+1}} = \mathbf{x_p}$ and if it is smaller only accept if it is larger than a random number between 1 and 0. Otherwise do not update the chain, set $\mathbf{x_{i+1}} = \mathbf{x_i}$. Repeat for the other $N_{chains} - 1$ chains. Add the updated links in all N_{chains} to $\mathbf{X_{history}}$.

6. Repeat steps 4 and 5 until convergence is met. Convergence can be determined by looking at the trace plots of $\mathbf{X_{history}}$ for each parameter or by using the Gelman-Rubin statistic on the set of N_{chains} chains. For this we use the algorithm from Eastman, Gaudi, & Agol 2013 which requires the Gelman-Rubin statistic to be less than 1.01 and the number if independent draws to be greater than 1000 for each parameter . Convergence typically occurs in less than 10^5 links in each of the N_{chains} for a total of $N_{chains} \times 10^5$ links. This is about an order of magnitude less than parallel tempering or pure Metropolis-Hastings.

5.3.2 The Forward Model

The forward model, $\mathbf{F}(\mathbf{x})$, is the most important part of any retrieval algorithm. It is what maps the state vector of retrievable parameters onto the observable. In the case of atmospheric retrieval, the forward model takes temperatures and compositions and generates a model spectrum. Our particular forward model numerically solves the planet-parallel thermal infrared radiation problem for an absorbing, emitting atmosphere (we neglect scattering). We first divide the atmosphere up into N_{lev} discretized atmospheric layers. The absorption optical depth for the k^{th} gas in the z^{th} layer at wavelength λ is

$$\Delta\tau_{k,z,\lambda} = f_{k,z}\sigma_{k,z,\lambda}\frac{\Delta P_z}{\mu_{atm}g} \tag{5.6}$$

where $f_{k,z}$ is the volume mixing ratio of the k^{th} gas at the z^{th} layer , $\sigma_{k,z,\lambda}$ is the absorption cross section per molecule of the k^{th} gas in z^{th} layer at wavelength λ, ΔP_z is pressure thickness of the z^{th} slab, μ_{atm} is the mean molecular weight of the atmosphere and g is the gravity. The absorption cross sections are pre-computed on a 1 cm^{-1} wavenumber grid at 20 evenly spaced temperature and log-pressure points from 500–3000K and 50–10^{-6} bars respectively (similar to Sharp & Burrows 2007). The cross sections for each wavelength on the pre-computed grid are interpolated to the atmospheric temperatures and pressures in the z^{th} slab. To compute the total slab optical depth we sum the contribution from each gas to obtain

$$\Delta\tau_{z,\lambda} = \sum_{k=1}^{N_{gas}} \Delta\tau_{k,z,\lambda} \tag{5.7}$$

Upon computing the optical depths at each level, we can now solve for the upwelling irradiance with

$$I_\lambda = \sum_{z=0}^{N_{lev}} B_\lambda(T_z) e^{-\sum_{j=z}^{N_{lev}} \Delta\tau_{j,\lambda}} \Delta\tau_{z,\lambda} \tag{5.8}$$

where N_{lev} is the number of atmospheric levels and $B_\lambda(T_z)$ is the Planck function at wavelength λ and temperature at the z^{th} slab. We use 90 atmospheric layers to compute the upwelling flux.

An important part of the forward model when using the optimal estimation approach is the computation of the Jacobian, or the sensitivity to the upwelling irradiance with respect to the desired retrievable parameters. When possible, it is preferable that the Jacobian be calculated analytically for both improvements in speed and in accuracy. We are interested in the retrieval of both abundances and temperatures so we must compute Jacobian with respect to both the abundances and temperatures. We make the assumption of vertically uniform gas mixing ratios and hence, $f_{k,z}$ is independent of z. We now differentiate Equation 5.8 with respect to the uniform gas mixing ratios for each gas f_k to obtain

$$\begin{aligned} \frac{\partial I_\lambda}{\partial f_k} &= \sum_{z=0}^{N_{lev}} B_\lambda(T_z) e^{-\sum_{j=z}^{N_{lev}} \Delta\tau_{j,\lambda}} \frac{\Delta\tau_{k,z,\lambda}}{f_k} \\ &- \sum_{z=0}^{N_{lev}} (B_\lambda(T_z) e^{-\sum_{j=z}^{N_{lev}} \Delta\tau_{j,\lambda}} \Delta\tau_{z,\lambda} \sum_{j=z}^{N_{lev}} \frac{\Delta\tau_{k,j,\lambda}}{f_k}) \end{aligned} \tag{5.9}$$

The first term is due to the changing emissivity of the emitting slab and the second term is how the change in transmittance affects the upwelling irradiance.

The sensitivity of the irradiance to a change in temperature in the z^{th} slab is given by

$$\frac{\partial I_\lambda}{\partial T_z} = (e^{-\sum_{j=z+1}^{N_{lev}} \Delta\tau_{j,\lambda}} - e^{-\sum_{j=z}^{N_{lev}} \Delta\tau_{j,\lambda}}) \frac{\partial B_\lambda(T_z)}{\partial T_z} \tag{5.10}$$

This equation is similar to equation 14 in Irwin et al. 2008 but we have neglected the first and last terms in their formula as they are small.

Since the observations are reported as the ratio of the planet flux to the stellar flux and not the irradiance, we perform a disk integration of equations 5.8-5.10 using four point Gaussian quadrature and then divide by an interpolated PHOENIX stellar flux grid model (Allard et al. 2000) .

We include only CH_4 , CO_2, CO, H_2O, H_2, and He in our model. H_2, and He are fixed in our models at thermochemically justifiable abundances. The exact abundances of these species is not critical as the sensitivity of the spectrum to H_2, and He is minimal. We retrieve only CH_4 , CO_2, CO, and H_2O. We choose these species because they are the most spectroscopically active and abundant species. Admittedly we could/should include every possible atmospheric constituent but this would be unwieldy and reliable high temperature absorption line lists only exist for a few. On that note, we use the HITEMP database (Rothman et al. 2010) to compute the tabulated cross sections for CO_2, CO, and H_2O and the STDS database for CH_4 (Wenger & Champion 1998). Below 1.7 μm for CH_4 we simply use the HITRAN (Rothman et al. 2009) database for lack of anything better (to the best of our knowledge). We use the Barysow et al. (2001;2002) and Jørgensen et al. (2000) databases for the computation of the H_2-H_2/He collision-induced opacities. The Reference Forward Model (RFM-http://www.atm.ox.ac.uk/RFM/) was used to compute the

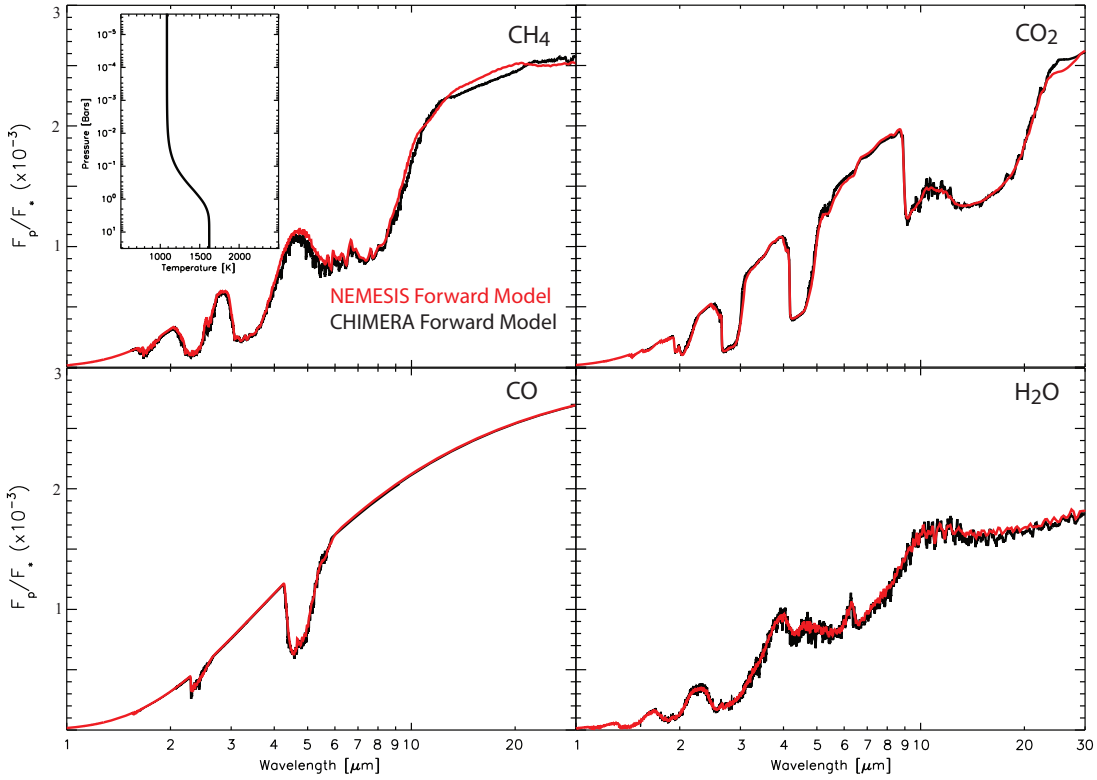

Figure 5.1: Comparison of the thermal emission spectrum from our forward model (black) with the NEMESIS forward model (red). The temperature-pressure profile is shown in the inset. For this comparison we assume uniform mixing ratios of 10^{-4} for CH_4 , CO_2, CO, and H_2O. H_2 is set to 0.85 and He is set to 0.15. This planet is assumed to be hydrogen-dominated (mean molecular weight of 2.3 amu) with a radius of $1R_J$, a gravity of 22 ms^{-1} orbiting a 5700 K pure blackbody star with a radius of $1R_{sun}$.

tabulated cross sections from the line strength databases. We have validated our forward model through a detailed comparison with the Oxford NEMESIS group (e.g., Lee et al. 2012) and our results agree to better than 5% (see Figure 5.1) (see online supplementary material).

An additional component of the forward model is the instrumental function used to convolve with the high-resolution model spectrum. For the broadband points we simply integrate the flux from the high-resolution model spectrum with the appropriate filter function for that point. When fitting higher resolution observations, the instrumental function is

assumed to be a Gaussian (valid for grating spectrometers) in wavelength with a Full Width at Half Max (FWHM) determined by observations.

Now that we have a well-defined forward model we can define our state vector. Again, we wish to retrieve the abundances of CH_4 , CO_2, CO, and H_2O and the temperature profile. More specifically, we choose to retrieve the log of the abundances as they can vary by orders of magnitude and to prevent negative mixing ratios. Our state vector is given by

$$\mathbf{x} = [log(f_{H_2O}), log(f_{CH_4}), log(f_{CO}), log(f_{CO_2}), T]^T. \tag{5.11}$$

where the f_k's are all assumed constant with altitude. We feel this is appropriate for two reasons. First, vertical mixing will smooth out the mixing ratio profiles over the thermal infrared photosphere (Line et al. 2010, Moses et al. 2011, Line et al. 2011), and secondly current observations simply do not have the information content to warrant the retrieval of vertical mixing ratio information (see Lee et al. 2012). In the next section we describe how to go about retrieving the temperature profile.

5.3.2.1 Parameterized vs. Level-By-Level (LBL) Temperature Profile

We employ two approaches to retrieve the temperature profiles. The first, and the most commonly used in Earth and solar system atmosphere retrieval problems, is the level-by-level approach. This is the approach used in Lee et al. 2012. The second is a parameterized temperature profile approach similar to the approach used in Madhusudhan & Seager 2009 and Line et al. 2012. Each has its advantages and disadvantages described below.

The level-by-level temperature retrieval approach seeks an estimate of the tempera-

ture at each of the N_{lev} model layers. This approach is advantageous in that there are no pre-conceived assumptions made about how the atmospheric temperature should be parameterized. If the spectral signal-to-noise and resolution are high enough, there is generally enough sensitivity to obtain information about the temperature at individual atmospheric layer. However, there is a finite vertical resolution given the quality of the observations. Typically this resolution is set by the width of the thermal emission weighting functions and how much they overlap. Generally, when the spectra are noisy the level-by-level approach fits the noise which results in unphysical structure in the retrieved temperature profile. This is analogous to fitting a high-degree polynomial to only a few points. There are ways to smooth unphysical structure, one of them to assume a correlation among the atmospheric layers (Rodgers 2000, Irwin 2008) implemented through the prior covariance matrix, $\mathbf{S_a}$, with

$$S_{a,ij} = (S_{a,ii} S_{a,jj})^{1/2} e^{\frac{-|ln(P_i/P_j)|}{h}}. \tag{5.12}$$

Here P_i and P_j are the pressures at the i^{th} and j^{th} levels, respectively, and h is the correlation length that controls the level of smoothing. It can be thought of as the number of scale heights over which the temperatures are correlated. For our simulations we choose $h = 7$ as this provides a sufficient level of detail without producing unphysical oscillations. When using this approach our state vector is exactly as it is in Equation 5.11 with T being an N_{lev} vector of temperatures at each level. The level-by-level approach is only appropriate when the information content of the spectra is sufficiently high such that the addition of the N_{lev} additional parameters is justified. For most current exoplanet spectra, this is an invalid approach.

The second temperature profile retrieval approach makes use of a parameterization. This approach is advantageous when the information content of a spectrum is low as the number of free variables is greatly reduce. However, they do force the retrieved atmospheric temperature structure to conform only to the profile shapes and physical approximations allowed by that parameterization. For our particular parameterization, we assume the atmosphere to be in radiative equilibrium based upon the analytic radiative equilibrium temperature profile of Guillot 2010 (and others such as Hansen 2008, Robinson & Catling 2012). This is the same parameterization used in Line et al. 2012. This profile assumes two independent downwelling visible channels of radiation and one upwelling stream of thermal emission. Briefly, the temperature as a function of the thermal optical depth,τ, is given by

$$T^4(\tau) = \frac{3T_{int}^4}{4}(\frac{2}{3} + \tau) + \frac{3T_{irr}^4}{4}(1-\alpha)\xi_{\gamma_1}(\tau) + \frac{3T_{irr}^4}{4}\alpha\xi_{\gamma_2}(\tau) \tag{5.13}$$

with

$$\xi_{\gamma_i} = \frac{2}{3} + \frac{2}{3\gamma_i}[1 + (\frac{\gamma_i\tau}{2} - 1)e^{-\gamma_i\tau}] + \frac{2\gamma_i}{3}(1 - \frac{\tau^2}{2})\mathrm{E}_2(\gamma_i\tau) \tag{5.14}$$

where γ_1 and γ_2 are the ratios of the Planck mean opacities in the visible streams to the thermal stream and the parameter α (range 0 to 1) partitions the flux between the two visible streams. $E_2(\gamma\tau)$ is the second order exponential integral function. The internal heat flux is parameterized by the temperature ,T_{int}, which is fixed as this term has little impact. The stellar input at the top of the atmosphere is represented by T_{irr} given by

$$T_{irr} = \beta(\frac{R_*}{2a})^{1/2}T_* \tag{5.15}$$

where R_* and T_* are the stellar radius and temperature, a is the semi-major axis, and β is a catch all term on the order of unity for the albedo, emissivity, and day-night redistribution. The grey infrared optical depth can be mapped onto pressure coordinates using

$$\tau = \frac{\kappa_{IR} P}{g} \tag{5.16}$$

where P is the pressure, g the surface gravity (at 1 bar), and κ_{IR} the Planck mean thermal infrared opacity. This $\tau - P$ mapping assumes a linear relation between the optical depth and pressure, or a pressure independent infrared opacity. More complicated mappings that account for the pressure dependence of κ_{IR} can also be used (see, e.g., Robinson & Catling 2012).

This temperature parameterization has 5 free parameters governing its structure: κ_{IR}, γ_{v_1}, γ_{v_2}, β, and α. Our parameterized state vector again, is given by Equation 5.11 but with T replaced with [κ_{IR}, γ_{v_1}, γ_{v_2}, β, α]. Combined with the gases this gives a total of 9 free parameters. The temperature *profiles* are then reconstructed from the probability distributions of those 5 parameters.

We should note that currently most exoplanet spectra often have fewer measurements than desired state variables. This means that each parameter cannot be uniquely determined. This is not a new problem (e.g., Madhusudhan & Seager 2009). This is why the prior is crucial. We can think of the prior as an "artificial" set of data from which the retrieval (all retrieval approaches) can rely on when the measurements are insufficient enough to constrain a given parameter. Therefore the resulting constraints on a given parameter are a combination of the information obtained from the spectra and the prior knowledge. In the

extreme case of no observational constraint, the posterior will simply be the prior. Hence, it is critical to choose an appropriate prior, especially for cases when there are more parameters than measurements.

With the optimal estimation formalism, we can assesss the degree to which the constraint comes from the measured spectra versus the prior through what is called the averaging kernel. The averaging kernel is an $m \times m$ matrix with elements given by

$$A_{ij} = \frac{\partial x_{i,retrieved}}{\partial x_{j,true}}. \tag{5.17}$$

where $x_{i,retrieved}$ is the retrieved value of the i^{th} parameter and $x_{j,true}$ is the true value of the j^{th} parameter. The diagonal elements tell us how much a retrieved parameter will respond to an actual change in that parameter in the atmosphere. For a given change in the true atmospheric state of some parameter i, if the measurements are perfect, we would expect to retrieve exactly that same change and hence, the value of A_{ii} would be one. If the measurements in no way contributes to our knowledge of parameter i, that is all of our knowledge of its value is from the prior, then A_{ii} will be zero. We can use this diagnostic to assesss how heavily our error estimations are informed by the measurements. This is most important when using the level-by-level temperature profile retrieval. The sum of the diagonal elements of this matrix determines the total number of independent pieces of information that can be retrieved from the measurements. This can never be larger than the total number of individual data points.

5.4 Test on Synthetic Measurements

In this section, we apply the CHIMERA to a set of synthetic measurements in order to assesss the robustness of each retrieval algorithm.

5.4.1 Synthetic Observations

We create a generic hydrogen-dominated hot Jupiter planet and derive its emission spectrum in three different observing scenarios. Table 5.1 summarizes the basic planet parameters used to generate the model atmosphere and contrast spectrum. For simplicity we assume that the trace species have mixing ratios that are constant with altitude. Equations 5.13-5.16 are used to generate the atmospheric temperature profile of the planet from the values in Table 5.1 . Figure 5.2 shows the model atmosphere and spectrum of the synthetic planet. The raw flux is divided by a PHOENIX stellar grid model that closely matches the chosen stellar properties. The thermal emission contribution functions suggest that most of the emission originates between a few bars and a few mbars. Our synthetic measurments only provide believable estimates for the temperatures and abundances over this region of the atmosphere. The thermal contribution functions indicate that the emission from shorter wavelengths comes from deeper layers in the atmosphere and regions of high opacity tend to push the emission to higher altitudes. In this example, water is the dominant opacity source and acts almost like a continuum absorber across the spectrum. If we had no absorbing molecular species other than H_2/He most emission would originate from the $\sim$10 bar level.

We now create simulated observations for our synthetic planet under three different

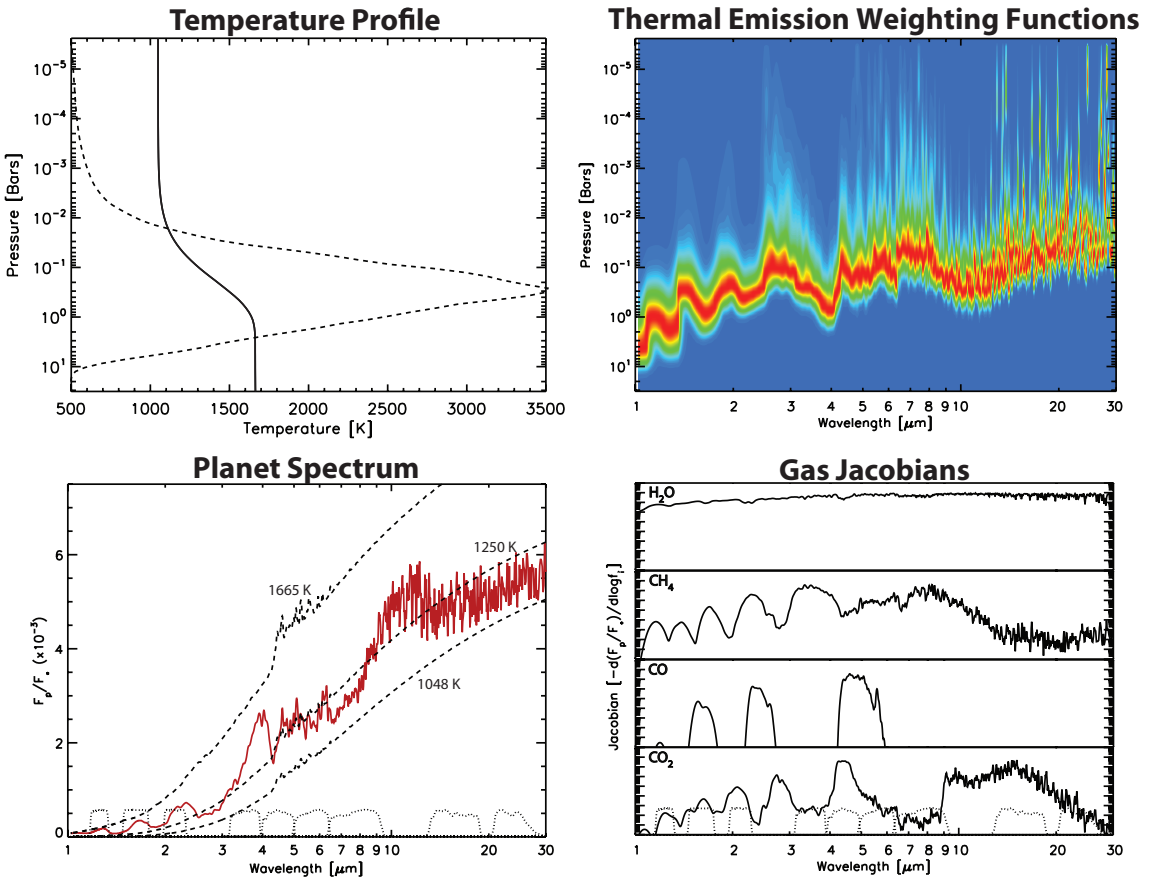

Figure 5.2: Synthetic planet atmosphere and spectrum. Top Left: Model temperature-pressure profile. The solid curve is the temperature profile and the dashed curve is the averaged thermal emission contribution function, or where the emission in the atmosphere is coming from. The temperature profile is constructed using equations 5.13-5.16 and the parameters in Table 5.1. Top Right: Thermal emission contribution function. This plot shows where the emission is coming from as a function of wavelength, smoothed to a resolution of 0.05 microns. Red corresponds to the peak of the thermal emission weighting functions, where the optical depth is unity, and blue represents zero emission. Most emission emanates between a few bars and 0.01 bars with deeper layers probed by shorter wavelengths. Bottom Left: Resulting spectrum smoothed to a resolution of 0.05 microns. Blackbodies for the hottest, coolest, and average temperatures are shown. The dotted curves at the bottom are the filter profiles for typical photometric observations. Bottom Right: Gas Jacobian generate from Equation 5.9. This plot shows the sensitivity of the flux contrast as a function of wavelength to the various absorbers (the units are arbitrary but consistent).

Table 5.1: Parameters used to generate the fictitious model atmosphere and spectrum. R_p is the planet radius in units of Jupiter radii, R_{star} is the stellar radius in units of solar radii, T_{star} is the stellar effective temperature, a is the semi-major axis, T_{int} is the internal heat flux temperature of the planet, g is the planetary surface gravity. γ_{v1}, γ_{v2}, κ_{IR}, α, and β are the parameters that control the shape of the radiative equilibrium temperature profile. The f_i's are the constant-with-altitude volume mixing ratios for each species in parts per million (ppm).

Parameter	Value
$R_p(R_J)$	1.138
$R_{star}(R_{sun})$	0.756
$T_{star}(K)$	5040
$a(AU)$	0.031
$T_{int}(K)$	100
$log(g)$ (cm s^{-2})	3.341
γ_{v1}	1.58×10^{-1}
γ_{v2}	1.58×10^{-1}
κ_{IR} (cm^2 g^{-1})	3×10^{-2}
α	0.5
β	1.0
f_{H2} (ppm)	8.5×10^5
f_{He} (ppm)	1.5×10^5
f_{H2O} (ppm)	370
f_{CH4} (ppm)	1
f_{CO} (ppm)	31.6
f_{CO2} (ppm)	0.2

regimes. The first regime is a set of broadband observations through four of the Spitzer Infrared Array Camera (IRAC) channels at 3.6, 4.5, 5.7, and 8 μm (Top Left, Figure 5.3). This represents the spectral quality that are most commonly available for hot-Jupiters today. To create the synthetic observations, the spectrum in Figure 5.1 is first integrated over the IRAC filter functions at each channel and then random noise is added to each channel controlled by the error bars size. The size of the error bars are representative of typical errors on IRAC observations (e.g., Machalek et al. 2009).

The second observational scenario is a multi-instrument case combining both Spitzer photometry, ground-based photometry, and Hubble Wide Field Camera 3 spectra (WFC3)

(Top Right Figure 5.3). This combined set of observations from various instruments is more representative of the current level of observations that can be made today, and likely for the next half-decade, for many planets (e.g., WASP12b, WASP4b, HD209458b). Again, we use the same four Spitzer IRAC channels and error bars as before but also include ground-based H and K_s band photometry points. The error bars are taken from Crossfield et al. (2012). To create the synthetic WFC3 measurements (1.15-1.63 μm), the high-resolution spectrum is convolved with a Gaussian instrumental profile with a FWHM of 0.0325 μm with error bars taken from Swain et al. (2012). Random noise is again, added to each point.

The third observational scenario illustrates the performance of a potential modest (by modest we mean reasonable cost) future space-based, FINESSE-like, telescope might produce (bottom, Figure 5.3). These simulated observations are created by convolving the high-resolution spectrum with a moderate resolution Gaussian instrumental profile with a FWHM of 0.0075 μm (R$\sim$300 at 2 μm). The measurement error bars, and hence random noise, are only suggestive and are based on a FINESSE-like noise model (Swain 2012). This spectral resolution is comparable to that of Exoplanet Characterization Observatory (EchO) below 5μ, but less than the James Webb Space Telescope (JWST) Near Infrared Spectrometer.

Aside from the potential development of a ground-based near-IR spectroscopy program, most observations for the foreseeable future are likely to fall somewhere between the first and second cases. We are also being optimistic in our "worst" case observational scenario by including 4 broadband points instead of the now typical two IRAC channels. In the latter case it is impossible to provide any unique constraints on the atmosphere without imposing

many pre-conceived assumptions and priors.

5.4.2 The Prior

As mentioned in §5.3.1.1, the prior is important when the spectral information content is limited. We use a prior on both the gases and the temperature profile. For the purposes of this synthetic study, we assume Gaussian priors on the parameters that control the temperature profile and on the gas abundances. We could have chosen flat (un-informed) priors, however, the formalism of optimal estimation requires that the prior be Gaussian, and hence we maintain this prior for all of the retrieval approaches. We choose extremely broad Gaussian priors as to mitigate the influence they have on the retrievals. For the temperature profile prior, we choose parameters that would reasonably match an atmosphere that is in radiative equilibrium over a wide range of conditions (e.g., variations in κ_{IR}, γ_{v_1}, γ_{v_2}, β, and α). Table 5.2 shows the prior parameters we use in terms of the prior mean, $\mathbf{x_a}$ and the prior covariance matrix, $\mathbf{S_a}$.

In addition to the Gaussian priors, we impose a lower limit on mixing ratios with a value 1×10^{-12} and an upper limit requiring the sum of the mixing ratios of the four retrieved gases to be less than 0.15. These limits attempt to bound what can be reasonably expected for the compositions of a hydrogen-dominated atmosphere. Also, it would be impossible to detect a gas with an abundance less than 1 ppt in these simulations. We also impose a limit on the parameters that govern the temperature structure. We do not allow κ_{IR} to go above or below 10 and 1×10^{-4}, respectively. The lower limit is roughly the order-of-magnitude value of the Planck mean opacity expected for an all hydrogen atmosphere. The upper

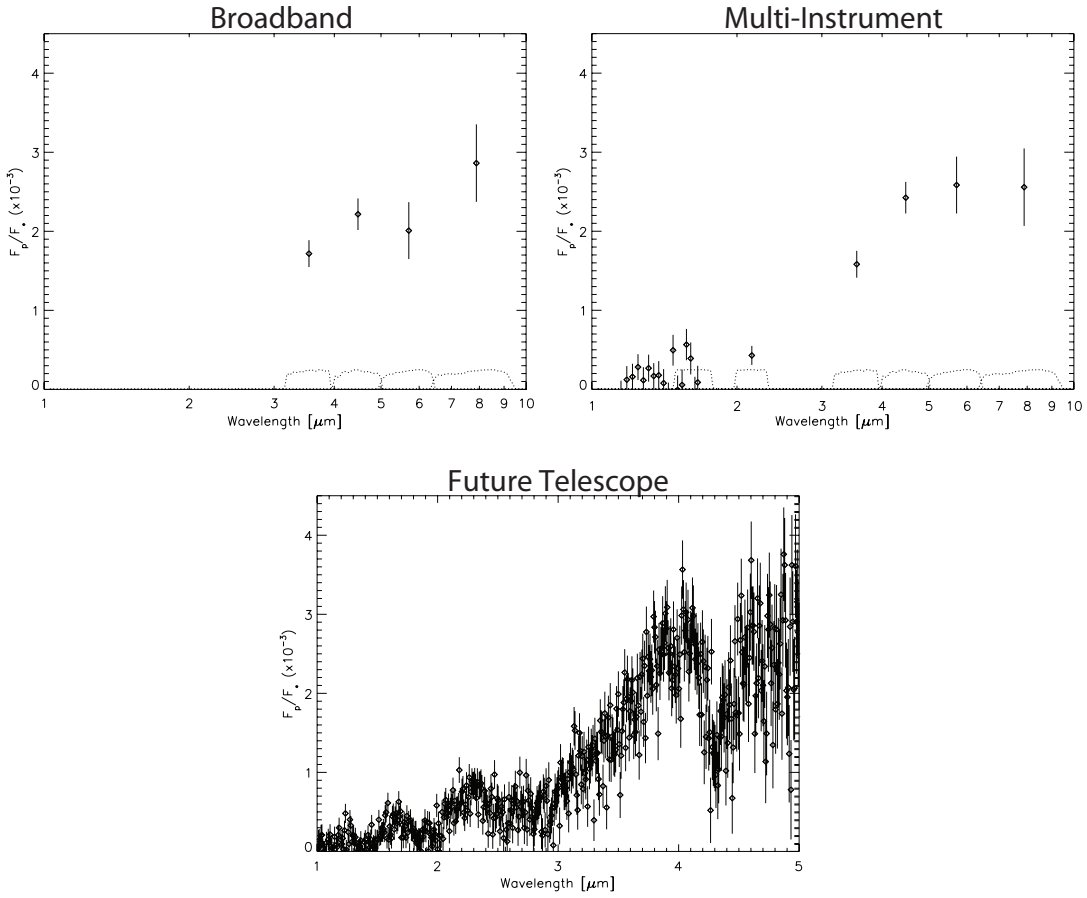

Figure 5.3: The spectrum of the synthetic hot Jupiter observed in three different scenarios. These "observations" are created by convolving the high-resolution spectrum in Figure 5.1 with the appropriate instrumental profiles. Random noise is then added to each data point. Top Left: Synthetic observations as viewed through the Spitzer broadband 3.6, 4.5, 5.7, and 8 μm channels. Top Right: Multi-instrument observations that include WFC3 (1.15-1.63 μm), ground-based H and K_s, and Spitzer broadband (3.6, 4.5, 5.7, and 8 μm). Bottom: Hypothetical future space-based observations. The dotted curves on the bottom of each plot are the photometric transmission functions.

limit is a bit extreme but would be representative of an extremely opaque atmosphere. The upper and lower bounds on γ_1 and γ_2 are between 10 and 1×10^{-4} and are chosen to allow for a reasonable span of temperature profiles ranging from ones with inversions to ones nearly transparent to solar radiation. α can only have physically meaningful values between 0 and 1. β cannot have values below 0, and we impose an artificial upper limit of 2. Generally these upper and lower limits rarely matter as most of the posteriors lie well within their ranges. Figure 5.4 shows the resulting temperature distribution and gas priors (inset). The prior temperature profile distributions are reconstructed by propagating the Gaussian prior probability distributions (including the above limits) of κ_{IR}, γ_{v_1}, γ_{v_2}, β, and α in Table 5.2 through equations 5.13-5.16. Upon reconstructing the temperature profiles there are thousands of temperatures for each pressure level. With these profiles a histogram of temperatures at each level can be constructed. Rather than show the "spaghetti diagram" with thousands of individual profiles, we show the 1σ (68%) and 2 σ (95 %) confidence intervals at each pressure level. These confidence intervals are what is shown in Figure 5.4.

Table 5.2: Gaussian prior parameter values and widths. The true state is the same as in Table 5.1 but in logarithmic units for some of the parameters. The mixing ratios of each gas, f_k, are in ppm. The infrared opacity, κ_{IR}, has units of $cm^2 g^{-1}$. γ_{v1}, γ_{v2}, α, and β are all unit-less. Note that we retrieve the log of all values except α and β.

Parameter	True	Prior State ($x_{a,i}$)	Prior Width ($\sqrt{(S_{a,ii})}$)
$log(\gamma_{v1})$	-0.8	-0.9	1
$log(\gamma_{v2})$	-0.8	-0.7	1
$log(\kappa_{IR})$	-1.52	-2.0	0.5
α	0.5	0.5	0.05
β	1	1	0.25
$log(f_{H2O})$	2.568	2	6
$log(f_{CH4})$	0.0	1	6
$log(f_{CO})$	2.663	2	6
$log(f_{CO2})$	-0.70	1	6

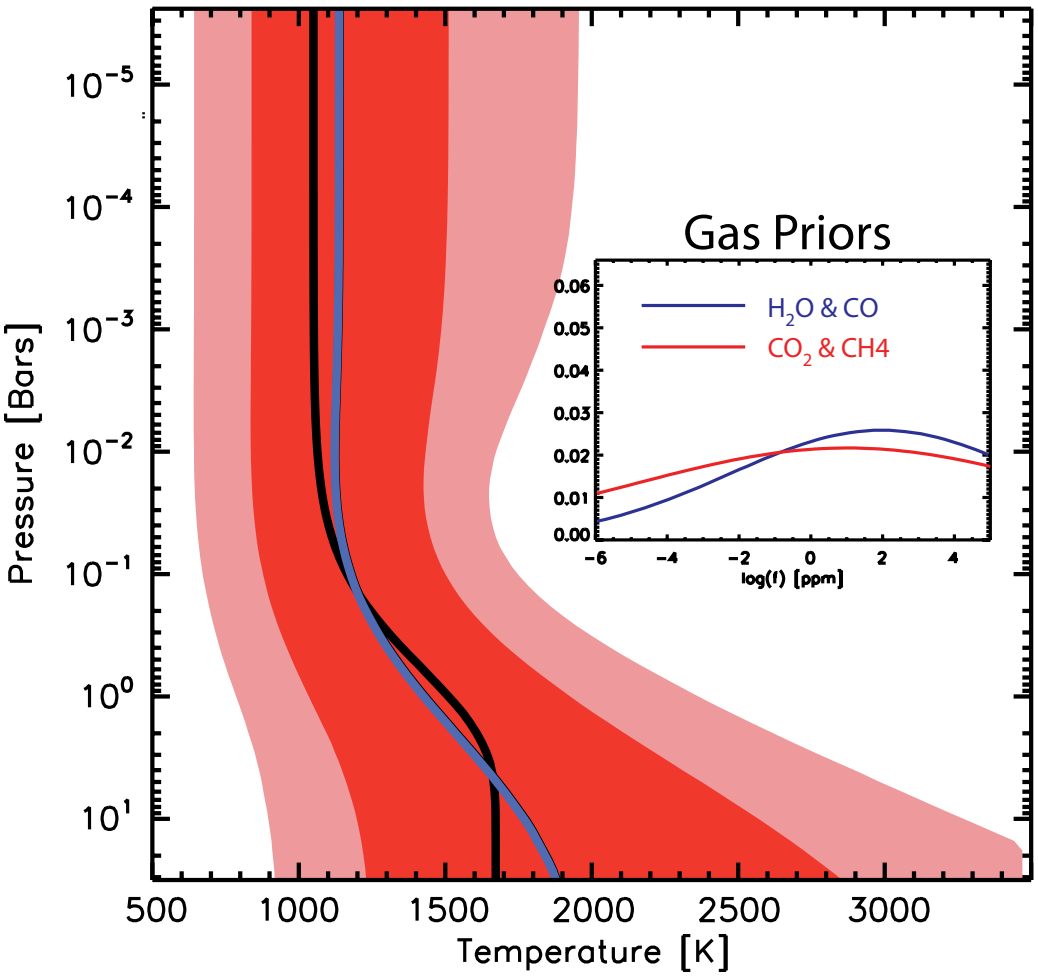

Figure 5.4: Temperature and gas priors (inset). Dark red represents the 1σ spread in the allowed temperature profiles as a result of the prior parameter distributions in Table 5.2. Light red is the 2σ spread allowed in the temperature profiles. The blue curve is the median temperature profile and the black curve is the temperature profile constructed from $\mathbf{x_a}$ in Table 5.2 . The gas priors are broad Gaussians. H_2O and CO have the same prior mean, CH_4 and CO_2 have the same prior mean. Note that the prior is Gaussian in *log* of the mixing ratios.

5.4.3 Results from the Parameterized Temperature Profile

We apply the three retrieval techniques to the three synthetic observations in Figure 5.3 under the radiative equilibrium temperature profile parameterization. This temperature profile has few parameters (5) because of the assumption of radiative equilibrium. The prior in Figure 5.4 is used in all three techniques for all three retrieval cases. In each case, we retrieve the parameter distributions for the following state vector:

$$\mathbf{x} = [log(f_{H_2O}), log(f_{CH_4}), log(f_{CO}), log(f_{CO_2}), \\ log(\kappa_{IR}), log(\gamma_{v_1}), log(\gamma_{v_2}), \beta, \alpha]^T. \quad (5.18)$$

where again, the f_is are the altitude independent volume mixing ratios. We start by first applying the optimal estimation approach. In order to ensure that the retrieval does not get stuck in a local minimum, multiple starting guesses are used. These typically all converge to the same temperature and gas solution. As described in §5.3.1.3, the covariance matrix and the best-fit from OE are then used to initialize the DEMC chains. Finally, the best-fit from OE is used to initialize the synthetic measurement realizations used in the BMC. Figures 5.5-5.8 and Table 5.3 summarize the retrieval results and form the basis for the comparisons. The bounds quoted in Table 5.3 are for the 68% confidence intervals.

We must be careful in interpreting the confidence interval values when the posteriors extend to the imposed upper and lower limits, especially when those limits are somewhat arbitrary. Parameters with posteriors that approach the imposed lower limit will result in an overestimate of the lower bound on the confidence interval and an underestimate in the

upper bound due to the imposed upper limit. In some cases if there were no Gaussian prior or no lower limit, the lower bound could extend to $-\infty$! Of course we would interpret such a case as only having an upper bound.

Figure 5.5 shows the spectral fits. The first row shows the single best-fit from optimal estimation. The second and third rows show the fits from the BMC and DEMC, respectively. Since the BMC and the DEMC provide many thousands of spectra, rather than plot each one, we summarize the fits by showing the median spectrum along with the 1- and 2σ spread at each wavelength. Illustrating the fits in this manner is more representative of the posterior than plotting spectra of different chi squared levels. In other words, if a random set of parameters is drawn from the posterior, there would be a 95% chance that the flux at any one wavelength of the spectrum resulting from that parameter draw would fall with in the 2σ spread, etc. There is little if any spread in the fits as the measurement quality improves. In the following subsections we summarize posteriors for the gas compositions, temperatures, and C-to-O ratios for each observational scenario.

5.4.3.1 Gas Abundance Retrievals

Figures 5.6 and 5.7 summarize the gas mixing ratio retrieval results. Figure 5.6 shows histograms of the *marginalized* posterior for each of the four gases as a result of each retrieval approach and observational scenario. We take the DEMC posterior (blue) to be representative of the true posterior. The optimal estimation posteriors (red) and the prior (dot-dashed red) are smooth because they are constructed analytically from the diagonal elements of $\hat{\mathbf{S}}$. Figure 5.7 is a "stair-step" plot that shows the correlations amongst the four gases comparing optimal estimation to the DEMC. For brevity, we do not show the

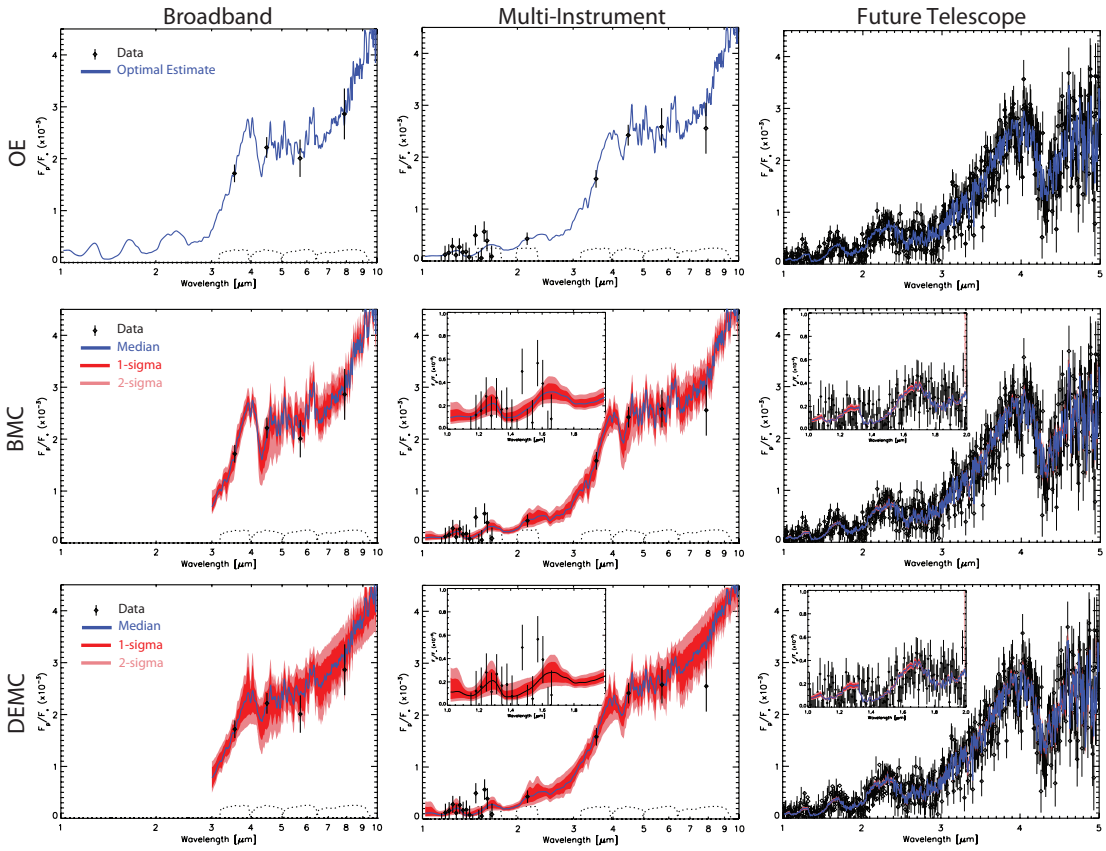

Figure 5.5: Fits to the three different sets of data (columns) from each of the three different retrieval techniques (rows). The first scenario consists of the four IRAC photometry channels. The second scenario consists of the four IRAC photometry channels, ground-based H and K_s band photometry, and HST WFC3 spectroscopy. The third scenario is representative of a FINESSE-like future, space-based telescope. For the optimal estimation, the single best-fit is shown in blue. The bootstrap Monte Carlo and the differential evolution Markov chain Monte Carlo approaches generate many thousands of spectra. The median of these spectra is shown in blue and the 1- and 2σ spread in the spectra are shown in dark and light red, respectively. The dotted curves at the bottom of each panel are the broadband filter transmission functions. The insets are a zoom in of a spectral region between 1and 2 μm to better show the spread in the spectra. Note that there is virtually no spread in the spectra for the future telescope case.

bootstrap Monte Carlo correlations. The solid blue filled regions are the 1 (dark) and 2 (light) sigma confidence intervals derived from the DEMC, and the red curves are the 1σ (inner) and 2σ(outer) confidence intervals derived from OE.

The first column of Figure 5.6 shows the marginalized gas posteriors for the broadband observational scenario and the top panel of Figure 5.7 shows the correlations amongst the gases. In this observational scenario, the three retrieval techniques produce quite different posteriors. H_2O has a fairly narrow posterior (relative to the prior) near the true state, suggesting that it is reasonably well constrained, at the 1σ level, by even this low information content spectra. This is unsurprising as water is prevalent across all of the channels in this spectrum (see Jacobian in Figure 5.2). At the 2σ level, however, the OE retrievals provide less of a constraint (Figure 5.7). The CH_4 and CO_2 posteriors abruptly fall off towards their upper end suggesting an upper bound constraint on these gases. The low end of their posteriors begin to track the prior down to the imposed lower limit indicating that from this observational scenario, there really is no observable lower limit to the abundances of these species. CH_4 has a better defined upper edge than CO_2 because both the 3.6 μm and 8 μm channels overlap with the strongest methane absorption bands. CO is virtually unconstrained by the synthetic broadband measurements as it closely matches the prior across the full range of values. The difficulty in constraining CO and CO_2 has to do with the inability of the 4.5 μm broadband photometric measurement to decouple the CO and CO_2 strong bands. There is a slight hint of an anti-correlation, as expected, from the optimal estimation results in Figure 5.7, however this correlation is not apparent from the DEMC results.

Our implementation of optimal estimation struggles to appropriately capture the errors in this observational scenario. This is because it approximates the posteriors with broad Gaussians which simply do not capture the appropriate structure. It does, however, do a fairly good job of determining the true state. The Gaussian approximation cannot appropriately handle upper bounds on CH_4 and CO_2, causing an overestimate of the 1σ upper bound. We note, that at least it is overestimating the errors rather than underestimating them. OE does a fine job at approximating the posterior for CO, which happens to be similar to the prior, again suggesting no constraint. This is reaffirmed by looking at the averaging kernel element, A, in Table 5.3 which shows that most (70%) of the information in constraining CO comes from the prior (see §5.3.2.1). The bootstrap Monte Carlo (green) completely fails to appropriately capture the posterior in this particular observational scenario. This is because the different realizations from the BMC approach produce parameter distributions that are confined to a small area of phase space localized near the best-fit solution from optimal estimation and cannot therefore sample the entirety of the posterior.

The second column of Figure 5.6 shows the gas posteriors for the multi-instrument observational scenario. The information gain from this synthetic observational scenario is only marginally higher in this case. Water has the largest improvement in uncertainty due to the leverage provided by the WFC3 spectra which covers the 1.15 μ and 1.4 μm water bands. Upon inspecting Figure 5.7 we find that the WFC3 data combined with the ground-based photometric points trims the 2σ tail but does little to improve the 1σ uncertainties. Sadly, there is virtually no reduction in the uncertainties on CH_4, CO, and CO_2. In fact

the marginalized posteriors (Figure 5.6) produced by DEMC in this observational scenario look nearly identical to the previous case. This is not surprising, as these molecules do not have strong features at the near-IR wavelengths of the WFC3 spectroscopy and the H and K_s photometry. optimal estimation provides an accurate error estimation for water but appears to provide an overly optimistic estimation of the uncertainties on CH_4. OE, as in the previous scenario, captures the essence of large uncertainties on CO and CO_2 with broad Gaussians. bootstrap Monte Carlo underestimates the uncertainties in all species with the exception of water.

Finally, results for a hypothetical future space-based telescope are shown in the last column of Figure 5.6 and bottom panel of Figure 5.7. The reduction in uncertainties are staggering when compared to the previous observational scenarios. All of the gases are constrained to within better than an order of magnitude. This is an orders-of-magnitude improvement over the previous cases. The high signal-to-noise and high spectral resolution combine to provide excellent coverage of each of the four gases. With this high-quality spectra, all three retrieval approaches give the same results. The Gaussian assumption used in optimal estimation is perfectly appropriate in this case with differences in the 1σ uncertainties of less than $\sim 10\%$ those from the DEMC. The two-dimensional confidence intervals in Figure 5.7 also agree quite well. The prior also plays very little role in the retrieval as shown with the near unit averaging kernel elements in Table 5.3.

5.4.3.2 Temperature Profile Retrievals

Figure 5.8 shows the temperature profile retrieval results (1σ (dark red) and 2σ (light red)) reconstructed from the posteriors of $log(\kappa_{IR}), log(\gamma_{v_1}), log(\gamma_{v_2}), f$, and α, as in Figure

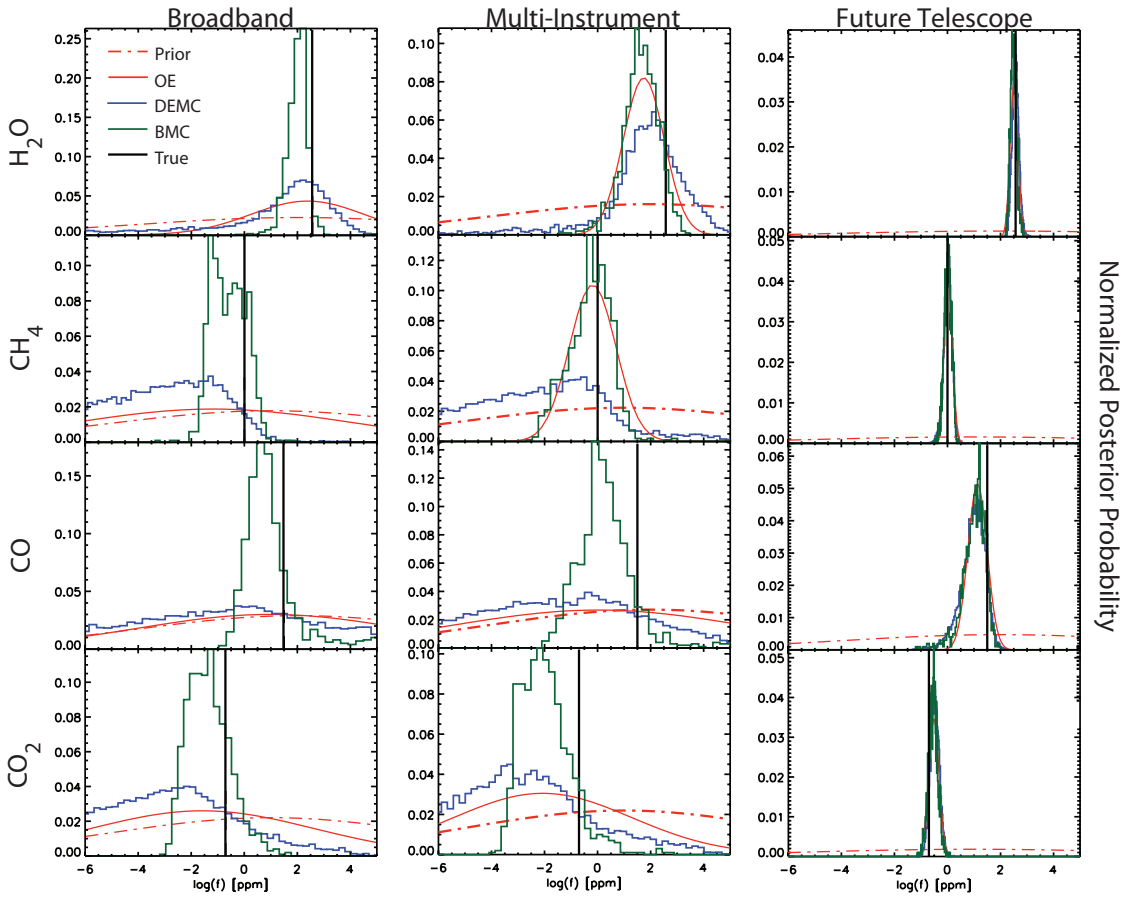

Figure 5.6: Marginalized posterior probability distributions for each of the retrieved gases (rows) and observational scenario (columns). In each panel the probability distribution for each retrieval technique are shown in different colors. The Gaussian probability distributions from optimal estimation are in red, differential evolution Markov chain Monte Carlo in blue, and bootstrap Monte Carlo in green. The priors for each gas are the dot-dashed red curve. The true answer is the vertical black line.

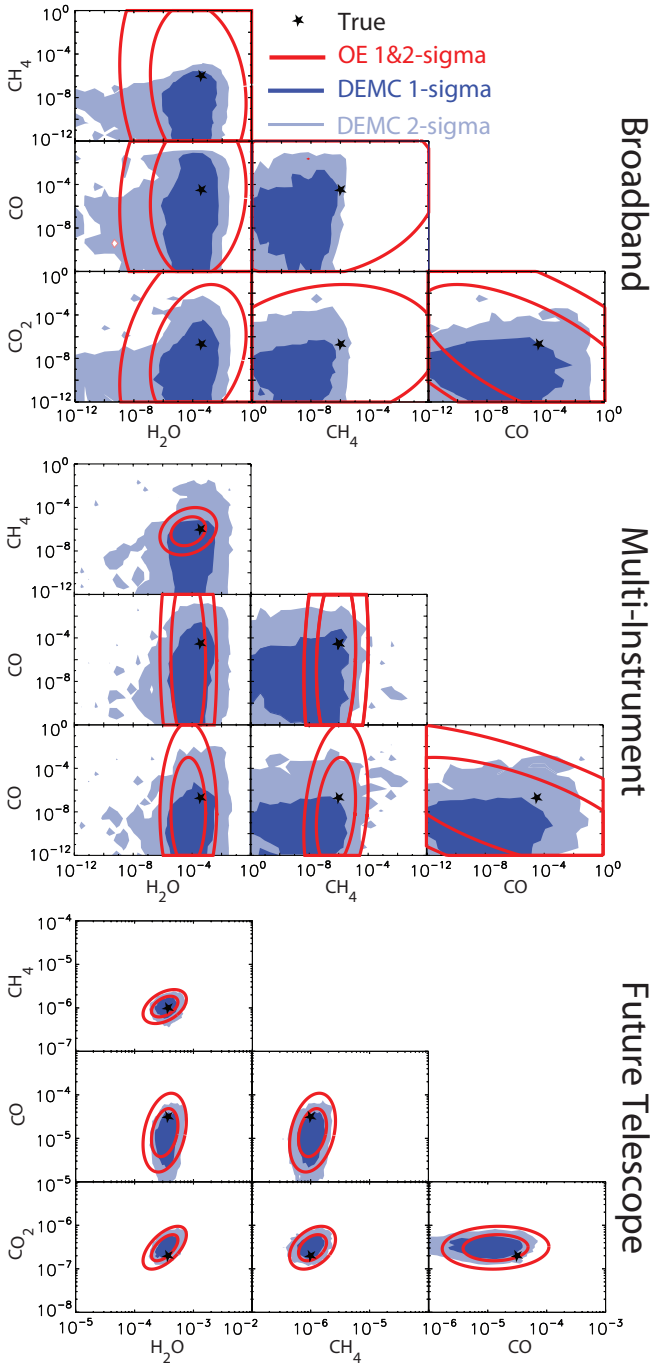

Figure 5.7: Gas correlations for each of the observing scenarios. The red curves in each are the analytic confidence intervals from the optimal estimation posterior covariance matrix ($\hat{\mathbf{S}}$). The inner ellipses are the 1σ (68%) and the outer ellipses are the 2σ (95%) confidence interval. The 1- and 2σ confidence intervals derived from the differential evolution Markov chain Monte Carlo are shown in dark and light blue, respectively. Note that the scales for the confidence intervals derived from the broadband observations (top) and the multi-instrument observations (middle) are the same. The scale on the future telescope (bottom) confidence intervals is much smaller.

5.4. The blue curve is the statistical median of these profiles. This median profile not representative of any one given temperature profile, and in fact this median profile may not even provide a good fit to the observations or adhere to the parameterization, but is shown to simply as a statistical summary of all possible temperature profiles. The black curve is the true temperature profile.

The temperature profile posteriors for the broadband scenario (first column Figure 5.8) from OE and DEMC have similar widths and both capture the entire true temperature profile within the 2σ interval. There is also a non-negligible ($\sim$ 30–50$\%$) reduction in the temperature precision compared with the prior, over the atmospheric region probed by these observations. Outside of the range spanned by the thermal emission contribution functions (Figure 5.2), the temperature uncertainty grows and begins to relax back towards the prior as there is no observational constraint. Again, the BMC approach completely underestimates the error when compared with the other two approaches because of its inability to fully characterize the posterior outside of a small region of phase space localized around the OE original best-fit.

Moving onto the multi-instrument observations (middle column Figure 5.8) we find a 22% reduction in the temperature uncertainty between 1 and 0.01 bars. The large number of spectral channels from the WFC3 data that have weighting functions over this region are the primary contributors to this increased precision. OE and BMC underestimate the temperature uncertainties relative to DEMC at 100 mbars, but the OE and DEMC have reasonable agreement over the entire profile.

The future space-based telescope observations improve the temperature uncertainties

by a remarkable factor of ~ 4.5 over the previous case. optimal estimation slightly overestimates the temperatures outside the atmospheric levels probed by the observations. This overestimate is due to the overestimation of the γ_{v1} and γ_{v2} posterior widths. These two parameters control the relative difference between the upper atmosphere and lower atmosphere temperatures. Hence, extreme values of γ_{v1} and γ_{v2} will effect these regions more than the middle atmosphere. This why the OE and the DEMC temperatures agree in the middle atmosphere but not outside of it.

5.4.3.3 C-to-O Ratios

Determination of the C-to-O ratios of explanatory atmospheres is critical to the understanding of their atmospheric chemistry (Lodders & Fegley 2002; Moses et al. 2012) and formation environments (Öberg, Murray-Clay, & Bergin 2011). Given the abundance posteriors derived with CHIMERA, we can compute C/O posterior distributions (Figure 5.9) . The C/O is calculated with the following formula,

$$C/O = \frac{\Sigma C}{\Sigma O} \approx \frac{CH_4 + CO + CO_2}{H_2O + CO + 2CO_2}. \tag{5.19}$$

Some simple things to note about this equation. When CO is the dominant species, C/O is 1. If CO_2 is the dominant species, C/O will be $1/2$. When methane dominates the C/O will be large and when H_2O dominates C/O will be small. The solar C/O is 0.55. A number of exoplanets have reported C/O's near 1. We can construct the C/O probability distributions by propagating the probability distributions of each gas through Equation 5.19, similar to how the temperature profile posteriors were constructed. Before inspecting the posteriors

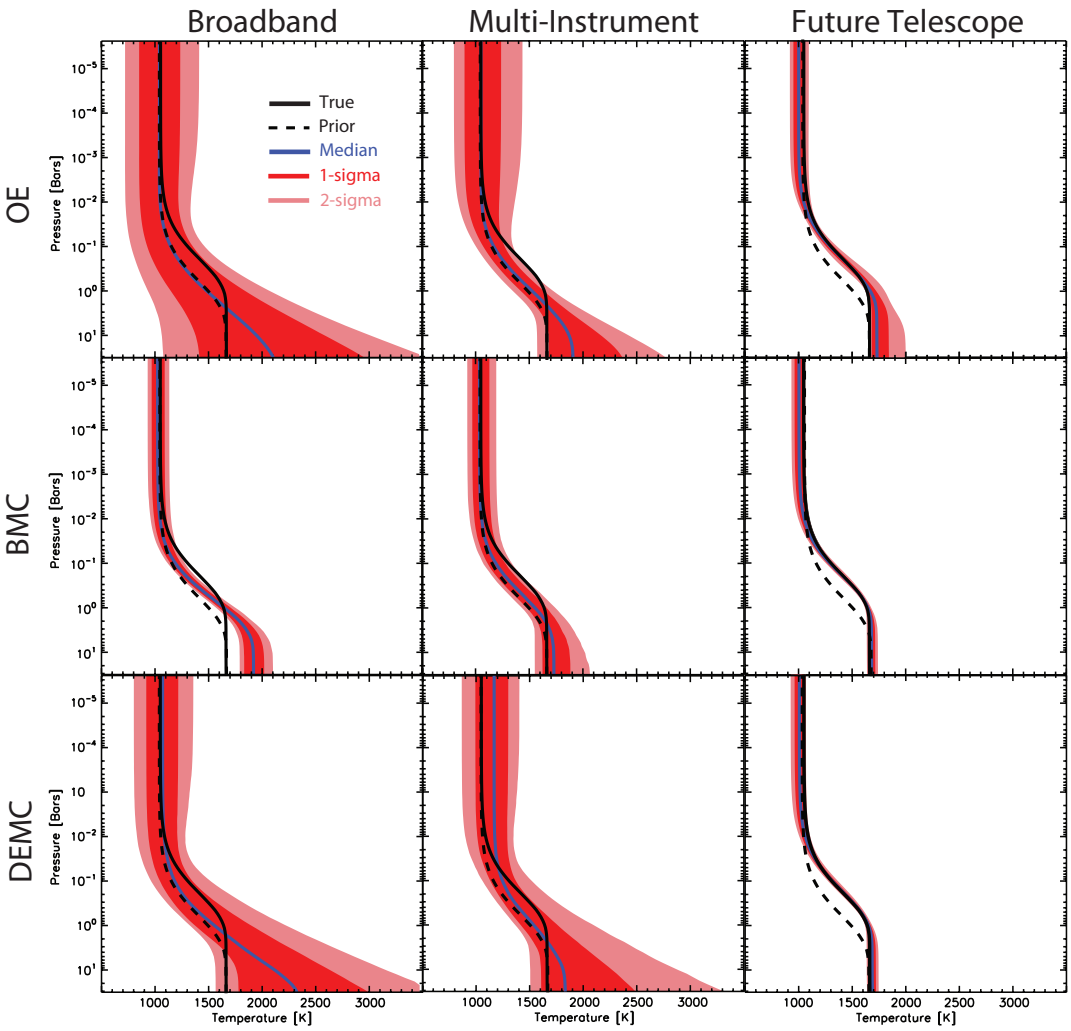

Figure 5.8: Temperature profile posteriors for each observational scenario (columns) and each retrieval technique (rows). The solid black curve in each panel is the true temperature profile constructed with Equations 5.13-5.16 and the parameters in Table 5.1. The dashed black curve is constructed from the temperature parameters, x_a, just as in Figure 5.4 The blue curve is the median temperature profile. The dark and light red regions are the 1- and 2σ (68% and 95%) uncertainties, respectively.

derived from CHIMERA, we find it illustrative to investigate the prior. Upon propagating the Gaussian priors (with the limits) of the gases through Equation 5.19 we obtain the C/O prior in Figure 5.9. We find that this prior has two peaks, one is at a C/O of 1 and the other is at a C/O of 0.5. The locations of these peaks are insensitive to whether or not the gas abundance priors are uniform or broad Gaussians. These peaks are also insensitive to the lower and upper bounds placed on either a uniform or Gaussian gas prior. These double peaks are due to an elegant mathematical misfortune. For illustrative purposes, let us assume we draw the set of 4 gases from a uniform log prior. We would expect then, that one gas will have a larger abundance than the other three $1/4$ of the time. This means that in roughly $1/4$ of the draws CO will dominate, which would cause the ratio in Equation 5.19 to be one, $1/4$ of the time. A similar argument goes for CO_2 resulting in a C/O of $1/2$ roughly $1/4$ of the time. So we see, that if we did not observe a particular planet, and assumed uniformed priors on each of the gases, we would naturally conclude that the planet has equal chances of having a C/O of one or one-half. However, our priors are not uniform, but rather broad Gaussians, but they are broad enough that this behavior still occurs, with a slight preference for a C/O of one.

If we observe this planet with the four broadband points we obtain the posteriors in the upper-left panel of Figure 5.9. OE and DEMC produce similar C/O posteriors both of which maintain the two peaked features at 1 and $1/2$ but with overall less power in the peaks. These features persist simply because the gas posteriors from DEMC and OE do not deviate too strongly from the prior. There is more probability in the lower C/O tail than in the prior because of the higher values of H_2O preferred by the measurements over the

prior. This is good, since the C/O for our fictitious planet is much less than one or one-half. BMC anomalously captures the true C/O at the peak of its posterior. Again, BMC greatly underestimates the posterior widths because it only searches a localized region about the OE best-fit. Since the OE best-fit gas abundances are very near truth, the BMC posteriors, which are highly localized about the OE best-fit parameters, will overemphasize the C/O derived by that best-fit.

The story is the same for the multi-instrument observational scenario. Unfortunately, at least in this example, it appears that the WFC3 and ground-based data provide very little additional constraints in reducing the C/O uncertainty, with the double-peaked feature from the prior persisting in the DEMC results.

Improving the observational quality further with a future space-based telescope essentially obtains the correct value to high precision. The peak of the posterior is far enough away from the double-peaked prior that the results appear to be less influenced by the prior than the previous cases. All three retrieval approaches give a nearly identical posterior.

From this exercise we have learned that it is difficult to constrain the C-to-O ratio of an exoplanet atmosphere. Simple, uninformed, or nearly uninformed priors on the gas abundances produce a double-peaked C/O prior at near solar value and one. Even in the best cases, current observations are likely to provide only an upper limit on this quantity. This result suggests that previously published claims to detect enhanced C-to-O ratios with photometry alone may be influenced by these subtle biases, and should be viewed with strong skepticism. We will discuss this issue in the context of specific exoplanets in part II.

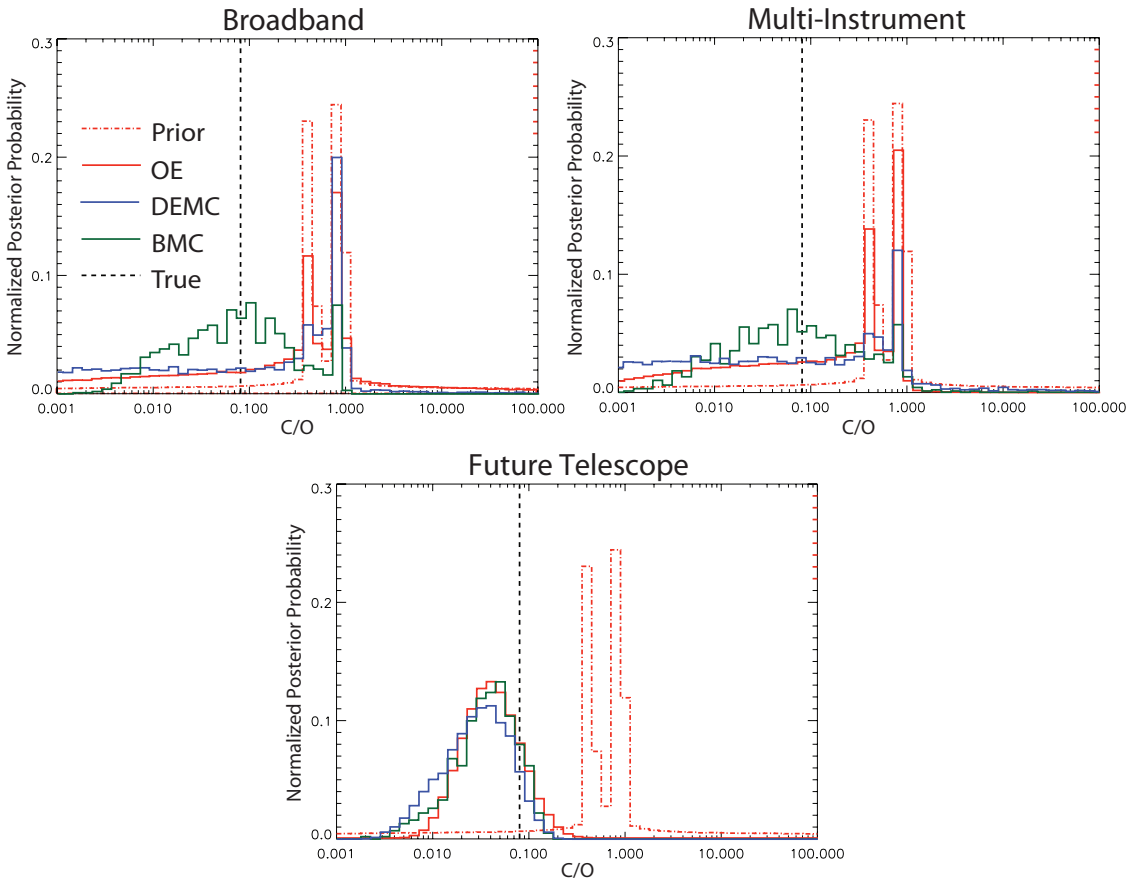

Figure 5.9: C-to-O ratio posteriors. The dot-dashed green curve is the prior, the solid red curve is from OE, blue is from DEMC, and green is from BMC. The vertical dashed line is the true C/O. The top left panel are the C/O's derived from the broadband observational scenario, top right are the C/O's derived from the multi-instrument scenario, and the bottom are the C/O's derived from the future space-based telescope scenario. Though it appears that the BMC characterizes the C/O errors well, it is for the wrong reasons. See §5.4.3.3

5.4.4 Results from the level-by-level Temperature Profile

The level-by-level temperature profile approach attempts to determine the temperature at each model layer. In contrast to the parameterized temperature profile which had only 5 parameters, the level-by-level approach requires as many parameters as model layers, for a total of 90 parameters. This is a larger number of parameters is far greater than the number of meaningful constraints provided by extrasolar planet observations. However, this approach makes no assumptions about the physical structure of the temperature profile (e.g., radiative, radiative-convective, advection, etc.). While there is no potentially biasing parameterization, the retrievals can result in unphysical temperature profiles. Obviously, the temperature at each of the 90 levels cannot be perfectly retrieved, but rather the retrievals have to depend on the prior when spectral information on the temperature is sparse.

For the level-by-level prior we assume an a prior covariance of 400 K and correlations amongst each level with all other levels given by Equation 5.12. The 400 K width is used to produce a similar temperature profile prior as in Figure 5.4. This correlation helps reduce the effective number of levels that have to be independently retrieved. Admittedly, the degree of correlation is somewhat of an external arbitrary parameter, but it is chosen to avoid over-fitting (i.e., fitting to the noise) without hindering the level-by-level flexibility. It can be thought of as a smoothing, or more specifically, a regularization. We can also use the averaging kernel profile to assess where the temperature is constrained by the measurements versus the prior. The gas priors are the same as before. We choose only to compare the results from optimal estimation and the bootstrap Monte Carlo. We do not attempt the DEMC approach on such a large ($\sim$100) number of parameters, as MCMC algorithms (to

the best of our knowledge) are not well suited for large numbers of parameters because of the large number of steps required to fully map the n-dimensional probability distribution when n is large.

Figure 5.10 shows the spectral fits as a result of OE and BMC using the level-by-level temperature approach, similar to Figure 5.5. Figure 5.11 shows the marginalized gas posteriors. We find the gas posteriors and the agreement amongst the retrieval techniques are very similar to those derived in Figure 5.6 using the parameterized temperature profile. This is somewhat surprising given the extremely different temperature profile retrieval approaches. This suggests that the gas abundances can be properly and consistently retrieved regardless of the temperature profile assumptions. We could, however, imagine a contrived example in which the true temperature profile is so wildly different from what can be reasonably approximated with the parameterization, that the two approaches would yield differing gas posteriors.

Figure 5.12 shows temperature profile posteriors under the level-by-level temperature profile assumption. For the broadband scenario, the uncertainties more or less do not improve much beyond the prior. The greatest gain in improvement is over the region spanned by the averaging kernel (green curve). The uncertainty reduces from the prior uncertainty of $+/-400$ K to $+/-265$ K at 100 mbars. The BMC approach using the level-by-level temperature profile produces a much smaller error than the OE approach, and at some levels the 2σ uncertainties do not even capture the true state. Again, this because the BMC is only able to characterize a highly localized region around the OE best-fit.

The reduction in temperature uncertainty due to the addition of the WFC3 and ground-

based photometry data is more apparent with the level-by-level approach than with the parameterized approach. The uncertainties in temperature at 100 mbars are reduced to +/- 177 K, though smaller uncertainties are achieved at deeper levels due to the addition of the WFC3 data which probe deeper atmospheric levels. This is why the averaging kernel profile peaks at a deeper level. The BMC results show a larger uncertainty than they do in the broadband observational scenario but still greatly underestimate the profile spread relative to optimal estimation.

The future space-based telescope observations reduce the temperature uncertainties to $+/-70$K, a factor of nearly four better than what can be done with the broadband observations. Outside of the region spanned by the averaging kernel uncertainties relax back to the prior widths. As before, in both cases the BMC approach underestimates the temperature uncertainties relative to the OE derived uncertainties. The uncertainties in temperature derived using the level-by-level temperatures are a factor of two larger than those derived with the parameterized temperature profile. This is because the retrievals with the parameterization only allow temperature profiles that conform to radiative equilibrium whereas the level-by-level retrievals can allow for a wider range of possibilities that do not necessarily have to conform to this constraint.

Another way to determine the robustness of the level-by-level retrieval is to explore the role of the prior temperature profile (see, e.g., Lee et al. 2012). For this, we investigate the effect of three different temperature priors (different prior profiles, $\mathbf{x_a}$ but same widths, $\mathbf{S_a}$) on the retrieved profiles and check to see if they are consistent with the estimated errors (Figure 5.13). The shaded grey region in Figure 5.13 is the 1σ retrieval uncertainty from

Figure 5.12 using the nominal prior. Two of the other priors are the nominal profile with a $+/-500$ K offset, and the third is an isothermal profile set to the equilibrium temperature of the planet. In all three cases we find that the retrieved profiles fall with in the 1σ bounds on the nominal retrieved profile. This suggests that though different temperature profile priors are used, they generally produce retrieved profiles that are statistically consistent with each other. As the spectral quality improves, the different priors produce identically the same retrieved profiles over the atmospheric regions spanned by the thermal emission weighting functions. Outside of this region, the profiles diverge and relax towards their respective priors with no consequence on the spectra. This serves as yet another demonstration that the spectra are only sensitive to a small region of the atmosphere between a few bars up to a few mbars. While some of these level-by-level profiles may not be physical, especially in the broadband observational scenario, they are a more direct reflection of the information provided by the measurements in the absence of a parameterized model.

5.5 Discussion & Conclusions

We have developed a new statistically robust suite of exoplanet atmospheric retrieval algorithms known as CHIMERA. This suite consists of the optimal estimation (OE, §5.3.1.1), bootstrap Monte Carlo (BMC, §5.3.1.2), and differential evolution Markov chain Monte Carlo (DEMC, §5.3.1.3) approaches and a validated forward model (§5.3.2). We have tested each of these approaches on the dayside thermal emission spectra for a synthetic planet under a variety of observational scenarios ranging from current observations to potential future observations (§5.4). In general, we find that the three retrieval approaches

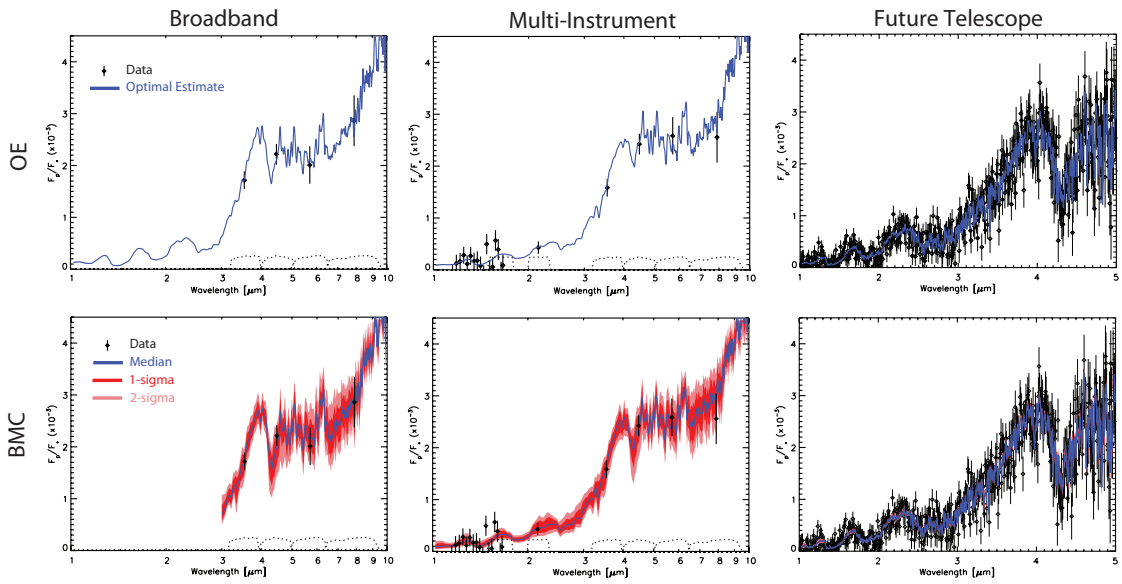

Figure 5.10: Fits to the three different sets of data (columns) from two of the retrieval techniques (rows) using the level-by-level temperature approach. For the optimal estimation approach, the single best-fit is shown in blue. The bootstrap Monte Carlo approach generates many thousands of spectra. The median of these spectra is shown in blue and the 1- and 2σ spread in the spectra are shown in dark and light red, respectively. The dotted curves at the bottom of each panel are the broadband filter transmission functions.

produce similar posteriors when the measurement quality is good, typically when there are more observed spectral channels than retrievable parameters (Figures 5.6 and 5.7). The Gaussian approximation made by optimal estimation breaks down for low-quality measurements, but is perfectly valid for high-quality measurements likely to come from future space-based observations. It also appropriately captures the correlations amongst the various parameters. This approach is much less of a computational burden than Monte Carlo approaches and will prove useful for quick reductions of large, high-quality data sets. The optimal estimation formalism also allows for the calculation of the averaging kernel (§5.3.2.1), a useful diagnostic to determine how much of the posterior is influenced by the prior versus the measurements. The bootstrap Monte Carlo approach generally fails to capture the essence of the posteriors. This is because the regeneration of synthetic measure-

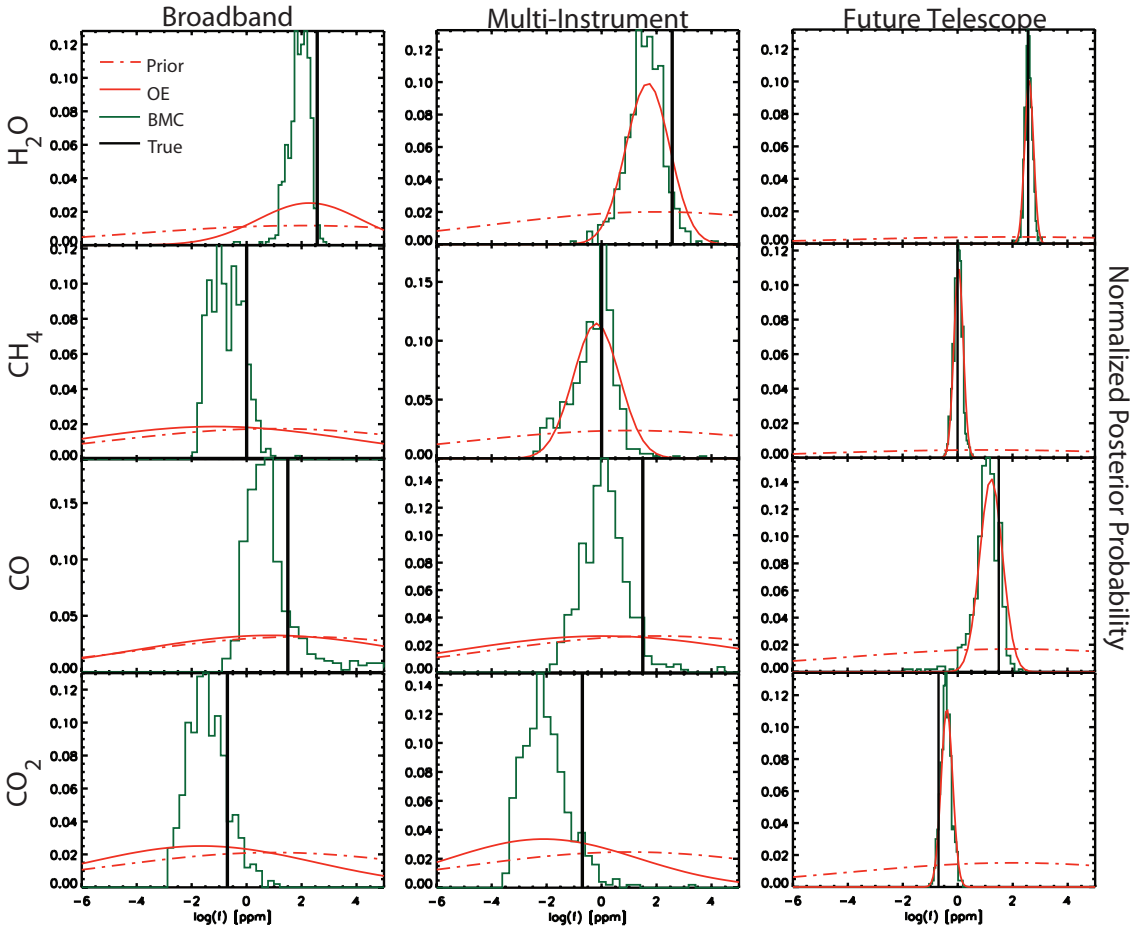

Figure 5.11: Marginalized posterior probability distributions for each of the retrieved gases (rows) and observational scenario (columns) using the level-by-level temperature profile approach. In each panel the posteriors for optimal estimation (red) and bootstrap Monte Carlo (green) are shown. The Gaussian priors for each gas are shown with the dot-dashed red curve. The true answer is the vertical black line.

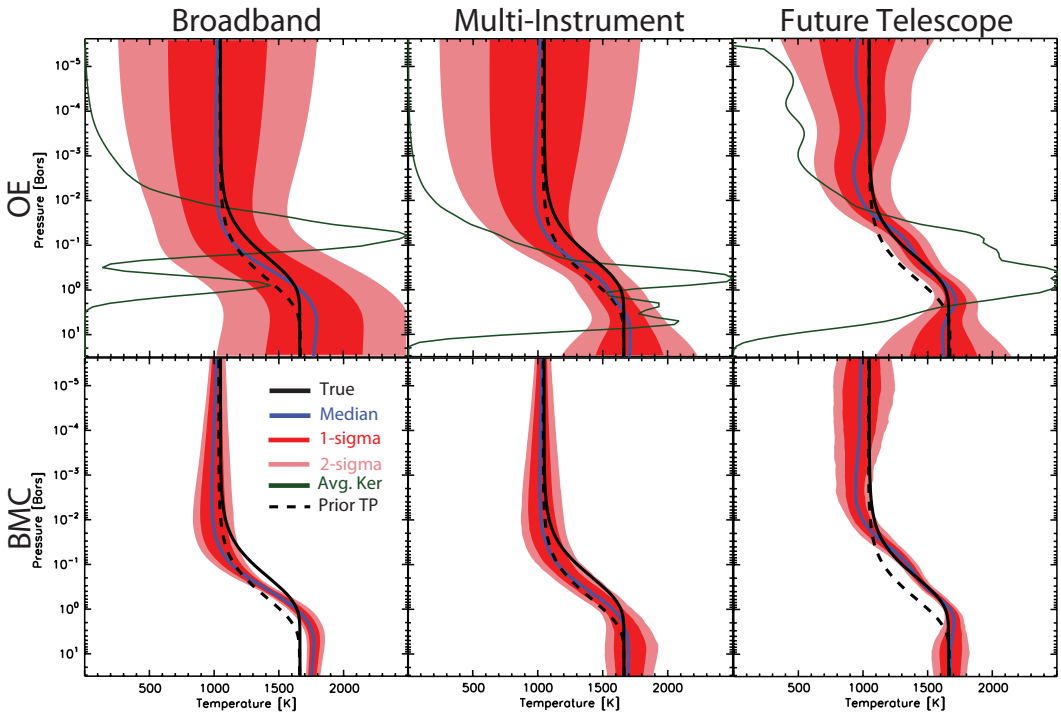

Figure 5.12: Temperature profile posteriors using the level-by-level temperature profile approach for each observational scenario (columns) and two of the retrieval technique (rows). The solid black curve in each panel is the true temperature profile constructed with equations 5.13-5.16 and the parameters in Table 5.1. The blue curve is the median temperature profile. The dashed black curve is the priortemperature profile constructed from $\mathbf{x_a}$, as in Figure 5.4. The prior widths for each level (not shown) are $+/-400$ K. The dark and light red regions are the 1- and 2σ (68% and 95%) uncertainties, respectively. The green curve is the averaging kernel profile for temperature. The atmospheric regions over which this is a maximum is where we can retrieve temperature information with less dependence on the prior (see text).

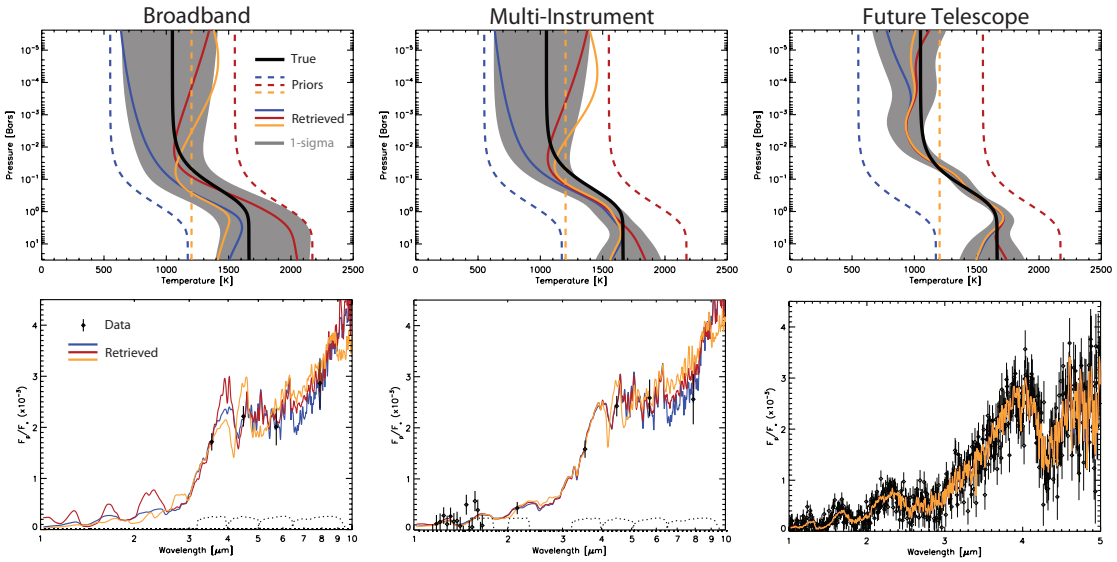

Figure 5.13: The effect of three different level-by-level temperature profile priors on the retrieved temperatures (top) and spectra (bottom). The different temperature profile priors are shown as the colored dashed curves. The prior widths (not shown) at each level are $+/-400$ K, similar to those in Figure 5.12. The resultant retrieved profiles are shown as the solid colored curves. The thick black curve is the true temperature profile. The solid grey region is the 1σ confidence interval from the retrievals in Figure 5.12. Note how the retrieved profiles all converge within the 1σ confidence interval regardless of the temperature prior. The best agreement is in the middle atmosphere where the thermal emission weighting functions are a maximum, and hence the averaging kernel profiles from Figure 5.12 are also a maximum. The spectra in the second row illustrate the effects of the different retrieved temperature profiles of corresponding color. There is virtually no difference in the resultant spectra for high-quality data. The dotted curves at the bottom are the broadband filter functions.

ment realizations based on the optimal estimation best-fit only sample a localized region of phase space near the best-fit solution. This is especially problematic in the cases where there are fewer spectral data points than parameters. In this scenario, even with small measurement error, there will still be many possible best-fit solutions, thus creating enormous degeneracies among the parameters. Since the BMC is initialized with only one possible best-fit set of parameters out of many, the derived parameter uncertainties will only be representative of the uncertainties about that localized best-fit. We therefore strongly advise against the bootstrap Monte Carlo approach when the number of parameters is larger than the number of spectral data points. In the high signal-to-noise and high spectral resolution regime, both the bootstrap and optimal estimation methods provide reasonable parameter uncertainties. We have also introduced the application of differential evolution Markov chain Monte Carlo to the spectral retrieval problem and found that convergence can be obtained efficiently by using an appropriate proposal distribution based on the chain history.

We find that for broadband observations typical of most hot Jupiters, very limited constraints on the gas abundances can be obtained. The Spitzer photometry does a particularly poor job constraining the relative abundance of CO, with most posteriors simply reflecting their priors (§5.4.3.1). The addition of WFC3 observations provide little additional constraint on the gas abundances derived from dayside thermal emission spectra, with the exception of a slight improvement on the water abundances. This is primarily due to the limited spectral coverage provided by the red grism on WFC3, which spans the wavelengths from 1.2-1.6 μm. As the measurement quality improves, the parameter uncertainties decrease and become more Gaussian. Modest future space-based instruments have the ca-

pability of obtaining better than order-of-magnitude constraints on gas compositions with their posteriors generally being independent of the prior. This is typically many orders of magnitude better than current observational capabilities (Table 5.3). The derived gas posteriors are also independent of whether or not a parameterized or level-by-level temperature profile is used (Figure 5.6 vs. Figure 5.11).

Constraining the C-to-O ratio of exoplanet atmospheres is very difficult due to the broad nature of some of the gas posteriors, especially CO. In the absence of valid observational constraints the posteriors for these molecules simply reflect the priors, which produce a double-peaked distiribution with maxima at C-to-O ratios of 0.5 and 1 (§5.4.3.3, Figure 5.9). Only high-quality observations from the future space-based telescope scenerio are independent of the double-peaked prior. As a result, caution must be taken when interpreting C-to-O ratios from broad gas posteriors.

Reasonable temperature constraints could be obtained in all observational scenarios and temperature retrieval approaches, though the bootstrap Monte Carlo approach again fails to fully capture the posterior (§5.4.3.2, Figure 5.8). The temperature profiles and corresponding uncertainties can only be trusted for the region over which the thermal emission contribution functions peak, typically between a few bars and a few mbars (Figure 5.2). Outside of this window, the temperature profiles are strongly effected by their priors. The level-by-level temperature profile approach overestimates the temperature uncertainties compared with the parameterization due to the allowance of more profiles (§5.4.4). These level-by-level profiles can be unphysical but are more reflective of the measurements without imposing preconceived notions of how the physical structure of the atmosphere should

behave. While this approach produces statistically consistent profiles in low-quality observational scenarios, we would still recommend using a parameterization for said cases. However, for high-quality spectra the level-by-level approach is recommended given its slightly more pessimistic temperature uncertainties and its non-dependence on a particular parameterization.

In part II we will use CHIMERA to perform a uniform analysis of an ensemble of secondary eclipse spectra. Such a study will allow us to determine the biases introduced by the choice of fitting method for individual planets and to derive a uniform set of relative abundances and temperatures for these planets that can be reliably inter-compared and trends identified. This kind of uniform analysis has the potential to provide invaluable insights into exoplanetary atmospheric processes and formation environments.

5.6 Acknowledgements

We thank John Johnson and Jonathan Fortney for highly useful conversations. We thank Jaimin Lee and Leigh Fletcher for their willingness to compare radiative transfer codes. A portion of this research was carried out at the Jet Propulsion Laboratory, California Institute of Technology, under contract with the National Aeronautics and Space Administration.

Table 5.3: Numerical summary of the retrieval results for several parameters as derived from each retrieval technique and observational scenario. For each parameter and each observational scenario we show the true value, the 1σ (68% confidence interval) marginalized prior uncertainties, and the 1σ marginalized uncertainties derived from optimal estimation (OE), bootstrap Monte Carlo (BMC), and differential evolution Markov chain Monte Carlo (DEMC) as well as the averaging kernal element for that parameter (A) . The gas abundances, f_i, are given in terms of volume mixing ratio. We also show a representative temperature (100 mbars temperature) and the C-to-O ratio. This table is laid out so that for a given parameter easy comparisons in either the observational scenario (left-right) or the retrieval techniques (top-bottom) can be made.

parameter		Broadband	Multi-Instrument	Future Telescope
f_{H2O}	True:	3.70×10^{-04}	3.70×10^{-04}	3.70×10^{-04}
	Prior:	$4.94 \times 10^{-10} - 3.92 \times 10^{-03}$	$4.94 \times 10^{-10} - 3.92 \times 10^{-03}$	$4.94 \times 10^{-10} - 3.92 \times 10^{-03}$
	OE:	$1.25 \times 10^{-06} - 7.82 \times 10^{-03}$	$3.68 \times 10^{-06} - 7.03 \times 10^{-04}$	$2.31 \times 10^{-04} - 4.56 \times 10^{-04}$
	BMC:	$5.74 \times 10^{-05} - 2.68 \times 10^{-04}$	$1.18 \times 10^{-05} - 2.45 \times 10^{-04}$	$2.44 \times 10^{-04} - 4.03 \times 10^{-04}$
	DEMC:	$1.84 \times 10^{-07} - 1.24 \times 10^{-03}$	$7.06 \times 10^{-06} - 1.40 \times 10^{-03}$	$2.83 \times 10^{-04} - 4.98 \times 10^{-04}$
	A:	0.872	0.983	0.999
f_{CH4}	True:	1.00×10^{-06}	1.00×10^{-06}	1.00×10^{-06}
	Prior:	$2.63 \times 10^{-10} - 2.55 \times 10^{-03}$	$2.63 \times 10^{-10} - 2.55 \times 10^{-03}$	$2.63 \times 10^{-10} - 2.55 \times 10^{-03}$
	OE:	$8.89 \times 10^{-11} - 5.73 \times 10^{-04}$	$4.54 \times 10^{-09} - 3.92 \times 10^{-05}$	$7.50 \times 10^{-07} - 1.54 \times 10^{-06}$
	BMC:	$6.40 \times 10^{-08} - 1.64 \times 10^{-06}$	$9.07 \times 10^{-08} - 3.89 \times 10^{-06}$	$7.62 \times 10^{-07} - 1.46 \times 10^{-06}$
	DEMC:	$2.21 \times 10^{-11} - 9.27 \times 10^{-07}$	$4.40 \times 10^{-11} - 1.96 \times 10^{-06}$	$7.39 \times 10^{-07} - 1.52 \times 10^{-06}$
	A:	0.259	0.979	0.999
f_{CO}	True:	3.16×10^{-05}	3.16×10^{-05}	3.16×10^{-05}
	Prior:	$4.94 \times 10^{-10} - 3.92 \times 10^{-03}$	$4.94 \times 10^{-10} - 3.92 \times 10^{-03}$	$4.94 \times 10^{-10} - 3.92 \times 10^{-03}$
	OE:	$4.97 \times 10^{-10} - 2.43 \times 10^{-03}$	$7.40 \times 10^{-10} - 4.13 \times 10^{-03}$	$5.87 \times 10^{-06} - 3.13 \times 10^{-05}$
	BMC:	$2.05 \times 10^{-06} - 6.10 \times 10^{-05}$	$3.00 \times 10^{-07} - 1.81 \times 10^{-05}$	$4.37 \times 10^{-06} - 2.76 \times 10^{-05}$
	DEMC:	$2.00 \times 10^{-10} - 5.32 \times 10^{-04}$	$8.89 \times 10^{-11} - 7.16 \times 10^{-05}$	$3.52 \times 10^{-06} - 2.66 \times 10^{-05}$
	A:	0.316	0.176	0.996
f_{CO2}	True:	2.00×10^{-07}	2.00×10^{-07}	2.00×10^{-07}
	Prior:	$2.63 \times 10^{-10} - 2.55 \times 10^{-03}$	$2.63 \times 10^{-10} - 2.55 \times 10^{-03}$	$2.63 \times 10^{-10} - 2.55 \times 10^{-03}$
	OE:	$7.73 \times 10^{-11} - 1.78 \times 10^{-04}$	$5.07 \times 10^{-09} - 4.25 \times 10^{-03}$	$1.94 \times 10^{-07} - 4.82 \times 10^{-07}$
	BMC:	$9.44 \times 10^{-09} - 3.61 \times 10^{-07}$	$1.64 \times 10^{-09} - 1.10 \times 10^{-07}$	$2.03 \times 10^{-07} - 4.29 \times 10^{-07}$
	DEMC:	$2.21 \times 10^{-11} - 9.27 \times 10^{-07}$	$2.33 \times 10^{-11} - 7.37 \times 10^{-07}$	$2.30 \times 10^{-07} - 5.06 \times 10^{-07}$
	A:	0.508	0.689	0.999
$T_{100mb}[K]$	True:	1313	1313	1313
	Prior:	$876 - 1503$	$876 - 1503$	$876 - 1503$
	OE:	$932 - 1358$	$1075 - 1274$	$1267 - 1340$
	BMC:	$1150 - 1249$	$1117 - 1284$	$1278 - 1327$
	DEMC:	$1050 - 1355$	$1136 - 1374$	$1294 - 1348$
C/O	True:	8.00×10^{-2}	8.00×10^{-2}	8.00×10^{-2}
	Prior:	$3.82 \times 10^{-02} - 8.00$	$3.82 \times 10^{-02} - 8.00$	$3.82 \times 10^{-02} - 8.00$
	OE:	$2.07 \times 10^{-03} - 1.00$	$6.26 \times 10^{-03} - 0.938$	$2.25 \times 10^{-2} - 8.93 \times 10^{-2}$
	BMC:	$1.60 \times 10^{-02} - 0.32$	$1.29 \times 10^{-02} - 0.427$	$1.81 \times 10^{-02} - 8.09 \times 10^{-2}$
	DEMC:	$3.53 \times 10^{-04} - 0.97$	$1.93 \times 10^{-04} - 0.721$	$1.27 \times 10^{-02} - 6.90 \times 10^{-2}$

Bibliography

Allard, F., Hauschildt, P. H., & Schweitzer, A. 2000, ApJ, 539, 366

Anderson, D. R., Gillon, M., Maxted, P. F. L., et al. 2010, VizieR Online Data Catalog, 351, 39003

Benneke, B., & Seager, S. 2012, ApJ, 753, 100

Berta, Z. K., Charbonneau, D., Désert, J.-M., et al. 2012, ApJ, 747, 35

Borysow, A. 2002, A&A, 390, 779

Borysow, A., Jørgensen, U.G., Fu, Y. 2001, JQSRT, 68, 235

Burrows, A., Hubeny, I., Budaj, J., Knutson, H. A., & Charbonneau, D. 2007, ApJl, 668, L171

Burrows, A., Hubeny, I., & Sudarsky, D. 2005, ApJl, 625, L135

Charbonneau, D., Allen, L. E., Megeath, S. T., et al. 2005, ApJ, 626, 523

Charbonneau, D., Knutson, H. A., Barman, T., et al. 2008, ApJ, 686, 1341

Conrath, B. J., Gierasch, P. J., & Ustinov, E. A. 1998, Icarus, 135, 501

Croll, B., Jayawardhana, R., Fortney, J. J., Lafrenière, D., & Albert, L. 2010, ApJ, 718, 920

Crossfield, I. J. M., Knutson, H., Fortney, J., et al. 2012, ApJ, 752, 81

Crouzet, N., McCullough, P. R., Burke, C., & Long, D. 2012, ApJ, 761, 7

Deming, D., Fraine, J. D., Sada, P. V., et al. 2012, ApJ, 754, 106

Deming, D., Wilkins, A., McCullough, P., et al. 2013, arXiv:1302.1141

Désert, J.-M., Sing, D., Vidal-Madjar, A., et al. 2011, A&A, 526, A12

Désert, J.-M., Bean, J., Miller-Ricci Kempton, E., et al. 2011, ApJl, 731, L40

Eastman, J., Gaudi, B. S., & Agol, E. 2013, PASP, 125, 83

Ford, E. B. 2005, AJ, 129, 1706

Fortney, J. J., Marley, M. S., Lodders, K., Saumon, D., & Freedman, R. 2005, ApJl, 627, L69

Fletcher, L. N., Irwin, P. G. J., Teanby, N. A., et al. 2007, Icarus, 189, 457

Gibson, N. P., Aigrain, S., Pollacco, D. L., et al. 2010, MNRAS, 404, L114

Gibson, N. P., Pont, F., & Aigrain, S. 2011, MNRAS, 411, 2199

Gillon, M., Triaud, A. H. M. J., Fortney, J. J., et al. 2012, A&A, 542, A4

Greathouse, T. K., Richter, M., Lacy, J., et al. 2011, Icarus, 214, 606

Grillmair, C. J., Charbonneau, D., Burrows, A., et al. 2007, ApJl, 658, L115

Grillmair, C. J., Burrows, A., Charbonneau, D., et al. 2008, Nature, 456, 767

Guillot, T. 2010, A&A, 520, A27

Harrington, J., Hansen, B. M., Luszcz, S. H., et al. 2006, Science, 314, 623

Harrington, J., Luszcz, S., Seager, S., Deming, D., & Richardson, L. J. 2007, Nature, 447, 691

Hansen, B. M. S. 2008, ApJs, 179, 484

Irwin, P. G. J., Teanby, N. A., de Kok, R., et al. 2008, JQSRT, 109, 1136

Jørgensen, U. G., Hammer, D., Borysow, A., & Falkesgaard, J. 2000, A&A, 361, 283

Knutson, H. A.,Charbonneau, D., Allen, L. E., et al. 2007, Nature, 447, 183

Knutson, H. A., Charbonneau, D., Allen, L. E., Burrows, A., & Megeath, S. T. 2008, ApJ, 673, 526

Knutson, H. A., Lewis, N., Fortney, J. J., et al. 2012, ApJ, 754, 22

Lee, J.-M., Fletcher, L. N., & Irwin, P. G. J. 2012, MNRAS, 420, 170

Line, M. R., Liang, M. C., & Yung, Y. L. 2010, ApJ, 717, 496

Line, M. R., Vasisht, G., Chen, P., Angerhausen, D., & Yung, Y. L. 2011a, ApJ, 738, 32

Line, M. R., Zhang, X., Vasisht, G., et al. 2012, ApJ, 749, 93

Lodders, K., & Fegley, B. 2002, Icarus, 155, 393

Madhusudhan, N., & Seager, S. 2009, ApJ, 707, 24

Madhusudhan, N., Harrington, J., Stevenson, K. B., et al. 2011, Nature, 469, 64

Machalek, P., McCullough, P. R., Burrows, A., et al. 2009, ApJ, 701, 514

Metropolis, N., Rosenbluth, A. W., Rosenbluth, M. N., Teller, A. H., Teller, E., 1953, The journal of chemical physics, 21, 1087

Moses, J. I., Visscher, C., Fortney, J. J., et al. 2011, ApJ, 737, 15

Nixon, C. A., Achterberg, R. K., Conrath, B. J., et al. 2007, Icarus, 188, 47

Öberg, K. I., Murray-Clay, R., & Bergin, E. A. 2011, ApJl, 743, L16

Press, W.H., Teukolksy, S., Vetterling, W.T., Fannery, B. 1995, Numerical Recipies: The art of scientific computing, sec. ed., Camb. Univ. Press

Robinson, T. D., & Catling, D. C. 2012, ApJ, 757, 104

Rodgers, C. D. 1976, Reviews of Geophysics and Space Physics, 14, 609

Rodgers, C.D., Inverse methods for atmospheric sounding, Theory and Practice, 2000

Rothman, L. S., Gordon, I. E., Barbe, A., et al. 2009, JQSRT, 110, 533

Rothman, L. S., Gordon, I. E., Barber, R. J., et al. 2010, JQSRT, 111, 2139

Stevenson, K. B., et al. 2010, Nature, 464, 1161

Swain, M. R., Vasisht, G., Tinetti, G., et al. 2009a, ApJl, 690, L114

Swain, M. R., Tinetti, G., Vasisht, G., et al. 2009b, ApJ, 704, 1616

Swain, M., Deroo, P., Tinetti, G., et al. 2012, arXiv:1205.4736

Swain, M. R. 2012, American Astronomical Society Meeting Abstracts 220, 220, 505.05

ter Braak, C. J. 2006, Statistics and Computing, 16, 239-249

ter Braak, C. J., & Vrugt, J. A. 2008, Statistics and Computing, 18, 435-446

Tinetti, G., Vidal-Madjar, A., Liang, M.-C., et al. 2007, Nature, 448, 169

Tinetti, G., Griffith, C. A., Swain, M. R., et al. 2010, Faraday Discussions, 147, 369

Tinetti, G., Deroo, P., Swain, M. R., et al. 2010, ApJl, 712, L139

Twomey, S., Herman, B., & Rabinoff, R. 1977, JAS, 34, 1085

Wenger, C., & Champion, J. P. 1998, JQSRT, 59, 471

Chapter 6

A Novel Diagnosis of Chemical Disequilibrium in Planetary Atmospheres

6.1 Summary

Chemical disequilibrium has recently become an exciting topic in the study of extrasolar planet atmospheres. We present a new way of assessing whether or not an atmosphere is in thermochemical equilibrium from observations of spectroscopically active gases H_2O, CH_4, CO, and H_2. Our hypothesis is that cooler atmospheres will show stronger signs of disequilibrium then hotter atmospheres. We verify this hypothesis with chemistry-transport models.

6.2 Introduction

Disequilibrium mechanisms play an important role in sculpting the atmospheric composition of planets and cool substellar objects. For instance, Prinn & Barshay (1977) showed that eddy mixing can explain the anomalously high abundance of CO in Jupiter's observable

atmosphere by the dredging up of CO rich gas from the hotter, deeper atmosphere. Photochemistry significantly alters the stratospheric compositions of all planetary atmospheres in our solar system by enhancing or depleting various species. Specifically, methane photolysis is responsible for the production of heavy hydrocarbons in the gas giant atmospheres (Yung & DeMore 1999). Zonal winds can transport photolytically produced species from the dayside to the nightside. It is not unreasonable to assume that these mechanisms play an equally important role in exoplanet atmospheres. In fact there have been some suggestions of disequilibrium in exoplanet atmospheres (Stevenson et al. 2010).

Under this assumption a variety of 1D photochemical-transport models have been used to explore the compositions of hot Jupiters (Liang et al. 2003, 2004; Zahnle 2009a,2009b; Line et al. 2010; Moses et al. 2011; Kopparapu et al. 2012; Venot et al. 2012), hot Neptunes (Line et al. 2011), and super Earths (Miller-Ricci Kempton et al. 2012; Hu et al. 2012) as well as some 3-D chemistry-transport models for hot Jupiters (e.g. Cooper & Showman 2005; Agúndez et al. 2012). The basic conclusion from most of these studies is that in cool atmospheres ($T \leq 1200$ K), as chemical reaction timescales increase, disequilibrium mechanisms become increasingly more important while in hot atmospheres thermochemical equilibrium prevails.

Also from these investigations we have learned that Jovian-like planetary atmospheres can be vertically divided into three basic chemical regimes. In the deep atmosphere where temperatures and pressures are high, chemical reaction timescales are short allowing the composition to achieve thermochemical equilibrium. At lower pressures and temperatures higher up in the atmosphere, chemical reaction timescales slow until the point at which

they are equal to the vertical transport timescale, thus quenching the abundances. Vertical mixing tends to smooth out the vertical mixing ratio profiles. At even higher altitudes in the atmosphere, ultraviolet photons can break apart stable molecules and alter the upper atmospheric composition.

From the aforementioned disequilibrium models we have also learned that vertical transport tends to have the greatest observational consequence for exo-planet atmospheres because the infrared photosphere of most exoplanets (with current instruments) tend to fall within the region of the atmosphere dominated by vertical mixing but not yet strongly affected by photochemistry. From this, it is our working hypothesis that, observationally, we would expect the compositions of cooler atmospheres to deviate strongly from thermochemical equilibrium, and hot atmospheres to be in thermochemical equilibrium. In §6.3 we describe a simple way of looking at planetary compositions in order to assess chemical disequilibrium. In §6.4 we show how our method compares with 1-D chemical transport models.

6.3 Theory

In order to address our hypothesis, we seek a quantity that relates a planets composition to its temperature. Given some measurement of the abundances of various gases, one could try to determine if any one of those gases are in or out of equilibrium. However, looking at individual gases is difficult because their abundances depend on the planetary elemental abundances as well as temperature. Therefore, we seek a relationship that relates composition to temperature in a metallicity and C/O ratio independent way. That quantitiy can be

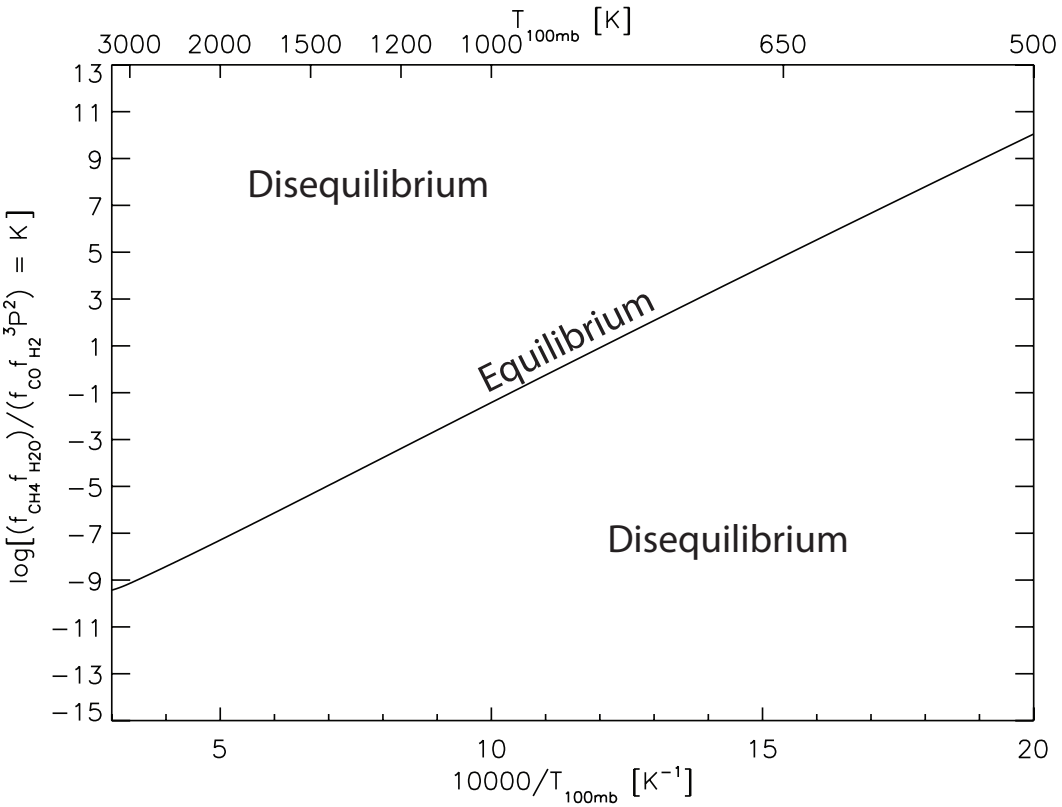

Figure 6.1: Log of the equilibrium constant as a function of temperature ($K_{eq}(T)$). If the ratio of gas mixing ratios in Equation 6.2 is in thermochemical equilibrium, it will fall on this line. If the ratio falls off of the thermochemical equilibrium line, then there must be some disequilibrium process occurring. The line is approximately linear in $1/T$ due to the functional form of the equilibrium constant

derived as follows. In thermochemical equilibrium the net reaction

$$CH_4 + H_2O = CO + 3H_2 \tag{6.1}$$

relates the abundances of CH_4, CO, and H_2O, and H_2. We choose these species because, generally, in Jovian-like atmospheres, these species are the most abundant and readily ob-

servable. From the law of mass action we can write down the relation

$$\frac{f_{CH_4} f_{H_2O}}{f_{CO} f_{H_2}^3 P^2} = K_{eq}(T) \tag{6.2}$$

where f_i is the mixing ratio of species i, P is the pressure at some specified level in the atmosphere (in bars), $K_{eq}(T)$ is the equilibrium constant at temperature T (Yung & DeMore 1999). The equilibrium constant only depends on temperature and the thermodynamic properties of the molecules and generally has the form

$$K_{eq}(T) = e^{-\Delta G/RT} = e^{-(\Delta H/RT - \Delta S/R)} \tag{6.3}$$

where ΔG, ΔH and ΔS are the change in Gibbs free energy, enthalpy and entropy, respectively, of formation of the molecules involved. Generally, ΔH has a dependence on temperature but for our discussion we will ignore this for now. These quantities can be looked up in any thermodynamic table (e.g., Burcat & Ruscic 2011). From this we see that if we can measure the abundances of CH_4, CO, H_2O, and H_2 we can relate them to a quantity that solely depends on temperature and the thermodynamic properties of each molecule. Figure 6.1 shows Equation 6.2 as a function of temperature at some specified pressure. In this case we choose the pressure at 100 mbars. This pressure level is where most secondary eclipse thermal emission weighting functions tend to peak (e.g., Knutson et al. 2009; Line et. al. 2013), and hence temperature and abundance determinations sample this region. If we determine the abundances of the aforementioned gases and find that the ratio on the left hand side of Equation 6.2 has the same value as the equilibrium constant,

K_{eq}, evaluated at the 100 mbar temperature, then we can confidently say that those four gases are in thermochemical equilibrium. This is equivalent to falling on the line in Figure 6.1. If however, the ratio on the left hand side of Equation 6.2 is not equal to the equilibrium constant at that temperature, then we can infer that the four gases are not in thermochemical equilibrium and that there must be some process driving those species away from equilibrium. For instance, as we will show in the next section, for cool atmospheres if vertical mixing is operating, CO will be dredged up from deeper, more CO rich regions thus causing the left-hand side of Equation 6.2 to be less than the equilibrium constant value. In this investigation we again, simply chose to focus on CH_4, CO, and H_2O, and H_2, but in principle, any set of gases can be related to an equilibrium constant.

6.4 Vertical Transport Model Results

We use a 1-D chemical kinetics model (Allen et al. 1981) modified for exoplanets (Line et al. 2011) to explore the consequences of vertical mixing on the relationship established in Equation 6.2 as a function of temperature. We do not focus on photochemistry in this investigation as it has been shown that the observational consequence on these species is minimal (Moses et al. 2011). The model can kinetically achieve thermochemical equilibrium in the deep atmosphere and seamlessly transition across the different chemical regimes (see Moses et al. 2011 for an in depth discussion on this topic). We generate a series of exoplanet temperature-pressure profiles under different levels of irradiation to produce a range of effective temperatures (given as 100 mbar temperature) using the Guillot (2010) analytic temperature relation (Figure 6.2a).

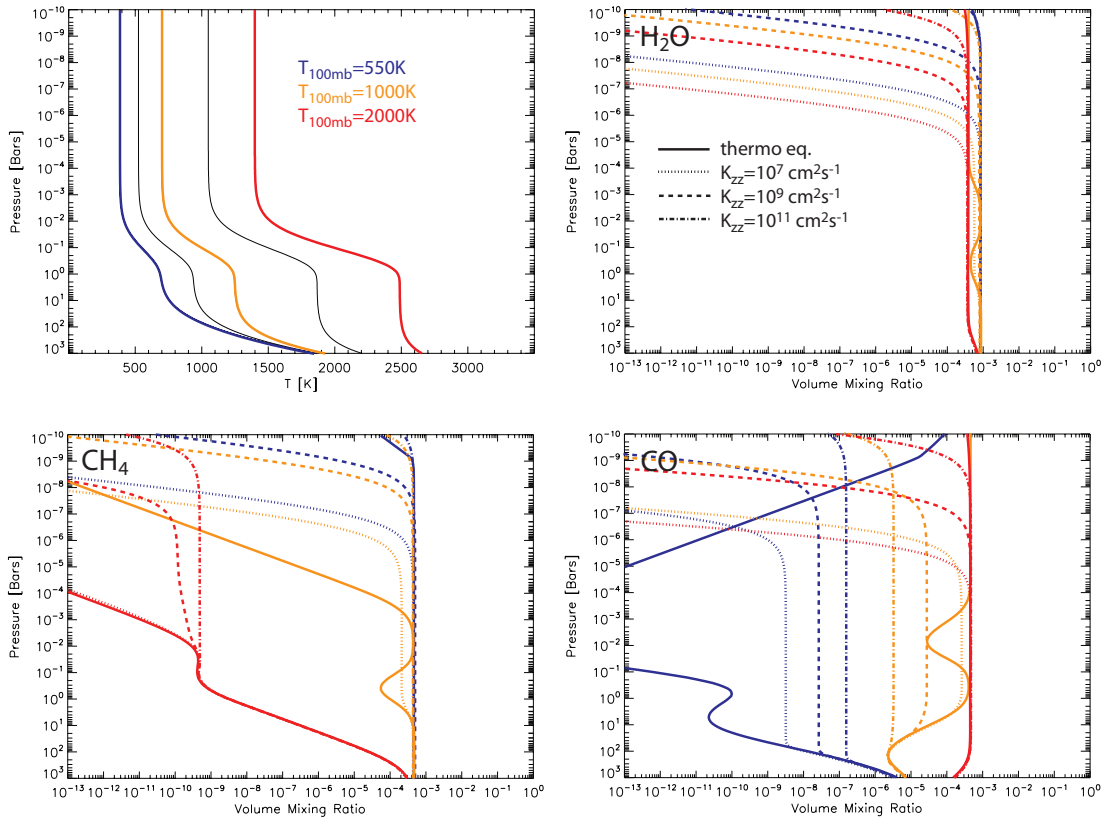

Figure 6.2: Model atmospheres subject to a variety of vertical mixing strengths (K_{zz}). The upper left panel shows 5 different temperature profiles with 100 mbar temperatures of 550, 750, 1000, 1200, 1500, and 2000 K. In the subsequent panels, for each colored temperature profile, the corresponding vertical mixing ratio profiles are shown for H_2O (top right), CH_4 (bottom left) and CO (bottom right) under different vertical mixing strengths. The thermochemical equilibrium derived mixing ratio profiles are solid, while the dotted mixing ratio profiles are derived with an eddy diffusion coefficient of 10^7 cm^2s^{-1}, the dashed with an eddy diffusion coefficient of 10^9 cm^2s^{-1}, and the dot-dashed with an eddy diffusion coefficient of 10^{11} cm^2s^{-1}

For each of the temperature profiles we first compute the thermochemical equilibrium composition under the assumption of solar elemental abundances (solid curves in Figures 6.2b,c, and d). For this we use the NASA Chemical Equilibrium with Applications model (Gordon & McBride 1996). Next we compute the disequilibrium compositions under the assumptions of different vertical mixing strengths. The vertical mixing strength is parameterized via eddy diffusion (K_{zz}). The strength of eddy diffusion in exoplanet atmospheres is not well known but can be estimated with a mixing length theory (e.g., Line et al. 2010, Moses et al. 2011, Line et al. 2011) using vertical wind profiles derived from General Circulation Models (Showman et al. 2009). This generally gives an order-of-magnitude estimate for the eddy mixing strengths. For reference, the eddy diffusion strength in Jupiter is thought to span 10^7-10^9 cm^{2}s^{-1} (Prinn & Barshay 1977) in order to explain the anomalous stratospheric CO abundance. A similar investigation by Griffith & Yelle (1999) estimate brown dwarf eddy diffusion strengths to be on the order of 10^6 cm^{2}s^{-1}. For simplicity, we assume constant-with-altitude eddy mixing profiles that span a reasonable range of plausible values from 10^7-10^{11} cm^{2}s^{-1} (dashed and dotted curves in Figures 6.2b,c, and d).

The gas vertical mixing ratio profiles all share some general features under vertical mixing. Deep in the atmosphere, where temperatures are high and reaction timescales are short, the profiles converge towards thermochemical equilibrium. As temperatures cool, vertical mixing dominates smoothing out the profiles to a constant-with-altitude vertical structure. At the highest region of the atmosphere molecular diffusion dominates and causes a rapid fall-off in the mixing ratios.

For water (Figure 6.2b) we find that there is little effect on the vertical composition due

to vertical mixing or temperature. Therefore water is not a good tracer for chemical disequilibrium, at least in the hot-Jovian-like atmosphere regime. Methane (Figure 6.2c) however, is more strongly effected by vertical mixing. At cool temperatures (blue) the vertical profile of methane is unaffected by disequilibrium due to its overwhelmingly large abundance, but is more strongly effected at higher temperatures because it becomes a trace species. At low eddy diffusion strength, however, the chemical equilibrium timescales overcome the eddy mixing strength to achieve thermochemical equilibrium. If we were to go to even higher temperatures, say, 2500 K, methane would maintain equilibrium throughout. CO is most effected by vertical mixing. At cool temperatures (blue) it is clear that vertical mixing can result in orders-of-magnitude changes in the CO abundances in the infrared photosphere. In the deep atmosphere, CO achieves thermochemical equilibrium, but readily moves towards disequilibrium near 100 bars. An increase in the eddy diffusion strength at these cool temperatures results in an increase in the disequilibrium CO abundance in the infrared photosphere due to the shape of the thermochemical profile in the deep atmosphere. At warm temperatures (orange) the reverse occurs. The shape of the thermochemical profile of CO changes, resulting in a decrease in the CO abundance with increasing mixing strength. And finally, at hot temperatures (red), there is virtually no effect of from vertical mixing in the IR photosphere region.

If for each of the models shown in Figure 6.2 we evaluate the left hand side of Equation 6.2 using the 100 mbar mixing ratios as a function of 100 mbar temperature we can place a point on Figure 6.1. These results are shown in Figure 6.3. We find that indeed, for the hottest planets, ($T_{100mb} >\sim$1200 K), that CH_4, CO, H_2O, and H_2 are in thermochemical

equilibrium (they fall on the thermochemical equilibrium line) even under a wide range of vertical mixing strengths. At the coolest temperatures, models subject to vertical mixing, begin to fall below the thermochemical equilibrium line due to the vertical transport of CO rich gas.

Since the vertical structure of H_2O and H_2 are generally independent of temperature we can better understand the ratio in Equation 6.2, and where points will fall in Figure 6.3 by looking at the ratio of CH_4/CO which is given as

$$\frac{f_{CH_4}}{f_{CO}} \propto P^2 K_{eq}(T(P)) = P^2 e^{-(\Delta H/RT(P) - \Delta S/R)} \approx P^2 e^{27086/T(P) - 30}. \tag{6.4}$$

From this we see that the detailed vertical structure of these two species will strongly depend on the functional form of $T(P)$. A high CH_4 abundance will be favored at high pressures and low temperatures. Low temperatures at high pressures are favored in overall cooler temperature structures. Conversely, CO will be favored at low pressures and high temperatures which occur in overall hotter temperature structures. In isothermal regions of the atmosphere, decreasing pressures will favor an increasing CO abundance.

Figure 6.3 shows some ambiguity at temperatures between $\sim$700 and $\sim$1100 K. Because of the structure of the temperature profile and how that plays into Equation 6.4 we find that near $\sim$750 K the CO thermochemical profile (not shown) is such that the mixing ratios near the quench level happen to be nearly identical to the mixing ratios at 100 mbars. So while though there is disequilibrium occurring, there is also a degeneracy in the thermochemical mixing ratio profile which is why in Figure 6.3, most of the points at 750 K seem to fall on the, or very nearly on, the thermochemical equilibrium line. The temperature

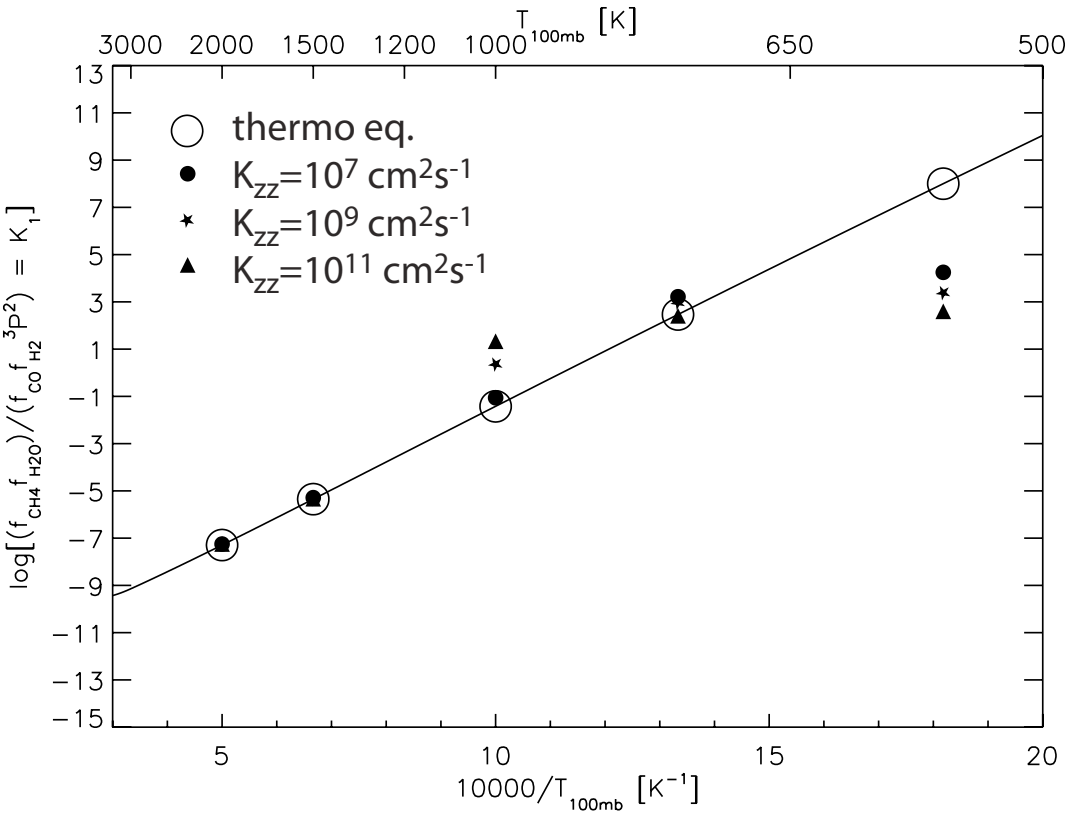

Figure 6.3: Log of the equilibrium constant as a function of temperature ($K_{eq}(T)$) compared with vertical transport models. Each point represents an evaluation of both sides of Equation 6.2 at the 100 mbar level from the models in Figure 6.2. The open circles represent these values for atmospheres in thermochemical equilibrium. The solid circles represent the atmospheres under an eddy diffusion coefficient of 10^7 cm^{2}s^{-1}, the star, an eddy diffusion coefficient of 10^9 cm^{2}s^{-1}, and the triangle with an eddy diffusion coefficient of 10^{11} cm^{2}s^{-1}. At hot temperatures all four points fall on top of each other, suggesting that the atmosphere is in thermochemical equilibrium at the 100 mbar pressure level.

structure in the 1000 K profile interactions with Equation 6.4 in such a way that near the CO quench level the slope of the CO mixing ratio profile (Figure 6.2,d) is positive. This is because the temperature at the CO quench levels is isothermal resulting in a $1/P^2$ dependence in the CO mixing ratio. This behavior does not occur in the less irradiated cooler profiles because the quench levels occur deeper in the region of the atmosphere where the temperature is always decreasing with altitude (faster than the $1/P^2$ dependence) resulting in a decreasing CO mixing ratio with altitude.

6.5 Discussion & Conclusions

We have developed a simple way of determining if a planetary atmosphere is subject to disequilibrium mechanisms (Figure 6.1). We have chosen CO, CH_4, H_2O, and H_2 as our tracer species as they are the most abundant radiatively active gases in a variety of observationally accessible planetary atmosphere environments. If we measure the abundances of CO, CH_4, H_2O, and H_2 we can assess whether or not these species in a planetary atmosphere are subject to some form of disequilibrium. If we observe that the ratio of these four species in Equation 6.2 is not equal to the equilibrium constant at the observed temperature, and hence does not fall on the equilibrium line in (Figure 6.1), then we can safely conclude that there is a process driving them out of equilibrium. If however, the observed ratio is consistent with equilibrium, we may conclude that either the atmosphere is indeed in equilibrium, or that the disequilibrium process interacts with the temperature-pressure profile in such a way as to make it appear as if the planetary atmosphere were in equilibrium. We also point to another caveat. In Jovian-type planets we cannot directly measure the H_2 mixing ratio at

this time. If the value of H_2 is assumed and we find that the observed planetary atmosphere falls off of the thermochemical equilibrium line, we might conclude either disequilibrium, or that our assumption of the H_2 mixing ratio is incorrect.

We also note that in this investigation we used vertical mixing as our example disequilibrium mechanism. There are other process such as photochemistry, biology, cloud formation, etc. For instance, in some extreme cases, photochemistry may drive the carbon out of CH_4 and into HCN. If the photochemistry is vigorous enough to deplete methane over the IR photosphere (unlikely), we might expect to find the planet to fall below the thermochemical equilibrium line. If we were to observe planets as cool as the Jovian's in our solar system, we would find that they fall way below the thermochemical equilibrium line because of the depletion of water due to condensation. So while we can determine if there is some disequilibrium process occurring, it may be difficult to disentangle what that process is, but simply identifying disequilibrium would be exciting enough to warrant future observations of that planet.

6.6 Acknowledgements

We thank Dave Stevenson, Pin Chen and Channon Visscher for useful discussions as well as the Yuk Yung group.

Bibliography

Allen, M., Yung, Y. L., & Waters, J. W. 1981, JGR, 86, 3617

Agúndez, M., Venot, O., Iro, N., et al. 2012, A&A, 548, A73

Burcat, A. & Ruscic, B., New NASA Thermodynamic Polynomials Database With Active Thermochemical Tables updates. Report ANL 05/20 TAE 960. Gordon, S., McBride, B.J., & NASA Tech. Info. Program, 1996, Computer program for calculation of complex chemical equilibrium compositions and applications, National Aeronautics and Space Administration, Office of Management, Scientific and Technical Information Program

Griffith, C. A., & Yelle, R. V. 1999, ApJL, 519, L85

Guillot, T. 2010, A&A, 520, A27

Knutson, H. A., et al. 2009, ApJ, 690, 822

Kopparapu, R. k., Kasting, J. F., & Zahnle, K. J. 2012, ApJ, 745, 77

Liang, M.-C., Parkinson, C. D., Lee, A. Y.-T., Yung, Y. L., & Seager, S. 2003, ApJL, 596, L247

Liang, M.-C., Seager, S., Parkinson, C. D., Lee, A. Y.-T., & Yung, Y. L. 2004, ApJL, 605, L61

Line, M. R., Liang, M. C., & Yung, Y. L. 2010, ApJ, 717, 496

Line, M. R., Vasisht, G., Chen, P., Angerhausen, D., & Yung, Y. L. 2011, ApJ, 738, 32

Line, M. R., Wolf, A., Zhang, X., et al. 2013, arXiv:1304.5561 Moses, J. I., Visscher, C., Fortney, J. J., et al. 2011, ApJ, 737, 15

Prinn, R. G., & Barshay, S. S. 1977, Science, 198, 1031

Showman, A. P., Fortney, J. J., Lian, Y., Marley, M. S., Freedman, R. S., Knutson, H. A., & Charbonneau, D. 2009, ApJ, 699, 564

Stevenson, K. B., et al. 2010, Nature, 464, 1161

Venot, O., Hébrard, E., Agúndez, M., et al. 2012, A&A, 546, A43

Yung, Y. L., & Demore, W. B. 1999, Photochemistry of planetary atmospheres New York : Oxford University Press. QB603.A85 Y86 1999

Zahnle, K., Marley, M. S., & Fortney, J. J. 2009, arXiv:0911.0728

Zahnle, K., Marley, M. S., Freedman, R. S., Lodders, K., & Fortney, J. J. 2009, ApJL, 701, L20

Appendix A

Reversing Kinetic Rate Coefficients

When modeling the chemical kinetics of a planetary atmosphere it is important that each and every reaction has a complimentary reverse reaction so that thermochemical equilibrium is allowable. These "reverse" reactions may either be taken from the literature or computed from the "forward" reaction rate. We choose to do the latter to ensure that thermochemical equilibrium is achieved in the absence of disequilibrium mechanisms. The approach is described as follows.

For a reaction of the form

$$aA + bB \rightarrow cC + dD \tag{A.1}$$

we can define a forward, k_f, and a reverse, k_r, rate coefficient. The forward reaction rate proceeding from left to right (in units of s^{-}1) is given by

$$r_f = k_f[A]^a[B]^b \tag{A.2}$$

while the reverse reaction proceeding from right to left is

$$r_r = k_r[C]^c[D]^d \tag{A.3}$$

where $[i]$ is the concentration of species i in units of number/Volume (typically cm^{-3}). In thermochemical equilibrium the forward rate is equal to the backwards rate so that

$$k_f[A]^a[B]^b = k_r[C]^c[D]^d \tag{A.4}$$

which can be re-arranged to yield

$$\frac{k_f}{k_r} = \frac{[C]^c[D]^d}{[A]^a[B]^b} = K_{eq,c} \tag{A.5}$$

where $K_{eq,c}$ is the concentration equilibrium constant. We really do not know what the value for $K_{eq,c}$ actually is, however, chemists like to measure the pressure equilibrium constant $K_{eq,p}$. This constant can be related to the partial pressures of the species, P_i, in reaction A.1 through

$$K_{eq,P} = \frac{P^c P^d}{P^a P^b} = e^{-\Delta G^\circ/RT} \tag{A.6}$$

where ΔG^{circ} is the standard Gibbs free energy (J mole^{-1}) from reaction A.1 at standard pressure (1 atm), and R is the ideal gas constant, 8.314 J k^{-1} mole^{-1}. The derivation of this expression, known as the "law of mass action" can be found in "Schroders Thermal Physics" (pp. 210-212) and "Castellans Physical Chemistry, Third Edition" (pp. 227-234), and many others.

Since we have a functional expression for $K_{eq,P}$ related to thermodynamic variables measured in a lab (Gibbs free energy), we want to relate it to what we actually want, $K_{eq,c}$. If we substitute the pressure with concentration in Equation A.6 using the ideal gas law, $P_i = [i]k_BT$, where k_B is Boltzman's constant and T is temperature we obtain

$$e^{-\Delta G^\circ/RT} = K_{eq,P} = \frac{P^c P^d}{P^a P^b} = \frac{[C]^c[D]^d}{[A]^a[B]^b}\left(\frac{k_BT}{10^6}\right)^{c+d-a-b} \tag{A.7}$$

The factor of 10^6 in the denominator is from converting the pressures which are measured in $bars$ in the laboratory and is what $K_{eq,P}$ is based on, to cgs units, that is 1 bar = 10^6 dynes cm^{-2} . With Equation A.7 we can then relate $K_{eq,P}$ to $K_{eq,c}$ to give

$$K_{eq,P} = e^{-\Delta G^\circ/RT} = K_{eq,c}\left(\frac{k_BT}{10^6}\right)^{c+d-a-b} \tag{A.8}$$

or

$$K_{eq,c} = e^{-\Delta G^\circ/RT}\left(\frac{k_BT}{10^6}\right)^{a+b-c-d} \tag{A.9}$$

Combining Equation A.5 with Equation A.9 gives the reverse reaction rate

$$k_r = k_f e^{-\Delta G^\circ/RT}\left(\frac{k_BT}{10^6}\right)^{\Delta\nu} \tag{A.10}$$

where we have defined $\Delta\nu = c + d - c - d$. This is the total number of products minus the total number of reactants. For the two body case this is 0 ($c + d - a - b = 0$), for the three body case this is -1, etc. Note that all units are in cgs! The change in Gibbs free energy at

standard pressure is determined by

$$\Delta G^{\circ} = \Delta G^{\circ}_{products} - \Delta G^{\circ}_{reactants} \tag{A.11}$$

where

$$\Delta G^{\circ}_{products} = \sum_{i=1}^{N_{prod}} \nu_i (\Delta H^{\circ}_i - T\Delta S^{\circ}_i) \tag{A.12}$$

and

$$\Delta G^{\circ}_{reactants} = \sum_{i=1}^{N_{reactants}} \nu_i (\Delta H^{\circ}_i - T\Delta S^{\circ}_i) \tag{A.13}$$

where ν_i is the stoichiometric coefficient (e.g., the values of a, b, c, d), ΔH°_i and ΔS°_i are respectively, the standard (1 bar) enthalpy and entropy of formation for species i. These thermodynamic parameters come from the NASA thermobuild website [1] . We generally reverse the rate coefficient one temperature at a time. We then empirically fit this reversed rate vs. temperature curve with the Arrhenius equation ($k = AT^n exp(-E_a/T)$) to obtain the functional form for the reversed rate coefficient.

[1] http://www.grc.nasa.gov/WWW/CEAWeb/ceaThermoBuild.htm

Bibliography

Kittel, C. & Kroemer, H., 1980, Thermal Physics, Freeman & Company

Shroeder, D.V., 2000, An Introduction to Thermal Physics, Addison Wesley

Appendix B

Kinetics Reaction Database

Here I present the chemical kinetics reaction database used in Chapter 3.

Table B.1: Photolysis Reactions for the $1\times$ solar abundance case with only H, C, O, and N species–no S. Photolysis rates given in s^{-1} at 1 μbar and at the top of the model atmosphere at 6×10^{-11}bar (TOA). UV absorption cross sections are from Moses et al. (2005) and references therein. The H_2S photolysis rates are given for the $1\times$ solar abundance case with the addition of SH and H_2S.

Reaction Index	Reaction	Photolysis Rate 1 μbar	Photolysis Rate TOA
R1	$H_2 + h\nu \rightarrow 2H$	0	1.605×10^{-08}
R2	$^3CH_2 + h\nu \rightarrow CH + H$	1.972×10^{-05}	2.415×10^{-05}
R3	$CH_3 + h\nu \rightarrow CH + H_2$	6.642×10^{-07}	5.202×10^{-06}
R4	$CH_3 + h\nu \rightarrow {}^1CH_2 + H$	6.020×10^{-07}	1.106×10^{-06}
R5	$CH_4 + h\nu \rightarrow CH_3 + H$	8.619×10^{-04}	1.535×10^{-03}
R6	$CH_4 + h\nu \rightarrow {}^1CH_2 + H_2$	1.013×10^{-03}	1.804×10^{-03}
R7	$CH_4 + h\nu \rightarrow {}^1CH_2 + 2H$	2.155×10^{-04}	3.839×10^{-04}
R8	$CH_4 + h\nu \rightarrow {}^3CH_2 + 2H$	9.697×10^{-04}	1.727×10^{-03}
R9	$CH_4 + h\nu \rightarrow CH + H$	1.724×10^{-04}	3.072×10^{-04}
R10	$C_2H_2 + h\nu \rightarrow C_2H + H$	6.808×10^{-04}	1.214×10^{-03}
R11	$C_2H_2 + h\nu \rightarrow C_2 + H_2$	2.272×10^{-04}	4.059×10^{-04}
R12	$C_2H_3 + h\nu \rightarrow C_2H_2 + H$	1.588×10^{-05}	1.588×10^{-05}

Reaction Index	Reaction	Photolysis Rate 1 μbar	Photolysis Rate TOA
R13	$C_2H_4 + h\nu \rightarrow C_2H_2 + H_2$	7.510×10^{-04}	1.330×10^{-03}
R14	$C_2H_4 + h\nu \rightarrow C_2H_2 + 2H$	1.906×10^{-03}	3.387×10^{-03}
R15	$C_2H_4 + h\nu \rightarrow C_2H_3 + H$	2.237×10^{-06}	2.959×10^{-06}
R16	$C_2H_5 + h\nu \rightarrow CH_3 + {}^1CH_2$	7.286×10^{-07}	7.286×10^{-07}
R17	$C_2H_6 + h\nu \rightarrow C_2H_4 + H_2$	1.248×10^{-04}	2.224×10^{-04}
R18	$C_2H_6 + h\nu \rightarrow C_2H_4 + 2H$	7.485×10^{-04}	1.334×10^{-03}
R19	$C_2H_6 + h\nu \rightarrow C_2H_2 + 2H_2$	8.734×10^{-04}	1.556×10^{-03}
R20	$C_2H_6 + h\nu \rightarrow CH_4 + {}^1CH_2$	5.988×10^{-04}	1.067×10^{-03}
R21	$C_2H_6 + h\nu \rightarrow 2CH_3$	1.497×10^{-04}	2.667×10^{-04}
R22	$O_2 + h\nu \rightarrow O + O$	7.419×10^{-07}	1.646×10^{-06}
R23	$O_2 + h\nu \rightarrow O + O({}^1D)$	7.278×10^{-06}	1.517×10^{-05}
R24	$OH + h\nu \rightarrow O + H$	1.515×10^{-03}	2.697×10^{-03}
R25	$H_2O + h\nu \rightarrow H + OH$	1.413×10^{-03}	2.514×10^{-03}
R26	$H_2O + h\nu \rightarrow 2H + O$	2.164×10^{-04}	3.855×10^{-04}
R27	$H_2O + h\nu \rightarrow H_2 + O({}^1D)$	1.803×10^{-04}	3.212×10^{-04}
R28	$CO + h\nu \rightarrow C + O$	1.122×10^{-09}	1.102×10^{-07}
R29	$CO_2 + h\nu \rightarrow CO + O$	2.702×10^{-10}	3.103×10^{-10}
R30	$CO_2 + h\nu \rightarrow CO + O({}^1D)$	7.396×10^{-06}	1.340×10^{-05}
R31	$HCO + h\nu \rightarrow H + CO$	1.347×10^{-04}	1.347×10^{-04}
R32	$H_2CO + h\nu \rightarrow HCO + H$	9.233×10^{-07}	9.233×10^{-07}
R33	$H_2CO + h\nu \rightarrow H_2 + CO$	1.250×10^{-03}	2.226×10^{-03}
R34	$H_2CO + h\nu \rightarrow 2H + CO$	1.248×10^{-03}	2.224×10^{-03}
R35	$CH_3OH + h\nu \rightarrow CH_3 + OH$	7.909×10^{-05}	1.409×10^{-04}
R36	$CH_3OH + h\nu \rightarrow H_2CO + H_2$	3.164×10^{-04}	5.637×10^{-04}
R37	$CH_3OH + h\nu \rightarrow CH_3O + H$	1.186×10^{-03}	2.113×10^{-03}
R38	$HCCO + h\nu \rightarrow CO + CH$	6.932×10^{-05}	6.932×10^{-05}
R39	$H_2CCO + h\nu \rightarrow {}^1CH_2 + CO$	6.932×10^{-05}	6.932×10^{-05}
R40	$CH_3CHO + h\nu \rightarrow CH_4 + CO$	9.243×10^{-09}	9.243×10^{-09}
R41	$CH_3CHO + h\nu \rightarrow CH_3 + HCO$	2.888×10^{-07}	2.888×10^{-07}
R42	$N_2 + h\nu \rightarrow N + N$	1.623×10^{-08}	6.017×10^{-07}
R43	$NH_3 + h\nu \rightarrow NH_2 + H$	2.895×10^{-06}	4.360×10^{-06}

Reaction Index	Reaction	Photolysis Rate 1 μbar	Photolysis Rate TOA
R44	$NH_3 + h\nu \rightarrow NH + H_2$	4.537×10^{-05}	8.089×10^{-05}
R45	$NH_3 + h\nu \rightarrow NH + 2H$	8.619×10^{-04}	1.535×10^{-03}
R46	$CN + h\nu \rightarrow C + N$	2.302×10^{-04}	4.108×10^{-04}
R47	$HCN + h\nu \rightarrow H + CN$	5.807×10^{-03}	1.035×10^{-02}
R48	$NO + h\nu \rightarrow N + O$	1.162×10^{-07}	1.176×10^{-07}
R49	$N_2H_4 + h\nu \rightarrow N_2H_3 + H$	1.716×10^{-03}	3.053×10^{-03}
R50	$CH_3NH_2 + h\nu \rightarrow HCN + H_2$	1.931×10^{-03}	3.439×10^{-03}
R51	$CH_3NH_2 + h\nu \rightarrow HCN + 2H_2$	7.954×10^{-05}	1.417×10^{-04}
R52	$CH_3NH_2 + h\nu \rightarrow CH_4 + NH$	9.078×10^{-05}	1.617×10^{-04}
R53	$CH_3NH_2 + h\nu \rightarrow {}^1CH_2 + NH_3$	9.078×10^{-05}	1.617×10^{-04}
R54	$CH_3NH_2 + h\nu \rightarrow CH_3 + NH_2$	8.401×10^{-04}	1.496×10^{-03}
R55	$CH_3NH_2 + h\nu \rightarrow CN + 2H_2$	5.111×10^{-04}	9.103×10^{-04}
R704	$H_2S + h\nu \rightarrow HS + H$	7.961×10^{-04}	1.417×10^{-03}

Table B.2: Two and three body reactions. The 2-body reactions are of the form A+B $\rightarrow$ C+D and their rate constants are in units of cm^3s^{-1}. The 3-body reactions are of the form A+B+M$\rightarrow$AB+M where M stands for a third body, in this case, H_2. There are two rate constants for the 3-body reactions. The first rate constant given is the low pressure limit (k_0) with units of cm^6s^{-1}. The second rate constant is the high-pressure limit (k_∞) and has units of cm^3s^{-1}. The total three body rate constant is given by $k = \frac{k_0 k_\infty}{k_0[M]+k_\infty}$ with units of cm^6s^{-1}. The thermal decomposition reactions AB + M$\rightarrow$A+B+M (often times the reverse of a 3-body reaction) have low pressure rate constant units of cm^3s^{-1} and high pressure rate constant units of s^{-1}. Reactions for which there are no references are the reverse of the reactions immediately above calculated via the method described in the text, unless otherwise specified. Most rate coefficients and their references are obtained via the

NIST Chemical Kinetics Database. A majority of the nitrogen reactions can be found in Gardiner's book, Gas Phase Combustion Chemistry.

Reaction Index	Reaction	Photolysis Rate 1 μbar	Photolysis Rate TOA
R56	$OH + CH_4 \rightarrow H_2O + CH_3$	$1.68 \times 10^{-18} T^{2.2} e^{-1227/T}$	Srinivasan et al. 2005
R57	$H_2O + CH_3 \rightarrow OH + CH_4$	$2.12 \times 10^{-21} T^{2.8} e^{-7619/T}$	
R58	$H + CH \rightarrow C + H_2$	$1.31 \times 10^{-10} e^{-80.00/T}$	Harding et al. 1993
R59	$C + H_2 \rightarrow H + CH$	$4.05 \times 10^{-11} T^{0.30} e^{-11763/T}$	
R60	$H + CH_4 \rightarrow CH_3 + H_2$	$2.20 \times 10^{-20} T^{3.0} e^{-4041/T}$	Baulch et al. 1992
R61	$CH_3 + H_2 \rightarrow H + CH_4$	$2.05 \times 10^{-24} T^{3.7} e^{-2903/T}$	
R62	$C_2H_2 + H \rightarrow H_2 + C_2H$	$1.00 \times 10^{-10} e^{-11197/T}$	Tsang & Hampson 1986
R63	$H_2 + C_2H \rightarrow C_2H_2 + H$	$7.10 \times 10^{-14} T^{0.50} e^{3538/T}$	
R64	$C_2H_3 + H \rightarrow C_2H_2 + H_2$	2.01×10^{-11}	Baulch et al. 1992
R65	$C_2H_2 + H_2 \rightarrow C_2H_3 + H$	$1.51 \times 10^{-11} T^{0.19} e^{-34328/T}$	
R66	$C_2H_5 + H \rightarrow CH_3 + CH_3$	5.99×10^{-11}	Baulch et al. 1992
R67	$CH_3 + CH_3 \rightarrow C_2H_5 + H$	$5.39 \times 10^{-16} T^{1.1} e^{-4576/T}$	
R68	$H + C_2H_5 \rightarrow C_2H_4 + H_2$	3.01×10^{-12}	Tsang & Hampson 1986
R69	$C_2H_4 + H_2 \rightarrow H + C_2H_5$	$1.64 \times 10^{-13} T^{0.57} e^{-33783/T}$	
R70	$H + C_2H_6 \rightarrow H_2 + C_2H_5$	$2.39 \times 10^{-15} T^{1.5} e^{-3728/T}$	Baulch et al. 1992
R71	$H_2 + C_2H_5 \rightarrow H + C_2H_6$	$3.01 \times 10^{-19} T^{2.1} e^{-5118/T}$	
R72	$CH + H_2 \rightarrow {}^3CH_2 + H$	$6.24 \times 10^{-16} T^{1.7} e^{-840.0/T}$	Zabarnick et al. 1986
R73	${}^3CH_2 + H \rightarrow CH + H_2$	$1.30 \times 10^{-14} T^{1.4} e^{286.2/T}$	
R74	$CH_3 + C_2H_3 \rightarrow CH_4 + C_2H_2$	6.51×10^{-13}	Tsang & Hampson 1986
R75	$CH_4 + C_2H_2 \rightarrow CH_3 + C_2H_3$	$1.18 \times 10^{-07} T^{-0.93} e^{-35975/T}$	
R76	$C_2H_5 + CH_3 \rightarrow CH_4 + C_2H_4$	$3.25 \times 10^{-11} T^{-0.50}$	Tsang & Hampson 1986
R77	$CH_4 + C_2H_4 \rightarrow C_2H_5 + CH_3$	$4.47 \times 10^{-07} T^{-1.0} e^{-35432/T}$	
R78	$C_2H + H \rightarrow H_2 + C_2$	$5.99 \times 10^{-11} e^{-14192/T}$	Tsang & Hampson 1986
R79	$H_2 + C_2 \rightarrow C_2H + H$	$7.23 \times 10^{-14} T^{0.84} e^{-7971/T}$	
R80	$CH_4 + C_2H \rightarrow C_2H_2 + CH_3$	$3.01 \times 10^{-12} e^{-250.0/T}$	Tsang & Hampson 1986
R81	$C_2H_2 + CH_3 \rightarrow CH_4 + C_2H$	$3.54 \times 10^{-13} T^{0.26} e^{-13827/T}$	
R82	$C_2H_6 + C_2H \rightarrow C_2H_2 + C_2H_5$	5.99×10^{-12}	Tsang & Hampson 1986
R83	$C_2H_2 + C_2H_5 \rightarrow C_2H_6 + C_2H$	$1.21 \times 10^{-12} T^{0.093} e^{-16140/T}$	

Reaction Index	Reaction	Rate Expression	Reference
R84	$C_2H_3 + H_2 \rightarrow C_2H_4 + H$	$5.00 \times 10^{-20} T^{2.6} e^{-4300/T}$	Tsang & Hampson 1986
R85	$C_2H_4 + H \rightarrow C_2H_3 + H_2$	$4.91 \times 10^{-16} T^{1.9} e^{-8355/T}$	
R86	$C_2H_3 + C_2H_3 \rightarrow C_2H_4 + C_2H_2$	1.60×10^{-12}	Tsang & Hampson 1986
R87	$C_2H_4 + C_2H_2 \rightarrow C_2H_3 + C_2H_3$	$4.71 \times 10^{-08} T^{-0.66} e^{-38618/T}$	
R88	$C_2H_4 + C_2H_4 \rightarrow C_2H_5 + C_2H_3$	$8.00 \times 10^{-10} e^{-35961/T}$	Tsang & Hampson 1986
R89	$C_2H_5 + C_2H_3 \rightarrow C_2H_4 + C_2H_4$	$4.67 \times 10^{-13} T^{0.25} e^{2075/T}$	
R90	$C_2H_3 + C_2H_5 \rightarrow C_2H_6 + C_2H_2$	8.00×10^{-13}	Tsang & Hampson 1986
R91	$C_2H_6 + C_2H_2 \rightarrow C_2H_3 + C_2H_5$	$1.88 \times 10^{-08} T^{-0.58} e^{-33162/T}$	
R92	$C_2H_5 + C_2H_5 \rightarrow C_2H_6 + C_2H_4$	2.31×10^{-12}	Tsang & Hampson 1986
R93	$C_2H_6 + C_2H_4 \rightarrow C_2H_5 + C_2H_5$	$4.41 \times 10^{-09} T^{-0.22} e^{-32633/T}$	
R94	$O + H_2 \rightarrow OH + H$	$8.51 \times 10^{-20} T^{2.6} e^{-3159/T}$	Baulch et al. 1992
R95	$OH + H \rightarrow O + H_2$	$5.93 \times 10^{-20} T^{2.6} e^{-2473/T}$	
R96	$O + CH \rightarrow CO + H$	6.59×10^{-11}	Baulch et al. 1992
R97	$CO + H \rightarrow O + CH$	$1.60 \times 10^{-10} T^{0.34} e^{-88294/T}$	
R98	$O + CH_3 \rightarrow H_2CO + H$	1.40×10^{-10}	Baulch et al. 1992
R99	$H_2CO + H \rightarrow O + CH_3$	$2.30 \times 10^{-08} T^{-0.30} e^{-34737/T}$	
R100	$O + CH_4 \rightarrow OH + CH_3$	$1.70 \times 10^{-15} T^{1.5} e^{-4329/T}$	Tsang & Hampson 1986
R101	$OH + CH_3 \rightarrow O + CH_4$	$1.16 \times 10^{-19} T^{2.1} e^{-2511/T}$	
R102	$O + C_2H \rightarrow CO + CH$	1.69×10^{-11}	Tsang & Hampson 1986
R103	$CO + CH \rightarrow O + C_2H$	$7.02 \times 10^{-15} T^{1.0} e^{-39170/T}$	
R104	$O + C_2H_2 \rightarrow CO + {}^3CH_2$	$6.78 \times 10^{-16} T^{1.5} e^{-850.3/T}$	Cvetanovic 1987
R105	$CO + {}^3CH_2 \rightarrow O + C_2H_2$	$2.62 \times 10^{-21} T^{2.7} e^{-24088/T}$	
R106	$C_2H_2 + O \rightarrow H + HCCO$	$1.50 \times 10^{-11} e^{-2280/T}$	Tsang & Hampson 1986
R107	$H + HCCO \rightarrow C_2H_2 + O$	$4.98 \times 10^{-11} T^{-0.20} e^{-12183/T}$	
R108	$O + C_2H_3 \rightarrow H_2CCO + H$	1.60×10^{-10}	Tsang & Hampson 1986
R109	$H_2CCO + H \rightarrow O + C_2H_3$	$8.72 \times 10^{-08} T^{-0.51} e^{-45619/T}$	
R110	$O + C_2H_3 \rightarrow C_2H_2 + OH$	$1.76 \times 10^{-12} T^{0.20} e^{215.2/T}$	Harding et al. 2005
R111	$C_2H_2 + OH \rightarrow O + C_2H_3$	$9.22 \times 10^{-13} T^{0.34} e^{-33433/T}$	
R112	$O + C_2H_3 \rightarrow HCO + {}^3CH_2$	2.00×10^{-11}	Baulch et al. 1992
R113	$HCO + {}^3CH_2 \rightarrow O + C_2H_3$	$4.08 \times 10^{-15} T^{0.74} e^{-13500/T}$	
R114	$O + C_2H_4 \rightarrow CH_3CO + H$	$7.90 \times 10^{-18} T^{1.8} e^{-91/T}$	Baulch et al. 1994

Reaction Index	Reaction	Rate Expression	Reference
R115	$CH_3CO + H \rightarrow O + C_2H_4$	$4.08 \times 10^{-16} T^{1.1} e^{-11425/T}$	
R116	$O + C_2H_4 \rightarrow HCO + CH_3$	$2.19 \times 10^{-16} T^{1.5} e^{-215.2/T}$	Tsang & Hampson 1986
R117	$HCO + CH_3 \rightarrow O + C_2H_4$	$1.46 \times 10^{-21} T^{2.5} e^{-13117/T}$	
R118	$O + C_2H_4 \rightarrow H_2CO + {}^3CH_2$	$1.35 \times 10^{-17} T^{1.8} e^{-90.00/T}$	Baulch et al. 1994
R119	$H_2CO + {}^3CH_2 \rightarrow O + C_2H_4$	$3.93 \times 10^{-22} T^{2.7} e^{-1985/T}$	
R120	$O + C_2H_4 \rightarrow H_2CCO + H_2$	$1.13 \times 10^{-18} T^{1.8} e^{-91./T}$	Baulch et al. 1992
R121	$H_2CCO + H_2 \rightarrow O + C_2H_4$	$1.28 \times 10^{-20} T^{2.2} e^{-41382/T}$	
R122	$C_2H_5 + O \rightarrow CH_3CHO + H$	1.33×10^{-10}	Tsang & Hampson 1986
R123	$CH_3CHO + H \rightarrow C_2H_5 + O$	$5.73 \times 10^{-08} T^{-0.40} e^{-38021/T}$	
R124	$O + C_2H_5 \rightarrow H_2CO + CH_3$	2.67×10^{-11}	Tsang & Hampson 1986
R125	$H_2CO + CH_3 \rightarrow O + C_2H_5$	$9.52 \times 10^{-15} T^{1.0} e^{-39062/T}$	
R126	$O + C_2H_6 \rightarrow OH + C_2H_5$	$1.99 \times 10^{-12} T^{0.60} e^{-3680/T}$	Tsang & Hampson 1986
R127	$OH + C_2H_5 \rightarrow O + C_2H_6$	$1.62 \times 10^{-16} T^{1.1} e^{-4375/T}$	
R128	$O + OH \rightarrow O_2 + H$	$7.47 \times 10^{-10} T^{-0.50} e^{-31.15/T}$	Tsang & Hampson 1986
R129	$O_2 + H \rightarrow O + OH$	$2.85 \times 10^{-07} T^{-0.90} e^{-8473/T}$	
R130	$O + HCO \rightarrow OH + CO$	5.00×10^{-11}	Tsang & Hampson 1986
R131	$OH + CO \rightarrow O + HCO$	$9.91 \times 10^{-13} T^{0.58} e^{-43502/T}$	
R132	$O + HCO \rightarrow CO_2 + H$	5.00×10^{-11}	Tsang & Hampson 1986
R133	$CO_2 + H \rightarrow O + HCO$	$4.31 \times 10^{-06} T^{-0.66} e^{-56370/T}$	
R134	$O + H_2CO \rightarrow OH + HCO$	$6.92 \times 10^{-13} T^{0.57} e^{-1390/T}$	Baulch et al. 1992
R135	$OH + HCO \rightarrow O + H_2CO$	$4.17 \times 10^{-16} T^{1.0} e^{-8280/T}$	
R136	$O + CH_2OH \rightarrow OH + H_2CO$	7.01×10^{-11}	Tsang 1987
R137	$OH + H_2CO \rightarrow O + CH_2OH$	$5.61 \times 10^{-12} T^{0.47} e^{-36427/T}$	
R138	$O + CH_3O \rightarrow O_2 + CH_3$	$3.55 \times 10^{-11} e^{-239.3/T}$	Cobos & Troe 1985
R139	$O_2 + CH_3 \rightarrow O + CH_3O$	$8.09 \times 10^{-15} T^{1.1} e^{-13677/T}$	
R140	$O + CH_3O \rightarrow OH + H_2CO$	1.00×10^{-11}	Tsang & Hampson 1986
R141	$OH + H_2CO \rightarrow O + CH_3O$	$1.00 \times 10^{-15} T^{1.2} e^{-39744/T}$	
R142	$CH_3 + {}^3CH_2 \rightarrow C_2H_4 + H$	7.01×10^{-11}	Baulch et al. 1992
R143	$C_2H_4 + H \rightarrow CH_3 + {}^3CH_2$	$7.31 \times 10^{-04} T^{-1.2} e^{-32930/T}$	
R144	$O + CH_3OH \rightarrow OH + CH_2OH$	$1.63 \times 10^{-11} e^{-2269/T}$	Grotheer et al. 1981
R145	$OH + CH_2OH \rightarrow O + CH_3OH$	$2.18 \times 10^{-14} T^{0.34} e^{-5214/T}$	

Reaction Index	Reaction	Rate Expression	Reference
R146	$O + H_2CCO \rightarrow CO + H_2CO$	$3.80 \times 10^{-12} e^{680/T}$	Baulch et al. 1992
R147	$CO + H_2CO \rightarrow O + H_2CCO$	$1.97 \times 10^{-15} T^{1.1} e^{-50916/T}$	
R148	$O + H_2CCO \rightarrow HCO + HCO$	$1.30 \times 10^{-12} e^{-680.0/T}$	Baulch et al. 1992
R149	$HCO + HCO \rightarrow O + H_2CCO$	$5.78 \times 10^{-18} T^{1.1} e^{-14093/T}$	
R150	$O + CH_3CO \rightarrow CO_2 + CH_3$	1.60×10^{-11}	Tsang & Hampson 1986
R151	$CO_2 + CH_3 \rightarrow O + CH_3CO$	$8.81 \times 10^{-14} T^{1.1} e^{-57811/T}$	
R152	$O + CH_3CO \rightarrow OH + H_2CCO$	9.96×10^{-11}	Herron 1988
R153	$OH + H_2CCO \rightarrow O + CH_3CO$	$9.67 \times 10^{-14} T^{0.82} e^{-29604/T}$	
R154	$O + CH_3CHO \rightarrow OH + CH_3CO$	$8.30 \times 10^{-12} e^{-902/T}$	Warnatz 1984
R155	$OH + CH_3CO \rightarrow O + CH_3CHO$	$4.41 \times 10^{-14} T^{0.17} e^{-7335/T}$	
R156	$O(^1D) + H_2 \rightarrow OH + H$	2.87×10^{-10}	Tully 1975
R157	$O(^1D) + CH_4 \rightarrow OH + CH_3$	1.35×10^{-10}	Atkinson 1992
R158	$O(^1D) + CH_4 \rightarrow H_2CO + H_2$	7.51×10^{-12}	DeMore 1994
R159	$O(^1D) + H_2O \rightarrow OH + OH$	2.20×10^{-10}	DeMore et al. 1997
R160	$O(^1D) + CO_2 \rightarrow O + CO_2$	2.52×10^{-10}	Tulley et al. 1975
R161	$O_2 + C \rightarrow O + CO$	$1.99 \times 10^{-10} e^{-2009/T}$	Dean et al. 1991
R162	$O + CO \rightarrow O_2 + C$	$9.07 \times 10^{-11} T^{0.18} e^{-71444/T}$	
R163	$O_2 + CH \rightarrow OH + CO$	5.50×10^{-11}	Baulch et al. 1992
R164	$OH + CO \rightarrow O_2 + CH$	$9.22 \times 10^{-13} T^{0.63} e^{-80082/T}$	
R165	$CH + O_2 \rightarrow O + HCO$	5.50×10^{-11}	Baulch et al. 1992
R166	$O + HCO \rightarrow CH + O_2$	$1.60 \times 10^{-10} T^{0.091} e^{-36842/T}$	
R167	$O_2 + {}^3CH_2 \rightarrow H_2O + CO$	4.00×10^{-13}	Tsang & Hampson 1986
R168	$H_2O + CO \rightarrow O_2 + {}^3CH_2$	$4.95 \times 10^{-14} T^{0.54} e^{-89209/T}$	
R169	$OH + H_2 \rightarrow H_2O + H$	$1.70 \times 10^{-16} T^{1.6} e^{-1659/T}$	Baulch et al. 1992
R170	$H_2O + H \rightarrow OH + H_2$	$3.16 \times 10^{-15} T^{1.4} e^{-9233/T}$	
R171	$OH + {}^3CH_2 \rightarrow H_2CO + H$	3.01×10^{-11}	Tsang & Hampson 1986
R172	$H_2CO + H \rightarrow OH + {}^3CH_2$	$4.42 \times 10^{-06} T^{-0.80} e^{-38978/T}$	
R173	$OH + CH_3 \rightarrow H_2O + {}^3CH_2$	$1.20 \times 10^{-10} e^{-1399/T}$	Baulch et al. 1994
R174	$H_2O + {}^3CH_2 \rightarrow OH + CH_3$	$6.56 \times 10^{-12} T^{0.31} e^{-5509/T}$	
R175	$OH + C_2H \rightarrow O + C_2H_2$	3.01×10^{-11}	Tsang & Hampson 1986
R176	$O + C_2H_2 \rightarrow OH + C_2H$	$1.02 \times 10^{-07} T^{-0.51} e^{-15486/T}$	

Reaction Index	Reaction	Rate Expression	Reference
R177	$OH + C_2H \rightarrow CO + {}^3CH_2$	3.01×10^{-11}	Tsang & Hampson 1986
R178	$CO + {}^3CH_2 \rightarrow OH + C_2H$	$5.08 \times 10^{-13} T^{0.71} e^{-38769/T}$	
R179	$OH + C_2H_3 \rightarrow H_2O + C_2H_2$	5.00×10^{-11}	Tsang & Hampson 1986
R180	$H_2O + C_2H_2 \rightarrow OH + C_2H_3$	$1.59 \times 10^{-09} T^{0.074} e^{-42041/T}$	
R181	$OH + C_2H_5 \rightarrow H_2O + C_2H_4$	4.00×10^{-11}	Tsang & Hampson 1986
R182	$H_2O + C_2H_4 \rightarrow OH + C_2H_5$	$1.16 \times 10^{-10} T^{0.27} e^{-41533/T}$	
R183	$OH + C_2H_6 \rightarrow H_2O + C_2H_5$	$1.46 \times 10^{-14} T^{1.0} e^{-912.8/T}$	Tsang & Hampson 1986
R184	$H_2O + C_2H_5 \rightarrow OH + C_2H_6$	$2.96 \times 10^{-17} T^{1.5} e^{-9856/T}$	
R185	$OH + OH \rightarrow O + H_2O$	$2.49 \times 10^{-15} T^{1.1} e^{-50.51/T}$	Baulch et al. 1992
R186	$O + H_2O \rightarrow OH + OH$	$7.38 \times 10^{-14} T^{1.0} e^{-8322/T}$	
R187	$OH + CO \rightarrow CO_2 + H$	$1.04 \times 10^{-17} T^{1.5} e^{250.1/T}$	Baulch et al. 1992
R188	$CO_2 + H \rightarrow OH + CO$	$4.19 \times 10^{-11} T^{0.25} e^{-12609/T}$	
R189	$HCO + OH \rightarrow CO + H_2O$	1.69×10^{-10}	Baulch et al. 1992
R190	$CO + H_2O \rightarrow HCO + OH$	$1.98 \times 10^{-10} T^{0.36} e^{-51884/T}$	
R191	$OH + H_2CO \rightarrow H_2O + HCO$	$5.69 \times 10^{-15} T^{1.1} e^{224.9/T}$	Baulch et al. 1992
R192	$H_2O + HCO \rightarrow OH + H_2CO$	$9.03 \times 10^{-17} T^{1.5} e^{-14922/T}$	
R193	$OH + CH_2OH \rightarrow H_2O + H_2CO$	4.00×10^{-11}	Tsang 1987
R194	$H_2O + H_2CO \rightarrow OH + CH_2OH$	$3.56 \times 10^{-10} T^{0.18} e^{-44930/T}$	
R195	$OH + CH_3O \rightarrow H_2O + H_2CO$	3.01×10^{-11}	Tsang & Hampson 1986
R196	$H_2O + H_2CO \rightarrow OH + CH_3O$	$2.36 \times 10^{-13} T^{1.0} e^{-48182/T}$	
R197	$OH + CH_3OH \rightarrow H_2O + CH_2OH$	$2.39 \times 10^{-18} T^{2.0} e^{423.3/T}$	Li et al. 1996
R198	$H_2O + CH_2OH \rightarrow OH + CH_3OH$	$6.45 \times 10^{-20} T^{2.2} e^{-10744/T}$	
R199	$OH + CH_3OH \rightarrow H_2O + CH_3O$	$1.66 \times 10^{-11} e^{-853.9/T}$	Warnatz et al. 1984
R200	$H_2O + CH_3O \rightarrow OH + CH_3OH$	$3.44 \times 10^{-10} T^{-0.53} e^{-8707/T}$	
R201	$OH + H_2CCO \rightarrow CO + CH_2OH$	1.00×10^{-11}	Baulch et al. 1992
R202	$CO + CH_2OH \rightarrow OH + H_2CCO$	$4.68 \times 10^{-14} T^{0.68} e^{-13748/T}$	
R203	$OH + H_2CCO \rightarrow HCO + H_2CO$	1.69×10^{-11}	Baulch et al. 1992
R204	$HCO + H_2CO \rightarrow OH + H_2CCO$	$1.11 \times 10^{-13} T^{0.69} e^{-6509/T}$	
R205	$OH + CH_3CO \rightarrow H_2O + H_2CCO$	2.01×10^{-11}	Tsang & Hampson 1986
R206	$H_2O + H_2CCO \rightarrow OH + CH_3CO$	$5.26 \times 10^{-13} T^{0.70} e^{-37852/T}$	
R207	$OH + CH_3CHO \rightarrow H_2O + CH_3CO$	1.66×10^{-11}	Warnatz et al. 1984

Reaction Index	Reaction	Rate Expression	Reference
R208	$H_2O + CH_3CO \rightarrow OH + CH_3CHO$	$2.16 \times 10^{-12} T^{0.065} e^{-14681/T}$	
R209	$CO_2 + CH \rightarrow CO + HCO$	$5.71 \times 10^{-12} e^{-345.1/T}$	Baulch et al. 1992
R210	$CO + HCO \rightarrow CO_2 + CH$	$1.53 \times 10^{-15} T^{0.74} e^{-32758/T}$	
R211	$CO_2 + {}^3CH_2 \rightarrow CO + H_2CO$	3.90×10^{-14}	Tsang & Hampson 1986
R212	$CO + H_2CO \rightarrow CO_2 + {}^3CH_2$	$9.41 \times 10^{-16} T^{0.48} e^{-26051/T}$	
R213	$HCO + H \rightarrow H_2 + CO$	1.50×10^{-10}	Baulch et al. 1992
R214	$H_2 + CO \rightarrow HCO + H$	$2.61 \times 10^{-12} T^{0.69} e^{-44097/T}$	
R215	$HCO + CH_3 \rightarrow CO + CH_4$	2.01×10^{-10}	Tsang & Hampson 1986
R216	$CO + CH_4 \rightarrow HCO + CH_3$	$3.79 \times 10^{-06} T^{-0.61} e^{-46015/T}$	
R217	$HCO + C_2H \rightarrow CO + C_2H_2$	1.00×10^{-10}	Tsang & Hampson 1986
R218	$CO + C_2H_2 \rightarrow HCO + C_2H$	$5.42 \times 10^{-09} T^{0.092} e^{-58930/T}$	
R219	$HCO + C_2H_3 \rightarrow C_2H_4 + CO$	1.50×10^{-10}	Tsang & Hampson 1986
R220	$C_2H_4 + CO \rightarrow HCO + C_2H_3$	$1.97 \times 10^{-07} T^{-0.24} e^{-48501/T}$	
R221	$HCO + C_2H_5 \rightarrow CO + C_2H_6$	2.01×10^{-10}	Tsang & Hampson 1986
R222	$CO + C_2H_6 \rightarrow HCO + C_2H_5$	$2.29 \times 10^{-07} T^{-0.17} e^{-43061/T}$	
R223	$HCO + HCO \rightarrow CO + H_2CO$	3.00×10^{-11}	Tsang & Hampson 1986
R224	$CO + H_2CO \rightarrow HCO + HCO$	$3.26 \times 10^{-09} T^{0.044} e^{-36803/T}$	
R225	$HCO + CH_2OH \rightarrow H_2CO + H_2CO$	3.01×10^{-10}	Tsang 1987
R226	$H_2CO + H_2CO \rightarrow HCO + CH_2OH$	$6.47 \times 10^{-08} T^{0.068} e^{-29601/T}$	
R227	$HCO + CH_2OH \rightarrow CO + CH_3OH$	2.01×10^{-10}	Tsang 1987
R228	$CO + CH_3OH \rightarrow HCO + CH_2OH$	$4.26 \times 10^{-08} T^{0.076} e^{-40986/T}$	
R229	$HCO + CH_3O \rightarrow CO + CH_3OH$	2.01×10^{-10}	Tsang 1987
R230	$CO + CH_3OH \rightarrow HCO + CH_3O$	$3.90 \times 10^{-11} T^{0.75} e^{-44244/T}$	
R231	$HCO + CH_3CO \rightarrow CO + CH_3CHO$	1.50×10^{-11}	Tsang 1987
R232	$CO + CH_3CHO \rightarrow HCO + CH_3CO$	$1.27 \times 10^{-10} T^{0.30} e^{-37196/T}$	
R233	$H_2CO + H \rightarrow HCO + H_2$	$3.64 \times 10^{-16} T^{1.7} e^{-1509/T}$	Tsang & Hampson1986
R234	$HCO + H_2 \rightarrow H_2CO + H$	$3.28 \times 10^{-19} T^{2.3} e^{-9090/T}$	
R235	$H_2CO + CH \rightarrow CO + CH_3$	$8.00 \times 10^{-11} e^{260.0/T}$	Baulch et al. 1992
R236	$CO + CH_3 \rightarrow H_2CO + CH$	$9.15 \times 10^{-12} T^{0.41} e^{-53757/T}$	
R237	$H_2CO + CH \rightarrow H_2CCO + H$	$8.00 \times 10^{-11} e^{260.0/T}$	Baulch et al. 1992
R238	$H_2CCO + H \rightarrow H_2CO + CH$	$4.13 \times 10^{-06} T^{-1.0} e^{-38320/T}$	

Reaction Index	Reaction	Rate Expression	Reference
R239	$H_2CO + CH_3 \rightarrow HCO + CH_4$	$9.20 \times 10^{-21} T^{2.8} e^{-2950/T}$	Tsang & Hampson 1986
R240	$HCO + CH_4 \rightarrow H_2CO + CH_3$	$1.42 \times 10^{-19} T^{2.5} e^{-11733/T}$	
R241	$H_2CO + C_2H_3 \rightarrow HCO + C_2H_4$	$9.00 \times 10^{-21} T^{2.8} e^{-2950/T}$	Tsang & Hampson 1986
R242	$HCO + C_2H_4 \rightarrow H_2CO + C_2H_3$	$9.71 \times 10^{-20} T^{2.6} e^{-14612/T}$	
R243	$H_2CO + C_2H_5 \rightarrow HCO + C_2H_6$	$9.13 \times 10^{-21} T^{2.8} e^{-2950/T}$	Tsang & Hampson 1986
R244	$HCO + C_2H_6 \rightarrow H_2CO + C_2H_5$	$9.24 \times 10^{-20} T^{2.6} e^{-9186/T}$	
R245	$H_2CO + CH_2OH \rightarrow HCO + CH_3OH$	$9.11 \times 10^{-21} T^{2.8} e^{-2950/T}$	Tsang 1987
R246	$HCO + CH_3OH \rightarrow H_2CO + CH_2OH$	$5.39 \times 10^{-21} T^{2.9} e^{-6929/T}$	
R247	$H_2CO + CH_3O \rightarrow HCO + CH_3OH$	$1.69 \times 10^{-13} e^{-1499/T}$	Tsang & Hampson 1986
R248	$HCO + CH_3OH \rightarrow H_2CO + CH_3O$	$1.42 \times 10^{-16} T^{0.88} e^{-8806/T}$	
R249	$CH_2OH + H \rightarrow OH + CH_3$	1.60×10^{-10}	Tsang 1987
R250	$OH + CH_3 \rightarrow CH_2OH + H$	$5.93 \times 10^{-14} T^{0.81} e^{-1653/T}$	
R251	$CH_2OH + H \rightarrow H_2CO + H_2$	1.00×10^{-11}	Tsang 1987
R252	$H_2CO + H_2 \rightarrow CH_2OH + H$	$1.67 \times 10^{-12} T^{0.48} e^{-37178/T}$	
R253	$CH_2OH + CH_3 \rightarrow H_2CO + CH_4$	4.00×10^{-12}	Tsang 1987
R254	$H_2CO + CH_4 \rightarrow CH_2OH + CH_3$	$1.51 \times 10^{-07} T^{-0.63} e^{-38806/T}$	
R255	$CH_2OH + C_2H \rightarrow H_2CO + C_2H_2$	5.99×10^{-11}	Tsang 1987
R256	$H_2CO + C_2H_2 \rightarrow CH_2OH + C_2H$	$5.00 \times 10^{-08} T^{-0.17} e^{-52122/T}$	
R257	$CH_2OH + C_2H_3 \rightarrow H_2CO + C_2H_4$	5.00×10^{-11}	Tsang 1987
R258	$H_2CO + C_2H_4 \rightarrow CH_2OH + C_2H_3$	$3.25 \times 10^{-07} T^{-0.37} e^{-41462/T}$	
R259	$C_2H_5 + CH_2OH \rightarrow CH_3OH + C_2H_4$	4.00×10^{-12}	Tsang 1987
R260	$CH_3OH + C_2H_4 \rightarrow C_2H_5 + CH_2OH$	$8.18 \times 10^{-10} T^{0.059} e^{-30461/T}$	
R261	$CH_2OH + C_2H_5 \rightarrow H_2CO + C_2H_6$	4.00×10^{-12}	Tsang 1987
R262	$H_2CO + C_2H_6 \rightarrow CH_2OH + C_2H_5$	$1.84 \times 10^{-08} T^{-0.28} e^{-35985/T}$	
R263	$CH_2OH + CH_2OH \rightarrow H_2CO + CH_3OH$	8.00×10^{-12}	Tsang 1987
R264	$H_2CO + CH_3OH \rightarrow CH_2OH + CH_2OH$	$4.43 \times 10^{-09} T^{-0.13} e^{-33833/T}$	
R265	$CH_2OH + CH_3O \rightarrow H_2CO + CH_3OH$	4.00×10^{-11}	Tsang 1987
R266	$H_2CO + CH_3OH \rightarrow CH_2OH + CH_3O$	$3.06 \times 10^{-11} T^{0.64} e^{-37163/T}$	
R267	$CH_3 + OH \rightarrow H + CH_3O$	$2.04 \times 10^{-15} T^{1.0} e^{-6012/T}$	Jasper et al. 2007
R268	$H + CH_3O \rightarrow CH_3 + OH$	$3.20 \times 10^{-09} T^{-0.55} e^{-1007/T}$	
R269	$CH_3O + H \rightarrow H_2CO + H_2$	$2.32 \times 10^{-07} T^{-0.58} e^{-855.1/T}$	Li et al. 2004

Reaction Index	Reaction	Rate Expression	Reference
R270	$H_2CO + H_2 \rightarrow CH_3O + H$	$2.33 \times 10^{-11} T^{0.78} e^{-41206/T}$	
R271	$CH_3O + CH_3 \rightarrow H_2CO + CH_4$	4.00×10^{-11}	Tsang & Hampson 1986
R272	$H_2CO + CH_4 \rightarrow CH_3O + CH_3$	$2.51 \times 10^{-09} T^{0.11} e^{-42174/T}$	
R273	$CH_3O + C_2H \rightarrow H_2CO + C_2H_2$	4.00×10^{-11}	Tsang & Hampson 1986
R274	$H_2CO + C_2H_2 \rightarrow CH_3O + C_2H$	$1.59 \times 10^{-11} T^{0.73} e^{-55248/T}$	
R275	$CH_3O + C_2H_3 \rightarrow H_2CO + C_2H_4$	4.00×10^{-11}	Tsang & Hampson 1986
R276	$H_2CO + C_2H_4 \rightarrow CH_3O + C_2H_3$	$2.50 \times 10^{-10} T^{0.44} e^{-44729/T}$	
R277	$CH_3O + C_2H_5 \rightarrow H_2CO + C_2H_6$	4.00×10^{-11}	Tsang & Hampson 1986
R278	$H_2CO + C_2H_6 \rightarrow CH_3O + C_2H_5$	$1.86 \times 10^{-10} T^{0.53} e^{-39260/T}$	
R279	$CH_3O + CH_3O \rightarrow CH_3OH + H_2CO$	1.00×10^{-10}	Tsang & Hampson 1986
R280	$CH_3OH + H_2CO \rightarrow CH_3O + CH_3O$	$7.44 \times 10^{-14} T^{1.4} e^{-40430/T}$	
R281	$CH_3O + CH_3OH \rightarrow CH_2OH + CH_3OH$	$5.00 \times 10^{-13} e^{-2049/T}$	Tsang 1987
R282	$CH_2OH + CH_3OH \rightarrow CH_3O + CH_3OH$	$7.81 \times 10^{-16} T^{0.76} e^{-5387/T}$	
R283	$CH_3O + CH_3CO \rightarrow H_2CCO + CH_3OH$	1.00×10^{-11}	Tsang 1987
R284	$H_2CCO + CH_3OH \rightarrow CH_3O + CH_3CO$	$3.32 \times 10^{-14} T^{1.1} e^{-30155/T}$	
R285	$CH_3O + CH_3CO \rightarrow H_2CO + CH_3CHO$	1.00×10^{-11}	Tsang & Hampson 1986
R286	$H_2CO + CH_3CHO \rightarrow CH_3O + CH_3CO$	$2.69 \times 10^{-13} T^{1.0} e^{-33351/T}$	
R287	$CH_3O + CH_3CHO \rightarrow CH_3CO + CH_3OH$	8.30×10^{-15}	Kelly et al. 1978
R288	$CH_3CO + CH_3OH \rightarrow CH_3O + CH_3CHO$	$5.54 \times 10^{-17} T^{0.58} e^{-6835/T}$	
R289	$HCO + {}^3CH_2 \rightarrow CO + CH_3$	3.01×10^{-11}	Tsang & Hampson 1986
R290	$CO + CH_3 \rightarrow HCO + {}^3CH_2$	$8.64 \times 10^{-10} T^{0.022} e^{-47837/T}$	
R291	$CH_2OH + {}^3CH_2 \rightarrow OH + C_2H_4$	4.00×10^{-11}	Tsang 1987
R292	$OH + C_2H_4 \rightarrow CH_2OH + {}^3CH_2$	$3.00 \times 10^{-07} T^{-0.51} e^{-34692/T}$	
R293	$CH_2OH + {}^3CH_2 \rightarrow H_2CO + CH_3$	2.01×10^{-12}	Tsang 1987
R294	$H_2CO + CH_3 \rightarrow CH_2OH + {}^3CH_2$	$3.38 \times 10^{-10} T^{-0.13} e^{-40831/T}$	
R295	$CH_3OH + H \rightarrow H_2O + CH_3$	$3.32 \times 10^{-10} e^{-2670/T}$	Hidaka et al. 1989
R296	$H_2O + CH_3 \rightarrow CH_3OH + H$	$3.39 \times 10^{-15} T^{1.0} e^{-15494/T}$	
R297	$CH_3OH + H \rightarrow CH_2OH + H_2$	$2.72 \times 10^{-17} T^{2.0} e^{-2270/T}$	Li et al. 1996
R298	$CH_2OH + H_2 \rightarrow CH_3OH + H$	$4.89 \times 10^{-20} T^{2.4} e^{-5892/T}$	
R299	$CH_3OH + {}^3CH_2 \rightarrow CH_2OH + CH_3$	$5.29 \times 10^{-23} T^{3.2} e^{-3609/T}$	Tsang 1987
R300	$CH_2OH + CH_3 \rightarrow CH_3OH + {}^3CH_2$	$2.51 \times 10^{-23} T^{3.1} e^{-10661/T}$	

Reaction Index	Reaction	Rate Expression	Reference
R301	$CH_3OH + {}^3CH_2 \rightarrow CH_3O + CH_3$	$2.39 \times 10^{-23} T^{3.1} e^{-3490/T}$	Tsang 1987
R302	$CH_3O + CH_3 \rightarrow CH_3OH + {}^3CH_2$	$8.63 \times 10^{-21} T^{2.2} e^{-7227/T}$	
R303	$CH_3OH + CH_3 \rightarrow CH_2OH + CH_4$	$5.29 \times 10^{-23} T^{3.2} e^{-3609/T}$	Tsang 1987
R304	$CH_2OH + CH_4 \rightarrow CH_3OH + CH_3$	$1.21 \times 10^{-21} T^{2.8} e^{-8394/T}$	
R305	$CH_3OH + CH_3 \rightarrow CH_3O + CH_4$	$2.39 \times 10^{-23} T^{3.1} e^{-3490/T}$	Tsang 1987
R306	$CH_3O + CH_4 \rightarrow CH_3OH + CH_3$	$3.30 \times 10^{-19} T^{1.9} e^{-4928/T}$	
R307	$CH_3OH + C_2H \rightarrow CH_2OH + C_2H_2$	1.00×10^{-11}	Tsang 1987
R308	$CH_2OH + C_2H_2 \rightarrow CH_3OH + C_2H$	$2.40 \times 10^{-11} T^{0.097} e^{-18347/T}$	
R309	$CH_3OH + C_2H \rightarrow CH_3O + C_2H_2$	2.01×10^{-12}	Tsang 1987
R310	$CH_3O + C_2H_2 \rightarrow CH_3OH + C_2H$	$4.01 \times 10^{-09} T^{-0.89} e^{-15043/T}$	
R311	$CH_3OH + C_2H_3 \rightarrow CH_2OH + C_2H_4$	$5.29 \times 10^{-23} T^{3.2} e^{-3609/T}$	Tsang 1987
R312	$CH_2OH + C_2H_4 \rightarrow CH_3OH + C_2H_3$	$7.25 \times 10^{-22} T^{2.9} e^{-11254/T}$	
R313	$CH_3OH + C_2H_3 \rightarrow CH_3O + C_2H_4$	$2.39 \times 10^{-23} T^{3.1} e^{-3490/T}$	Tsang 1987
R314	$CH_3O + C_2H_4 \rightarrow CH_3OH + C_2H_3$	$2.45 \times 10^{-19} T^{2.0} e^{-7816/T}$	
R315	$CH_3OH + C_2H_5 \rightarrow CH_2OH + C_2H_6$	$5.29 \times 10^{-23} T^{3.2} e^{-4610/T}$	Tsang 1987
R316	$CH_2OH + C_2H_6 \rightarrow CH_3OH + C_2H_5$	$7.57 \times 10^{-22} T^{2.9} e^{-6843/T}$	
R317	$CH_3OH + C_2H_5 \rightarrow CH_3O + C_2H_6$	$2.39 \times 10^{-23} T^{3.1} e^{-4499/T}$	Tsang 1987
R318	$CH_3O + C_2H_6 \rightarrow CH_3OH + C_2H_5$	$2.46 \times 10^{-19} T^{2.1} e^{-3410/T}$	
R319	$HCCO + H \rightarrow CO + {}^3CH_2$	2.49×10^{-10}	Frank et al. 1988
R320	$CO + {}^3CH_2 \rightarrow HCCO + H$	$3.50 \times 10^{-16} T^{1.4} e^{-13363/T}$	
R321	$H_2CCO + H \rightarrow CO + CH_3$	$1.28 \times 10^{-15} T^{1.4} e^{-1399/T}$	Senosiain et al. 2006
R322	$CO + CH_3 \rightarrow H_2CCO + H$	$2.64 \times 10^{-21} T^{2.9} e^{-16823/T}$	
R323	$H_2CCO + {}^3CH_2 \rightarrow CO + C_2H_4$	2.09×10^{-10}	Frank et al. 1986
R324	$CO + C_2H_4 \rightarrow H_2CCO + {}^3CH_2$	$1.53 \times 10^{-08} T^{0.075} e^{-48582/T}$	
R325	$H_2CCO + {}^3CH_2 \rightarrow CH_3 + HCCO$	1.00×10^{-17}	Banyard et al. 1980
R326	$CH_3 + HCCO \rightarrow H_2CCO + {}^3CH_2$	$1.55 \times 10^{-17} T^{0.016} e^{-2069/T}$	
R327	$CH_3CO + H \rightarrow H_2CCO + H_2$	3.32×10^{-11}	Warnatz et al. 1984
R328	$H_2CCO + H_2 \rightarrow CH_3CO + H$	$4.35 \times 10^{-14} T^{0.88} e^{-30273/T}$	
R329	$CH_3CO + H \rightarrow HCO + CH_3$	3.32×10^{-11}	Warnatz et al. 1984
R330	$HCO + CH_3 \rightarrow CH_3CO + H$	$5.15 \times 10^{-18} T^{1.6} e^{-1591/T}$	
R331	$CH_3CO + {}^3CH_2 \rightarrow H_2CCO + CH_3$	3.01×10^{-11}	Tsang & Hampson 1986

Reaction Index	Reaction	Rate Expression	Reference
R332	$H_2CCO + CH_3 \rightarrow CH_3CO + {}^3CH_2$	$2.49 \times 10^{-11} T^{0.32} e^{-33841/T}$	
R333	$CH_3CO + CH_3 \rightarrow H_2CCO + CH_4$	1.01×10^{-11}	Hassinen et al. 1990
R334	$H_2CCO + CH_4 \rightarrow CH_3CO + CH_3$	$1.54 \times 10^{-09} T^{-0.15} e^{-31786/T}$	
R335	$CH_3CO + CH_3 \rightarrow CO + C_2H_6$	4.90×10^{-11}	Adachi et al. 1981
R336	$CO + C_2H_6 \rightarrow CH_3CO + CH_3$	$1.11 \times 10^{-09} T^{0.32} e^{-40091/T}$	
R337	$CH_3CO + C_2H \rightarrow H_2CCO + C_2H_2$	3.00×10^{-11}	Tsang & Hampson 1986
R338	$H_2CCO + C_2H_2 \rightarrow CH_3CO + C_2H$	$7.44 \times 10^{-11} T^{0.34} e^{-45036/T}$	
R339	$CH_3CO + CH_3CO \rightarrow H_2CCO + CH_3CHO$	1.49×10^{-11}	Hassinen et al. 1990
R340	$H_2CCO + CH_3CHO \rightarrow CH_3CO + CH_3CO$	$5.45 \times 10^{-12} T^{0.56} e^{-23281/T}$	
R341	$CH_3CHO + H \rightarrow CH_3CO + H_2$	$6.64 \times 10^{-11} e^{-2120/T}$	Warnatz et al. 1984
R342	$CH_3CO + H_2 \rightarrow CH_3CHO + H$	$5.44 \times 10^{-13} T^{0.22} e^{-9247/T}$	
R343	$CH_3CHO + {}^3CH_2 \rightarrow CH_3CO + CH_3$	$2.76 \times 10^{-12} e^{-1768/T}$	Bohland et al. 1985
R344	$CH_3CO + CH_3 \rightarrow CH_3CHO + {}^3CH_2$	$6.30 \times 10^{-12} T^{-0.24} e^{-12334/T}$	
R345	$CH_3CO + CH_4 \rightarrow CH_3CHO + CH_3$	$3.60 \times 10^{-21} T^{2.8} e^{-10800/T}$	Tsang & Hampson 1986
R346	$CH_3CHO + CH_3 \rightarrow CH_3CO + CH_4$	$3.95 \times 10^{-23} T^{3.4} e^{-2528/T}$	
R347	$CH_3CHO + C_2H_3 \rightarrow CH_3CO + C_2H_4$	$1.35 \times 10^{-13} e^{-1849/T}$	Scherzer et al. 1987
R348	$CH_3CO + C_2H_4 \rightarrow CH_3CHO + C_2H_3$	$1.00 \times 10^{-11} T^{-0.46} e^{-13022/T}$	
R349	$C_2H_6 + CH_3CO \rightarrow CH_3CHO + C_2H_5$	$2.99 \times 10^{-20} T^{2.7} e^{-8819/T}$	Tsang & Hampson 1986
R350	$CH_3CHO + C_2H_5 \rightarrow C_2H_6 + CH_3CO$	$4.36 \times 10^{-22} T^{3.1} e^{-3074/T}$	
R351	$H_2 + CH_3O \rightarrow CH_3OH + H$	$2.10 \times 10^{-25} T^{4.0} e^{-2470/T}$	Jodkowski et al. 1999
R352	$CH_3OH + H \rightarrow H_2 + CH_3O$	$1.63 \times 10^{-25} T^{4.3} e^{-2169/T}$	
R353	$CH + CH_4 \rightarrow C_2H_4 + H$	$5.00 \times 10^{-11} e^{200./T}$	Baulch et al. 1992
R354	$C_2H_4 + H \rightarrow CH + CH_4$	$1.69 \times 10^{-07} T^{-0.6} e^{-30192/T}$	
R355	$CH + C_2H_4 \rightarrow C_2H_2 + CH_3$	$2.23 \times 10^{-10} e^{173.0/T}$	Baulch et al. 1992
R356	$C_2H_2 + CH_3 \rightarrow CH + C_2H_4$	$1.33 \times 10^{-10} T^{0.07} e^{-32444/T}$	
R357	${}^3CH_2 + CH_4 \rightarrow CH_3 + CH_3$	$7.10 \times 10^{-12} e^{-5051/T}$	Bohland et al. 1985
R358	$CH_3 + CH_3 \rightarrow {}^3CH_2 + CH_4$	$1.83 \times 10^{-13} T^{0.29} e^{-7347/T}$	
R359	${}^3CH_2 + C_2H_3 \rightarrow C_2H_2 + CH_3$	3.00×10^{-11}	Tsang & Hampson 1986
R360	$C_2H_2 + CH_3 \rightarrow {}^3CH_2 + C_2H_3$	$1.67 \times 10^{-08} T^{-0.38} e^{-37925/T}$	
R361	${}^3CH_2 + C_2H_5 \rightarrow CH_3 + C_2H_4$	3.00×10^{-11}	Tsang & Hampson 1986
R362	$CH_3 + C_2H_4 \rightarrow {}^3CH_2 + C_2H_5$	$1.37 \times 10^{-09} T^{0.021} e^{-37397/T}$	

Reaction Index	Reaction	Rate Expression	Reference
R363	$C_2 + CH_4 \rightarrow C_2H + CH_3$	$5.05 \times 10^{-11} e^{-297.0/T}$	Pitts et al. 1982
R364	$C_2H + CH_3 \rightarrow C_2 + CH_4$	$3.65 \times 10^{-12} T^{0.080} e^{-5367/T}$	
R365	$CH_3O + {}^3CH_2 \rightarrow H_2CO + CH_3$	3.00×10^{-11}	Tsang & Hampson 1986
R366	$H_2CO + CH_3 \rightarrow CH_3O + {}^3CH_2$	$4.15 \times 10^{-12} T^{0.71} e^{-44067/T}$	
R367	${}^3CH_2 + C_2H_5 \rightarrow C_2H_4 + CH_3$	3.00×10^{-11}	Tsang & Hampson 1986
R368	$C_2H_4 + CH_3 \rightarrow {}^3CH_2 + C_2H_5$	$1.37 \times 10^{-09} T^{0.021} e^{-37397/T}$	
R369	$O + {}^3CH_2 \rightarrow CO + H_2$	9.96×10^{-11}	Frank et al. 1984
R370	$CO + H_2 \rightarrow O + {}^3CH_2$	$2.27 \times 10^{-11} T^{0.60} e^{-89595/T}$	
R371	$H + {}^1CH_2 \rightarrow CH + H_2$	$1.00 \times 10^{-11} e^{900/T}$	Baulch et al. 1992
R372	$CH + H_2 \rightarrow H + {}^1CH_2$	$4.81 \times 10^{-13} T^{0.33} e^{-227/T}$	
R373	${}^1CH_2 + H_2 \rightarrow {}^3CH_2 + H_2$	1.26×10^{-11}	Moses 2000a/Braun et al. 1970
R374	${}^3CH_2 + H_2 \rightarrow {}^1CH_2 + H_2$	$1.17 \times 10^{-11} T^{-0.16} e^{-4739/T}$	
R375	${}^1CH_2 + H_2 \rightarrow CH_3 + H$	9.24×10^{-11}	Moses 2000a/Langford et al. 1983
R376	$CH_3 + H \rightarrow {}^1CH_2 + H_2$	$4.09 \times 10^{-08} T^{-0.64} e^{-8195/T}$	
R377	${}^1CH_2 + CH_4 \rightarrow {}^3CH_2 + CH_4$	1.20×10^{-11}	Moses 2000a/Bohland et al. 1985
R378	${}^3CH_2 + CH_4 \rightarrow {}^1CH_2 + CH_4$	$1.63 \times 10^{-11} T^{-0.16} e^{-4739/T}$	
R379	$CH_4 + {}^1CH_2 \rightarrow CH_3 + CH_3$	5.90×10^{-11}	Moses 2000a/Bohland et al. 1985
R380	$CH_3 + CH_3 \rightarrow CH_4 + {}^1CH_2$	$2.18 \times 10^{+03} T^{-5.5-} e^{18953/T}$	
R381	${}^3CH_2 + {}^3CH_2 \rightarrow C_2H_2 + 2H$	$1.80 \times 10^{-10} e^{-400/T}$	Moses 2000a/Baulch et al. 1992
R382	$C_2H_2 + 2H \rightarrow {}^3CH_2 + {}^3CH_2$	$2.06 \times 10^{-33} T^{-0.83} e^{-14131/T}$	
R383	$O + {}^3CH_2 \rightarrow CO + 2H$	1.20×10^{-10}	Baulch et al. 1992
R384	$2H + CO \rightarrow O + {}^3CH_2$	$2.95 \times 10^{-37} T^{1.-} e^{36152/T}$	
R385	$O + C_2H_4OH \rightarrow OH + CH_3CHO$	1.50×10^{-10}	Grotheer et al. 1988
R386	$OH + CH_3CHO \rightarrow O + C_2H_4OH$	$7.65 \times 10^{+03} T^{-3.8} e^{-47939/T}$	
R387	$O_2 + {}^3CH_2 \rightarrow OH + CO$	1.00×10^{-12}	Moses et al. 2000b/Tsang & Hampson 1986
R388	$H + CO \rightarrow OH + O_2$	$1.75 \times 10^{-43} T^{1.9-} e^{26725/T}$	
R389	$C_2H_4OH + H \rightarrow CH_3CHO + H_2$	8.30×10^{-11}	Moses et al. 2000b/Bartels et al. 1992
R390	$CH_3CHO + H_2 \rightarrow C_2H_4OH + H$	$5.16 \times 10^{+03} T^{-3.72} e^{-48581/T}$	
R391	$C_2H_4OH + CH_3 \rightarrow CH_3CHO + CH_4$	4.00×10^{-11}	Moses et al. 2000b
R392	$CH_3CHO + CH_4 \rightarrow C_2H_4OH + CH_3$	$1.35 \times 10^{+09} T^{-4.95} e^{-50371/T}$	
R393	$N + CH_3 \rightarrow H_2 + HCN$	$4.30 \times 10^{-11} e^{-420.0/T}$	Marston et al. 1989

Reaction Index	Reaction	Rate Expression	Reference
R394	H_2 + HCN → N + CH_3	$5.64 \times 10^{-11} T^{0.11} e^{-58487/T}$	
R395	N + C_2H_4 → CH_3 + HCN	$2.66 \times 10^{-14} e^{-352.3/T}$	Paraskevopoulos & Winkler 1967
R396	CH_3 + HCN → N + C_2H_4	$2.84 \times 10^{-18} T^{0.76} e^{-29111/T}$	
R397	N + CH → NH + C	$7.39 \times 10^{-13} T^{0.65} e^{-1209/T}$	Mayer & Schieler 1996
R398	NH + C → N + CH	$1.60 \times 10^{-13} T^{0.80} e^{-676.2/T}$	
R399	N + $^3CH_2$ → NH + CH	$9.96 \times 10^{-13} e^{-20400/T}$	Mayer et al. 1967
R400	NH + CH → N + $^3CH_2$	$2.56 \times 10^{-14} T^{0.21} e^{-9321/T}$	
R401	N + OH → NH + O	$1.06 \times 10^{-11} T^{0.10} e^{-10701/T}$	Cohen & Westberg 1991
R402	NH + O → N + OH	$9.75 \times 10^{-12} T^{0.022} e^{841.8/T}$	
R403	N + OH → NO + H	4.70×10^{-11}	Baulch et al. 1994
R404	NO + H → N + OH	$1.67 \times 10^{-09} T^{-0.30} e^{-24273/T}$	
R405	N + H_2O → NH + OH	$6.48 \times 10^{-14} T^{1.2} e^{-19301/T}$	Cohen & Westberg 1991
R406	NH + OH → N + H_2O	$2.68 \times 10^{-15} T^{1.2} e^{477.7/T}$	
R407	N + O_2 → O + NO	$2.36 \times 10^{-11} e^{-5319/T}$	Valli et al. 1995
R408	O + NO → N + O_2	$2.08 \times 10^{-12} T^{0.10} e^{-21146/T}$	
R409	N + CO_2 → NO + CO	$3.20 \times 10^{-13} e^{-1710/T}$	Avramenko & Krasnenkov 1967
R410	NO + CO → N + CO_2	$3.14 \times 10^{-18} T^{0.92} e^{-13139/T}$	
R411	N + NH → H + N_2	$1.06 \times 10^{-12} T^{0.51} e^{-9/T}$	Caridade et al. 2005
R412	H + N_2 → N + NH	$3.92 \times 10^{-11} T^{0.46} e^{-73507/T}$	
R413	N + NO → O + N_2	$3.40 \times 10^{-11} e^{-24.05/T}$	Duff & Sharma 1996
R414	O + N_2 → N + NO	$3.66 \times 10^{-11} T^{0.17} e^{-37751/T}$	
R415	N + H_2 → NH + H	$4.65 \times 10^{-10} e^{-16597/T}$	Koshi et al. 1990
R416	NH + H → N + H_2	$2.73 \times 10^{-10} T^{-0.12} e^{-4358/T}$	
R417	N + CN → N_2 + C	3.00×10^{-10}	Baulch et al. 1992
R418	N_2 + C → N + CN	$2.41 \times 10^{-10} T^{0.13} e^{-23331/T}$	
R419	NCO + N → N_2 + CO	3.30×10^{-11}	Baulch et al. 1992
R420	N_2 + CO → NCO + N	$1.88 \times 10^{-15} T^{1.2} e^{-85806/T}$	
R421	NH + CH_4 → NH_2 + CH_3	$9.41 \times 10^{-18} T^{2.2} e^{-10232/T}$	Wang et al. 1999
R422	NH_2 + CH_3 → NH + CH_4	$1.49 \times 10^{-20} T^{2.7} e^{-3333/T}$	
R423	NH + C_2H_6 → NH_2 + C_2H_5	$7.20 \times 10^{-14} T^{0.68} e^{-8154/T}$	Xu et al. 1999
R424	NH_2 + C_2H_5 → NH + C_2H_6	$1.59 \times 10^{-16} T^{0.97} e^{-3788/T}$	

Reaction Index	Reaction	Rate Expression	Reference
R425	NH + OH → NH_2 + O	$1.66 \times 10^{-12} T^{0.10} e^{-5800/T}$	Cohen & Westberg 1991
R426	NH_2 + O → NH + OH	$3.84 \times 10^{-11} T^{-0.15} e^{-719.5/T}$	
R427	NH + H_2O → NH_2 + OH	$1.99 \times 10^{-16} T^{1.6} e^{-14071/T}$	Cohen & Westberg 1991
R428	NH_2 + OH → NH + H_2O	$2.09 \times 10^{-16} T^{1.4} e^{-756.2/T}$	
R429	NH + O → H + NO	1.16×10^{-10}	Cohen & Westberg 1991
R430	H + NO → NH + O	$3.24 \times 10^{-09} T^{-0.18} e^{-35760/T}$	
R431	NH + O_2 → NO + OH	$7.48 \times 10^{-16} T^{0.79} e^{-601.3/T}$	Romming & Wagner 1996
R432	NO + OH → NH + O_2	$7.91 \times 10^{-17} T^{0.96} e^{-27986/T}$	
R433	NH + O_2 → O + HNO	$7.64 \times 10^{-19} T^{2.0} e^{-3270/T}$	Miller & Melius 1992
R434	O + HNO → NH + O_2	$4.24 \times 10^{-17} T^{1.5} e^{-4313/T}$	
R435	NH + NH → N + NH_2	$9.90 \times 10^{-22} T^{2.8} e^{1019/T}$	Zu et al. 1997
R436	N + NH_2 → NH + NH	$2.86 \times 10^{-20} T^{2.6} e^{-5460/T}$	
R437	NH + NO → N_2 + OH	$1.01 \times 10^{-10} T^{-0.50} e^{-60.13/T}$	Bozzelli et al. 1994
R438	N_2 + OH → NH + NO	$1.30 \times 10^{-10} T^{-0.26} e^{-49338/T}$	
R439	NH + NH_2 → H + N_2H_2	$2.48 \times 10^{-09} T^{-0.50}$	Davidson et al. 1990
R440	H + N_2H_2 → NH + NH_2	$7.35 \times 10^{-03} T^{-1.7} e^{-14867/T}$	
R441	NH + NO → N_2H + O	$9.28 \times 10^{-12} T^{0.21} e^{-5469/T}$	Bozzelli et al. 1994
R442	N_2H + O → NH + NO	$2.95 \times 10^{-10} T^{-0.14} e^{375.4/T}$	
R443	NH_2 + NO → N_2H + OH	$6.87 \times 10^{-15} T^{1.4} e^{894/T}$	Park & Lin 1999
R444	N_2H + OH → NH_2 + NO	$9.94 \times 10^{-15} T^{1.2} e^{1652/T}$	
R445	NH_2 + N_2H_4 → N_2H_3 + NH_3	$7.99 \times 10^{-24} T^{3.6} e^{-386.0/T}$	Li & Zhang 2006
R446	N_2H_3 + NH_3 → NH_2 + N_2H_4	$9.45 \times 10^{-23} T^{3.5} e^{-16100/T}$	
R447	NH_2 + NH_2 → NH_3 + NH	$1.92 \times 10^{-22} T^{3.0} e^{-232.1/T}$	Xu et al. 1998
R448	NH_3 + NH → NH_2 + NH_2	$2.39 \times 10^{-21} T^{3.0} e^{-8387/T}$	
R449	NH_2 + NH_2 → N_2H_2 + H_2	1.30×10^{-12}	Stothard et al. 1995
R450	N_2H_2 + H_2 → NH_2 + NH_2	$2.06 \times 10^{-07} T^{-0.93} e^{-20614/T}$	
R451	NH_2 + NO → H_2O + N_2	$2.07 \times 10^{-11} T^{-1.6} e^{-150.3/T}$	Park & Lin 1999
R452	H_2O + N_2 → NH_2 + NO	$2.68 \times 10^{-11} T^{-1.2} e^{-62743/T}$	
R453	NH_2 + H_2 → NH_3 + H	$2.72 \times 10^{-21} T^{2.8} e^{-3639/T}$	Corchado & Espinosa-Garcia 1997
R454	NH_3 + H → NH_2 + H_2	$5.94 \times 10^{-19} T^{2.4} e^{-6039/T}$	
R455	NH_2 + H → NH + H_2	$1.05 \times 10^{-10} e^{-4450/T}$	Rohrig & Wagner 1994

Reaction Index	Reaction	Rate Expression	Reference
R456	$NH + H_2 \rightarrow NH_2 + H$	$5.70 \times 10^{-12} T^{0.32} e^{-10198/T}$	
R457	$NH_2 + H_2O \rightarrow NH_3 + OH$	$1.52 \times 10^{-22} T^{3.1} e^{-5110/T}$	Mebel et al. 1999
R458	$NH_3 + OH \rightarrow NH_2 + H_2O$	$1.83 \times 10^{-21} T^{2.9} e^{60.00/T}$	
R459	$NH_2 + OH \rightarrow NH_3 + O$	$3.39 \times 10^{-14} T^{0.40} e^{-250.1/T}$	Baulch et al. 1992
R460	$NH_3 + O \rightarrow NH_2 + OH$	$1.05 \times 10^{-11} T^{0.071} e^{-3334/T}$	
R461	$NH_2 + O \rightarrow NO + H_2$	8.30×10^{-12}	Cohen & Westberg 1991
R462	$NO + H_2 \rightarrow NH_2 + O$	$5.71 \times 10^{-12} T^{0.23} e^{-41377/T}$	
R463	$NH_2 + O_2 \rightarrow HNO + OH$	$2.50 \times 10^{-12} T^{-0.39} e^{-18161/T}$	Bozzelli et al. 1989
R464	$HNO + OH \rightarrow NH_2 + O_2$	$6.55 \times 10^{-12} T^{-0.58} e^{-24299/T}$	
R465	$NH_2 + HNO \rightarrow NO + NH_3$	$6.01 \times 10^{-17} T^{1.6} e^{630./T}$	Mebel et al. 1996
R466	$NO + NH_3 \rightarrow NH_2 + HNO$	$2.07 \times 10^{-17} T^{1.9} e^{-28712/T}$	
R467	$NH_2 + N_2H_2 \rightarrow N_2H + NH_3$	$1.45 \times 10^{-25} T^{4.0} e^{809./T}$	Linder et al. 1996
R468	$N_2H + NH_3 \rightarrow NH_2 + N_2H_2$	$4.90 \times 10^{-28} T^{4.6} e^{-22385/T}$	
R469	$NH_3 + CH_3 \rightarrow NH_2 + CH_4$	$4.15 \times 10^{-21} T^{2.8} e^{-7340/T}$	Yu et al. 1998
R470	$NH_2 + CH_4 \rightarrow NH_3 + CH_3$	$2.49 \times 10^{-19} T^{2.4} e^{-6105/T}$	
R471	$N_2H + O \rightarrow N_2 + OH$	$4.31 \times 10^{-14} T^{0.70} e^{1167/T}$	Haworth et al. 2003
R472	$N_2 + OH \rightarrow N_2H + O$	$1.12 \times 10^{-15} T^{1.3} e^{-53880/T}$	
R473	$N_2H + H \rightarrow N_2 + H_2$	1.66×10^{-12}	Bozzelli & Dean 1995
R474	$N_2 + H_2 \rightarrow N_2H + H$	$5.65 \times 10^{-14} T^{0.71} e^{-55720/T}$	
R475	$N_2H + OH \rightarrow H_2O + N_2$	$3.97 \times 10^{-02} T^{-2.8} e^{-1230/T}$	Bozzelli & Dean 1995
R476	$H_2O + N_2 \rightarrow N_2H + OH$	$2.55 \times 10^{-01} T^{-2.6} e^{-64959/T}$	
R477	$N_2H_2 + H \rightarrow N_2H + H_2$	$1.40 \times 10^{-19} T^{2.6} e^{115./T}$	Linder et al. 1996
R478	$N_2H + H_2 \rightarrow N_2H_2 + H$	$2.26 \times 10^{-24} T^{3.6} e^{-20718/T}$	
R479	$N_2H_2 + OH \rightarrow N_2H + H_2O$	$9.82 \times 10^{-23} T^{3.4} e^{686/T}$	Linder et al. 1996
R480	$N_2H + H_2O \rightarrow N_2H_2 + OH$	$1.33 \times 10^{-26} T^{4.3} e^{-27554/T}$	
R481	$N_2H_3 + H \rightarrow NH_2 + NH_2$	2.66×10^{-12}	von Gehring et al. 1971
R482	$NH_2 + NH_2 \rightarrow N_2H_3 + H$	$2.40 \times 10^{-19} T^{1.4} e^{-4213/T}$	
R483	$N_2H_4 + O \rightarrow H_2O + N_2H_2$	$1.41 \times 10^{-10} e^{-602.5/T}$	von Gehring et al. 1969
R484	$H_2O + N_2H_2 \rightarrow N_2H_4 + O$	$7.05 \times 10^{-12} T^{0.4} e^{-45944/T}$	
R485	$N_2H_4 + C_2H_5 \rightarrow N_2H_3 + C_2H_6$	$8.32 \times 10^{-14} e^{-2310/T}$	Edwards et al. 1966
R486	$N_2H_3 + C_2H_6 \rightarrow N_2H_4 + C_2H_5$	$3.38 \times 10^{-11} T^{-0.31} e^{-14229/T}$	

Reaction Index	Reaction	Rate Expression	Reference
R487	$N_2H_4 + H \rightarrow N_2H_3 + H_2$	$1.17 \times 10^{-11} e^{-1260/T}$	Vaghijiani 1995
R488	$N_2H_3 + H_2 \rightarrow N_2H_4 + H$	$4.99 \times 10^{-13} T^{0.32} e^{-14543/T}$	
R489	$N_2H_4 + CH_3 \rightarrow N_2H_3 + CH_4$	$1.31 \times 10^{-24} T^{4.0} e^{-2037/T}$	Li & Zhang 2006
R490	$N_2H_3 + CH_4 \rightarrow N_2H_4 + CH_3$	$1.60 \times 10^{-21} T^{3.4} e^{-16590/T}$	
R491	$NO + C_2H_6 \rightarrow C_2H_5 + HNO$	$1.66 \times 10^{-10} e^{-26219/T}$	Laidler & Wojciechowski 1961
R492	$C_2H_5 + HNO \rightarrow NO + C_2H_6$	$6.46 \times 10^{-12} T^{0.026} e^{-561.8/T}$	
R493	$NO + {}^3CH_2 \rightarrow OH + HCN$	$8.32 \times 10^{-13} e^{-1439/T}$	Bauerle et al. 1995
R494	$OH + HCN \rightarrow NO + {}^3CH_2$	$1.84 \times 10^{-11} T^{-0.13} e^{-38810/T}$	
R495	$NO + CH \rightarrow O + HCN$	1.37×10^{-10}	Bergeat et al. 1998
R496	$O + HCN \rightarrow NO + CH$	$2.29 \times 10^{-07} T^{-0.52} e^{-37071/T}$	
R497	$NO + CH \rightarrow NCO + H$	4.00×10^{-11}	Bergeat et al. 1998
R498	$NCO + H \rightarrow NO + CH$	$1.98 \times 10^{-05} T^{-1.0} e^{-40691/T}$	
R499	$NO + C_2H_3 \rightarrow HCN + H_2CO$	$1.37 \times 10^{-02} T^{-3.3} e^{-540./T}$	Striebel et al. 2004
R500	$HCN + H_2CO \rightarrow NO + C_2H_3$	$4.06 \times 10^{-01} T^{-3.3} e^{-44749/T}$	
R501	$NO + CH_3 \rightarrow H_2O + HCN$	$4.00 \times 10^{-12} e^{-7899/T}$	Hennig & Wagner 1994
R502	$H_2O + HCN \rightarrow NO + CH_3$	$9.35 \times 10^{-12} T^{0.096} e^{-49486/T}$	
R503	$NO + HCO \rightarrow HNO + CO$	1.20×10^{-11}	Tsang & Herron 1991
R504	$HNO + CO \rightarrow NO + HCO$	$2.76 \times 10^{-10} T^{-0.12} e^{-17280/T}$	
R505	$NO + H_2CO \rightarrow HNO + HCO$	$1.69 \times 10^{-11} e^{-20446/T}$	Tsang & Herron 1991
R506	$HNO + HCO \rightarrow NO + H_2CO$	$8.68 \times 10^{2} T^{-6.2} e^{-51345/T}$	
R507	$NO + HCCO \rightarrow CO_2 + HCN$	$3.69 \times 10^{-10} T^{-0.72} e^{200/T}$	Carl et al. 2002
R508	$CO_2 + HCN \rightarrow NO + HCCO$	$3.21 \times 10^{-07} T^{-0.88} e^{-63730/T}$	
R509	$NO + CN \rightarrow NCO + N$	$1.60 \times 10^{-10} e^{-21167/T}$	Tsang 1992
R510	$NCO + N \rightarrow NO + CN$	$1.22 \times 10^{-05} T^{-1.0} e^{-12266/T}$	
R511	$NO + NO \rightarrow O_2 + N_2$	$5.15 \times 10^{-11} e^{-31751/T}$	Yuan et al. 1959
R512	$O_2 + N_2 \rightarrow NO + NO$	$1.17 \times 10^{-09} T^{.0087} e^{-53762/T}$	
R513	$HNO + CH_3O \rightarrow NO + CH_3OH$	5.25×10^{-11}	He et al. 1988
R514	$NO + CH_3OH \rightarrow HNO + CH_3O$	$1.22 \times 10^{-13} T^{1.0} e^{-26741/T}$	
R515	$HNO + H \rightarrow NO + H_2$	$1.64 \times 10^{-12} T^{0.62} e^{-179.2/T}$	Nguyen et al. 2004
R516	$NO + H_2 \rightarrow HNO + H$	$1.63 \times 10^{-15} T^{1.4} e^{-27050/T}$	
R517	$HNO + OH \rightarrow NO + H_2O$	$1.98 \times 10^{-15} T^{1.1} e^{-168.3/T}$	Nguyen et al. 2004

Reaction Index	Reaction	Rate Expression	Reference
R518	NO + H_2O → HNO + OH	$3.09 \times 10^{-17} T^{1.8} e^{-34571/T}$	
R519	HNO + CN → NO + HCN	3.00×10^{-11}	Tsang 1992
R520	NO + HCN → HNO + CN	$4.38 \times 10^{-11} T^{0.042} e^{-37676/T}$	
R521	NCO + O → NO + CO	7.51×10^{-11}	Tsang 1992
R522	NO + CO → NCO + O	$2.27 \times 10^{-15} T^{1.1} e^{-48013/T}$	
R523	NCO + O → O_2 + CN	$1.39 \times 10^{-06} T^{-1.4} e^{-3499/T}$	Tsang 1992
R524	O_2 + CN → NCO + O	$1.61 \times 10^{-10} T^{-0.46} e^{3457/T}$	
R525	NCO + H → O + HCN	$1.10 \times 10^{-13} T^{0.90} e^{-2920/T}$	Tsang 1992
R526	O + HCN → NCO + H	$1.56 \times 10^{-16} T^{1.4} e^{841.5/T}$	
R527	CN + H_2O → OH + HCN	$3.82 \times 10^{-11} e^{-6700/T}$	Wang et al. 2002
R528	OH + HCN → CN + H_2O	$6.35 \times 10^{-09} T^{-0.65} e^{-10072/T}$	
R529	CN + NH_3 → NH_2 + HCN	$1.52 \times 10^{-11} e^{180.4/T}$	Sims & Smith 1988
R530	NH_2 + HCN → CN + NH_3	$2.08 \times 10^{-10} T^{-0.44} e^{-8360/T}$	
R531	CN + OH → O + HCN	$1.00 \times 10^{-11} e^{-999.4/T}$	Tsang 1992
R532	O + HCN → CN + OH	$4.99 \times 10^{-08} T^{-0.79} e^{-12646/T}$	
R533	CN + HCO → CO + HCN	1.00×10^{-10}	Tsang 1992
R534	CO + HCN → CN + HCO	$1.18 \times 10^{-08} T^{-0.22} e^{-55174/T}$	
R535	CN + H_2 → H + HCN	$3.20 \times 10^{-20} T^{2.8} e^{-820.2/T}$	Baulch et al. 1994
R536	H + HCN → CN + H_2	$1.00 \times 10^{-16} T^{2.0} e^{-11768/T}$	
R537	CN + C_2H_2 → C_2H + HCN	2.20×10^{-10}	Sayah et al. 1988
R538	C_2H + HCN → CN + C_2H_2	$3.29 \times 10^{-10} T^{-0.27} e^{3837/T}$	
R539	CN + C_2H_4 → C_2H_3 + HCN	2.09×10^{-10}	Sayah et al. 1988
R540	C_2H_3 + HCN → CN + C_2H_4	$7.26 \times 10^{-11} T^{-0.14} e^{-6902/T}$	
R541	CN + C_2H_6 → C_2H_5 + HCN	$2.00 \times 10^{-19} T^{2.7} e^{899.6/T}$	Balla et al. 1991
R542	C_2H_5 + HCN → CN + C_2H_6	$6.24 \times 10^{-20} T^{2.5} e^{-11406/T}$	
R543	CN + CH_4 → CH_3 + HCN	$1.50 \times 10^{-19} T^{2.6} e^{150.3/T}$	Baulch et al. 1994
R544	CH_3 + HCN → CN + CH_4	$2.77 \times 10^{-20} T^{2.6} e^{-9597/T}$	
R545	CN + H_2CO → HCO + HCN	7.00×10^{-11}	Tsang 1992
R546	HCO + HCN → CN + H_2CO	$1.71 \times 10^{-10} T^{-0.28} e^{-18508/T}$	
R547	CN + OH → NCO + H	7.00×10^{-11}	Tsang 1992
R548	NCO + H → CN + OH	$2.03 \times 10^{-04} T^{-1.3} e^{-15382/T}$	

Reaction Index	Reaction	Rate Expression	Reference
R549	CN + CN → C_2 + N_2	1.66×10^{-11}	Baulch et al. 1981
R550	C_2 + N_2 → CN + CN	$4.72 \times 10^{-10} T^{-0.31} e^{-5456/T}$	
R551	HCN + O → NH + CO	$9.00 \times 10^{-16} T^{1.2} e^{-3849/T}$	Tsang & Herron 1991
R552	NH + CO → HCN + O	$4.57 \times 10^{-19} T^{2.0} e^{-19810/T}$	
R553	HCN + O → OH + CN	$3.29 \times 10^{-16} T^{1.4} e^{-3799/T}$	Tsang & Herron 1991
R554	OH + CN → HCN + O	$1.12 \times 10^{-19} T^{2.1} e^{7782/T}$	
R555	N_2 + $^3CH_2$→ HCN + NH	$8.00 \times 10^{-12} e^{-17999/T}$	Sanders et al. 1987
R556	HCN + NH → N_2 + $^3CH_2$	$1.87 \times 10^{-10} T^{-0.41} e^{-6137/T}$	
R557	N_2 + CH → HCN + N	$6.10 \times 10^{-17} T^{1.4} e^{-10400/T}$	Miller & Walch 1997
R558	HCN + N → N_2 + CH	$5.13 \times 10^{-14} T^{0.79} e^{-9652/T}$	
R559	N_2 + H → NH + N	$3.05 \times 10^{-11} T^{0.50} e^{-74459/T}$	Caridade et al. 2005
R560	NH + N → N_2 + H	$2.80 \times 10^{-13} T^{0.67} e^{-727.7/T}$	
R561	NO + NH → N_2 + OH	$1.01 \times 10^{-10} T^{-0.50} e^{-60.01/T}$	Bozzelli et al. 1994
R562	N_2 + OH → NO + NH	$1.30 \times 10^{-10} T^{-0.26} e^{-49338/T}$	
R563	C + NO → CN + O	$3.44 \times 10^{-10} T^{-0.32}$	Andersson et al. 2003
R564	CN + O → C + NO	$5.38 \times 10^{-10} T^{-0.29} e^{-14429/T}$	
R565	CH + N → CN + H	$2.77 \times 10^{-11} T^{-0.09}$	Brownsword et al. 1996
R566	CN + H → CH + N	$1.83 \times 10^{-10} T^{0.06} e^{-49568/T}$	
R567	NH_3 + O(^{1}D) → NH_2 + OH	2.51×10^{-10}	DeMore et al. 1997
R568	NO + O(^{1}D) → O + NO	4.00×10^{-11}	Doroshenko et al. 1992
R569	NO + $^1CH_2$→ OH + HCN	3.65×10^{-12}	Fikri et al. 2001
R570	OH + HCN → NO + $^1CH_2$	$1.80 \times 10^{-10} T^{-0.35} e^{-42181/T}$	
R571	H + H + M → H_2 + M	$k_0 = 2.70 \times 10^{-31} T^{-0.6}$	Baulch et al. 1992
		$k_\infty = 3.31 \times 10^{-06} T^{-1.0}$	Jacobs et al. 1965
R572	H_2 + M → H + H + M	$k_0 = 6.00 \times 10^{-07} T^{-0.6} e^{-52505/T}$	
		$k_\infty = 3.07 \times 10^{+18} T^{-0.9} e^{-52366/T}$	
R573	H + $^3CH_2$+ M → CH_3 + M	$k_0 = 3.40 \times 10^{-32} e^{-736.0/T}$	Moses et al. 2000a
		$k_\infty = 7.30 \times 10^{-12}$	Moses et al. 2000
R574	CH_3 + M → H + $^3CH_2$+ M	$k_0 = 4.14 \times 10^{-04} T^{-0.80} e^{-57301/T}$	
		$k_\infty = 1.70 \times 10^{+16} T^{-0.60} e^{-56199/T}$	
R575	H + CH_3 + M → CH_4 + M	$k_0 = 1.52 \times 10^{-23} T^{-2.1}$	Golden 2008

Reaction Index	Reaction	Rate Expression	Reference
		$k_\infty = 3.5 \times 10^{-10}$	Golden et al. 2008
R576	$CH_4 + M \rightarrow H + CH_3 + M$	$k_0 = 4.78 \times 10^{+08} T^{-3.7} e^{-55001/T}$	
		$k_\infty = 3.22 \times 10^{+20} T^{-1.1} e^{-54344T}$	
R577	$H + C_2H + M \rightarrow C_2H_2 + M$	$k_0 = 1.26 \times 10^{-18} T^{-3.1} e^{-721.0/T}$	Moses et al. 2000a/Tsang & Hampson 1986
		$k_\infty = 3.73 \times 10^{-11} T^{0.32}$	Harding et al. 2005
R578	$C_2H_2 + M \rightarrow H + C_2H + M$	$k_0 = 5.21 \times 10^{+09} T^{-3.6} e^{-67941/T}$	
		$k_\infty = 3.01 \times 10^{+17} T^{-0.28} e^{-67422/T}$	
R579	$H + C_2H_2 + M \rightarrow C_2H_3 + M$	$k_0 = 1.04 \times 10^{-07} T^{-7.2} e^{-3629/T}$	Tsang & Hampson 1986
		$k_\infty = 9.13 \times 10^{-12} e^{-1219/T}$	Warnatz 1984
R580	$C_2H_3 + M \rightarrow H + C_2H_2 + M$	$k_0 = 4.62 \times 10^{+16} T^{-7.2} e^{-21462/T}$	
		$k_\infty = 5.66 \times 10^{+11} T^{0.28} e^{-18830/T}$	
R581	$H + C_2H_3 + M \rightarrow C_2H_4 + M$	$k_0 = 1.50 \times 10^{-27}$	Moses et al. 2000a/Fahr et al. 1991
		$k_\infty = 6.46 \times 10^{-11} T^{0.20}$	Harding et al. 2005
R582	$C_2H_4 + M \rightarrow H + C_2H_3 + M$	$k_0 = 7.07 \times 10^{+02} T^{-1.0} e^{-57169/T}$	
		$k_\infty = 5.52 \times 10^{+18} T^{-0.64} e^{-56829/T}$	
R583	$H + C_2H_4 + M \rightarrow C_2H_5 + M$	$k_0 = 7.69 \times 10^{-30} e^{-380.0/T}$	Baulch et al. 1994
		$k_\infty = 2.81 \times 10^{-14} T^{1.0} e^{-730.0/T}$	Curran 2006
R584	$C_2H_5 + M \rightarrow H + C_2H_4 + M$	$k_0 = 6.27 \times 10^{-05} T^{-0.37} e^{-18804/T}$	
		$k_\infty = 3.83 \times 10^{+10} T^{0.91} e^{-18937/T}$	
R585	$H + C_2H_5 + M \rightarrow C_2H_6 + M$	$k_0 = 5.50 \times 10^{-22} T^{-2.0} e^{-1040/T}$	Moses et al. 2000a
		$k_\infty = 9.04 \times 10^{-11} T^{0.16}$	Harding et al. 2005
R586	$C_2H_6 + M \rightarrow H + C_2H_5 + M$	$k_0 = 1.10 \times 10^{+08} T^{-2.8} e^{-52604/T}$	
		$k_\infty = 3.99 \times 10^{+18} T^{-0.55} e^{-51300/T}$	
R587	$C + H_2 + M \rightarrow {}^3CH_2 + M$	$k_0 = 6.89 \times 10^{-32}$	Husain & Young 1975
		$k_\infty = 2.06 \times 10^{-11} e^{-57.00/T}$	Harding et al. 1993
R588	$^3CH_2 + M \rightarrow C + H_2 + M$	$k_0 = 1.63 \times 10^{-05} T^{-0.67} e^{-39749/T}$	
		$k_\infty = 2.90 \times 10^{+15} T^{-0.61} e^{-39754/T}$	
R589	$CH + H_2 + M \rightarrow CH_3 + M$	$k_0 = 3.40 \times 10^{-31} e^{736/T}$	Moses et al. 2000a/Becker et al. 1991
		$k_\infty = 7.30 \times 10^{-11}$	Moses et al. 2000a/Becker et al. 1991
R590	$CH_3 + M \rightarrow CH + H_2 + M$	$k_0 = 2.05 \times 10^{-02} T^{-0.96} e^{-54336/T}$	
		$k_\infty = 3.42 \times 10^{+18} T^{-0.93} e^{-55040/T}$	

Reaction Index	Reaction	Rate Expression	Reference
R591	O + H + M → OH + M	$k_0 = 1.29 \times 10^{-29} T^{-1.0}$	Tsang & Hampson 1986
R592	OH + M → O + H + M	$k_0 = 4.05 \times 10^{-06} T^{-0.85} e^{-51430/T}$	
R593	O + CO + M → CO_2 + M	$k_0 = 1.70 \times 10^{-33} e^{-1510/T}$	Tsang & Hampson 1986
		$k_\infty = 2.66 \times 10^{-14} e^{-1459/T}$	Simonaitis & Heieklen 1972
R594	CO_2 + M → O + CO + M	$k_0 = 3.48 \times 10^{-04} T^{-0.89} e^{-65280/T}$	
		$k_\infty = 2.96 \times 10^{+17} T^{-1.3} e^{-66272/T}$	
R595	OH + H + M → H_2O + M	$k_0 = 1.25 \times 10^{-26} T^{-1.8} e^{-251.0/T}$	Sellevag et al. 2008
		$k_\infty = 4.26 \times 10^{-11} T^{0.23} e^{57.49/T}$	Sellevag et al. 2008
R596	H_2O + M → OH + H + M	$k_0 = 1.11 \times 10^{+01} T^{-2.3} e^{-60985/T}$	
		$k_\infty = 5.59 \times 10^{+15} T^{0.068} e^{-60261/T}$	
R597	OH + CH_3 + M → CH_3OH + M	$k_0 = 4.37 \times 10^{-05} T^{-8.2}$	Baulch et al. 1994
		$k_\infty = 1.04 \times 10^{-10} T^{-0.02} e^{16.71/T}$	Jasper et al. 2007
R598	CH_3OH + M → OH + CH_3 + M	$k_0 = 4.24 \times 10^{+27} T^{-9.8} e^{-47865/T}$	
		$k_\infty = 1.11 \times 10^{+21} T^{-1.3} e^{-47436/T}$	
R599	OH + C_2H_2 + M → CH_3CO + M	$k_0 = 4.99 \times 10^{-25} T^{-2.0}$	Baulch et al. 1992
		$k_\infty = 1.06 \times 10^{-07} T^{-1.9}$	Baulch et al. 1992
R600	CH_3CO + M → OH + C_2H_2 + M	$k_0 = 1.41 \times 10^{+06} T^{-3.5} e^{-34293/T}$	
		$k_\infty = 1.12 \times 10^{+23} T^{-3.3} e^{-34137/T}$	
R601	OH + C_2H_3 + M → CH_3CHO+ M	$k_0 = 1.00 \times 10^{-31}$	Moses et al. 2000b
		$k_\infty = 5.00 \times 10^{-11}$	Tsang & Hampson 1986
R602	CH_3CHO + M → OH + C_2H_3 + M	$k_0 = 3.31 \times 10^{+01} T^{-1.6} e^{-61434/T}$	
		$k_\infty = 5.83 \times 10^{+22} T^{-1.7} e^{-61771/T}$	
R603	H_2O + CH + M → CH_2OH + M	$k_0 = 1.00 \times 10^{-31}$	Moses et al. 2000b
		$k_\infty = 9.48 \times 10^{-12} e^{380.0/T}$	Zabarnic et al. 1988
R604	CH_2OH + M → H_2O + CH + M	$k_0 = 1.40 \times 10^{-01} T^{-1.1} e^{-45041/T}$	
		$k_\infty = 8.11 \times 10^{+18} T^{-1.3} e^{-45034/T}$	
R605	CO + H + M → HCO + M	$k_0 = 5.29 \times 10^{-34} e^{-370.4/T}$	Baulch et al. 1994
		$k_\infty = 1.96 \times 10^{-13} e^{-1369/T}$	Arai 1981
R606	HCO + M → CO + H + M	$k_0 = 3.55 \times 10^{-09} T^{-0.34} e^{-8263/T}$	
		$k_\infty = 3.31 \times 10^{+11} T^{-0.16} e^{-6356/T}$	
R607	CO + CH_3 + M → CH_3CO + M	$k_0 = 3.95 \times 10^{-10} T^{-7.5} e^{-5490/T}$	Tsang & Hampson 1986

Reaction Index	Reaction	Rate Expression	Reference
		$k_\infty = 5.14 \times 10^{-19} T^{2.2} e^{-3033/T}$	Huynh et al. 2008
R608	$CH_3CO + M \rightarrow CO + CH_3 + M$	$k_0 = 1.46 \times 10^{+22} T^{-9.5} e^{-11778/T}$	
		$k_\infty = 1.05 \times 10^{+12} T^{0.62} e^{-8985/T}$	
R609	$HCO + CH_3 + M \rightarrow CH_3CHO + M$	$k_0 = 1.00 \times 10^{-31}$	Moses et al. 2000b
		$k_\infty = 3.00 \times 10^{-11}$	Tsang & Hampson 1986
R610	$CH_3CHO + M \rightarrow HCO + CH_3 + M$	$k_0 = 1.14 \times 10^{+03} T^{-2.0} e^{-44104/T}$	
		$k_\infty = 7.59 \times 10^{+22} T^{-1.9} e^{-43866/T}$	
R611	$H + H_2CO + M \rightarrow CH_3O + M$	$k_0 = 5.66 \times 10^{-34} T^{-0.10} e^{3966/T}$	Rev. k_0, R612
		$k_\infty = 3.99 \times 10^{-11} e^{-2068/T}$	Curran 2006
R612	$CH_3O + M \rightarrow H + H_2CO + M$	$k_0 = 1.28 \times 10^{-06} T^{-1.20} e^{-7800/T}$	Page et al. 1989
		$k_\infty = 6.14 \times 10^{+16} T^{-1.0} e^{-13795/T}$	
R613	$CH_3 + CH_3 + M \rightarrow C_2H_6 + M$	$k_0 = 3.50 \times 10^{-07} T^{-7.0} e^{-1390/T}$	Baulch et al. 1994
		$k_\infty = 1.58 \times 10^{-09} T^{-0.54} e^{-68.55/T}$	Klippenstein et al. 2006
R614	$C_2H_6 + M \rightarrow CH_3 + CH_3 + M$	$k_0 = 1.49 \times 10^{+28} T^{-9.1} e^{-48460/T}$	
		$k_\infty = 1.41 \times 10^{+25} T^{-2.4} e^{-46890/T}$	
R615	$C + N + M \rightarrow CN + M$	$k_0 = 9.40 \times 10^{-33}$	Kley et al. 1974
R616	$CN + M \rightarrow C + N + M$	$k_0 = 8.00 \times 10^{-15} T^{1.7} e^{-85016/T}$	
R617	$N + H_2 + M \rightarrow NH_2 + M$	$k_0 = 1.00 \times 10^{-26}$	Avramenko & Krasenkov 1966
R618	$NH_2 + M \rightarrow N + H_2 + M$	$k_0 = 7.46 \times 10^{-01} T^{-0.57} e^{-34710/T}$	
R619	$N + H + M \rightarrow NH + M$	$k_0 = 5.02 \times 10^{-32}$	Brown 1973
R620	$NH + M \rightarrow N + H + M$	$k_0 = 6.98 \times 10^{-08} T^{-0.11} e^{-40274/T}$	
R621	$N + O + M \rightarrow NO + M$	$k_0 = 6.89 \times 10^{-33} e^{135/T}$	Campbell & Thrush 1967
R622	$NO + M \rightarrow N + O + M$	$k_0 = 3.33 \times 10^{-11} T^{0.7} e^{-73377/T}$	
R623	$N + N + M \rightarrow N_2 + M$	$k_0 = 1.38 \times 10^{-33} e^{502.9/T}$	Clyne & Stedman 1967
		$k_\infty = 5.00 \times 10^{-16}$	Takahashi & Miyazaki 1977
R624	$N_2 + M \rightarrow N + N + M$	$k_0 = 0$	
		$k_\infty = 7.65 \times 10^{+10} T^{-0.29} e^{-11401/T}$	
R625	$NH_2 + CH_3 + M \rightarrow CH_3NH_2 + M$	$k_0 = 6.03 \times 10^{-18} T^{-3.8}$	Jodkowski et al. 1995
		$k_\infty = 1.18 \times 10^{-11} T^{0.42}$	Jodkowski et al. 1995
R626	$CH_3NH_2 + M \rightarrow NH_2 + CH_3 + M$	$k_0 = 9.13 \times 10^{+17} T^{-6.3} e^{-45394/T}$	
		$k_\infty = 9.69 \times 10^{+21} T^{-1.4} e^{-44520/T}$	

Reaction Index	Reaction	Rate Expression	Reference
R627	$NH_2 + H + M \rightarrow NH_3 + M$	$k_0 = 9.27 \times 10^{-35} T^{0.36} e^{7683/T}$	Rev. k_0, R628
		$k_\infty = 3.96 \times 10^{-09} T^{0.24} e^{5764/T}$	Rev. k_∞, R628
R628	$NH_3 + M \rightarrow NH_2 + H + M$	$k_0 = 4.17 \times 10^{-08} e^{-47200/T}$	Hanson & Salimian 1984
		$k_\infty = 6.60 \times 10^{+17} e^{-48955/T}$	Cardelino et al. 2003
R629	$H + N_2 + M \rightarrow N_2H + M$	$k_0 = 7.08 \times 10^{-35} T^{0.22} e^{-6256/T}$	Rev. k_0, R630
		$k_\infty = 6.77 \times 10^{-09} T^{-0.16} e^{-7116/T}$	Rev. k_∞, R630
R630	$N_2H + M \rightarrow H + N_2 + M$	$k_0 = 2.15 \times 10^{-10} T^{-0.11} e^{-2509/T}$	Bozzelli & Dean 1995
		$k_\infty = 2.66 \times 10^{+16} T^{-0.53} e^{-3403/T}$	Caridade et al. 2005
R631	$NO + H + M \rightarrow HNO + M$	$k_0 = 9.57 \times 10^{-29} T^{-1.1} e^{-212.0/T}$	Tsang & Herron 1991
		$k_\infty = 2.52 \times 10^{-09} T^{-0.41}$	Tsang & Herron 1991
R632	$HNO + M \rightarrow NO + H + M$	$k_0 = 3.09 \times 10^{-01} T^{-2.0} e^{-25912/T}$	
		$k_\infty = 1.29 \times 10^{+17} T^{-0.72} e^{-25112/T}$	
R633	$CN + H + M \rightarrow HCN + M$	$k_0 = 8.30 \times 10^{-25} T^{-2.0} e^{-521.0/T}$	Tsang 1992
		$k_\infty = 2.98 \times 10^{-09} T^{-0.50}$	Tsang 1992
R634	$HCN + M \rightarrow CN + H + M$	$k_0 = 1.28 \times 10^{+03} T^{-2.6} e^{-63557/T}$	
		$k_\infty = 3.55 \times 10^{+19} T^{-1.3} e^{-63565/T}$	
R635	$NH_2 + NH_2 + M \rightarrow N_2H_4 + M$	$k_0 = 8.74 \times 10^{-20} T^{-3.9}$	Fagerstrom et al. 1995
		$k_\infty = 2.53 \times 10^{-11} T^{0.27}$	Fagerstrom et al. 1995
R636	$N_2H_4 + M \rightarrow NH_2 + NH_2 + M$	$k_0 = 6.00 \times 10^{+13} T^{-5.7} e^{-35018/T}$	
		$k_\infty = 5.61 \times 10^{+21} T^{-1.3} e^{-34855/T}$	
R637	$N + CH_3CHO \rightarrow HCO + H_2 + HCN$	1.99×10^{-14}	Lambert et al. 1968
R638	$HCO + H_2 + HCN \rightarrow N + CH_3CHO$	$4.47 \times 10^{-54} T^{3.72} e^{-10704/T}$	
R639	$N + CH_4 \rightarrow H + H_2 + HCN$	2.51×10^{-14}	Takahashi 1972
R640	$H + H_2 + HCN \rightarrow N + CH_4$	$8.35 \times 10^{-42} T^{0.65} e^{-4748/T}$	
R641	$2NH \rightarrow 2H + N_2$	1.16×10^{-9}	Meaburn & Gordon 1968
R642	$2H + N_2 \rightarrow 2NH$	$5.19 \times 10^{-33} T^{0.28} e^{-32806/T}$	
R643	$NH_2 + NO \rightarrow H + N_2 + OH$	1.49×10^{-12}	VanDooren et al. 1994
R644	$H + N_2 + OH \rightarrow NH_2 + NO$	$7.27 \times 10^{-37} T^{0.22} e^{-2991/T}$	
R645	$2N_2H_3 \rightarrow N_2 + N_2H_4 + H_2$	6.00×10^{-11}	est. based on Pagsberg et al. 1979
R646	$N_2 + N_2H_4 + H_2 \rightarrow 2N_2H_3$	$2.95 \times 10^{-52} T^{4.7} e^{-29974/T}$	
R647	$NO + C_2H_2 \rightarrow H + CO + HCN$	$8.97 \times 10^{-12} e^{-19001/T}$	Benson 1994

Reaction Index	Reaction	Rate Expression	Reference
R648	H + CO + HCN → NO + C_2H_2	$4.46 \times 10^{-42} T^{1.7} e^{-26590/T}$	
R649	2NCO → N_2 + 2CO	3.00×10^{-11}	Tsang 1992
R650	N_2 + 2CO →2NCO	0	
R651	N_2 + H_2 → 2NH	$8.45 \times 10^{-08} e^{-81515/T}$	Fegley & Lodders 1994
R652	2NH →N_2 + H_2	$5.29 \times 10^{-10} e^{4436/T}$	
R653	CH_3NH_2+ H → CH_2NH_2+ H_2	$9.30 \times 10^{-16} T^{1.5} e^{-2750./T}$	Dean & Bozzelli 2000
R654	CH_2NH_2+ H_2 → CH_3NH_2+ H	$1.18 \times 10^{-17} T^{1.7} e^{-7484./T}$	
R655	CH_2NH + H → H_2CN + H_2	$4.00 \times 10^{-16} T^{1.5} e^{-3685./T}$	Dean & Bozzelli 2000
R656	H_2CN + H_2 → CH_2NH + H	$2.90 \times 10^{-18} T^{1.9} e^{-10641/T}$	
R657	CH_2NH_2 → CH_2NH + H	$3.2 \times 10^{+46} T^{-9.9} e^{-26940/T}$	Dean & Bozzelli 2000
R658	CH_2NH + H → V + CH_2NH_2	$6.50 \times 10^{+19} T^{-9.2} e^{-8008/T}$	
R659	H_2CN + CH_3 → HCN + CH_4	$1.34 \times 10^{-18} T^{1.8} e^{560.0/T}$	Dean & Bozzelli 2000
R660	HCN + CH_4 → H_2CN + CH_3	$4.53 \times 10^{-15} T^{1.3} e^{-40463/T}$	
R661	H_2CN + OH → HCN + H_2O	$1.99 \times 10^{-18} T^{2.0} e^{600.0/T}$	Dean & Bozzelli 2000
R662	HCN + H_2O → H_2CN + OH	$7.01 \times 10^{-19} T^{2.4} e^{-46392/T}$	
R663	H_2CN + H → HCN + H_2	$3.98 \times 10^{-16} T^{1.5} e^{450.0/T}$	Dean & Bozzelli 2000
R664	HCN + H_2 → H_2CN + H	$4.49 \times 10^{-18} T^{2.1} e^{-38892/T}$	
R665	H_2CN + NH_2 → HCN + NH_3	$1.52 \times 10^{-18} T^{1.9} e^{580.0/T}$	Dean & Bozzelli 2000
R666	HCN + NH_3 → H_2CN + NH_2	$9.66 \times 10^{-18} T^{2.0} e^{-41317/T}$	
R667	H_2CN + O → HCN + OH	$2.82 \times 10^{-16} T^{1.5} e^{450.0/T}$	Dean & Bozzelli 2000
R668	HCN + OH → H_2CN + O	$1.81 \times 10^{-18} T^{2.1} e^{-38174/T}$	
R669	CH_3 + NO → H_2CN + OH	$3.65 \times 10^{-15} T^{0.75} e^{-5900./T}$	Dean & Bozzelli 2000
R670	H_2CN + OH → CH_3 + NO	$1.40 \times 10^{-14} T^{0.50} e^{-392.9/T}$	
R671	CH_3 + N → H_2CN + H	$1.01 \times 10^{-09} T^{-0.31} e^{-145.0/T}$	Dean & Bozzelli 2000
R672	H_2CN + H → CH_3 + N	$1.57 \times 10^{-07} T^{-0.87} e^{-18931/T}$	
R673	$^3CH_2$ +NO →H_2CN +O	$1.34 \times 10^{-16} T^{1.4} e^{-2070./T}$	Dean & Bozzelli 2000
R674	H_2CN + O → $^3CH_2$+ NO	$2.10 \times 10^{-13} T^{0.76} e^{-689.6/T}$	
R675	CH_2NH + O → H_2CN + OH	$2.82 \times 10^{-16} T^{1.5} e^{-2330./T}$	Dean & Bozzelli 2000
R676	H_2CN + OH → CH_2NH + O	$1.38 \times 10^{-18} T^{1.9} e^{-8597./T}$	
R677	CH_2NH + OH → H_2CN + H_2O	$1.99 \times 10^{-18} T^{2.0} e^{45.00/T}$	Dean & Bozzelli 2000
R678	H_2CN + H_2O → CH_2NH + OH	$2.53 \times 10^{-19} T^{2.3} e^{-14476/T}$	

Reaction Index	Reaction	Rate Expression	Reference
R679	$CH_2NH + CH_3 \rightarrow H_2CN + CH_4$	$1.36 \times 10^{-18} T^{1.8} e^{-3585./T}$	Dean & Bozzelli 2000
R680	$H_2CN + CH_4 \rightarrow CH_2NH + CH_3$	$1.67 \times 10^{-16} T^{1.5} e^{-11742/T}$	
R681	$CH_2NH + NH_2 \rightarrow H_2CN + NH_3$	$1.52 \times 10^{-18} T^{1.9} e^{-2235./T}$	Dean & Bozzelli 2000
R682	$H_2CN + NH_3 \rightarrow CH_2NH + NH_2$	$2.55 \times 10^{-18} T^{2.0} e^{-11598/T}$	
R683	$CH_3 + NH_2 \rightarrow CH_2NH + H_2$	$4.81 \times 10^{-12} T^{-0.40} e^{-10320/T}$	Dean & Bozzelli 2000
R684	$CH_2NH + H_2 \rightarrow CH_3 + NH_2$	$2.35 \times 10^{-08} T^{-1.1} e^{-40293/T}$	
R685	$NH + CH_3 \rightarrow CH_2NH + H$	6.64×10^{-11}	Dean & Bozzelli 2000
R686	$CH_2NH + H \rightarrow NH + CH_3$	$3.30 \times 10^{-06} T^{-0.96} e^{-24113/T}$	
R687	$CH_2NH_2+ H \rightarrow CH_2NH + H_2$	$6.64 \times 10^{-16} T^{1.5} e^{450.0/T}$	Dean & Bozzelli 2000
R688	$CH_2NH + H_2 \rightarrow CH_2NH_2+ H$	$4.13 \times 10^{-19} T^{2.4} e^{-32773/T}$	
R689	$CH_2NH_2+ CH_3 \rightarrow CH_2NH + CH_4$	$2.65 \times 10^{-18} T^{1.8} e^{315.0/T}$	Dean & Bozzelli 2000
R690	$CH_2NH + CH_4 \rightarrow CH_2NH_2+ CH_3$	$4.20 \times 10^{-16} T^{1.7} e^{-34561/T}$	
R691	$CH_2NH_2+ OH \rightarrow CH_2NH + H_2O$	$3.98 \times 10^{-18} T^{2.0} e^{600.0/T}$	Dean & Bozzelli 2000
R692	$CH_2NH + H_2O \rightarrow CH_2NH_2+ OH$	$1.32 \times 10^{-19} T^{2.6} e^{-40377/T}$	
R693	$CH_3NH_2+ OH \rightarrow CH_2NH_2+ H_2O$	$5.97 \times 10^{-18} T^{2.0} e^{-120.0/T}$	Dean & Bozzelli 2000
R694	$CH_2NH_2+ H_2O \rightarrow CH_3NH_2+ OH$	$1.15 \times 10^{-18} T^{2.0} e^{-12401/T}$	
R695	$CH_3NH_2+ CH_3 \rightarrow CH_2NH_2+ CH_4$	$2.49 \times 10^{-18} T^{1.8} e^{-4615./T}$	Dean & Bozzelli 2000
R696	$CH_2NH_2+ CH_4 \rightarrow CH_3NH_2+ CH_3$	$4.35 \times 10^{-16} T^{1.2} e^{-10522/T}$	
R697	$CH_3NH_2+ NH_2 \rightarrow CH_2NH_2+ NH_3$	$4.64 \times 10^{-18} T^{1.9} e^{-2765./T}$	Dean & Bozzelli 2000
R698	$CH_2NH_2+ NH_3 \rightarrow CH_3NH_2+ NH_2$	$1.20 \times 10^{-17} T^{1.7} e^{-9890./T}$	
R699	$HCN + H + M \rightarrow H_2CN + M$	$k_0 = 4.40 \times 10^{-24} T^{-2.7} e^{-3859/T}$	Tsang & Herron 1991
		$k_\infty = 5.50 \times 10^{-11} e^{-2440/T}$	Tsang & Herron 1991
R700	$H_2CN + M \rightarrow HCN + H + M$	$k_0 = 1.13 \times 10^{+03} T^{-3.1} e^{-16657/T}$	
		$k_\infty = 7.21 \times 10^{+13} T^{0.02} e^{-14877/T}$	
R701	$H_2S + H \rightarrow HS + H_2$	$1.96 \times 10^{-17} T^{2.1} e^{-352/T}$	Youshimura et al. 1992
R702	$HS + H_2 \rightarrow H_2S + H$	$3.25 \times 10^{-19} T^{2.5} e^{-6633/T}$	
R703	$H_2S + OH \rightarrow H_2O + HS$	$1.61 \times 10^{-11} e^{-541/T}$	Mousavipour et al. 2003
R704	$H_2O + HS \rightarrow H_2S + OH$	$4.35 \times 10^{-12} T^{0.3} e^{-14378/T}$	

Bibliography

Adachi, H., Basco, N., James, D.G.L. 1981, Int. J. Chem. Kinet. 13, 1251

Andersson, S., Markovic, N., Nyman, G. 2003, J. Phys. Chem. A 107, 5439

Arai, H., Nagai, S., Hatada, M. 1981, Radiat. Phys. Chem. 17, 211

Atkinson, R., Baulch, D.L., Cox, R.A.,Hampson Jr., R.F., Kerr, J.A., Troe, J. 1992, J. Phys. Chem. Ref. Data 21, 1125

Avramenko, L.I., Krasnen'kov, V.M. 1966, Bull. Acad. Sci. USSR Div. Chem. Sci. (Engl. Transl.) 0, 394

Balla, R.J., Casleton, K.H., Adams, J.S., Pasternack, L. 1991, J. Phys. Chem. 95, 8694

Banyard, S.A., Canosa-Mas, C.E., Ellis, M.D., Frey, H.M., Walsh, R. 1980, J. Chem. Soc. Chem. Commun. 0, 1156

Bartels, M., Hoyermann, K., Sievert, R. 1982, Symp. Int. Combust. Proc. 19, 61

Bauerle, S., Klatt, M., Wagner, H.Gg. 1995, Ber. Bunsenges. Phys. Chem. 99, 97

Baulch, D.L., Cobos, C.J., Cox, R.A., Esser, C., Frank, P., Just, Th., Kerr, J.A., Pilling, M.J., Troe, J., Walker, R.W., Warnatz, J. 1992, J. Phys. Chem. Ref. Data 21, 411

Baulch, D.L., Cobos, C.J., Cox, R.A., Frank, P., Hayman, G., Just, Th., Kerr, J.A., Murrells, T., Pilling, M.J., Troe, J., Walker, R.W., Warnatz, J. 1994, J. Phys. Chem. Ref. Data 23, 847

Becker, K.H., Kurtenbach, R., Wiesen, P. 1991, J. Phys. Chem. 95, 2390

Benson, S.W., 1994, Int. J. Chem. Kinet. 26, 997

Bergeat, A., Calvo, T., Daugey, N., Loison, J.C., Dorthe, G. 1998, J. Phys. Chem. A 102, 8124

Bohland, T., Dobe, S., Temps, F., Wagner, H.Gg. 1985, Ber. Bunsenges. Phys. Chem. 89, 1110

Bozzelli, J.W., Chang, A., Dean, A.M., 1994 Symp. Int. Combust. Proc. 25, 965

Bozzelli, J.W., Dean, A.M. 1995, Int. J. Chem. Kinet. 27, 1097

Braun, W., Bass, A.M., Pilling, M. 1970, J. Chem. Phys. 52, 5131

Brouard, M., Macpherson, M.T., Pilling, M.J. 1989, J. Phys. Chem. 93, 4047

Brown, R.L. 1973, Int. J. Chem. Kinet. 5, 663

Brownsword, R.A., Gatenby, S.D., Herbert, L.B., Smith, I.W.M., Stewart, D.W.A., Symonds, A.C. 1996, J. Chem. Soc. Faraday Trans. 92, 723

Campbell, I.M., Thrush, B.A. 1967, Proc. R. Soc. London 296, 222

Cardelino, B.H., Moore, C.E., Cardelino, C.A., McCall, S.D., Frazier, D.O., Bachmann, K.J., 2003, J. Phys. Chem. A 107, 3708

Caridade, P.JSB., Rodrigues, S.PJ., Sousa, F., Varandas, A.JC. 2005, J. Phys. Chem. A 109, 2356

Caridade, P.JSB., Rodrigues, S.PJ., Sousa, F., Varandas, A.JC., 2005 J. Phys. Chem. A 109, 2356

Caridade, P.JSB., Rodrigues, S.PJ., Sousa, F., Varandas, A.JC., 2005, J. Phys. Chem. A 109, 2356

Carl, S.A., Sun, Q., Vereecken, L., Peeters, J. 2002, J. Phys. Chem. A 106, 12242

Clyne, M.A.A., Stedman, D.H., 1967, J. Phys. Chem. 71,3071

Cobos, C.J., Troe, J. 1985, J. Chem. Phys. 83, 1010

Cohen, N., Westberg, K.R. 1991, J. Phys. Chem. Ref. Data 20, 1211

Corchado, J.C., Espinosa-Garcia, J. 1997, J. Chem. Phys. 106, 4013

Curran, H.J. 2006, Int. J. Chem. Kinet. 38, 250

Cvetanovic, R.J. 1987, J. Phys. Chem. Ref. Data 16, 261

Davidson, D.F., Kohse-Hoinghaus, K., Chang, A.Y., Hanson, R.K. 1990, Int. J. Chem. Kinet. 22, 513

Dean, A.J., Davidson, D.F., Hanson, R.K. 1991, J. Phys. Chem. 95, 183

DeMore, W.B., Sander, S.P., Golden, D.M., Hampson, R.F., Kurylo, M.J., Howard, C.J., Ravishankara, A.R., Kolb, C.J., Molina, M.J. 1994, JPL Publication 94-26,1

DeMore, W.B., Sander, S.P., Golden, D.M., Hampson, R.F., Kurylo, M.J., Howard, C.J., Ravishankara, A.R., Kolb, C.J., Molina, M.J. 1997, JPL Publication 97-40, 1

Duff, J.W., Sharma, R.D. 1996, Geophys. Res. Lett. 23, 2777

Edwards, D.A., Kerr, J.A., Lloyd, A.C., Trotman-Dickenson, A.F. 1966, J. Chem. Soc. A 0, 1500

Fagerstrom, K., Jodkowski, J.T., Lund, A., Ratajczak, E., 1995, Chem. Phys. Lett. 236, 103

Fegley, B., Lodders, K., 1994, Icarus 110, 117 Fahr, A., Laufer, A., Klein, R., Braun, W. 1991, J. Phys. Chem. 95, 3218

Frank, P., Bhaskaran, K.A., Just, Th. 1986, J. Phys. Chem. 90, 2226

Frank, P., Bhaskaran, K.A., Just, Th. 1988, Symp. Int. Combust. Proc. 21, 885

Golden, D.M. 2008, Int. J. Chem. Kinet. 40, 310

Grotheer, H.H., Just, T. 1981, Chem. Phys. Lett. 78, 71

Hanson, R.K., Salimian, S., 1984, Combustion Chemistry, ed. W.C. Gardiner, Jr., Springer-Verlag, NY

Harding, L.B., Georgievskii, Y., Klippenstein, S.J. 2005, J. Phys. Chem. A 109, 4646

Harding, L.B., Guadagnini, R., Schatz, G.C. 1993, J. Phys. Chem. 97, 5472

Hassinen, E., Kalliorinne, K., Koskikallio, J. 1990, Int. J. Chem. Kinet. 22, 741

Haworth, N.L., Mackie, J.C., Bacskay, G.B. 2003, J. Phys. Chem. A 107, 6792

He, Y., Sanders, W.A., Lin, M.C. 1988, J. Phys. Chem., 92, 5474

Hennig, G., Wagner, H.Gg. 1994, Ber. Bunsenges. Phys. Chem. 98, 749

Herron, J.T. 1988, J. Phys. Chem. Ref. Data 17, 967

Hidaka, Y., Oki, T., Kawano, H. 1989, J. Phys. Chem. 93, 7134

Husain, D., Young, A.N. 1975, J. Chem. Soc. Faraday Trans. 2 71, 525

Huynh, L.K., Violi, A. 2008, J. Org. Chem. 73, 94

Jacobs, T.A., Giedt, R.R., Cohen, N. 1965, J. Chem. Phys. 43, 3688

Jasper, A.W., Klippenstein, S.J., Harding, L.B., Ruscic, B. 2007, J. Phys. Chem. A 111, 3932

Jodkowski, J.T., Ratajczak, E., Fagerstrom, K., Lund, A., Stothard, N.D., Humpfer, R., Grotheer, H-H., 1995, Chem. Phys. Lett. 240, 63

Jodkowski, J.T., Rayez, M.-T., Rayez, J.-C., 1999 J. Phys. Chem. A 103, 3750

Kelly, N., Heicken, J. 1978, J. Photochem. 8, 83

Kley, D., Washida, N., Groth, W. 1974, Ber. Bunsenges. Phys. Chem. 78, 205

Klippenstein, S.J., Georgievskii, Y., Harding, L.B. 2006, Phys. Chem. Chem. Phys. 8, 1133

Koshi, M., Yoshimura, M., Fukuda, K., Matsui, H. 1990, J. Chem. Phys. 93, 8703

Laidler, K.J., Wojciechowski, B.W. 1961, Proc. R. Soc. London A 260, 103

Lambert, R.M., Christie, M.I., Golesworthy, R.C., Linnett, J.W., 1968, Proc. R. Soc. London A 302

Langford, A.O., Petek, H., Moore, C.B. 1983, J. Chem. Phys. 78, 6650

Li, Q.S., Zhang, Y., Zhang, S.W. 2004, J. Chem. Phys., 121, 9474

Li, Q.S., Zhang, X. 2006, J. Chem. Phys. 125, 64304

Li, S.C., Williams, F.A., 1996, Symp. Int. Combust. Proc. 26, 1017

Linder, D.P., Duan, X., Page, M. 1996, J. Chem. Phys. 104, 6298

Marston, G., Nesbitt, F.L., Stief, L.J. 1989, J. Chem. Phys. 91, 3483

Mayer, S.W., Schieler, L. 1966, J. Chem. Phys. 45, 385

Meaburn, G.M., Gordon, S., 1968, J. Phys. Chem. 72

Mebel, A.M., Moskaleva, L.V., Lin, M.C. 1999, J. Mol. Struct. Thermochem. 461, 223

Miller, J.A., Melius, C.F. 1992, Symp. Int. Combust. Proc. 24, 719

Miller, J.A., Walch, S.P. 1997, Int. J. Chem. Kinet. 29, 253

Moses, J.I., Bezard, B., Lellouch, E., Gladstone, R.G., Feuchtgruber, H., Allen, M. 2000a, Icarus, 143, 244

Moses, J.I., Bezard, B., Lellouch, E., Gladstone, R.G., Feuchtgruber, H., Allen, M. 2000b, Icarus, 145, 166

Mousavipour, S.H., Namdar-Ghanbari, M.A., Sadeghian, L., 2003, J. Phys. Chem. A 107, 3752

Nguyen, H.MT., Zhang, S.W., Peeters, J., Truong, T.N., Nguyen, M.T. 2004, Chem. Phys. Lett. 388, 94

Page, M., Lin, M.C., He, Y., Choudhury, T.K. 1989, J. Phys. Chem. 93, 4404

Pagsberg, P.B., Eriksen, J., Christensen, 1979, H.C., J. Phys. Chem. 83

Paraskevopoulos, G., Winkler, C.A. 1967, J. Phys. Chem. 71, 947

Park, J., Lin, M.C. 1999, J. Phys. Chem. A 103, 8906

Pitts, W.M., Pasternack, L., McDonald, J.R. 1982, Chem. Phys. 68, 417

Rohrig, M., Wagner, H.G. 1994, Symp. Int. Combust. Proc. 25, 975

Romming, H.J., Wagner, H.Gg. 1996, Symp. Int. Combust. Proc. 26, 559

Sanders, W.A., Lin, C.Y., Lin, M.C. 1987, Combust. Sci. Technol. 51, 103

Sayah, N., Li, X., Caballero, J.F., Jackson, W.M. 1988, J. Photochem. Photobiol. A 45, 177

Scherzer, K., Loser, U., Stiller, W. 1987, Z. Chem. 27, 300

Sellevag, S.R., Georgievskii, Y., Miller, J.A. 2008, J. Phys. Chem. A 112, 5085

Senosiain, J.P., Klippenstein, S.J., Miller, J.A. 2006, J. Phys. Chem. A 110, 5772

Simonaitis, R., Heicklen, J. 1972, J. Chem. Phys. 56, 2004

Sims, I.R., Smith, I.W.M. 1988, J. Chem. Soc. Faraday Trans. 2 84, 527

Srinivasan, N.K., Su, M.C., Sutherland, J.W., Michael, J.V. 2005, J. Phys. Chem. A 109, 1857

Stothard, N., Humpfer, R., Grotheer, H-H. 1995, Chem. Phys. Lett. 240, 474

Striebel, F., Jusinski, L.E., Fahr, A., Halpern, J.B., Klippenstein, S.J., Taatjes, C.A. 2004, Phys. Chem. Chem. Phys. 6, 2216

Takahashi, S., 1972, Mem. Def. Acad., Math., Phys., Chem. Eng. 12

Tsang, W. 1987, J. Phys. Chem. Ref. Data 16, 471

Tsang, W. 1992, J. Phys. Chem. Ref. Data 21, 753

Tsang, W., Hampson, R.F. 1986, J. Phys. Chem. Ref. Data 15, 1087

Tsang, W., Herron, J.T. 1991, J. Phys. Chem. Ref. Data 20, 609

Tully, J.C. 1975, J. Chem. Phys. 62, 1893

Vaghjiani, G.L. 1995, Int. J. Chem. Kinet., 27, 777

Valli, G.S., Orru, R., Clementi, E., Lagana, A., Crocchianti, S., 1995 J. Chem. Phys. 102, 2825

VanDooren, J., Bian, J., Van Tiggelen, P.J., 1994, Combust. Flame 98, 402

von Gehring, M., Hoyermann, K., Wagner, H.G., Wolfrum, J. 1969, Ber. Bunsenges. Phys. Chem. 73, 956

von Gehring, M., Hoyermann, K., Wagner, H.Gg., Wolfrum, J. 1971, Ber. Bunsenges. Phys. Chem. 75, 1287

Wang, B., Hou, H., Gu, Y. 1999, J. Phys. Chem. A., 103, 9049

Wang, C.Y., Zhang, S.E., Li, Q.S. 2002, Theor. Chem. Acct. 108, 341

Warnatz, J 1984, ”Rate Coefficients in the C/H/O System”, Combustion Chemistry by Gardiner, Springer-Verlag, NY

Xu, Z.-F., Li, S.-M., Yu, Y.-X., Li, Z.-S., Sun, C.-C. 1999, J. Phys. Chem. A 103, 4910

Yoshimura, M., Koshi, M., Matsui, H., Kamiya, K., Umeyama, H.,1992, Chem. Phys.

Lett. 189, 199

Yu, Y-X., Li, S-M., Xu, Z-F., Li, Z-S., Sun, C-C. 1998, Chem. Phys. Lett. 296, 131

Yuan, E.L., Slaughter, J.I., Koerner, W.E., Daniels, F. 1959, J. Phys. Chem. 63, 952

Zabarnick, S., Fleming, J.W., Lin, M.C. 1986, J. Chem. Phys. 85, 4373

Zabarnick, S., Fleming, J.W., Lin, M.C. 1988, Symp. Int. Combust. Proc. 21, 713

Zu, Z-F., Fang, D-C., Fu, X-Y. 1997, Chem. Phys. Lett. 275, 386